

# **Experimental Investigation and Modeling the Heat of Hydration in Mass Concrete Structures**

BY  
**Muneer Qaid Saeed**

A Dissertation Presented to the  
DEANSHIP OF GRADUATE STUDIES

**KING FAHD UNIVERSITY OF PETROLEUM & MINERALS**

DHAHRAN, SAUDI ARABIA

In Partial Fulfillment of the  
Requirements for the Degree of

**DOCTOR OF PHILOSOPHY**

In  
**CIVIL ENGINEERING**

**December 2013**

KING FAHD UNIVERSITY OF PETROLEUM AND MINERALS

DHAHRAN, SAUDI ARABIA  
DEANSHIP OF GRADUATE STUDIES

This dissertation, written by **Muneer Qaid Saeed** under the direction of his Dissertation advisor and approved by his Dissertation committee, has been presented to and accepted by the Dean of Graduate Studies, in partial fulfillment of the requirements for the degree of **DOCTOR OF PHILOSOPHY IN CIVIL ENGINEERING**.

DISSERTATION COMMITTEE



Dr. Mohammed H. Baluch (Chairman)



DR. Muhammed K. Rahman (Co — Chairman)




DR. Ali H. Al-Gadhib (Member)




DR. Omar S.B. Al-Amoudi (Member)



DR. Shamshad Ahmad (Member)

  
DR. Nedal Ratrouf  
(Department Chairman)

  
DR. Salam Zummo  
(Dean of Graduate Studies)

Date

19/2/14

09 FEB 2013



*This dissertation  
is dedicated to  
my parents and my wife  
for their  
Innumerable prayers,  
encouragement and patience*

## ACKNOWLEDGEMENTS

My thanks and gratitude go first to ALLAH, my Creator, for his endless blessing. Then, I would like to thank my advisor, Dr. Mohammed H. Baluch, for his continued attention, guidance, and support throughout this work. I also would like to express my sincere gratitude to Dr. M.K.Rahman, my co-advisor, for his guidance, efforts and valuable support. I also would like to thank my dissertation committee members, Dr. Ali H.Al.Gadhib, Prof. .Omar S. Baghabra. Al- AMoudi and Dr. Shamshad Ahmad, for their valuable suggestions and comments. I am grateful to the laboratory personnel, Mr. Mukaram and Mr. Omar, for their help and assistance.

I would like to express my sincere thanks to Saudi Ready Mix Company, especially Mr. Radwan Hameed, and Mr. Kaldoon Saliaia, for giving me a chance to work in their lab and to use their facilities such as iQdrum calorimeter and mixer. This work would not have been completed without their support.

I would like to extend my sincerest thanks to my friend Eng. Lutf Tooti for his assistance in preparing the mockup specimens during summer months.

I would like to acknowledge the Deanship of Scientific Research, King Fahd University of Petroleum and Minerals (KFUPM) for the financial support provided under research Grant No. RG 1222-1&2. The Research Institute in King Fahd University of Petroleum and Minerals (KFUPM) is also acknowledged.

Finally, thanks to my parents, my wife, and my sons, Ayman and Ayham for their love, patience, and encouragement.



## TABLE OF CONTENTS

<b>ACKNOWLEDGEMENTS .....</b>	<b>iii</b>
<b>LIST OF TABLES.....</b>	<b>ix</b>
<b>LIST OF FIGURES.....</b>	<b>xii</b>
<b>NOMENCLATURE .....</b>	<b>xxv</b>
<b>THESIS ABSTRACT .....</b>	<b>xxviii</b>
<b>THESIS ABSTRACT (ARABIC).....</b>	<b>xxx</b>
<b>1 CHAPTER 1 INTRODUCTION.....</b>	<b>1</b>
1.1 Need for Research.....	4
1.2 Research Approach .....	6
1.3 Project Objectives .....	7
<b>2 CHAPTER 2 LITERATURE REVIEW.....</b>	<b>9</b>
2.1 Introduction.....	9
2.2 Hydration of Portland Cement Concrete .....	9
2.2.1 Heat of Hydration Stages .....	11
2.3 Properties of Cementitious Materials .....	13
2.3.1 Ordinary Portland cement (OPC) .....	13
2.3.2 Fly Ash.....	16
2.3.3 Ground Granulated Blast Furnace Slag (GGBFS).....	17
2.3.4 Micro-Silica .....	17
2.4 Thermal Load due to Cement Hydration .....	18
2.5 Modeling the Cement Hydration .....	20

2.6	Monitoring the temperature rise and the maximum temperature .....	23
2.7	Finite Element Modeling .....	27
<b>3</b>	<b>CHAPTER 3 EXPERIMENTAL PROGRAM .....</b>	<b>.34</b>
3.1	Laboratory Tests .....	34
3.1.1	Measuring the Heat of Hydration .....	34
3.1.2	Measuring the Tensile Strength of Concrete at Early Age .....	39
3.1.3	Measuring the Compressive Strength of Concrete .....	39
3.1.4	Measuring the Modulus of Elasticity.....	40
3.1.5	Measuring the Properties of Self Compacting Concrete .....	41
3.1.6	Mix Proportioning.....	43
3.1.7	Materials Properties .....	48
3.2	Field Monitoring.....	51
3.2.1	Monitoring of KFUPM Mock-up Specimens (KMUS).....	51
3.2.2	Monitoring of Dammam Coast Mock-up Specimens (DMUS).....	55
3.2.3	Monitoring of Jeddah Mockup (JMUS).....	59
3.2.4	Pile Cap Monitoring.....	61
<b>4</b>	<b>CHAPTER 4 HYDRATION MODEL .....</b>	<b>.64</b>
4.1	Maturity Concept .....	64
4.1.1	Nurse-Saul Equation .....	65
4.1.2	Arrhenius Equation .....	66
4.2	Adiabatic Heat of Hydration Model .....	66
4.2.1	Determining the Hydration Parameters from Chemical Compositions of Mix .....	68

4.2.2	Determining the Hydration Parameters from Semi adiabatic Test .....	70
<b>5</b>	<b>CHAPTER 5 FINITE ELEMENT SIMULATION .....</b>	<b>.77</b>
5.1	Temperature Evolution Simulation.....	77
5.1.1	Thermal conductivity and Specific heat .....	77
5.1.2	Thermal Expansion of Concrete .....	78
5.1.3	Convection Coefficient .....	79
5.1.4	Ambient Temperature .....	81
5.1.5	Solar Radiation .....	81
5.2	Structural (Stress) Simulation.....	85
5.2.1	Cracking Model .....	85
5.2.2	Discrete Crack Approach.....	85
5.2.3	Smeared Crack Approach .....	86
5.2.4	Strain Analysis.....	90
5.2.5	Stress Analysis.....	93
5.2.6	Interaction between soil and concrete.....	95
5.3	Types of Elements Used in FEM Simulation .....	98
<b>6</b>	<b>CHAPTER 6 EXPERIMENTAL RESULTS .....</b>	<b>101</b>
6.1	Experimental Results.....	101
6.1.1	Lab. Tests Results .....	101
6.2	Field Monitoring Results .....	147
6.2.1	Field Monitoring Results of KMUS .....	147
6.2.2	Monitoring Results of DMUS.....	160
6.2.2.1	Temperature Monitoring Results of DMUS .....	160

6.2.3	Monitoring Results of JMUS .....	168
6.2.4	Monitoring Results of Bridge Piles- Cap.....	170
<b>7</b>	<b>CHAPTER 7 FINITE ELEMENT SIMULATION RESULTS.....</b>	<b>173</b>
7.1	Introduction.....	173
7.2	Heat Transfer Analysis Results .....	173
7.2.1	Temperature Simulation Results of KMUS.....	173
7.2.2	Temperature Simulation Results of DMUS.....	180
7.2.3	Temperature Simulation Results of JMUS .....	185
7.2.4	Temperature Simulation Results of Piles-Cap.....	187
7.3	Stress Analysis Results .....	191
7.3.1	Stresses Results of KMUS.....	192
7.3.2	Stresses Results of DMUS .....	198
7.3.3	Stresses Results of JMUS .....	202
7.3.4	Stresses Results of Piles-Cap.....	205
<b>8</b>	<b>CHAPTER 8 PARAMETRIC STUDY .....</b>	<b>210</b>
8.1	Introduction.....	210
8.2	Size of Mockup Specimens .....	210
8.3	Effect of Placement Temperature .....	211
8.4	Effect of Solar Radiation .....	212
8.5	Effect of Ambient Temperature.....	215
8.6	Type of Formwork.....	216
8.7	Effect of Mineral Admixtures.....	222
8.8	Effect of Interface Elements .....	236

<b>9</b>	<b>CHAPTER 9 SUMMARY AND RECOMMENDATIONS .....</b>	<b>240</b>
9.1	Summary .....	240
9.2	CONCLUSIONS .....	242
9.3	Recommendations for Future Research .....	245
<b>10</b>	<b>REFERENCES. ....</b>	<b>246</b>
<b>11</b>	<b>APPENDIX A. ....</b>	<b>252</b>
<b>12</b>	<b>APPENDIX B. ....</b>	<b>270</b>
<b>13</b>	<b>VITA.....</b>	<b>282</b>



## LIST OF TABLES

Table 2-1: Typical Composition of Portland Cement [12] .....	10
Table 2-2: Typical Oxide Composition of OPC [12] .....	14
Table 2-3: Typical Compound Composition and Properties of Portland Cement [12] ....	15
Table 2-4: Comparison of Chemical And Physical Characteristics — Portland Cement, Fly Ash, Slag Cement, and Silica Fume [15] .....	18
Table 2-5: Thermal and Physical Tests Conducted in Florida University [23]. .....	25
Table 2-6: Mixture Designs for Large-Scale Block Specimens. ....	25
Table 3-1: Mix Proportions for the First Group of Mixes. ....	43
Table 3-2: Mix Proportions for the Second Group of Mixes.....	44
Table 3-3: Mix Proportions for the Third Group of Mixes.....	44
Table 3-4: Mix Proportions for the Fourth Group of Mixes.....	45
Table 3-5: Mix Proportions for the Fifth Group of Mixes.....	46
Table 3-6: Mix Proportions for the Sixth Group of Mixes. ....	46
Table 3-7: Mix Proportions for the Seventh Group of Mixes.....	47
Table 3-8: Mix Proportions for the Eighth Group of Mixes.....	47
Table 3-9: Mix Proportions for the Ninth Group of Mixes. ....	48
Table 3-10: Mix Proportions for the Tenth Group of Mixes. ....	48
Table 3-11: Chemical and Physical Properties of Cement Type I.....	49
Table 3-12: Chemical and Physical Properties of GGBFS.....	50
Table 3-13: Physical Properties of GGBFS.....	50
Table 3-14: Mechanical Properties of Fly Ash. ....	51
Table 3-15: Mix Proportions, Location, and Dimensions of Mockup Specimens .....	60

Table 4-1 : Hydration Parametrs for The Mixes in The Group #1 .....	73
Table 4-2: Hydration Parameters for The Mixes in The Group #2 .....	73
able 4-3: Hydration Parameters for The Mixes in The Group #3 .....	73
Table 4-4: Hydration Parameters for The Mixes in The Group #4 .....	74
Table 4-5: Hydration Parameters for The Mixes in The Group #5 .....	74
Table 4-6: Hydration Parameters for The Mixes in The Group #6 .....	74
Table 4-7: Hydration Parameters for The Mixes in The Group #7 .....	75
Table 4-8: Hydration Parameters for The Mixes in The Group #8 .....	75
Table 4-9: Hydration Parameters for The Mixes in The Group #9 .....	75
Table 4-10: Hydration Parameters for The Mixes in The Group #10 .....	76
Table 5-1: Influences of Aggregates on CTE (Chandra at all. [44]) .....	80
Table 5-2: Constitutive law for frictional behavior of interface [55] .....	99
Table 6-1: Results of Self Compactibility Tests on Fresh Concrete.....	115
Table 6-2: Summary of Peak Temperatures and Max. Differences for the Mock-Up	
Specimen #1 .....	151
Table 6-3: Summary of Peak Temperatures and Max. Differences for the Mock-Up	
Specimen #2 .....	154
Table 6-4: Summary of Peak Temperatures and Max. Differences for the Mock-Up	
Specimen #2 .....	158
Table 6-5: Maximum Temperatures at varying locations in DMUS .....	166
Table 6-6: Temperature Differences between the Core and the Top Center of Surface	167
Table 6-7: Temperature Differences between the Core and the Sides .....	168
Table 6-8: Max. Temperatures and Temperature Differences for the JMUS .....	169

Table 6-9: Max. Temperatures and Temperature Differences for the Piles-Cap.....	172
Table 7-1: Thermal Properties of Materials Used in FE Simulation .....	174

## LIST OF FIGURES

Figure 2-1: Reaction Stages During Cement Hydration Process (Schindler[10]) .....	12
Figure 2-2: Fastening Thermocouples Prior to Concrete Placement [10] .....	21
Figure 2-3: Locations for Temperature and Stress Measurements in a Reinforced Concrete Wall (Machida And Uehara [21]) .....	24
Figure 2-4: Large Scale Block Testing Configuration [23] .....	26
Figure 2-5: Temperature Sensors before Concrete Placement [31].....	31
Figure 2-6: Temperature Bar 4 after Installation [31] .....	32
Figure 3-1: Types of iQdrum Calorimeter. ....	35
Figure 3-2: Temperature in Concrete Specimen, Ambient Temperature and Heat Loss [32]. .....	36
Figure 3-3: Adiabatic Heat Rise and Its Rate Versus Equivalent Age [32]. ....	36
Figure 3-4: Adiabatic Temperature Rise and Its Rate Versus Equivalent Age [32].....	37
Figure 3-5: Heat-Box and Concrete Sample.....	38
Figure 3-6: Measured Temperature and Calculated Heat of Hydration Using Heat-Box.	38
Figure 3-7: Measuring the Splitting Tensile Strength of Concrete.....	39
Figure 3-8: Measuring the Compressive Strength of Concrete .....	40
Figure 3-9: Measuring the Concrete Modulus of Elasticity .....	40
Figure 3-10: Measuring the Flowability and T50 of Self Compacting Concrete .....	41
Figure 3-11: V-Funnel for Measuring Flowability and Viscosity of SCC .....	42
Figure 3-12 : L-Box for Measuring the Passing Ability of SCC .....	42
Figure 3-13: Thermocouple and Strain Gauges Locations .....	52
Figure 3-14: Data Logger and Computer for Data Acquisition.....	52

Figure 3-15: Locations of an Isolated Rebars .....	53
Figure 3-16: Plywood Formwork for KMUS .....	53
Figure 3-17: Curing of KMUS.....	54
Figure 3-18: Obtaining Drilled Concrete Cores .....	54
Figure 3-19: DMUS with Steel Formwork. ....	55
Figure 3-20: Epoxy Steel Reinforcement of DMUS. ....	55
Figure 3-21: Thermocouple and Strain Gauges Locations .....	56
Figure 3-22: Data Acquisition System.....	56
Figure 3-23: Locations of an Isolated Rebars .....	57
Figure 3-24: Insulation the Top Surface of Concrete .....	57
Figure 3-25: Covering the Top Surfaces with Burlap.....	58
Figure 3-26: Covering the DMUS with Burlap. ....	58
Figure 3-27: Thermocouples Locations (Plan) .....	59
Figure 3-28: Thermocouples Locations (Over Depth). ....	60
Figure 3-29: Reinforcement in the Pile Cap .....	62
Figure 3-30: Casting of Concrete in Pile Cap.....	62
Figure 3-31: Thermocouple Locations: (A) Plan View; (B) Section A-A .....	63
Figure 3-32: Sensors Connected to Data Logger .....	63
Figure 3-33: Ice Blocks for Cooling Curing Water .....	63
Figure 4-1: General Shape of Adiabatic Heat of Hydration Rise Curve .....	67
Figure 4-2: Effect of Increasing $\alpha_U$ on the Hydration Curve .....	68
Figure 4-3: Effect of Increasing T on The Hydration.....	69
Figure 4-4: Effect of Increasing $\beta$ on The Hydration Curve .....	69



Figure 5-1: Solar Radiation Analysis Using Ecotect Software.....	82
Figure 5-2: Angle of Solar Radiation Incident .....	83
Figure 5-3: Flow Chart For Heat Tranfer Analysis .....	84
Figure 5-4: Concrete Cracking Models: (A) Discrete Inter-Element Crack Pproach; (B) Discrete Intra-Element Crack Approach; (C) Smeared Crack Approach (Crosses The Shaded Element Are The Cracked Integration Points). ....	86
Figure 5-5: Multi-Directional Fixed Crack Model .....	89
Figure 5-6: Flow Chart for Stress Analysis .....	95
Figure 5-7: Coulomb Friction Criterion.....	97
Figure 5-8: Types of Elements Used in FE Simulation .....	100
Figure 5-9: Geometry of Quarter of Mockup Specimen.....	100
Figure 6-1: Adiabatic Heat of Hydration Rise for the Mixes of Group#1 .....	102
Figure 6-2: Hydration Parameters of Mixes in The Group#1 : A) Ultimate Heat of Hydration ( $H_u$ ); B) $\beta$ Hydration Parameter ; And C) $\tau$ Hydration Parameter .....	103
Figure 6-3: Adiabatic Heat of Hydration Rise for the Mixes of Group#2.....	104
Figure 6-4:Hydration Parameters of Mixes in The group #2: a) Ultimate Heat of Hydration ( $H_u$ ); b) $\beta$ Hydration Parameter ; and c) $\tau$ Hydration Parameter .....	105
Figure 6-5: Adiabatic Heat of Hydration Rise for the Mixes of Group#3.....	107
Figure 6-6: Hydration Parameters of Mixes in The Group #3: A) Ultimate Heat of Hydration ( $H_u$ ); B) $\beta$ Hydration Parameter; And C) $\tau$ Hydration Parameter .....	108
Figure 6-7: Adiabatic Heat of Hydration Rise for the Mixes in Group#4 .....	109

Figure 6-8: Adiabatic Heat of Hydration Rise for the Mixes of Group#5.....	110
Figure 6-9: Adiabatic Heat of Hydration Rise for the Mixes of Group#6.....	111
Figure 6-10: Hydration Parameters of Mixes In The Group #6: A) Ultimate Heat of Hydration ( $H_u$ ); B) $\beta$ Hydration Parameter; And C) $\tau$ Hydration Parameter .....	112
Figure 6-11: Adiabatic Heat of Hydration Rise for The Mixes of Group#7 .....	113
Figure 6-12: Adiabatic Heat of Hydration Rise for the Mixes of Group#8.....	116
Figure 6-13: Adiabatic Temperature Rise for the Mixes of Group#9 .....	117
Figure 6-14: Adiabatic Temperature Rise for the Mixes of Group#10 .....	118
Figure 6-15: Development of Tensile Strength with Time for the Mixes in Group#1 ..	119
Figure 6-16: Development of Tensile Strength with Time for the Mixes in Group#2 ...	120
Figure 6-17: Development of Tensile Strength with Time for the Mixes in Group#3 ...	121
Figure 6-18: Development of Tensile Strength with Time for the Mixes in Group#4 ...	122
Figure 6-19: Development of Tensile Strength with Time for the Mixes in Group#5 ...	123
Figure 6-20: Development of Tensile Strength with Time for the Mixes in Group#6 ...	124
Figure 6-21: Development of Tensile Strength with Time for the Mixes in Group#7 ...	125
Figure 6-22: Development of Tensile Strength with Time for the Mixes in Group#8 ...	126
Figure 6-23: Development of Tensile Strength with Time for the Mixes in Group#9 ...	127
Figure 6-24: Development of Tensile Strength with Time for the Mixes in Group#10.	128
Figure 6-25: Development of Modulus of Elasticity with Time for the Mixes in Group#1 .....	129
Figure 6-26: Development of Modulus of Elasticity with Time for the Mixes in Group#2 .....	130

Figure 6-27:Development of Modulus of Elasticity with Time for the Mixes in Group#3	131
Figure 6-28: Development of Modulus of Elasticity with Time for the Mixes in Group#4	132
Figure 6-29: Development of Modulus of Elasticity with Time for the Mixes in.....	133
Figure 6-30: Development of Modulus of Elasticity with Time for the Mixes in the Group#6 .....	134
Figure 6-31: Development of Modulus of Elasticity with Time for the Mixes in the Group#7 .....	135
Figure 6-32: Development of Modulus of Elasticity with Time for the Mixes in the Group#8 .....	135
Figure 6-33: Development of Modulus of Elasticity with Time for the Mixes in the Group#9 .....	137
Figure 6-34: Development of Modulus of Elasticity with Time for the Mixes in the Group#10 .....	137
Figure 6-35: Development of Compressive Strength with Time for the Mixes in the Group#1 .....	138
Figure 6-36: Development of Compressive Strength with Time for the Mixes in the Group#2 .....	139
Figure 6-37: Development of Compressive Strength with Time for the Mixes in the Group#3 .....	140
Figure 6-38: Development of Compressive Strength with Time for the Mixes in the Group#4 .....	141

Figure 6-39: Development of Compressive Strength with Time for the Mixes in the	
Group#5 .....	142
Figure 6-40: Development of Compressive Strength with Time for the Mixes in the	
Group#6 .....	143
Figure 6-41: Development of Compressive Strength with Time for the Mixes in the	
Group#7 .....	144
Figure 6-42: Development of Compressive Strength with Time for the Mixes in the	
Group#8 .....	145
Figure 6-43: Development of Compressive Strength with Time for the Mixes in the	
Group#9 .....	146
Figure 6-44: Development of Compressive Strength with Time for the Mixes in the	
Group#10 .....	147
Figure 6-45: Temperature rise at Location 1 (Top, Center, and Bottom).....	148
Figure 6-46: Temperature rise at Location 2 (Top, Center, and Bottom).....	148
Figure 6-47: Temperature rise at Location 3 (Top, Center, and Bottom).....	149
Figure 6-48: Temperature rise at Location 4 (Top, Center, and Bottom).....	149
Figure 6-49: Temperature rise at Location 5 (Top, Center, and Bottom).....	150
Figure 6-50: Temperature rise at Location 6 (Top, Center, and Bottom).....	150
Figure 6-51: Temperature rise at Location 1 (Top, Center, and Bottom).....	151
Figure 6-52: Temperature rise at Location 2 (Top, Center, and Bottom).....	152
Figure 6-53: Temperature rise at Location 3 (Top, Center, and Bottom).....	152
Figure 6-54: Temperature rise at Location 4 (Top, Center, and Bottom).....	153
Figure 6-55: Temperature rise at Location 5 (Top, Center, and Bottom).....	153

Figure 6-56: Temperature rise at Location 6 (Top, Center, and Bottom).....	154
Figure 6-57: Temperature rise at Location 1 (Top, Center, and Bottom).....	155
Figure 6-58: Temperature rise at Location 2 (Top, Center, and Bottom).....	155
Figure 6-59: Temperature rise at Location 3 (Top, Center, and Bottom).....	156
Figure 6-60: Temperature rise at Location 4 (Top, Center, and Bottom).....	156
Figure 6-61: Temperature rise at Location 5 (Top, Center, and Bottom).....	157
Figure 6-62: Temperature rise at Location 6 (Top, Center, and Bottom).....	157
Figure 6-63: Strain Evolution with Time at Location#1 (Top and Center) .....	158
Figure 6-64: Strain Evolution with Time at Location#2 (Top and Center) .....	159
Figure 6-65: Strain Evolution with Time at Location#3 (Top, Center, and Bottom) .....	159
Figure 6-66: Strain Evolution with Time at Location#4 (Top, Center, and Bottom) .....	160
Figure 6-67: Temperature rise at Location 1 (Top, Center, and Bottom).....	160
Figure 6-68: Temperature rise at Location 2 (Top, Center, and Bottom).....	161
Figure 6-69: Temperature rise at Location 3 (Top, Center, and Bottom).....	161
Figure 6-70: Temperature rise at Location 4 (Top, Center, and Bottom).....	162
Figure 6-71: Temperature rise at Location 1 (Top, Center, and Bottom).....	162
Figure 6-72: Temperature rise at Location 2 (Top, Center, and Bottom).....	163
Figure 6-73: Temperature rise at Location 3 (Top, Center, and Bottom).....	163
Figure 6-74: Temperature rise at Location 4 (Top, Center, and Bottom).....	164
Figure 6-75: Temperature rise at Location 1 (Top, Center, and Bottom).....	164
Figure 6-76: Temperature rise at Location 2 (Top, Center, and Bottom).....	165
Figure 6-77: Temperature rise at Location 3 (Top, Center, and Bottom).....	165
Figure 6-78: Temperature rise at Location 4 (Top, Center, and Bottom).....	166



Figure 6-79: Temperature rise at Location 1 (Top, Center, and Bottom).....	168
Figure 6-80: Temperature rise at Location 2 (Top, Center, and Bottom).....	169
Figure 6-81: Temperature rise at Location 3 (Top, Center, and Bottom).....	169
Figure 6-82: Temperature rise at Location 1 (Top, Center, and Bottom).....	170
Figure 6-83: Temperature rise at Location 2 (Top, Center, and Bottom).....	171
Figure 6-84: Temperature rise at Location 3 (Top, Center, and Bottom).....	171
Figure 6-85: Temperature rise at Location 4 (Top, Center, and Bottom).....	171
Figure 6-86: Temperature rise at Location 5 (Top, Center, and Bottom).....	172
Figure 7-1: Dimensions of Quarter of Mock-Up Specimen used in Simulation .....	174
Figure 7-2: Geometry of FEM with Element Types.....	175
Figure 7-3: Temperature Rise at Location 1 for Mockup#1 in KMUS (100% OPC) ....	176
Figure 7-4: Temperature Rise at Location 2 for Mockup#1 in KMUS (100% OPC) ....	176
Figure 7-5: Temperature Rise at Location 3 for Mockup#1 in KMUS ( 100% OPC) ..	177
Figure 7-6: Temperature Rise at Location 1 for Mockup#2 in KMUS (40% Fly Ash) .	177
Figure 7-7: Temperature Rise at Location 2 for Mockup#2 (40% Fly Ash) .....	178
Figure 7-8: Temperature Rise at Location 3 for Mockup#2 in KMUS (40% Fly Ash) .	178
Figure 7-9: Temperature Rise at Location 1 for Mockup#3 in KMUS (60% GGBFS)	179
Figure 7-10: Temperature Rise at Location 2 for Mockup#3 in KMUS (60% GGBFS)	179
Figure 7-11: Temperature Rise at Location 3 for Mockup#3 in KMUS (60% GGBFS)	180
Figure 7-12: Temperature Rise at Location#1 for Mockup#1 in DMUS (50% GGBFS)	181
Figure 7-13: Temperature Rise at Location#2 for Mockup#1 in DMUS (50% GGBFS)	181
Figure 7-14: Temperature Rise at Location#3 for Mockup#1 in DMUS (50% GGBFS)	182
Figure 7-15: Temperature Rise at Location#1 for Mockup#2 in DMUS (65% GGBFS)	182

Figure 7-16: Temperature Rise at Location#2 for Mockup#2 in DMUS (65% GGBFS)	183
Figure 7-17: Temperature Rise at Location#3 for Mockup#2 in DMUS (65% GGBFS)	183
Figure 7-18: Temperature Rise at Location#1 for Mockup#3 in DMUS (70% GGBFS)	184
Figure 7-19: Temperature Rise at Location#2 for Mockup#3 in DMUS (70% GGBFS)	184
Figure 7-20: Temperature Rise at Location#3 for Mockup#3 in DMUS (70% GGBFS)	185
Figure 7-21: Temperature Rise at Location#1 for JMUS .....	185
Figure 7-22: Temperature Rise at Location#2 for JMUS .....	186
Figure 7-23: Temperature Rise at Location#3 for JMUS .....	186
Figure 7-24: Contours of Temperature Distribution at Different Ages .....	187
Figure 7-25: Dimensions of Quarter of Pile Cap Used in Simulation .....	187
Figure 7-26: Element Types in finite Element Simulation of Piles-Cap .....	189
Figure 7-27: Comparison of Measured and Finite Element Results of Evolution of Temperature at Various Locations in Piles Cap. ....	190
Figure 7-28: Contours of Temperature Distribution in the Piles-Cap at Different Ages	191
Figure 7-29: Locations of Elements for Stress Analysis .....	193
Figure 7-30: Stresses in X Direction ( $S_{xx}$ ) for the Element Located at Top Surfaces of KMUS.....	193
Figure 7-31: Stresses in X Direction ( $S_{xx}$ ) for the Element Located at Core of KMUS	194
Figure 7-32: Stresses in X Direction ( $S_{xx}$ ) for the Element Located at Bottom of KMUS .....	195
Figure 7-33: Evolution of Temperature, Cracking Index, and Stresses ( $S_{xx}$ ) Across the Depth AB (Fig.7-34) of Mockup Specimens (After 30 Hours From Casting) .....	196

Figure 7-34: Crack Pattern in the Mockup Specimens after 40 Hours from Casting .....	197
Figure 7-35: Cracking Index of Element Located at the Top Centre of the Surface .....	198
Figure 7-36: Stresses in X Direction ( $S_{xx}$ ) for the Element Located at Top Surfaces of DMUS.....	198
Figure 7-37: Stresses in X Direction ( $S_{xx}$ ) for the Element Located at Core of DMUS	199
Figure 7-38: Stresses in X Direction ( $S_{xx}$ ) for the Element#250 Located at Bottom of DMUS.....	200
Figure 7-39: Evolution of Temperature, Cracking Index, and Stresses ( $S_{xx}$ ) Across the Depth AB (Fig.7-34) of Mockup Specimens (After 30 Hours From Casting) .....	200
Figure 7-40: Crack Pattern in the DMUS after 40 Hours from Casting .....	201
Figure 7-41: Cracking Index of Elements 205, 230, and 250.....	201
Figure 7-42: Stresses in X Direction ( $S_{xx}$ ) for the Elements Located at Top, Center, and Bottom of Center Line of JMUS .....	202
Figure 7-43: Evolution of Temperature, Cracking Index, and Stresses ( $S_{xx}$ ) Across the Concrete Depth AB (Fig.7-29) of JMUS (After 30 Hours from Casting).	203
Figure 7-44: Cracking Index of Elements 201,221 and 246.....	203
Figure 7-45: Crack Pattern in the JMUS after 30 Hours from Casting .....	204
Figure 7-46: Contour plots of Principal Stresses ( $S_1$ ) at Different Ages .....	205
Figure 7-47: Stresses in X Direction ( $S_{xx}$ ) for the Elements Located at Top, Center, and Bottom of Center Line of Piles-Cap.....	206
Figure 7-48: Cracking Index, and Stresses ( $S_{xx}$ ) Across the Concrete Depth AB Piles-Cap (After 30 Hours from Casting) .....	207

Figure 7-49: Temperature Evolution across the Central Depth of Piles-Cap at Different Ages .....	208
Figure 7-50: Cracking Index of Elements 12362, 12454, and 12546.....	208
Figure 7-51: evolution of Contours Plot for the Cracking Index (Icr) in the Pile-cap ...	209
Figure 8-1: Effect of Mass Concrete Sizes on the Temperature Rise.....	211
Figure 8-2: Effect of Placement Temperature on the Temperature Rise .....	212
Figure 8-3: Effect of Solar Radiation in the Temperature Rise on Mass Concrete .....	213
Figure 8-4: Effect of Solar Radiation on Cracking Index.....	214
Figure 8-5: Effect of Ambient Temperature in the Temperature Rise on Mass Concrete	215
Figure 8-6: Effect of Ambient Temperature in the Cracking Index of Mass Concrete ..	216
Figure 8-7: Effect of Formwork Type in the Temperature Rise on Mass Concrete .....	217
Figure 8-8: Temperature Rise of the top and central elements neat to side.....	218
Figure 8-9: Effect of Formwork Type in the Cracking Index of Mockup Specimen .....	219
Figure 8-10: Effect of Formwork Type in the Cracking Index of Mockup Specimen along Side Line CD .....	220
Figure 8-11: Crack Patterns of Mockup Specimen with a) Plywood Formwork, b) Steel Formwork .....	221
Figure 8-12: Temperature Rise at the Core of Mockup Specimen for the Mixes of Group#1 .....	223
Figure 8-13: Cracking Index of the Element Located at Top Center of MUS For the Mixes of Group#1 .....	223
Figure 8-14: Temperature Rise at the Core of Mockup Specimen for the Mixes of Group#2 .....	224

Figure 8-15: Cracking Index of the Element Located at Top Center of MUS For the Mixes of Group#2.....	225
Figure 8-16: Temperature Rise at the Core of Mockup Specimen for the Mixes of Group#3 .....	226
Figure 8-17: Cracking Index of the Element Located at Top Center of MUS For the Mixes of Group#3.....	227
Figure 8-18: Temperature Rise at the Core of Mockup Specimen for the Mixes of Group#4 .....	227
Figure 8-19: Cracking Index of the Element Located at Top Center of MUS For the Mixes of Group#4.....	228
Figure 8-20: Temperature Rise at the Core of Mockup Specimen for the Mixes of Group#5 .....	229
Figure 8-21: Cracking Index of the Element Located at Top Center of MUS For the Mixes of Group#5.....	229
Figure 8-22: Temperature Rise at the Core of Mockup Specimen for the Mixes of Group#6 .....	230
Figure 8-23: Cracking Index of the Element Located at Top Center of MUS For the Mixes of Group#6.....	231
Figure 8-24: Effect of w/cm Ratio in the Temperature Rise at the Core of Mock-up Specimen .....	232
Figure 8-25: Effect of Varying W/CM on the Cracking Index of Element Located at Top Center of MUS .....	233



Figure 8-26: The Effect of Cement Content on the Temperature Rise at the Core of MUS .....	233
Figure 8-27: The Effect of Cement Content on the Cracking Index of MUS .....	234
Figure 8-28: Effect of Steel and Polypropylene fibers on Temperature Rise.....	235
Figure 8-29: Effect of Steel and Polypropylene fibers on the Cracking Index.....	236
Figure 8-30: Effect of Interaction between Concrete and Soil on the Cracking Index ..	237
Figure 8-31: Effect of Interaction between Concrete and Soil on the Number of Cracked Elements .....	238
Figure 8-32: Effect of Interaction between Concrete and Soil on the Crack Patterns....	239

## NOMENCLATURE

### ABBREVIATIONS

ACI	American Concrete Institute
ASTM	American Society for Testing and Materials
ATR	Adiabatic Temperature Rise
CTE	Coefficient of Thermal Expansion
DMUS	Dammam Mockup Specimens
GGBFS	Ground Granulated Blast Furnace Slag
FA	Fly Ash
JMUS	Jeddah Mockup Specimen
KMUS	King Fahd University Mockup Specimens
MS	Micro Silica
OPC	Ordinary Portland Cement

### ENGLISH AND GREEK SYMBOLS

$\beta$	Slope Hydration Parameter
$c$	Specific heat capacity
$D_{nn}$	Normal stiffness at interface
$D_{tt}$	Tangential stiffness at interface
$E$	Activation energy
$E_{\text{beam}}$	Direct or beam radiation
$E_{ci}$	Modulus of elasticity at 28 days
$E_{ci(t)}$	Modulus of elasticity at an age t days

$E_{\text{diffuse}}$	Diffuse sky radiation
$E_{\text{soil}}$	Young Modulus of Soil
$\varepsilon_{c,ult}$	Concrete Tensile Strength
$f_{ct,28}$	Tensile strength at age of 28 days
$f_{ct}$	Tensile strength of concrete
$F_{\text{sky}}$	Fraction of the diffuse sky actually visible
$G_f$	Concrete fracture energy
$h_b$	Crack bandwidth
$h_{\text{free}}$	Free convection heat transfer coefficient
$I_{cr}$	Cracking index
$k_X$	Thermal conductivities of concrete in the x coordinate
$k_Y$	Thermal conductivities of concrete in the y coordinate
$k_Z$	Thermal conductivities of concrete in the z coordinate
$M$	The equivalent age maturity function
$n$	Number of iterations in the finite difference analysis
$\rho$	Density of material
$Q_h$	Heat generated due to cement hydration and external sources
$r$	Degree of reaction
$R$	Universal gas constant.
$t_{e(\text{Tr})}$	Equivalent age at the reference curing temperature
$T_C$	Temperature of Concrete
$T_{\text{amb}}$	Ambient Temperature
$T_{\text{ea}}$	Equivalent Temperature of Solar Radiation
$t_0$	Time equivalent age in days

$\tau$	Time Hydration Parameter
$\nu$	Wind velocity
$\alpha_s$	Solar Absorptivity
$\phi$	Interface friction

## **DISSERTATION ABSTRACT**

<b>Full Name</b>	<b>Muneer Qaid Saeed Abdo</b>
<b>Title of Study</b>	<b>Experimental Investigation and Modeling of Heat of Hydration in Mass Concrete Structures</b>
<b>Major Field</b>	<b>Civil Engineering (Structures)</b>
<b>Date of Degree</b>	<b>December 2013</b>

The hydration of cement in mass concrete structures produces high temperature. The temperature in the core of the mass concrete structures is higher than the temperature in the surfaces that are closer to ambient air. This temperature gradient leads to the development of thermal stresses, which may cause cracking if thermal stresses exceed the tensile strength of concrete at early age. This research focuses on conducting an experimental program for 46 different mixes using iQdrum heat signature and heat box to obtain the heat of hydration and temperature rise. The mechanical properties of these concrete mixes such as tensile strength, compressive strength, and modulus of elasticity were also conducted. The effect of mineral admixtures, such as fly ash, ground granulated blast furnace (GGBFS) slag, and silica fume, on heat of hydration was investigated. The effect of steel and polypropylene fibers on the heat of hydration and on the cracking index of mass concrete at early age was studied. The temperature rise, the peak temperatures, and strains for different seven mock-up specimens and for actual structures such as piles-cap, were monitored. The viscoelastic behavior of mass concrete at early age was simulated by using the finite element nonlinear approach The finite element

model predicted the temperature rise in the mass concrete structures, and associated thermal stresses. The finite element model has ability to indicate to whether the cracks will form or not.

Based on experimental and numerical investigations, guidelines will be developed for mass concrete in Kingdom of Saudi Arabia (KSA). These guidelines will help in reducing the risk of cracking due to high temperature gradient between core of concrete and its surface.

**Doctor of Philosophy**

**KING FAHD UNIVERSITY OF PETROLEUM AND MINERALS**

**Dhahran, Saudi Arabia**

**December 2013**

## ملخص الرسالة

الاسم منير قائد سعيد عبده  
عنوان الرسالة التحقيق المخبري والنمذجة للحرارة الناتجة اماهة المواد الاسمنية في المنشآت الخرسانية ذات الكتل الكبيرة .

التخصص هندسه مدنيه (إنشاءات)

تاريخ التخرج اكتوبر 2013

عملية اماهة الاسمنت في المنشآت الخرسانية ذات الكتل الكبيرة تولد درجات حرارة عالية .درجة الحرارة في مركز او وسط الكتل الخرسانية الكبيرة أعلى منها في السطوح المعرضة لدرجة الحرارة الخارجية .الفرق بين درجة الحرارة في مركز الكتلة الخرسانية ووسطها قد يؤدي الى توليد الاجتهادات الحرارية والتي يمكن ان تسبب في تشكل الشقوق وذلك في حالة تجاوز الاجتهادات الناتجة عن الحرارة مقاومة الخرسانة للشد في عمر مبكر (مرحلة مابعد الصب) .هذا البحث سوف يركز على إجراء التجارب المخبرية باستخدام جهاز الكلروميتر اوالصندوق الحراري على 46 خلطات خرسانية مختلفة تم قياس الخواص الميكانيكية للخلطات المدروسة مثل مقاومة الضغط ومقاومة الشد وعامل المرونه . تمت دراسة تأثير الاضافات الخرسانية في الحرارة الناتجة من اماهة الاسمنت . لقد تم قياس تغير درجة الحرارة ودرجة الحرارة الاعظمية لكتل والتشوهات لسبع عينات خرسانية تجريبية (موكب) ولمنشآت خرسانية ذات كتل كبيره مثل بلاطة الخوازيق ذات السماكات الكبيرة .لقد اجريت نمذجة السلوك اللزج المرن للخرسانة في عمر مبكر (مرحلة مابعد الصب ) باستخدام طريقة العناصر المنتهية اللاخطية .نموذج العناصر المنتهية سوف يقوم بتقدير درجات الحرارة في الكتل الخرسانية و الاجهادات الحرارية وتحديد فيما إذا كان سوف يتم تشكل الشقوق نتيجة تلك الاجهادات .بالاعتماد على النتائج المخبرية و العددية سوف يتم كتابة اشتراطات خاصة بالمنشآت الخرسانية ذات الكتل الكبيرة في المملكة العربية السعودية . تلك الاشتراطات سوف تعمل على تخفيف خطر التشققات الناتجة عن الفرق الحراري بين مركز الكتلة الخرسانية وسطحها .

دكتوراه في الهندسة  
جامعة الملك فهد للبترول والمعادن  
الظهران ، المملكة العربية السعودية  
ديسمبر 2013

# **CHAPTER 1**

## **INTRODUCTION**

Mass concrete is defined by the American Concrete Institute (ACI) “any volume of concrete with dimensions large enough to require measures to be taken to cope with generation of heat from cement hydration” (ACI 207.1-R96).

Mass concrete is basic concrete made from fine and coarse aggregate, water and Portland cement. Usually it contains larger aggregate size and smaller cement content. The main characteristic of mass concrete structure is strength. However economy, durability, and workability must be considered too. Mass concrete structures are required for large volume of concrete pours; therefore the need for economy in the use of concrete is modified [1]. In mass concrete structures, temperature rise that occurs in hardening from the hydration process is a serious problem nowadays. In the process of temperature rise, structures expand. However, structures are usually constrained from deforming and this constraint prevents expansion. Stresses are consequently induced in structures, and often, when the magnitude of these stresses is high, cracking occurs [2].

Mass concrete is concrete used mostly for dams, large bridge piers, foundations and other massive structures. Although massive concrete has low cement content, the heat that has been developed in these structures can produce significant stresses. A structure must be thermally controlled otherwise cracking due to thermal behavior may cause loss of structural integrity of monolithic action, or may cause excessive



seepage and shortening of the service life of the structures, or may be esthetically objectionable [3].

When water and cement react, the heat of hydration starts to be generated. The heat generated produces high temperature which cannot dissipate quickly. When the heat being generated in the concrete is dissipated to the surrounding environment, the temperature at the surface of the concrete becomes lower than the temperature at the interior of the concrete. Since the concrete in the exterior region of mass concrete is being cooled by the ambient environment, contraction will occur. This contraction is restrained by the hotter interior concrete that does not contract as rapidly as the surface. This restraint will cause tensile stresses to develop, creating the possibility that cracks will occur at or close to the surface of the concrete. For this reason, the maximum allowable temperature differential between the exterior and interior portions of mass concrete elements during curing should be limited to 20°C [4]. In many situations, limiting the temperature difference to 20°C is overly restrictive; thermal cracking may not even occur at higher temperature difference. In other cases, significant thermal cracking may still occur even when the temperature difference is less than 20°C [5]. The magnitude of thermal gradients experienced by concrete depends on the initial placing temperature, thermal properties (specific heat, thermal conductivity), environmental temperature, and convection, coefficient which depends on wind speed, radiation and geometry of the concrete surface. According to one school of thought [5-9], "primary" ettringite, formed at early age is destroyed when the temperature exceeds 70°C. Therefore, the maximum concrete temperature is limited approximately to 70° C for a variety of reasons. The primary reason is to prevent damage to the concrete. Studies have shown that the long-term durability of certain concretes can be compromised if the maximum temperature after placement

exceeds 70° C. The primary damage mechanism is delayed ettringite formation (DEF). DEF can cause internal expansion and cracking of concrete, which may not be evident for several years after placement [1].

Thermal stresses are a function of concrete mechanical properties such as thermal expansion, tensile strength, and elastic modulus, as well as the size and restraints of the concrete element.

The magnitude of thermal stress ( $\sigma_t$ ) can be calculated by the following formula Schindler [10]:

$$\sigma_t = \Delta T \cdot \alpha \cdot E_c \cdot k \quad (1.1)$$

where,

$\Delta T$      magnitude of the temperature change

$\alpha$        the concrete coefficient of thermal expansion

$E_c$       modulus of elasticity

$K$        degree of restraint factor

In recent years, there have been some efforts to develop models to simulate the hydration process of cement, degree of hydration and the temperature rise in concrete temperature. Some of these models are mentioned in the section of literature review.

In this research, the heat of hydration for different mixes was measured using iQdrum heat signature and isothermal calorimeter. The temperature rise and the peak temperature for mass concrete at early age in mock-up and in actual structures such as thick raft foundations were monitored. The viscoelastic behavior of mass concrete at early age was simulated by a Maxwell model using the finite element nonlinear approach. Based on the experimental and simulation results, general guidelines for mass concreting in KSA were developed.

## **1.1 Need for Research**

The high amount of heat that develops during the hydration of massive concrete structures produces very high temperatures throughout the structure. The variation in the rate of heat production at different locations within the concrete results in temperature gradients that have the potential to cause micro cracking as some sections cool down towards ambient temperature while others are still being heated. The maximum allowable temperature differential between the center of a mass concrete element and its surface should not exceed 20°C.

In Saudi Arabia, Concrete is subjected to very high ambient temperature and extreme temperature difference between day and night. None of the local specifications addresses the heat of hydration (even for mass concrete).

Further, the weather in Saudi Arabia is very hot during summer; the peak temperature of mass concrete may exceed 70°C which in turn creates many problems with mass concrete. In the Harbor project in Jubail, the contractor responsible for the project ran into problems with huge concrete blocks of dimensions of 3×3×3 m that were cast in summer and the core temperature began to exceed 70°C. Delayed ettringite formation (DEF) phenomenon is likely to be activated when the internal temperature exceeds 70°C. The delayed ettringite formation causes sulfate to be trapped in hydration products that will be released later to potentially form ettringite in the meso-pores. Expansive pressures may occur in these pores during ettringite formation, causing cracking in the subsequently hardened concrete.

In view of the huge on-going construction in Saudi Arabia, research on local materials is very important. There isn't enough data about the performance of the available raw and cementitious materials in the local markets regarding heat of hydration.

Mass concrete is still being poured for some projects in KSA without addressing the heat of hydration issue and no quality control or quality assurance is being taken into consideration. Consequently, cracks may appear on the concrete and it is repaired and sealed by the contractor without further investigation.

In KSA , some main projects where the maximum temperature and differential temperature is specified, the consultants do not allow to use more than certain specified quantity (e.g. 25% fly ash max) which may not be enough to attain the maximum temp. Having enough data and research about heat of hydration done using local materials will save time in projects and will be more convincing to consultants than data obtained from research done outside the region.

Obviously, in KSA, in the summer months, high ambient temperature and solar radiation can generate extreme heat in addition to the heat developed from the hydration of cementitious material. The local concrete ready mix suppliers face a big challenge in proper design of mixes to minimize the heat generated in mass concrete structures. This research will address this problem, inclusive of problem of weak local aggregate, extremely high ambient temperature, solar radiation and moisture loss.

Most importantly, in hot environment, moisture loss is accelerated. Consequently, this leads not only creating additional drying strains, but also reducing the hydration and that weakens concrete and its strength potential dramatically.

This research focuses on conducting an experimental program for eighteen different mixes by using iQdrum heat signature calorimeter and isothermal calorimetry. The change of mechanical properties of these mixes with time was studied. The temperature rise and the peak temperature in mockups and actual mass concrete structures such as thick pile-cap in hot or cold weather conditions was

monitored, and the viscoelastic behavior for mass concrete was modeled using a finite element analysis approach. The finite element model was utilized in selection of appropriate mixes for use in mass concrete structures in Saudi Arabia. A set of guidelines for mass concrete in Saudi Arabia was developed to help in mitigating the risk of cracking due to delayed ettringite formation and reduce risk of cracking in cold weather due to high temperature gradient between core of concrete and its surface.

## **1.2 Research Approach**

This research includes two main parts (a) the experimental program and (b) modeling using finite element method. In the experimental program, the effect of a change in the mixtures proportions on the heat of hydration development was determined. The control mix consists of 100% cement and then mineral mixtures will be used with cement in different percentages. By using different replacement levels of fly ash, ground granulated blast furnace slag, and micro silica, the effect of these materials on the hydration of the total cementitious system will be studied. The adiabatic temperature rise curves obtained from the iQdrum heat signature technique was used as an input in the finite element modeling. The modeling of mass concrete structures was done with the aid of commercially available finite element software. The analysis, which is essentially a multi physics simulation problem, is divided in two parts, first a thermal analysis, in which thermal properties are modeled, the hydration process simulated, and the resulting temperature distribution obtained. The second part of the analysis will be a stress analysis in which the physical properties such as elastic modulus and coefficient of thermal expansion are used along with the temperature histories obtained in thermal analysis to calculate the stresses and strains produced by thermal gradients. The model can predict the distribution of temperature

within the mass concrete, thermal stresses and indicates whether or not the cracks will form.

### **1.3 Project Objectives**

The main objectives of this research are as follows:

1. To conduct an experimental program for different mixes of concrete, typical of use in mass concrete in Saudi Arabia using iQdrum heat signature calorimeter in order to obtain the adiabatic heat of hydration and adiabatic temperature rise.
2. The effect of mineral mixtures commonly used in Saudi Arabia (Fly ash and ground granulated blast furnace slag (ggbfs)) in reducing the heat of hydration in mass concrete will be studied.
3. To monitor the temperature rise and the peak temperature for mass concrete at early age in mock up and in actual structures such as thick raft foundations which will cast in hot weather or in cold weather.
4. To simulate numerically using finite element approach for the evolution of the heat of hydration in mass concrete at early age. The variation of temperature with time will be obtained.
5. Using the distribution of temperature obtained from (4), the resulting thermal stresses accounting for variation in modulus of elasticity, tensile strength, and tensile strain limit will be obtained. This finite element model will include development of cracks and their effect on stress distribution.
6. To develop guidelines for mass concreting in Saudi Arabia. These guidelines will help in mitigating the risk of cracking due to delayed ettringite formation

and reduce risk of cracking in cold weather due to high temperature gradient between core of concrete and its surface.

## **CHAPTER 2**

### **LITERATURE REVIEW**

#### **2.1 Introduction**

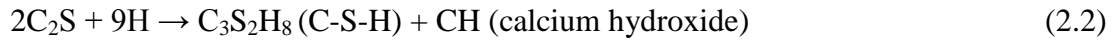
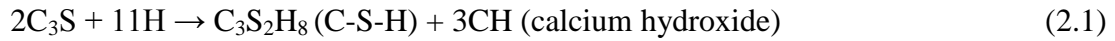
The heat evolution due to an exothermic reaction between cementitious materials and water plays a significant role in the temperature rise in concrete at an early age. The temperature at the core of mass concrete is generally higher than the temperature at the surfaces due to the environment conditions. The difference between the temperature in the core of mass concrete and its surface produces thermal stresses. These thermal stresses have been a major cause for the early age cracking of concrete since the beginning of the 20th century, and it continues to be a problem today. This probability of cracking has generated a lot of research on the topic over the years.

#### **2.2 Hydration of Portland Cement Concrete**

Cement hydration is a complex set of exothermic reactions that occurs when cement and water are mixed together. This reaction can liberate relatively large amounts of energy - up to 500 Joules per gram of cement, which may cause high thermal gradients given that concrete is a relatively poor conductor [11]. This is particularly true when the surface of mass concrete structures becomes cool due to environment conditions.

When the cement hydrates, two main cementitious reactions are of interest. These two reactions involve a reaction between water and the dicalcium silicates and the tricalcium silicates to form calcium silicate hydrates (CSH) and hydrated lime, as shown in the following two simplified equations:





The calcium silicate hydrates (C-S-H) can account for about 50 to 60% of the volume of the hydrated paste as shown in Table 2-1. This C-S-H paste controls the strength and durability of the concrete paste.

**Table 2-1: Typical Composition of Portland Cement [12]**

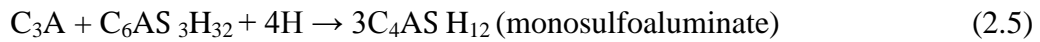
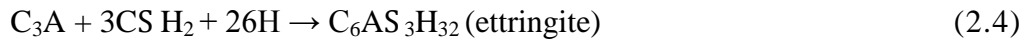
Chemical Name	Chemical formula	Shorthand Notation	Weight percent
Tricalcium silicate(alite)	$3CaOSiO_2$	$C_3S$	55
Dicalcium silicate (belite)	$2CaOSiO_2$	$C_2S$	18
Tricalcium aluminate	$3CaOAl_2O_3$	$C_3A$	10
Tetracalcium aluminoferrite	$4CaOAl_2O_3Fe_2O_3$	$C_4AF$	8
Calcium sulfate didydrate (Gypsum)	$CaSO_4 \cdot 2H_2O$	$CSH_2$	6

A secondary product, calcium hydroxide ( $Ca(OH)_2$ ) is also formed during these reactions. This compound is less dense than the C-S-H, and contributes essentially nothing to the strength of the paste. However, in the presence of fly ash, this calcium hydroxide will react to produce additional C-S-H paste as shown in Eq. (2.3), which results in a denser concrete. This reaction occurs much more slowly than the dicalcium silicate and tricalcium silicate reactions however.



There are also secondary reactions that take place involving the reaction of tricalcium aluminate ( $C_3A$ ) with water. The rapid hydration of  $C_3A$  can be slowed down by the addition of gypsum. Therefore, the final hydration products vary with

the gypsum content. The hydration products of C<sub>3</sub>A are commonly formed of ettringite in the first stage and monosulfoaluminate later (Eq. 2.4). The precipitation of ettringite contributes to stiffening, setting, and early strength development. After the depletion of sulfate, ettringite becomes unstable and is gradually converted into monosulfoaluminate (Eq.2.5). If a new source of sulfate is added, monosulfoaluminate can convert back to ettringite again. Tricalcium aluminate (C<sub>3</sub>A) contributes little to the strength of cement paste.



### **2.2.1 Heat of Hydration Stages**

For a normal concrete, all abovementioned reactions proceed in a particular order, which is often divided into five stages for discussion [12]. The five stages of cement hydration are shown in Figure 2-1, which shows both the rate of heat evolution and degree of hydration, both as a function of time.

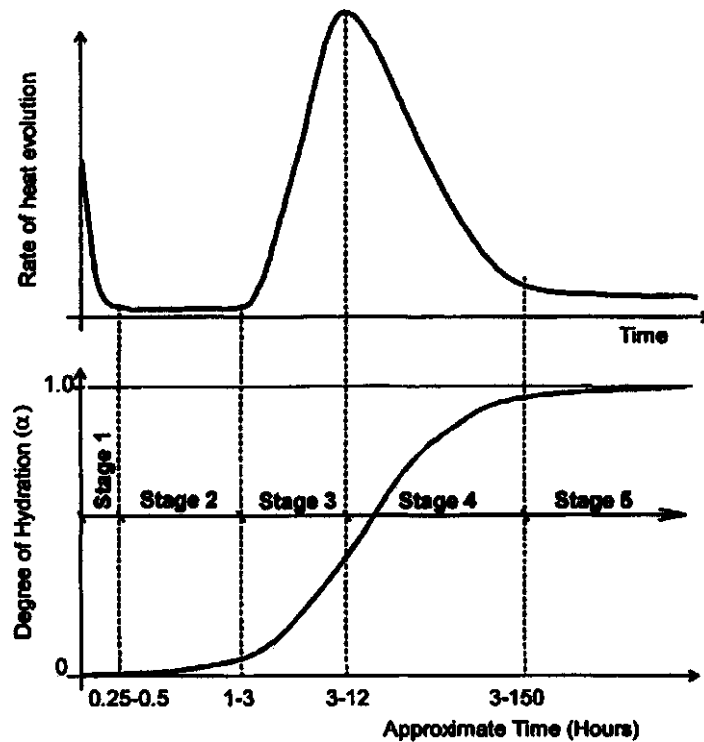


**Figure 2-1: Reaction Stages During Cement Hydration Process (Schindler[10])**

In Stage I (the dissolution stage), the reaction occurs immediately after contact with water because ions dissolved in water react with  $C_3A$  and gypsum. The formation of ettringite produced after initial hydration reactions sharply reduces the rate of the reaction in the latter part of State I. This stage will occur in the batch mixer or ready mix truck. As a result, this stage mainly impacts the placement temperature of the concrete (Schindler, [10]).

In Stage II (the induction [dormant] period), the concrete remains plastic and workable; and can be handled and placed easily. The concentration of calcium and hydroxide ions build throughout this stage, and when a critical value is reached, the reaction of  $C_3S$  and  $C_3A$  proceed at a rapid rate, this stage generally lasts between one to three hours. This stage does not develop concrete strength. However, it is important for workability and transportation of concrete because this stage allows concrete to be transported to a job site.

In Stage III (the acceleration stage), the alite ( $C_3S$ ) and belite ( $C_2S$ ) in the cement start to hydration and release heat. In this stage concrete setting begins and heat generation is rapidly accelerated. The silicate reaches a high rate of hydration at the end of the Stage III. Concrete strength is developed in this stage in which final setting has been finished and early hardening has begun. Therefore, the acceleration stage is a very important characteristic in concrete. Depending on the mix, this stage can last for three to twelve hours, or longer.

In stage IV (the deceleration stage), the rate of heat generation again decreases. By this point, the majority of the  $C_3S$  and  $C_3A$  have reacted, in addition to any reactions due to fly ash or slag to continue building strength at a relatively slow rate. This stage can last from four to 150 hours or longer.

In stage V (the steady stage), the thicker layer of hydrates around the cement particles reduces the rate of hydration remarkably. It is difficult in this stage for hydrates to be precipitated because the space originally filled by water is covered with hydrated cement. There will be some additional strength gain during this phase, and the concrete will continue to develop certain resistances to outside attack.

## **2.3 Properties of Cementitious Materials**

### **2.3.1 Ordinary Portland cement (OPC)**

OPC is the major component of cementitious materials that used in the production of concrete structures. It is hydraulic cement and consists primarily of alite ( $C_3S$ ), belite ( $C_2S$ ), aluminate ( $C_3A$ ), and aluminoferrite ( $C_4AF$ ). These four major compounds determine the hydraulic properties of cement because they account for over 90 % of Portland cement [13]. The typical composition of OPC is listed in Table 2-1.

Chemical compositions of cement are commonly given sums of oxides. Most widely used abbreviations are listed in Table 2.2. The chemical composition of OPC can be

determined by many methods, with X-ray Florescence (XRF) Spectroscopy and chemical methods most commonly used.

**Table 2-2: Typical Oxide Composition of OPC [12]**

Oxide	Shorthand Notation	Common Name	Weight Percent
CaO	C	Lime	64.47
SiO <sub>2</sub>	S	Silica	21.03
Al <sub>2</sub> O <sub>3</sub>	A	Alumina	6.16
Fe <sub>2</sub> O <sub>3</sub>	F	Ferric oxide	2.58
MgO	M	Magnesia	2.62
K <sub>2</sub> O	K 1	Alkalis	0.61
Na <sub>2</sub> O	N J		0.34
SO <sub>3</sub>	S	Sulfur trioxide	2.03
CO <sub>2</sub>	C	Carbon dioxide	-
H <sub>2</sub> O	H	Water	-

Various types of Portland cement have been developed to meet different physical and chemical requirements for specific construction conditions. These cement types are produced by adjusting the chemical composition and the fineness of cement. Usually, cement types are primarily classified according to ASTM C 150 into five classes:

**Type I** cement is a general purpose cement suitable for all types of structures such as pavements, floors, reinforced concrete buildings, bridges, tanks, reservoirs, pipe, masonry units, and precast concrete products. This type is not requiring special properties like other types.

**Type II** cement is used where relatively low heat generation is desired or where moderate sulfate attack may occur. The C<sub>3</sub>A content increase of early heat in this cement is comparatively lower than that of other cement types

**Type III** cement provides more rapid development of strength at an early age after contact with water because of its higher surface area and increased C<sub>3</sub>S content. It is used when high early strength is desirable.

**Type IV** cement is needed where heat generation from hydration should be minimized such as in mass concrete structures. It generates less heat at a slower rate than the other types because its C<sub>2</sub>S content is higher and its C<sub>3</sub>S content is lower. In addition, this cement has somewhat greater resistance to sulfate attack than for Type I or Type II, and has less rapid strength development with equal strength at advanced ages. This cement is rarely available in the United States where reduction methods of cement hydration using various cementitious materials are much preferred. However, it is commonly found in Korea, especially in mass concrete structures.

**Type V** cement is used where high sulfate resistance is desired such as in foundation and marine structures. The C<sub>3</sub>A content of the cement is limited to less than 5 percent in the specification when a sulfate expansion test is not available.

Typical chemical composition and properties of portland cement for the five types is given in Table 2.3.

**Table 2-3: Typical Compound Composition and Properties of Portland Cement [12]**

	I	II	III	IV	V
C <sub>3</sub> S	55	55	55	42	55
C <sub>2</sub> S	18	19	17	32	22
C <sub>3</sub> A	10	6	10	4	4
C <sub>4</sub> AF	8	11	8	15	12
Fineness (Blaine, m <sup>2</sup> /kg)	365	375	550	340	380
Compressive strength (1day, MPa)	15	14	24	4	12
Heat of hydration (7days,KJ/kg)	350	265	370	235	310

### 2.3.2 Fly Ash

Fly Ash is produced from the combustion of pulverized coal in electric power generation plants. When the pulverized coal is ignited in the combustion chamber, the carbon and volatile materials are burned off. However, some of the mineral impurities of clay, shale, feldspars, etc., are fused in suspension and carried out of the combustion chamber in the exhaust gases. As the exhaust gases cool, the fused materials solidify into spherical glassy particles called Fly Ash. The size of the Fly Ash particles varies but tends to be similar to slightly larger than Type I Portland Cement. The Fly Ash is collected from the exhaust gases by electrostatic precipitators or bag filters. The Chemical composition of Fly Ash is primarily silicate glass containing silica, alumina, iron and calcium. Color generally ranges from dark grey to yellowish tan for Fly Ash used for concrete. Fly ash reacts with calcium hydroxide ( $\text{Ca(OH)}_2$ ) which results from hydration of cement to form secondary CSH as shown in Eq. 2.3

ASTM C 618 Standard Specification for Coal Fly Ash and Raw or Natural Pozzolan for Use as Mineral Admixture in Concrete has two designations for Fly Ash used in concrete - Class F and Class C.

Class F Fly Ash is normally produced from burning anthracite or bituminous coal that meets the applicable requirements. This class of Fly Ash has pozzolanic properties and will have a minimum silica dioxide plus aluminum oxide plus iron oxide of 70%.

Class C Fly Ash is normally produced from sub bituminous coal that meets the applicable requirements. This class of Fly Ash, in addition to having pozzolanic

properties, also has some cementitious properties and will have a minimum silica dioxide plus aluminum oxide plus iron oxide content of 50%.

### **2.3.3 Ground Granulated Blast Furnace Slag (GGBFS)**

Ground granulated blast furnace slag (GGBS) is a by-product from the blast-furnaces used to make iron. These operate at a temperature of about 1500 °C and are fed with a carefully controlled mixture of iron-ore, coke and limestone. The iron ore is reduced to iron and the remaining materials form a slag that floats on top of the iron. This slag is periodically tapped off as a molten liquid and if it is to be used for the manufacture of GGBS it has to be rapidly quenched in large volumes of water. The quenching, optimises the cementitious properties and produces granules similar to a coarse sand. This 'granulated' slag is then dried and ground to a fine powder to form GGBFS.

GGBS replaces a substantial portion of the normal Portland cement content, generally about 50%, but sometimes up to 70%. The higher the proportion, the better is the durability. The disadvantage of the higher replacement level is that early-age strength development is somewhat slower.

GGBFS is hydraulic cement, though its reaction may be partially pozzolanic; its chemical composition is similar to that of cement, though it tends to have a higher silica and alumina content than Portland cement. The slag reaction will proceed even if there is no cement present.

### **2.3.4 Micro-Silica**

Micro-Silica is a very fine non-crystalline produced in electric arc furnaces as a by-product of the production of elemental silicon or alloys containing silicon [14]



.Micro-Silica is usually categorized as a supplementary materials that are used in a concrete in addition to Portland cement. Micro-Silica is a very reactive pozzolanic material in concrete. As the Portland cement in concrete begins to react chemically, it releases a calcium hydroxide. The silica fume reacts with this calcium hydroxide to form additional binder material called calcium silicate hydrate (C-S-H) which is very similar to the calcium silicate hydrate form the Portland cement.

Table 2-4 presents a comparison of silica fume and other commonly used supplementary cementitious materials. Silica fume is typically much more reactive, particularly at early age, because of its higher silicon dioxide content and because of its very small particle size.

**Table 2-4: Comparison of Chemical And Physical Characteristics — Portland Cement, Fly Ash, Slag Cement, and Silica Fume [15]**

Property	Portland Cement	Class F Fly Ash	Class C Fly Ash	Slag Cement	Silica Fume
SiO <sub>2</sub> content, %	21	52	35	35	85 to 97
Al <sub>2</sub> O <sub>3</sub> content, %	5	23	18	12	
Fe <sub>2</sub> O <sub>3</sub> content, %	3	11	6	1	
CaO content, %	62	5	21	40	<1
Fineness as surface area, m <sup>2</sup> /kg	370	420	420	400	15,000 to 30,000
Specific gravity	3.15	2.38	2.65	2.94	2.22
General use in concrete	Primary binder	Cement replacement	Cement replacement	Cement replacement	Property enhancer

**Note:** The values in the table are approximate values. Values for a specific material may vary from what is shown.

## 2.4 Thermal Load due to Cement Hydration

Heat generated by hydration of cement warms concrete to a different degree depending on size and mixture of concrete blocks and surrounding temperature.

Dissipation of temperature depends on ambient temperature, but also on type of formwork and number of surfaces exposed to ambient air. The temperature quickly dissipates from surfaces that are closer to ambient air. The temperature in the core of the block is high and dissipates slowly. This is the reason for the development of stresses. The outer surfaces dry quickly and tend to shrink. This outer region is also in contact with the ambience which may be significantly cooler than the core during hydration. This is the reason for generation of tensile stresses. However, in the core, compression usually dominates. Once tensile stresses become larger than tensile strength, concrete cracking occurs. More complications occur due to loss of moisture, which also may create new cracks [1]. Volume change due to shrinkage and resulting stresses would require the solution of a three phase multi-physics problem (moisture movement, heat transfer and stress evolution).

Heat generation is actually the outcome of the chemical process between cement and pozzolan in concrete. Most of the heat is generated in the first seven days after mixing. In the same time, the concrete is gaining its early strength [1].

Different processes for temperature control in concrete have been used. One of the factors that plays an important role in choosing which process will be applied for temperature control is economy. Some of the ways to solve this problem are: low-heat generating cement, pozzolans, aggregate size, precooling of aggregates and water, appropriate block size, construction schedules, circulating cold water through embedded piping, etc. [2].

The most effective way to reduce temperature is the use of low cement content. This rule has limitations because construction requires a minimum amount of cement to provide workability.

In addition, pozzolans generate heat. Pozzolans are materials that replace cement in concrete structures. Usually pozzolanic materials, fly ash or a natural pozzolan, replace 35% of Portland cement [3]. The reason for this replacement is that pozzolans generate about 40% less heat than cement.

Concrete structures are subjected to volume change. If volume change is uniform, it will not produce cracks. Uniform volume change occurs if a structure is relatively free to expand or contract in all directions. Free volume change is very rare in mass concrete [4]. Mass concrete is usually constrained. This constraint is in many cases enough to produce cracking.

## **2.5 Modeling the Cement Hydration**

A general hydration model for cementitious materials to predict the temperature gain in hardening concrete pavements was developed and calibrated by Schindler [10]. The model accounted for different pavement thicknesses, mixture proportions, cement chemical composition, and cement fineness, amount of cement, mineral mixtures, material types, climatic conditions, and different construction scenarios. This model was developed to control the in place temperature development of early-age concrete, as this will improve the performance of PCC pavements constructed under hot weather conditions. The model was validated by monitoring the temperature developed in PPC pavement in hot weather using thermocouples at the top, middle and bottom of pavement as shown in Figure 2-2.

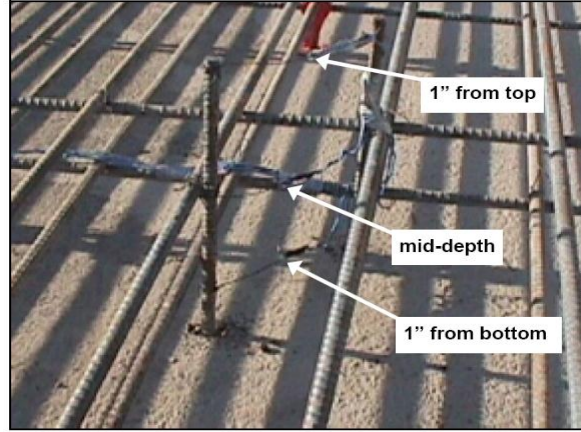


**Figure 2-2: Fastening Thermocouples Prior to Concrete Placement [10]**

The iQdrum semi-adiabatic calorimeter is used in this study [10], which provides a convenient indirect means to characterize the formation of hydration products by measuring the heat released during hydration. Results from semi-adiabatic tests revealed that complete hydration does not occur in any of the concretes tested. This is attributed to the low water-cement ratios used in the concretes tested. This directly affected the total amount of heat released during hydration.

Based on isothermal and adiabatic hydration tests, a new general hydration model has been developed, valid both for Portland cement and blast furnace slag cement. This hydration model enables the calculation of the heat production rate as a function of the actual temperature and the degree of hydration (De Schutter and Taerwe[16]).

The heat production rate was calculated as a function of the actual temperature  $\theta$  and degree of reaction  $r$  [16]. The hydration model for Portland cement is given as

$$q(r, \theta) = q_{max,20} \cdot f(r) \cdot g(\theta) \quad (2.9)$$

where,  $q_{\max,20}$  is the maximum heat production rate at 20°C;  $f(r)$  is the function describing the influence of the degree of reaction  $r$  on the heat production rate; and  $g(\theta)$  is the function describing the influence of the temperature on the heat production rate.

Based on extensive experimental research carried out at the Mager Laboratory for Concrete Research by De Schutter and Taerwe [17], the mechanical behaviour of the hardening concrete was intrinsically related to the degree of hydration, as illustrated with following relations:

$$\frac{f_c(r)}{f_c(r=1)} = \left( \frac{r-r_o}{1-r_o} \right)^a \quad (2.10)$$

where,  $f_c(r)$  is the compressive strength at degree of reaction  $r$ ;  $f_c(r=1)$  is the compressive strength at degree of reaction  $r=1$ ; and  $r_o$ ,  $a$  are the parameters depending on the concrete composition.

$$\frac{E_{co}(r)}{E_{co}(r=1)} = \left( \frac{r-r_o}{1-r_o} \right)^b \quad (2.11)$$

where,  $E_{co}(r)$ , Young's modulus at degree of reaction  $r$ ;  $E_{co}(r=1)$  Young's modulus at degree of reaction  $r=1$ ; and  $r_o$ ,  $b$ , parameters depending on the concrete composition.

$$\frac{f_{ct}(r)}{f_{ct}(r=1)} = \left( \frac{r-r_o}{1-r_o} \right)^c \quad (2.12)$$

where,  $f_{ct}(r)$  is the tensile strength at degree of reaction  $r$ ;  $f_{ct}(r=1)$  is the tensile strength at degree of reaction  $r=1$ ; and  $r_o$ ,  $c$ , parameters depending on the concrete composition.

Alexandra G. et al. [18] presented a data mining approach for modeling the adiabatic temperature rise during concrete hydration. The model was developed based on experimental data obtained in the last thirty years for several mass concrete structures in Brazil. This work presented an integrated hybrid model identification approach that combines fuzzy cluster analysis, radial basis function and genetic algorithm. The numerical results obtained agreed with the experimental results.

Several multicomponent hydration models based on microstructure modeling have been proposed previously (CEMHYD3D [18], DUCOM [19] or even HYMOSTRUC [20]). These models are usually used to describe the microstructure evolution during hardening with great realism but they require long computing time, which is not really appropriate for applications in structural finite element modeling with a large number of nodes.

## **2.6 Monitoring the temperature rise and the maximum temperature**

As part of a field study (Machida and Uehara [21]), a wall structure consisting of reinforced concrete measuring 1.0m thick, varying height of 3.9–4.73m, and 15.0m long was cast on a 1.5m thick base mat concrete slab as shown in Figure 2-3. The wall was instrumented with thermocouples, effective stress meters, mold type strain gages, and strain gages, to capture the temperatures, strain and stress responses at different locations within the wall, as shown in Figure 2-3. The measurement time interval used for this instrumentation setup was one hour in the first three days, three hours until the seventh day, and six hours until the thirtieth day, the last day of the experiment.

The concrete stress and strain condition immediately after placing was unstable, with recordings becoming stable after 6 hours. The tensile strength was measured

using the cleavage test, and the elastic modulus taken as the secant modulus of one-third the collapse strength. The stress-strain relation of one of the non-stress gages was used to calculate the coefficient of thermal expansion which was then assumed to be a constant value throughout the experiment [22].

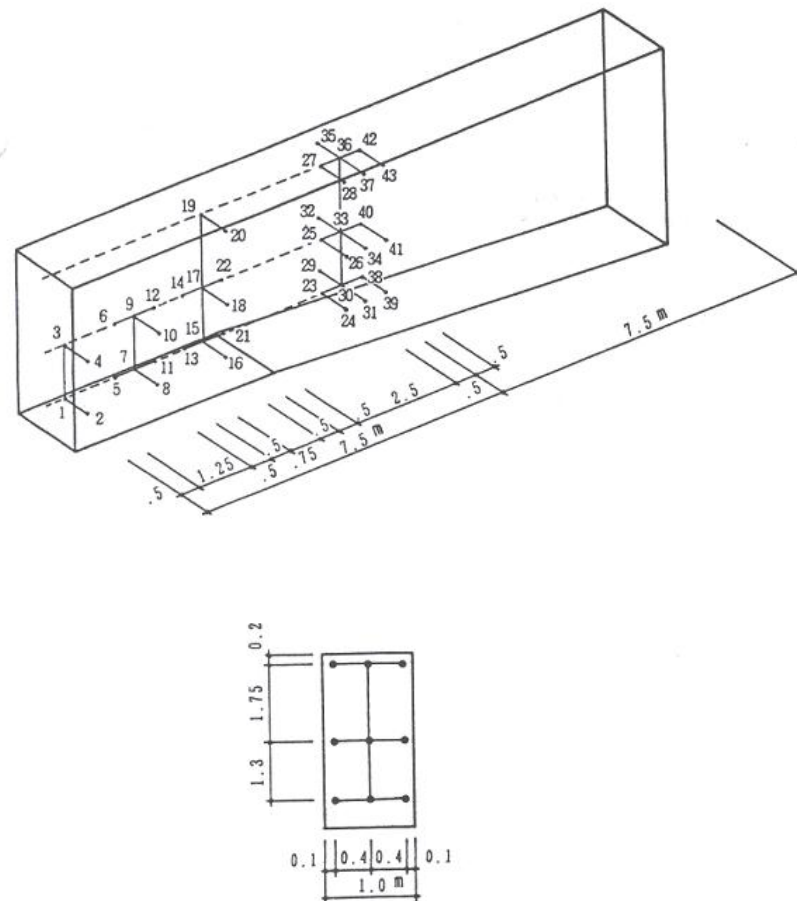


**Figure 2-3: Locations for Temperature and Stress Measurements in a Reinforced Concrete Wall (Machida And Uehara [21])**

The relationships between temperature history and physical properties of concrete materials were studied in Florida University [23]. Thermal and physical tests conducted are summarized in Table 2-5.

**Table 2-5: Thermal and Physical Tests Conducted in Florida University [23].**

Thermal Tests	Physical Tests
<ul style="list-style-type: none"> <li>• Isothermal conduction calorimetry</li> <li>• Semi-adiabatic calorimetry</li> <li>• Sure Cure/adiabatic calorimetry</li> <li>• Heat of solution calorimetry (ASTM C186)</li> <li>• Thermal diffusivity (CRD C 36-73)</li> <li>• Specific heat capacity</li> </ul>	<ul style="list-style-type: none"> <li>• Compressive strength (ASTM C39/109)</li> <li>• Compressive modulus of elasticity (ASTM C469)</li> <li>• Splitting tensile strength (ASTM C496)</li> <li>• Flexural Strength (ASTM C-78)</li> <li>• Tensile Modulus of elasticity</li> <li>• Coefficient of thermal expansion (AASHTO TP60)</li> </ul>

In this research, Christopher [23], different mixes were tested to study the effect of replacing the ordinary Portland cement with GGBFS, fly ash, micro silica, and fibers in reducing the heat of hydration produced at early age. Table 2-6 shows the mixes used for large-scale block specimens. The blocks were instrumented with many thermocouples and the heat of hydration with an associated temperature increase was recorded.

**Table 2-6: Mixture Designs for Large-Scale Block Specimens.**

Mix No.	Cement (lb/yd <sup>3</sup> )	GGBFS (lb/yd <sup>3</sup> )	Fly Ash (lb/yd <sup>3</sup> )	w/c	Coarse agg. (lb/yd <sup>3</sup> )	Fine agg. (lb/yd <sup>3</sup> )
Mix 1(100% PC)	681	-	-	0.5	1650	1095
Mix 2(50% OPC+50% Slag)	341	341	-	0.5	1668	1088
Mix 3(65% OPC+35% FA )	443	-	238	0.5	1660	1036
Mix 4 (30% Slag+20% FA )	341	204	136	0.5	1650	1050



The approximate size of each large-scale specimen is 3.5'× 3.5'× 3.5', with an approximate weight of 5,800 lbs. Figure 2-4 shows a typical large block testing setup [23].



**Figure 2-4: Large Scale Block Testing Configuration [23]**

The results of thermal tests showed that, isothermal conduction calorimetry is a viable testing method for the measurement of heat of hydration of cementitious materials and the calculation of activation energy using isothermal calorimetry testing provides larger values when compared with the calculation of  $E_a$  using the standardized test method per ASTM 1074.

Semi-adiabatic calorimetry does not measure the same level energy evolved from a cementitious system when compared with isothermal or solution calorimetry. Isothermal calorimetry measured the largest amount of heat evolved from a cementitious system and therefore is the most conservative method currently available for the measurement of heat of hydration of cementitious systems [23].

## 2.7 Finite Element Modeling

The Long Spruce Dam in northern Manitoba, Canada, was found to have a crack that runs from the downstream side to the upstream side of the structure. In order to perform an effective rehabilitation procedure, an in-depth analysis to understand the stresses involved in the failure of the crack was undertaken. A 2-D Finite Element Analysis with the aid the commercial software ANSYS was conducted to achieve this goal by Radovanovic [24].

It was found that the  $0.6\text{m} \times 0.6\text{m}$  laboratory specimen was rather small to realistically predict the behavior of massive concrete structures. This led to the enlargement of the FE model by the two, five and ten orders of magnitude. The size that came closest to a realistic characterization of the behavior of the Long Spruce Dam was the  $6\text{m} \times 6\text{m}$  model. However the maximum temperature for this size model was much higher than the dam specimen. The reason given was that the dam specimen was cast in September, when the outside temperature was much lower than the initial temperature used for the laboratory specimen. It was concluded that assumptions made in the calculation of the heat generation rates, material properties and boundary conditions were reasonable and that the finite element algorithm was accurate enough to predict the early age thermal behavior of the laboratory concrete specimen and dam [24].

Haung [25] has numerically simulated the temperature rise, stresses, and the crack development in a freshly cast concrete wall with length of 10 m and thickness of 0.5 m. The wall was constructed on top of a foundation of  $2.0 \times 0.8$  m. The model predicted well occurrence and development of cracks.

The James Bay concrete monolith project (Ayotta et al. [26]), a joint effort between the Societed'Energie de la Baie James (SEBJ) and the EcolePolytechnique de Montreal, focused on developing a methodology, based on finite elements, that could be used to predict the heat generated and resulting thermal stresses in mass concrete. The project included both an experimental component and a modeling component. Three concrete monoliths were built directly on bedrock in the St. James Bay Territory in Northern Quebec Canada, on the site of a major hydroelectric project. Two and three dimensional modeling of the concrete thermal behavior was conducted using the finite element software ADINA-T while the mechanical response, stresses and strains, were obtained using ADINA. To accommodate simultaneous changes of temperature and mechanical property, a modeling technique which employed a step-by-step incremental approach of calculating thermally induced strains was developed to bypass the link between ADINA-T and ADINA [26].

De Shutter [27 ] carried out a realistic three dimensional simulation of early age thermal cracking in hardening massive concrete unit, considering the degree of hydration as fundamental parameter. The time dependent material behavior was implemented by means of a Kelvin chain. The finite element model has showed a good agreement with experimental results.

The major issue that preventing the widespread application of high volume fly ash concrete (HVFAC) is the reduction in the early age (less than 7 days) strength. The strength versus age prediction model for HVFAC mixtures (F and C class fly ash) with varying percentage of cement replacement was developed by Upadhyaya [28]. In this study, the effect of curing condition on the hydration rate for strength

development and the evaluation of activation energy for various fly ash concrete mixes was conducted.

Mortar cubes of HVFA mixtures have shown increased long-term strengths when cured at higher temperatures as compared to cubes cured at lower temperatures [28].

A numerical modeling technique for early age concrete properties was developed by Yan Zhou [29]. The young modulus, tensile strength and limiting tensile strain were accounted for, and the variation of temperature and moisture fields with time was solved. The developed finite element code was used to model thermo mechanical behavior of a newly constructed concrete dam, an arch dam, in China.

The developed finite element code was used to analyze the temperature and stress fields in a concrete dam during pouring and curing stages. In addition, parametric studies were performed to investigate the effect of wind speed and protection layer on the computed temperature and tensile stress fields [29].

An experimental program was conducted to measure the developing temperature and stresses during hydration in concrete members having different shapes and sizes [30]. The experimental studies include determining the compressive stress-strain relationships, the tensile strength, the elastic modulus, creep and shrinkage at ages less than 24 hours up to 28 days.

Arshad [30] developed 2-D finite element transient thermal analysis using a modified version of the computer program (DETECT) (determination of temperature in construction) to predict the temperature variation both in space and time. This program was originally developed by Polivka and Wilson (1976).

The program was developed for the purpose of evaluating the temperature distribution during construction of massive structures such as dams, foundation and bridge piers.

The temperature was predicted for girder with depth of 2300 mm and web thickness of 150 mm and for columns with dimensions of 1×1×2 m using many thermocouples at the surface and center of column [30].

A software developed as part of research project [31], called ConcreteWorks, can estimate the concrete temperature development for mass concrete, pavements, bridge decks, and precast concrete beams, the early-age cracking probability of several mass concrete members, and the service life for mass concrete and bridge deck members. In order to make the software more user friendly, ConcreteWorks allows the user to select from a set of commonly used concrete member shapes and boundary conditions.

Concrete from five different construction projects in the state of Texas was tested onsite to determine their heat of hydration. In the first project, the temperature was predicted for column with dimension of 1.8×3.1× 9.1 and footing with dimensions of 3.1 × 3.1 × 1.9 using many thermocouples at the surface and center of column. In the second project, the temperature was monitored for a Dolphin (a large concrete member used as a bumper to protect the causeway against barge impact) with dimensions of 4.9 × 4.9 × 2.7. In the third, fourth and fifth project, the temperature monitored for Causeway Footing with dimensions of (18.3 × 4.1 × 2.0), Rectangular Bent Cap with dimensions of (1.0 × 1.0), and for Pilaster with dimensions of (2.7 × 1.8 × 1.7) respectively [31].

The mixes belong to aforementioned projects included the supplementary cementitious materials (fly ash and GGBFS) with different proportions to reduce the heat generated from cement hydration [31].

The concrete heat of hydration was tested using a semi-adiabatic calorimeter. The semi-adiabatic calorimeter is an insulated steel drum with a cavity inside for a concrete cylinder. The semi-adiabatic calorimetry was performed on a 150 mm by 300mm (6 in. by 12 in.) concrete cylinder. The semi-adiabatic calorimeter was placed in the nearest temperature controlled building or shed provided by the contractor. The concrete cylinders were made onsite using concrete sampled from the ready mixed truck or pump, and then transported to the nearby calorimeter [31].

The temperature profile resulting from the heat of hydration was measures for different structural members such as bridge deck, piers, etc. Figure 2-5and Figure 2-6 show thermal sensors and thermal bar installation on bridge deck and bridge piers, respectively [31].

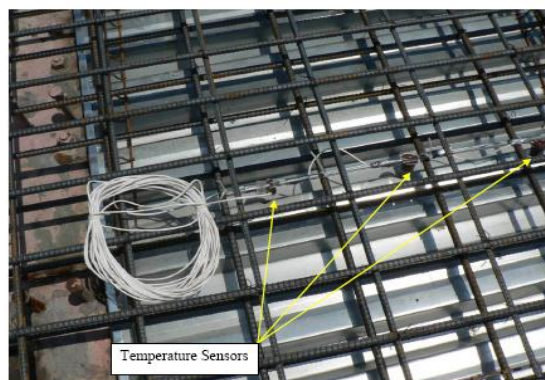


**Figure 2-5: Temperature Sensors before Concrete Placement [31]**



**Figure 2-6: Temperature Bar 4 after Installation [31]**

Despite the existence of considerable literature in studying the temperature distribution and the probability of cracking in mass concrete structures, No research has been conducted in KSA to study the effect of heat of hydration in thermal distribution and associated risk of cracking in mass concrete structures. None of the local specifications addresses the heat of hydration (even for mass concrete) and there is a shortage in data about the performance of the available raw and cementitious materials in the local markets regarding heat of hydration.

In view of the huge on-going construction in Saudi Arabia, research on local materials is very important. Having enough data and research about heat of hydration done using local materials will save time in projects and will be more convincing to consultants than data obtained from research done outside the region.

The mechanical and thermal properties of different mixes will be studied. The IQdrum will be used to obtain the adiabatic heat of hydration for each mix. The results of experimental program will be used in the finite element model to simulate the temperature distribution and thermal stresses in mock-up specimens and actual

raft foundation. The finite element model will be utilized in selection of appropriate mixes for use in mass concrete structures in Saudi Arabia.



## **CHAPTER 3**

### **EXPERIMENTAL PROGRAM**

The experimental program consists of two main parts:

1) Laboratory Tests

2) Field Tests

#### **3.1 Laboratory Tests**

In this research, the measurements of heat of hydration and mechanical properties of 46 mixes were carried out.

##### **3.1.1 Measuring the Heat of Hydration**

###### **3.1.1.1 Measuring the Heat of Hydration Using iQdrum Calorimeter**

The semi-adiabatic calorimeter (iQdrum) was used to measure the generated heat from hydration of cement. The heat of hydration was measured for different 45 mixes. The effect of mineral mixtures (granulated blast furnace slag (GGBFS), fly ash, and micro silica) with different ratios in reducing the heat of hydration in mass concrete was studied. The effect of water cement ratio and chemical admixture (ADVA 314) in heat of hydration was also studied. After mixing the different proportions of mix, the plastic cylinder with dimensions of 6×12 inch, as shown in Figure 3-1, was filled with the mix.

The cylinder 6×12 inch was closed with a plastic cover. A hole is punched in the top cover to allow entry of thermal sensor which is inserted inside the fresh concrete mix. The specimen is kept in an isolated environment (adiabatic) to ensure that one obtains the maximum adiabatic heat of hydration and adiabatic temperature rise. The iQdrum calorimeter includes an automated method of measuring concrete heat of hydration and its

rate versus curing age using full size (up to 6in.× 12 in.) standard test cylinder. The measurements are carried out using an iQdrum calorimeter via the internet and are recorded and analyzed in the Quadrel software program that includes a database of all the measurements.



**Figure 3-1: Types of iQdrum Calorimeter.**

The test requires from 7 to 14 days of test time based on the type of mix. The mixes with high content of cement will take less time of test when compared with mixes having high content of fly ash or GGBFS. The calorimeter technology uses results in perfect adiabatic (no heat loss) measurements by recording accurately and automatically correcting for the calorimeter heat loss. The calorimeter technology provides the plot of heat generated data versus the maturity equivalent age (rather than the clock-time curing age) to normalize the curing age to a standard equivalent age at 20 °C.

For each test, one obtains the raw data which includes the temperature in the concrete specimen, ambient temperature and the heat loss as shown in Figure 3-2.

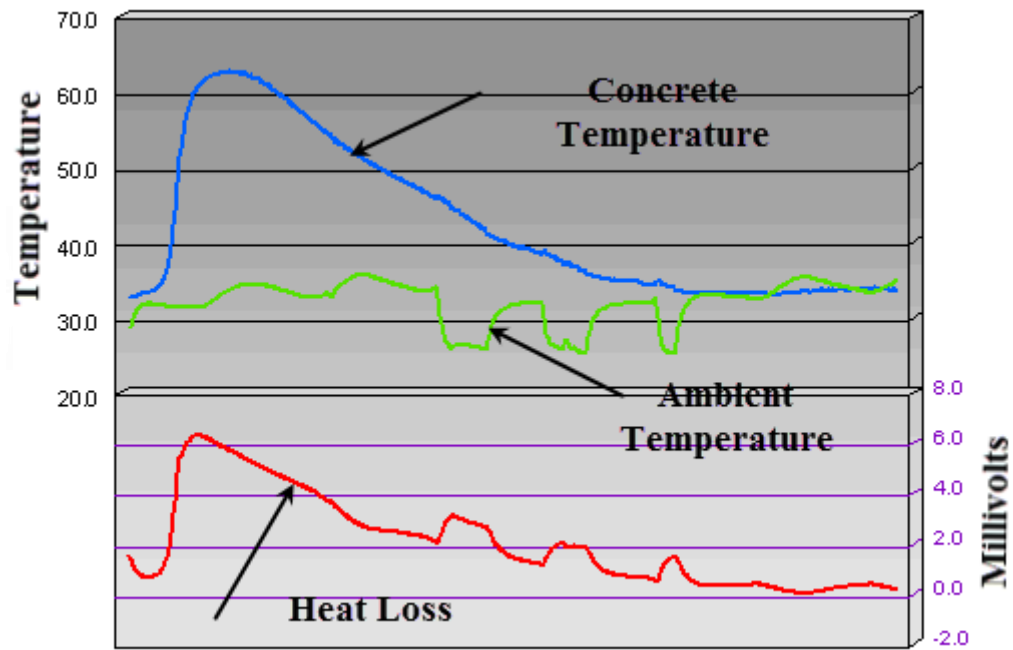


**Figure 3-2: Temperature in Concrete Specimen, Ambient Temperature and Heat Loss [32].**

The experimental test allows viewing the heat data versus the equivalent curing age at 20 °C in two ways. The heat signature software provides the adiabatic heat of hydration and its rate or the temperature rise and its rate as shown in Figure 3-3 and Figure 3-4 respectively.

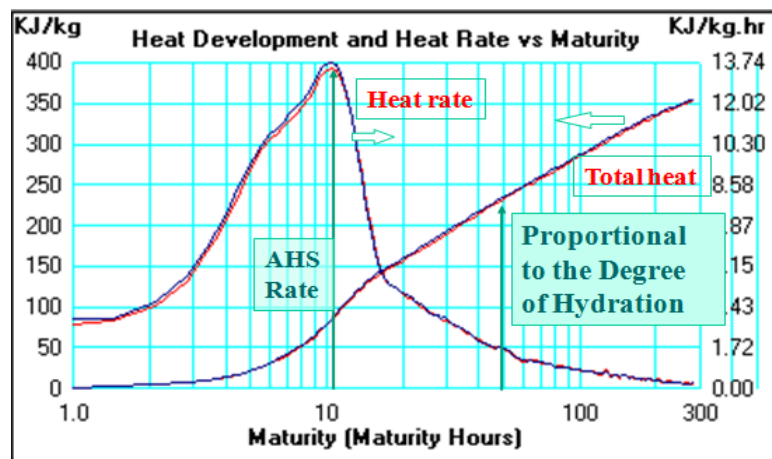


**Figure 3-3: Adiabatic Heat Rise and Its Rate Versus Equivalent Age [32].**

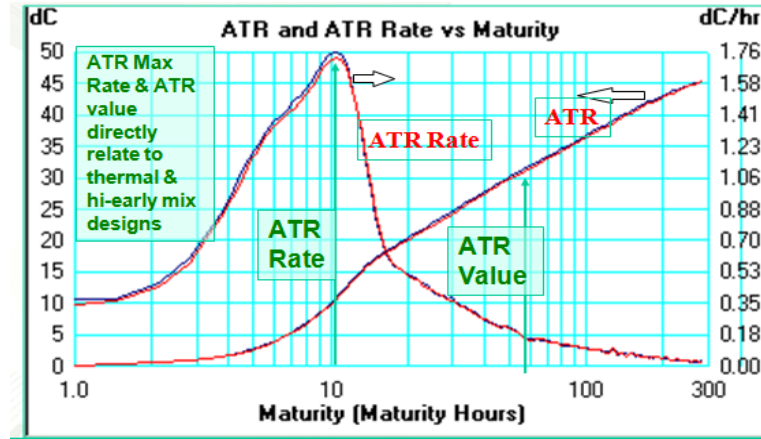


**Figure 3-4: Adiabatic Temperature Rise and Its Rate Versus Equivalent Age [32].**

The calorimeter used in the test is considered a semi adiabatic calorimeter but the heat loss is added to the temperature in concrete to work as adiabatic calorimeter.

The heat of hydration can be converted to temperature using following equation:

$$ATR = \frac{Q \cdot W_{cm}}{\gamma \cdot c} \quad (1.3)$$

where

Q is the heat of hydration (KJ/kg)

$W_{cm}$  weight of cementitious material per cubic meter ( $\text{kg/m}^3$ )

$\gamma$  unit weight of concrete ( $\text{kg/m}^3$ )

c specific heat ( $\text{KJ/m}^3\text{-}^\circ\text{C}$ )

### 3.1.1.2 Measuring the Heat of Hydration Using Heat Box

The Heat-Box is shaped as a cube with the dimensions of  $0.6\text{m} \times 0.6\text{m} \times 0.6\text{m}$  as shown in Figure 3-5. It is insulated from inside to provide an adiabatic condition. The Heat-Box

contains a space for a cylindrical concrete sample with the dimensions of 150mm×300mm.

The Heat-Box is a semi-adiabatic calorimeter. When fresh concrete is placed in the Heat-Box, the evolution of the temperature is recorded in addition to the ambient temperature. When the measuring is finished the software is calculating the corresponding adiabatic development of the Heat of Hydration. A screen-dump from the software is shown on Figure 3-6.



- 1 – Thermocouple to measure the concrete temperature
- 2- Data logger
- 3- Thermocouple to measure the ambient temperature

**Figure 3-5: Heat-Box and Concrete Sample.**

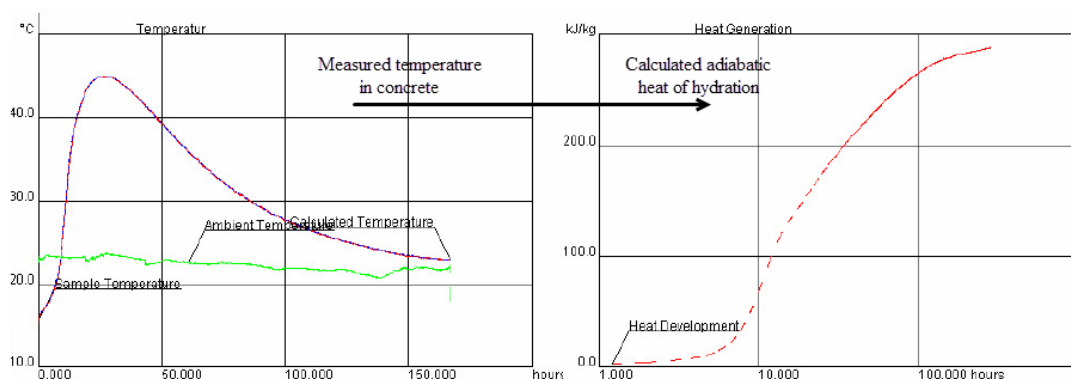


**Figure 3-6: Measured Temperature and Calculated Heat of Hydration Using Heat-Box.**

In the right side of the screen-dump, is shown the heat development which calculated from the measured temperature rise in concrete.

### **3.1.2 Measuring the Tensile Strength of Concrete at Early Age**

For each mix, the splitting tensile strength was carried out at ages 2, 4, 7, 28 and 56 days as shown in Figure 3-7. The obtained values of concrete tensile strength were used as input in finite element model.



**Figure 3-7: Measuring the Splitting Tensile Strength of Concrete**

### **3.1.3 Measuring the Compressive Strength of Concrete**

The compressive strength test was carried out according to ASTM C39 at ages 2, 4, 7, 28, 56 and 90 days as shown in Figure 3-8. The compressive strength was measured for concrete cylinders with dimensions of 6 in  $\times$  12 in and, then repeated for cylinders with dimensions of 3 in  $\times$  6 in to get more reliable results. All cylinders were capped with a sulfur mortar.



**Figure 3-8: Measuring the Compressive Strength of Concrete**

#### **3.1.4 Measuring the Modulus of Elasticity**

The modulus of elasticity of concrete cylinders with dimensions of 3×6 in was measured at ages 2, 4,7,28 and 56 days. Two strain gauges were bonded with a adhesive to the surface of concrete cylinders. A load cell was used to measure the load applied. The strain gauges and the load cell were connected to a data logger as shown in Figure 3-9.

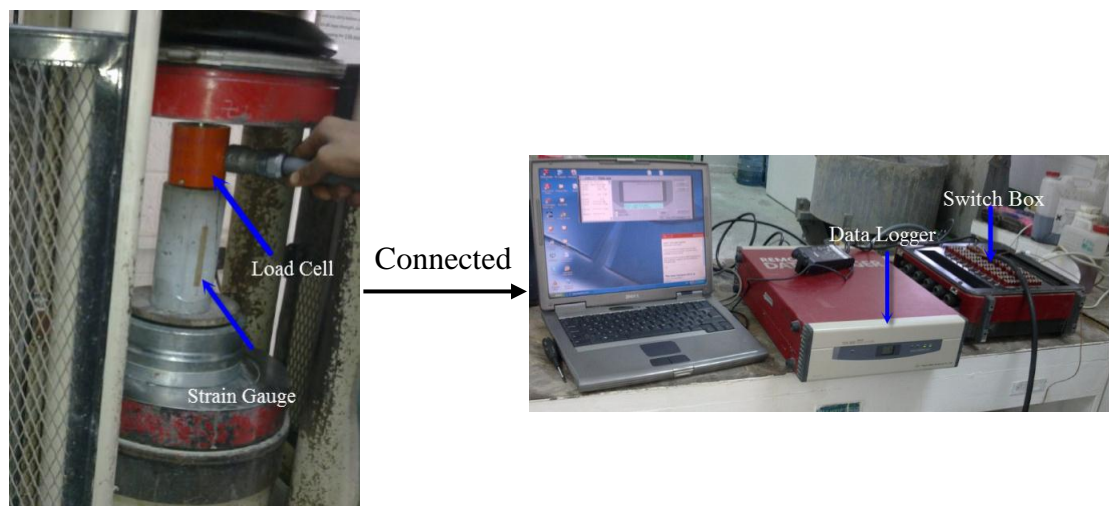


**Figure 3-9: Measuring the Concrete Modulus of Elasticity**



### 3.1.5 Measuring the Properties of Self Compacting Concrete

An experimental program was conducted to study the generation of heat of hydration in ten different types of normal, flowing and self-compacting concretes using iQdrum heat signature calorimeter. The flowability, passing ability, and filling ability of flowing and self-compacting concrete were evaluated by conducting the Slump flow, V-funnel and L-Box. In slump flow test, the Abrams cone was filled with concrete and then lifted vertically and the time measurement started to record as shown in Figure 3-10. The spread diameter T50 (i.e., the time of flow to reach a diameter of 500 mm) and the general visual appearance of the concrete were recorded. V-funnel test was used to evaluate the viscosity of SCC as shown in Figure 3-12. The test was carried out by filling a V-shaped funnel with fresh concrete and then measuring the time in seconds that the concrete took to drain of the funnel. The L-Box was filled with fresh concrete, and then the gate between the vertical and horizontal parts was raised so that the concrete flows into the horizontal section of the box as shown in Figure 3-11. When movement of concrete has ceased, the ratio  $H_1/H_2$  was started to be determined.



**Figure 3-10: Measuring the Flowability and T50 of Self Compacting Concrete**





**Figure 3-11: V-Funnel for Measuring Flowability and Viscosity of SCC**



**Figure 3-12 : L-Box for Measuring the Passing Ability of SCC**

### 3.1.6 Mix Proportioning

Forty six mixes were investigated in the experimental program. Tenth different the groups have been studied. The first the group consists of six different mixes. The reference mix (REF) contains  $480 \text{ kg/m}^3$  Type I cement and water/binder ratio of 0.28. In other, the cement was replaced with different percentages Fly Ash (20%, 30%, 40%, 50%, and 60%) and the same water to binder ratio was maintained for all the mixes (0.28). The coarse aggregate content was  $1210 \text{ kg/m}^3$  and the fine aggregate content was  $569 \text{ kg/m}^3$ . The mix proportions of first the group mixes are shown in

Table 3-1.

**Table 3-1: Mix Proportions for the First Group of Mixes.**

Mix No.	Cement ( $\text{kg/m}^3$ )	GGBFS ( $\text{kg/m}^3$ )	Fly Ash ( $\text{kg/m}^3$ )	w/c	Coarse agg. ( $\text{kg/m}^3$ )	Fine agg. ( $\text{kg/m}^3$ )
Mix 1(100% PC)	480	-	-	0.28	1210	569
Mix 2(20% FA)	384	-	96	0.28	1210	569
Mix 3(30% FA )	330	-	150	0.28	1210	569
Mix 4(40% FA )	288	-	192	0.28	1210	569
Mix 5(50% FA )	240	-	240	0.28	1210	569
Mix 6(60% FA )	192	-	288	0.28	1210	569
Mix 7(50% FA+Ret.* )	240	-	240	0.28	1210	569

\* Retarder (Type Warda 8)

The second group consists of six different mixes. The reference mix (REF) is the same mix used in the group #1. In others, the cement was replaced with different percentages GGBFS (20%, 30%, 40%, 50%, 60%, and 70%) and the same water to binder ratio was maintained for all the mixes (0.28). The coarse aggregate content was  $1210 \text{ kg/m}^3$  and the fine aggregate content was  $569 \text{ kg/m}^3$ . The mix proportions of fourth the group mixes are shown in Table 3-2.

**Table 3-2: Mix Proportions for the Second Group of Mixes.**

Mix No.	Cement (kg/m <sup>3</sup> )	GGBFS (kg/m <sup>3</sup> )	Fly Ash (kg/m <sup>3</sup> )	W/C	Coarse agg. (kg/m <sup>3</sup> )	Fine agg. (kg/m <sup>3</sup> )
Mix 1 (100% PC)	480	-	-	0.28	1210	569
Mix8 (20% GGBFS)	384	96	-	0.28	1210	569
Mix9 (30% GGBFS )	330	150	-	0.28	1210	569
Mix 10 (40% GGBFS )	288	192	-	0.28	1210	569
Mix 11 (50% GGBFS )	240	240	-	0.28	1210	569
Mix 12 (60% GGBFS )	192	288	-	0.28	1210	569
Mix 13 (70% GGBFS )	144	336	-	0.28	1210	569
Mix 14 (50% GGBFS+Ret.* )	240	-	240	0.28	1210	569

The third group consists of five different mixes. The reference mix (REF) is the same mix used in the group #1. In other mixex, the cement was replaced with different percentages GGBFS and Fly ash (10% FA+10%GGBFS, 15% FA+15%GGBFS, 20% FA+20%GGBFS, 25% FA+25%GGBFS, and 30%FA+30% GGBFS) and the same water to binder ratio was maintained for all the mixes (0.28). The coarse aggregate content was 1210 kg/m<sup>3</sup> and the fine aggregate content was 569 kg/m<sup>3</sup>. The mix proportions of third the group mixes are shown in Table 3-3.

**Table 3-3: Mix Proportions for the Third Group of Mixes.**

Mix No.	Cement (kg/m <sup>3</sup> )	GGBFS (kg/m <sup>3</sup> )	Fly Ash (kg/m <sup>3</sup> )	w/c	Coarse agg. (kg/m <sup>3</sup> )	Fine agg. (kg/m <sup>3</sup> )
Mix 1 (100% PC)	480	-	-	0.28	1210	569
Mix15 (10% FA+10%GGBFS)	384	48	48	0.28	1210	569
Mix16 (15% FA+15%GGBFS)	330	75	75	0.28	1210	569
Mix 17 (20% FA+20%GGBFS)	288	96	96	0.28	1210	569
Mix 18 (25% FA+25%GGBFS)	240	120	120	0.28	1210	569
Mix 19 (30% FA+30%GGBFS)	192	144	144	0.28	1210	569

The fourth group consists of four different mixes. The reference mix (REF) contains 350 kg/m<sup>3</sup> Type I cement and water/binder ratio of 0.38. In other, the cement was replaced with different percentages Fly ash (10% FA, 30% FA, 40% FA, and 50% FA) and the same water to binder ratio was maintained for all the mixes (0.38). The coarse aggregate content was 1218 kg/m<sup>3</sup> and the fine aggregate content was 650 kg/m<sup>3</sup>. The mix proportions of fourth the group mixes are shown in Table 3-4.

**Table 3-4: Mix Proportions for the Fourth Group of Mixes.**

Mix No.	Cement (kg/m <sup>3</sup> )	GGBFS (kg/m <sup>3</sup> )	Fly Ash (kg/m <sup>3</sup> )	w/c	Coarse agg. (kg/m <sup>3</sup> )	Fine agg. (kg/m <sup>3</sup> )
Mix 20 (100% PC)	350	-	-	0.38	1218	650
Mix21 (20% FA)	280	-	70	0.38	1218	650
Mix22 (30% FA)	245	-	105	0.38	1218	650
Mix 23 (40% FA)	210	-	140	0.38	1218	650
Mix 24 (50% FA)	175	-	175	0.38	1218	650

The fifth group consists of four different mixes. The reference mix (REF) is the same mix used in the group#4. In other, the cement was replaced with different percentages Fly ash (10% GGBFS, 30% GGBFS, 40% GGBFS, and 50% GGBFS) and the same water to binder ratio was maintained for all the mixes (0.38). The coarse aggregate content was 1218 kg/m<sup>3</sup> and the fine aggregate content was 650 kg/m<sup>3</sup>. The mix proportions of fifth the group mixes are shown in Table 3-5.

**Table 3-5: Mix Proportions for the Fifth Group of Mixes.**

Mix No.	Cement (kg/m <sup>3</sup> )	GGBFS (kg/m <sup>3</sup> )	Fly Ash (kg/m <sup>3</sup> )	w/c	Coarse agg. (kg/m <sup>3</sup> )	Fine agg. (kg/m <sup>3</sup> )
Mix 20 (100% PC)	350	-	-	0.38	1218	650
Mix25 (20%GGBFS)	280	-	70	0.38	1218	650
Mix26 (30%GGBFS)	245	-	105	0.38	1218	650
Mix 27 (40%GGBFS)	210	-	140	0.38	1218	650
Mix 28 (50%GGBFS)	175	-	175	0.38	1218	650

The sixth group consists of four different mixes. The reference mix (REF) is the same mix used in the group#1. In other, the cement was replaced with different percentages Micro-Silica (10% Micro-Silica, 20% Micro-Silica, 30% Micro-Silica, and 40% Micro-Silica) and the same water to binder ratio was maintained for all the mixes (0.28). The coarse aggregate content was 1210 kg/m<sup>3</sup> and the fine aggregate content was 569 kg/m<sup>3</sup>. The mix proportions of sixth the group mixes are shown in Table 3-6.

**Table 3-6: Mix Proportions for the Sixth Group of Mixes.**

Mix No.	Cement (kg/m <sup>3</sup> )	GGBFS (kg/m <sup>3</sup> )	MS (kg/m <sup>3</sup> )	w/c	Coarse agg. (kg/m <sup>3</sup> )	Fine agg. (kg/m <sup>3</sup> )
Mix 1(100% PC)	480	-	-	0.28	1210	569
Mix 29 (10% MS)	432	-	48	0.28	1210	569
Mix 30 (20% MS )	384	-	96	0.28	1210	569
Mix 31 (30% MS )	330	-	150	0.28	1210	569
Mix 32 (40% MS )	288	-	192	0.28	1210	569

In the seventh group, the effect of water cementitious materials ratio in heat of hydration has been studied. The mix proportions of seventh the group mixes are shown in Table 3-7.

**Table 3-7: Mix Proportions for the Seventh Group of Mixes.**

Mix No.	Cement (kg/m <sup>3</sup> )	GGBFS (kg/m <sup>3</sup> )	Fly Ash (kg/m <sup>3</sup> )	w/c	Coarse agg. (kg/m <sup>3</sup> )	Fine agg. (kg/m <sup>3</sup> )
Mix 3 (30% FA)	336	-	144	0.28	1210	569
Mix 33 (30% FA)	336	-	144	0.33	1210	569
Mix 34 (30% FA)	336	-	144	0.38	1210	569

In the eighth group, the influence of concrete type in heat of hydration and in the evolution of temperature in mass concrete structures has been investigated. Nine mixes of flowable concrete, normal slump concrete, and self-compacting concrete (SCC) have been investigated.

**Table 3-8: Mix Proportions for the Eighth Group of Mixes.**

Material/ Mix No.	Cement (kg/m <sup>3</sup> )	Fly Ash (kg/m <sup>3</sup> )	Water (liter)	Aggregate 20 mm (kg/m <sup>3</sup> )	Aggregate 10 mm (kg/m <sup>3</sup> )	Aggregate 5 mm (kg/m <sup>3</sup> )	Sand (kg/m <sup>3</sup> )	Admix. ADVA314 (liter)
Mix 1 (100% OPC (REF))	480	-	134	510	500	200	569	3
Mix 2 (20% FA) (FC**)	384	96	134	510	500	200	569	3
Mix 3 (30% FA) (FC)	330	150	134	510	500	200	569	3
Mix 4 (40% FA) (FC)	288	192	134	510	500	200	569	2
Mix 35 (20% FA) (NC*)	384	96	134	510	500	200	569	1.5
Mix 36 (30% FA) (NC)	330	150	134	510	500	200	569	1.5
Mix 37 (40% FA) (NC)	288	192	134	510	500	200	569	1
Mix 38 (20% FA) (SCC***)	384	96	134	455	395	225	650	3
Mix 39 (30% FA) (SCC)	330	150	134	455	395	225	650	3
Mix 40 (40% FA) (SCC)	288	192	134	455	395	225	650	2

\* NC Normal concrete

\*\* FC Flowable concrete

\*\*\* SCC Self Compacting concrete

The effect of using high content of cement in mass concrete structures has been investigated. Mixes with 480kg of cement, 700kg, and 900 kg have been studied. The mix proportions of this group are shown in Table 3-9.

**Table 3-9: Mix Proportions for the Ninth Group of Mixes.**

Mix No.	Cement (kg/m <sup>3</sup> )	GGBFS (kg/m <sup>3</sup> )	Fly Ash (kg/m <sup>3</sup> )	w/c	Coarse agg. (kg/m <sup>3</sup> )	Fine agg. (kg/m <sup>3</sup> )
Mix 1	480	-	-	0.28	1210	569
Mix 41	700	-	-	0.28	920	435
Mix 42	900	-	-	0.28	720	326

In the tenth the group, the effect of steel and Polypropylene fibers in the heat of hydration and in the mechanical properties of concrete at early age has been investigated. The mix proportions of tenth the group mixes are shown in Table 3-10.

**Table 3-10: Mix Proportions for the Tenth Group of Mixes.**

Material/ Mix No.	Cement (kg/m <sup>3</sup> )	Fly Ash (kg/m <sup>3</sup> )	Water (liter)	Coarse Agg. (kg/m <sup>3</sup> )	Fine Agg. (kg/m <sup>3</sup> )	Steel Fibers (kg/m <sup>3</sup> )	Poly. Fibers (kg/m <sup>3</sup> )
Mix 4 (40 % FA) (REF)	288	192	134	1210	569	-	-
Mix 43 (40 % FA)	288	192	134	1210	569	23.5	-
Mix 44 (40 % FA)	288	192	134	1210	569	46.62	-
Mix 45 (40 % FA)	288	192	134	1210	569	-	2.8
Mix 46 (40% FA)	288	192	134	1210	569	-	5

### 3.1.7 Materials Properties

The coarse aggregates used in this study were from the quarries of Riyadh Road, Saudi Arabia. The maximum aggregate size was 20 mm and the average values of specific gravity and absorption of coarse aggregates, determined in accordance with ASTM C128, were 2.6, and 2 %, respectively. Local dune sand was used as fine aggregate. The specific gravity and absorption of fine aggregate was 2.6, and 0.7%, respectively. Cement of Type I was used in this study and the specific gravity of it was 3.15. GGBFS, Fly ash, and Micro silica were used as fillers. The chemical and physical properties of cement,

GGBFS, and Fly Ash are summarized in Tables 3-11 to 3-13. The polycarboxylate based superplasticizer, ADVA 314, was used as high range water reducing superplasticizer. The specific gravity of super- plasticizer was 1.106.

ADVA 314 is a high efficiency liquid superplasticiser which has been designed to improve the slump retaining properties of high workability concretes. It is also beneficial in improving cohesion of concretes especially in applications where difficult or inaccessible pours are to be made. ADVA 314 is based on modified synthetic carboxylated polymers and is manufactured under controlled conditions to give a consistent product.

**Table 3-11: Chemical and Physical Properties of Cement Type I.**

<b>CHEMICAL ANALYSIS</b>			<b>Results</b>	<b>Specifications</b>
Silicon dioxide	SiO <sub>2</sub>	%	20.64	
Aluminium oxide	Al <sub>2</sub> O <sub>3</sub>	%	5.40	
Ferric oxide	Fe <sub>2</sub> O <sub>3</sub>	%	3.27	
Calcium oxide	CaO	%	63.91 •	
Magnesium oxide	MgO	% -	1.84	6.0 Max.
Sulfur trioxide	SO <sub>3</sub>	%	2.56	3.5 Max.
Loss on ignition	L.O.I.	%	1.85	3.0 Max.
Insoluble residue	I.R.	%	0.69	0.75 Max
Alkalies (Na <sub>2</sub> O + 0.658 *K <sub>2</sub> O)		%	0.49	
Lime saturation factor	LSF		93.55	
Tricalcium silicate	C <sub>3</sub> S	%	55.06	
Dicalcium silicate	C <sub>2</sub> S	%	17.64	
Tricalcium aluminate	C <sub>3</sub> A	%	8.78	
Tetracalcium aluminoferrite	C <sub>4</sub> AF	%	9.95	
C <sub>4</sub> AF+2C <sub>3</sub> A		%	27.50	
Chloride	CI	%	0.001	
<b>Physical Tests</b>				
Air content of mortar ( by volume )		%	6.0	12 Max.
Fineness, Air permeability Test		m <sup>2</sup> /kg	342	260 Min.
Soundness, Autoclave Test		%	0.06	0.80 Max.
<b>Compressive Strength</b>				
3 days		MPa (psi)	19.3 ( 2800 )	12 (1740) Mm.
7 days		Mpa (psi)	26.3 ( 3810 )	19(2760) Min.
28 days		Mpa (psi)		28 (4060) Min.
Setting Time (VicatTest)	Initial	minutes	145	45 Min
	Final	minutes	210	375 Max.



**Table 3-12: Chemical and Physical Properties of GGBFS.**

Chemical Properties		
Type of Test	Result % by wt. of material	BS 6699 : 1992 Requirements
Insoluble Residue (%)	1.22	1.5 Max.
Loss on Ignition (%)	1.2	3.0 Max.
Sulphate Content as SO <sub>3</sub> (%)	0.3	2.5 Max.
Chloride Content as Cl (%)	0.003	0.10 Max.
Magnesium Oxide as MgO (%)	8.17	14.0 Max.
Iron Oxide as Fe <sub>2</sub> O <sub>3</sub> (%)	2.04	-
Aluminium Oxide as Al <sub>2</sub> O <sub>3</sub> (%)	14.56	-
Silicon Oxide as SiO <sub>2</sub> (%)	34.53	-
Calcium Oxide as CaO (%)	36.47	—
Sodium Oxide (%)	0.31	
Potassium Oxide (%)	0.60	
Equivalent Alkalies (Na <sub>2</sub> O + 0.658 K <sub>2</sub> O)	0.69	—
( CaO+MgO ) / SiO <sub>2</sub>	1.29	1.0 Min.
CaO+MgO+SiO <sub>2</sub>	79.17	66.6 Min.
CaO / SiO <sub>2</sub>	1.06	1.4 Max.

**Table 3-13: Physical Properties of GGBFS.**

Physical Properties of GGBFS			
Test Carried Out	Test Method	Results	BS 6699 : 1992 Requirements
Fineness of Cement (cm <sup>3</sup> /g) (Blaine Air Permeability)	BS EN 196-3: 1992, CI.4	4275	2750 Min.
Compressive Strength (N/mm <sup>2</sup> ) at 7 days at 28 days	BS EN 196-1 : 1995	27 45.6	12 Min. 32.5 Min.
Setting Time (Min.) - Initial Setting Time - Final Setting Time	BS EN 196-3: 1995	135 230	Not less than IST of OPC used
Specific Gravity	BS 812-Part 2: 1995	2.712	-
Soundness (mm)	BS EN 196-3: 1995, CI.7	1	10 Max.
Moisture Content (%)	BS 6699:1992	0.3	1.0 Max.

**Table 3-14: Mechanical Properties of Fly Ash.**

<b>Physical Characteristics:</b>			
Moisture content @ 105°C	—	wt. %	0.10
<b>Chemical Composition</b>			
Silicon dioxide	(SiO <sub>2</sub> )	wt. %	64.7
Aluminum oxide	(Al <sub>2</sub> O <sub>3</sub> )	wt. %	29.7
Iron oxide	(Fe <sub>2</sub> O <sub>3</sub> )	wt. %	3.01
Calcium oxide	(CaO)	wt. %	LT 0.01
Magnesium oxide	(MgO)	wt. %	0.58
Sulphur trioxide	(SO <sub>3</sub> )	wt. %	0.60
Chloride	(Cl)	wt. %	0.03
Sodium oxide	(Na <sub>2</sub> O)	wt. %	0.04
Potassium oxide	(K <sub>2</sub> O)	wt. %	0.16
Loss of Ignition @ 950°C	(LOI)	wt. %	0.13
<b>Calculated Values:</b>			
Available Alkalies (Na <sub>2</sub> O + 0.658 K <sub>2</sub> O)		wt. %	0.05

### 3.2 Field Monitoring

The temperature rise resulting from the heat of hydration was monitored for seven mock-up specimens. Three of mockup specimens with dimensions of 2m×2m×2m are located in KFUPM campus and three located near to Dammam city coast. One mockup specimen is located in Jeddah city. The temperature rise also monitored for a piles-cap with dimensions of 9.1m×9.1m×1.7m. The strains in the mock-up specimens and in the piles-cap were also monitored at different locations.

#### 3.2.1 Monitoring of KFUPM Mock-up Specimens (KMUS)

The temperature rise due to the heat of hydration in the concrete mockup specimens with dimensions of 2m×2m×2m was monitored by using 54 thermocouples. Thermocouples were installed and embedded to concrete at the top, middle, and bottom. Figure 3-13 shows the layout for thermocouples and strains in plan and side view of

concrete mockup specimen respectively. Thermocouples were connected to an automated data logger as shown in Figure 3-14. The readings were recorded every ten minutes.

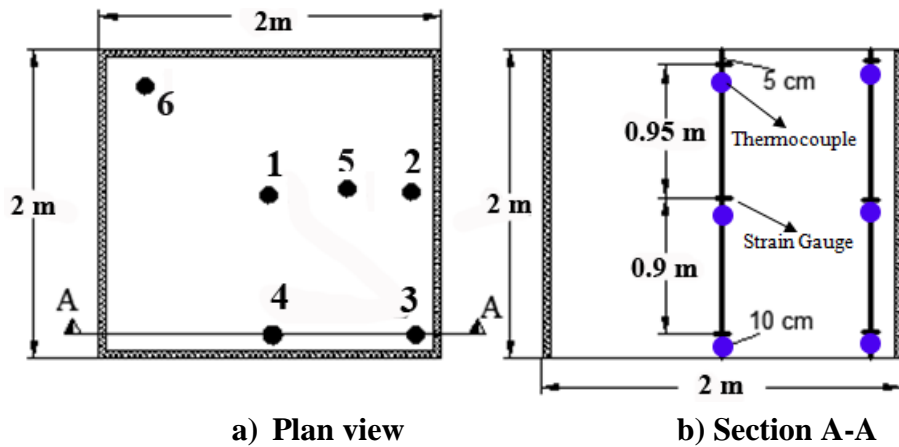


**Figure 3-13: Thermocouple and Strain Gauges Locations**

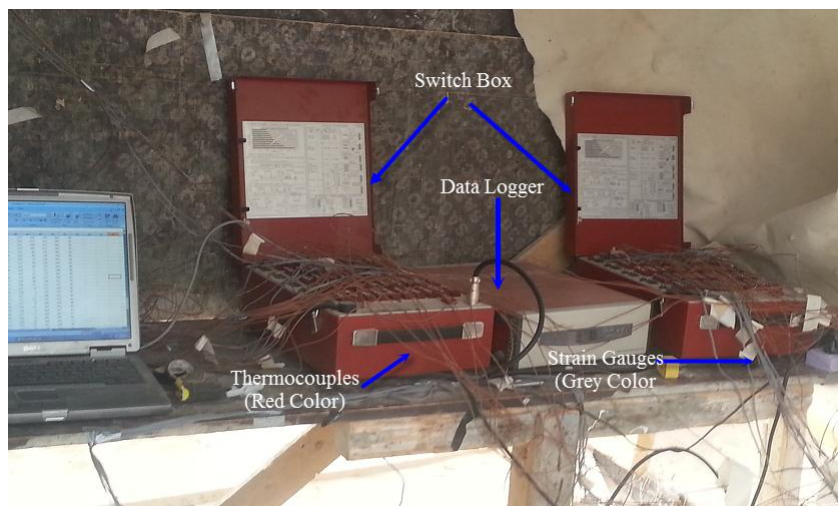


**Figure 3-14: Data Logger and Computer for Data Acquisition.**

Thermocouples were fixed to an isolated rebars. The rebars were installed in their locations by fixing them to the reinforcement of mockup specimen as shown in Figure 3-15.



**Figure 3-15: Locations of an Isolated Rebars**

The ply wood formwork was used in these three mock-up specimens as shown in Figure 3-16. The temperature monitoring started from the time of casting (5:08 pm, 20/6/2013) and continued for twenty days. When the concrete of mockup specimens reached to its final set, the curing started to apply. After about 12 hours from casting, the top surfaces of mockup specimens were covered with a burlap as shown in Figure 3-17. Water sprayed onto the mockup specimen's surface with hand held hose pipe. The thickness of curing water layer was about 2 cm. The curing continued for a week. The plywood formwork was removed after four days from casting.



**Figure 3-16: Plywood Formwork for KMUS**



**Figure 3-17: Curing of KMUS.**

A control mix contains  $480 \text{ kg/m}^3$  (100% OPC) was used in the mockup specimen #1. The cement was replaced with 60% GGBFS and 40 fly ash in the mockup#2 and mockup#3 respectively. The water/binder ratio was 0.28 for the three mixes of mockup specimens. The coarse aggregate content was  $1120 \text{ kg/m}^3$  and the fine aggregate content was  $560 \text{ kg/m}^3$ .

Many cores were taken from sides and top surfaces (as shown in Figure 3-18) to measure the mechanical properties of concrete and to visualize the status of concrete.



**Figure 3-18: Obtaining Drilled Concrete Cores**



### 3.2.2 Monitoring of Dammam Coast Mock-up Specimens (DMUS)

Three mockup specimens with dimensions of 2m×2m×2m were monitored. They are located on the coast line of the Arabian Gulf in the city of Dammam in Saudi Arabia. In these three mockup specimens, the steel formwork was used instead of plywood formwork as shown in Figure 3-19. The mock-up specimens were reinforced with two layers of epoxy steel reinforcement at top and bottom ( $7\phi 12/m$ ) as shown in Figure 3-20.



**Figure 3-19: DMUS with Steel Formwork.**



**Figure 3-20: Epoxy Steel Reinforcement of DMUS.**

The temperature rise due to the heat of hydration in the concrete mockup specimens with dimensions of  $2\text{m} \times 2\text{m} \times 2\text{m}$  was monitored by using 48 thermocouples. Thermocouples were installed and embedded to concrete at the top, middle, and bottom as shown in

Figure 3-21 shows the layout for thermocouples and strains in plan and side view of concrete mockup specimen respectively. Thermocouples were connected to an automated data logger as shown in Figure 3-22. The readings were recorded every ten minutes.

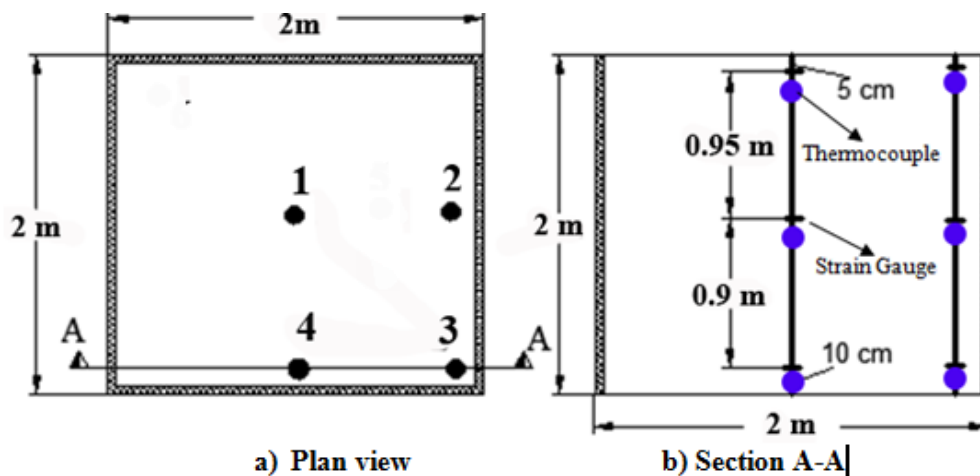


**Figure 3-21: Thermocouple and Strain Gauges Locations**

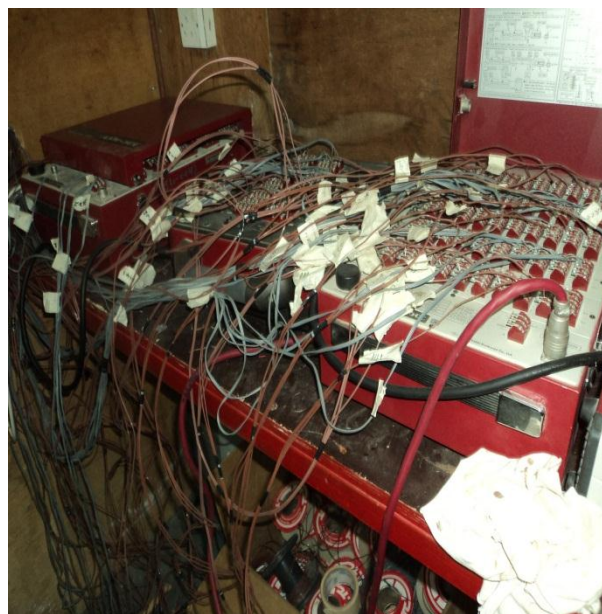


**Figure 3-22: Data Acquisition System.**

Thermocouples were fixed to an isolated rebars . The rebars were installed in their locations by fixing them to the reinforcement of mockup specimen as shown in Figure 3-23.



**Figure 3-23: Locations of an Isolated Rebars**

The temperature monitoring started from the time of casting (5:08 pm, 4/9/2013) and continued for twenty days. When the concrete of mockup specimen reached to its final set, the polystyrene foam boards were installed at the top surface of mockup specimens as shown in Figure 3-24.



**Figure 3-24: Insulation the Top Surface of Concrete**



The insulation was applied to reduce the temperature difference between the core and its surface. After about 12 hours from casting, the top surfaces of mockup specimens were covered with burlap as shown in Figure 3-25. Then, water sprayed onto the mock-up specimen's surface with hand held hose pipes.



**Figure 3-25: Covering the Top Surfaces with Burlap.**

The curing continued for a week. The steel formwork was removed from sides of mockup specimens after six days from casting.

The six faces of mockup specimens were covered with burlap as shown in Figure 3-26. The curing with water continued for two weeks.



**Figure 3-26: Covering the DMUS with Burlap.**

A mix contains 200 kg/m<sup>3</sup> cement Type II and 200 kg/m<sup>3</sup> GGBFS was used in casting one of Dammam mock-up specimens . The mix used in the second mockup specimen contains 140 kg/m<sup>3</sup> cement Type II and 260 kg/m<sup>3</sup> GGBFS. The mix used in the third mockup specimen contains 120 kg/m<sup>3</sup> cement Type II and 280kg/m<sup>3</sup> GGBFS. The water/binder ratio was 0.33 for the three mixes of Dammam mockup specimens.

### 3.2.3 Monitoring of Jeddah Mockup (JMUS)

The temperature rise in a mockup with dimensions of 3m×3m×3m was monitored. The mockup specimen is located in Jeddah city. The monitoring was done by Saudi Ready Mix Company.

The concrete mix used in the mock up consisted of 65% cement (330 kg/m<sup>3</sup>), 35% fly ash (180 kg/m<sup>3</sup>) and 0.29 water/binder ratio. The flow slump of the mix was 550 mm. Nine thermocouples were installed and embedded in the concrete at the top, middle, and bottom. The layout for thermocouples in plan and side view of the concrete mock-up is shown in Figure 3-27 and Figure 3-28, respectively. Thermocouples were connected to a digital data logger. The readings were recorded every ten minutes.

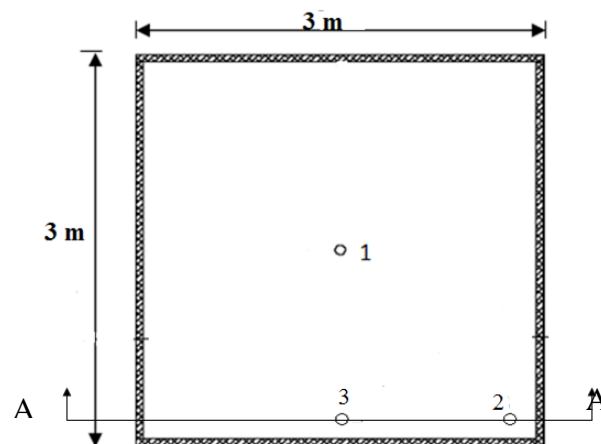


**Figure 3-27: Thermocouples Locations (Plan)**

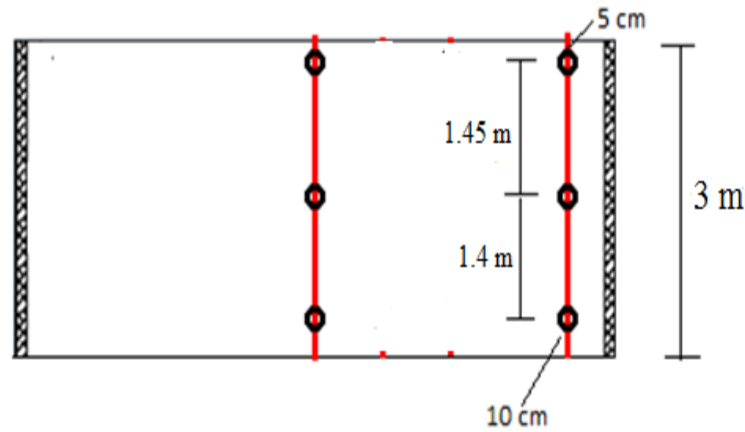


**Figure 3-28: Thermocouples Locations (Over Depth).**

The temperature monitoring continued for one week. When the concrete mock-up reached to its final set, the curing was initiated. Water was sprayed onto the mock-up surface with hand held hose pipes. The thickness of curing water layer was about 2 cm. The curing continued for four days by using normal water. The plywood formwork was removed from the sides of the mock-up specimen after four days from casting.

The dimensions, location, and mix type of each mockup specimens are summarized in Table 3-15.

**Table 3-15: Mix Proportions, Location, and Dimensions of Mockup Specimens**

Mock-up Specimen NO.	Mix Proportions				Dimensions	Location
	Cement (kg/m <sup>3</sup> )	Fly Ash (kg/m <sup>3</sup> )	GGBFS (kg/m <sup>3</sup> )	Water (liter)		
1	480	-	-	134	2m×2m×2m	Dhahran-KFUPM
2	288	192	-	134	2m×2m×2m	Dhahran-KFUPM
3	192	-	288	134	2m×2m×2m	Dhahran-KFUPM
4	200	-	200	136	2m×2m×2m	Dammam Coast
5	140	-	260	136	2m×2m×2m	Dammam Coast
6	120	-	280	136	2m×2m×2m	Dammam Coast
7	330	180		148	3m×3m×3m	Jeddah

### 3.2.4 Pile Cap Monitoring

The pile cap monitored is located on the coast line of the Arabian Gulf in the city of Dammam in Saudi Arabia. The pile cap 9.1m x 9.1 m in plan and a thickness of 1.7m transfers the load from two pier column bent of a 55m span concrete bridge to 16 cast-in-place bored piles. The pile cap is heavily reinforced as shown in Figure 3-29. The formwork on sides was plywood supported by steel plates. A concrete mix of 40 Mpa strength using ordinary Portland cement (OPC) and silica fume was specified for the pile cap in the original specifications. The OPC concrete resulted in high temperature in the core due to heat of hydration in a mock-up specimen. A temperature on about 80°C was observed in the core of the concrete specimen. The mix design was subsequently changed to incorporate blast furnace slag (GGBFS). The concrete mix used in the pile cap investigated contains 143 (kg/m<sup>3</sup>) cement of Type I, 267 (kg/m<sup>3</sup>) GGBFS, and water/binder ratio of 0.28. The coarse aggregate content was 1150 kg/m<sup>3</sup> and the fine aggregate content was 620 kg/m<sup>3</sup>.

The temperature rise due to the heat of hydration in the concrete pile cap was monitored by using 15 thermocouples installed in the pile cap at various locations and depth. Thermocouples were installed and embedded in the concrete at the top, middle, and bottom of the pile cap. Thermocouples were attached to the reinforcement without touching it. The wires were taken out through a PVC pipe as shown in Figure 3-30. The location of thermocouples in the pile cap is shown schematically in Figure 3-31. Thermocouple wires were connected to a data logger Figure 3-32 and the readings were recorded every ten minutes from the time of starting of concreting. The placing of concrete in the pile cap started at 5:00 pm on September 11, 2012 and was completed around 1:00 pm in the night. The ambient temperature at the start of casting was 35°C and the concrete temperature was kept at 28°C using ice. The monitoring of temperature and

strains in the concrete continued for two weeks. The ambient temperature varied ranging between 35°C and 42°C.



**Figure 3-29: Reinforcement in the Pile Cap**



**Figure 3-30: Casting of Concrete in Pile Cap**

When the concrete in the pile cap reached to its final set, curing of concrete at the top surface was initiated. Water was sprayed onto the pile cap surface with hand held hose pipes. The depth of the curing water layer was about 2 cm. The contractor also decided to use ice blocks on the top of the pile cap as shown in Figure 3-33, to keep the temperature of curing water low. The ice blocks were used for the first two days and the curing continued for a further two days by using normal water. The total curing period was four days. The plywood formwork was removed from the sides of pile cap after four days.

Three layers of bituminous membrane waterproofing system were applied immediately after removing the formwork. The total thickness of bituminous layers was about 1 cm.

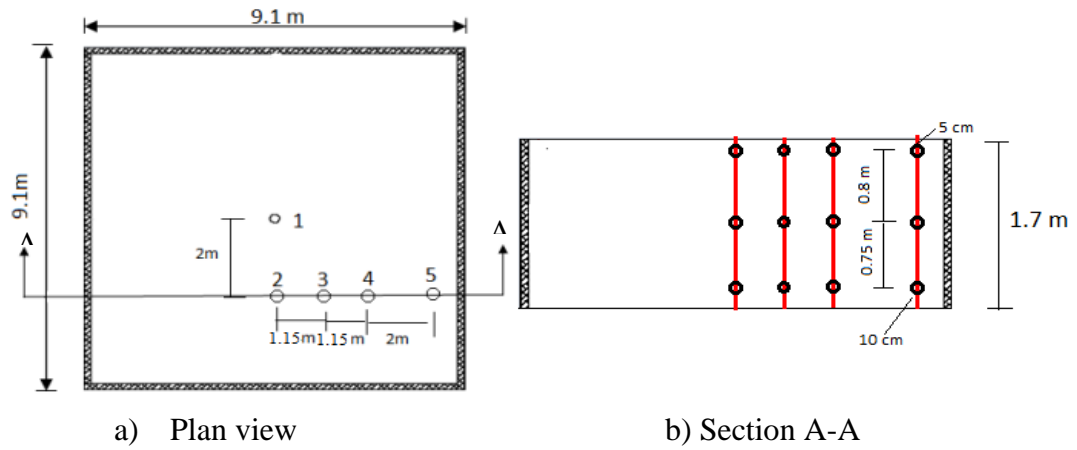


**Figure 3-31: Thermocouple Locations: (A) Plan View; (B) Section A-A**



**Figure 3-32: Sensors Connected to Data Logger**



**Figure 3-33: Ice Blocks for Cooling Curing Water**



## CHAPTER 4

### HYDRATION MODEL

#### 4.1 Maturity Concept

The maturity method accounts for the combined effects of time and temperature in concrete strength development. The strength of a given concrete mixture that has been properly placed, consolidated, and cured, is a function of its age and temperature history.

The maturity concept is a useful tool in several specialties within the concrete industry. This is especially true among fabricators of prestressed and other prefabricated concrete products where it is essential to obtain strength information at an early age and with minimal cost.

Early research was conducted by Saul [33] who introduced and defined the term “maturity” as follows during his investigation on steam curing of concrete: “the maturity of concrete may be defined as its age multiplied by the average temperature above freezing that it has maintained.” Over the years, Saul’s work has been confirmed and refined by other researches Nurse [34], and Carino and Tank [35].

Maturity testing provides strength evaluation by the monitoring of internal concrete temperature in the field. The basis of maturity is that each concrete mixture has a unique strength-time/temperature relationship. Therefore, for concrete of a specific mixture, the same strength will develop at a given maturity value.

The maturity value is the sum of the degree-hours from initial concrete placement to given time during the curing process. The maturity concept is especially useful for pavements, where it is essential to evaluate strength at early ages in order to determine the time at which they may be opened to traffic.

The maturity test can be carried out by following steps:

- Prepare a minimum of 20 cylinders or beams using the same size of specimen which will be used later in the project for verification.
- Perform compression or flexural tests at ages 1,3,5,7,14, and 28 days
- Test three specimens at each age and compute the average strength
- The maturity index from specimens with thermocouples should be recorded at each age
- Determine the best-fit curve through the data
- The resulting curve is the strength maturity relationship to be used for estimating the in-place strength of concrete.
- Embed sensors in field and get the maturity index
- Use the strength maturity curve to predict the strength in field

#### 4.1.1 Nurse-Saul Equation

The Nurse-Saul equation calculates the time-temperature factor (TTF) using following equation (ASTM C1074 [36]):

$$M(t) = \sum (T_a - T_0) \Delta t \quad (4.1)$$

Where

$M(t)$  = temperature-time factor at time t, degree-days or degree-hours

$\Delta t$  = time interval, days or hours

$T_a$  = average concrete temperature during time interval, °C

$T_0$  = datum temperature at which it is assumed that concrete ceases to gain strength with time, °C



This equation (Nurse-Saul) is the most popular in use by state DOTs.

#### 4.1.2 Arrhenius Equation

The Arrhenius equation is used to calculate the “equivalent age” maturity index. The equivalent age can be defined as equivalent duration of curing at the reference temperature that would result in the same value of maturity as the curing period at a given average temperature (ASTM C1074 [36]). Hansen and Pederson [37] proposed the following equation to calculate equivalent age:

$$t_e = \sum_{0}^t e^{-\left(\frac{E_a}{R}\right)\left(\frac{1}{T_c+273} - \frac{1}{T_r+273}\right)} \Delta t \quad (4.2)$$

Where the  $t_e$  = equivalent age at reference temperature ( $T_r$ ),  $T_c$  = temperature of the concrete ( $^{\circ}\text{C}$ ),  $E_a$  = activation energy (J/mol),  $\Delta t$  = time interval, and  $R$  = natural gas constant (8.314 J/mol/ $^{\circ}\text{C}$ ).

Activation energy  $E_a$  is the energy to be overcome in order for cement hydration to occur. The Hansen and Pederson model have assumed that the activation energy depends on the initial temperature of concrete mix as follows:

$$\left. \begin{aligned} E &= 33,500 \text{ J/mole, for } T > 20 \text{ }^{\circ}\text{C} \\ E &= 33,500 + 1,470 (20-T), \text{ for } T < 20 \text{ }^{\circ}\text{C} \end{aligned} \right\} \quad (4.3)$$

The Arrhenius relationship may be more appropriate in case of a wide variation in concrete temperature such as mass concrete at early age.

In this dissertation, the Arrhenius relationship was used to calculate maturity index.

#### 4.2 Adiabatic Heat of Hydration Model

The heat of hydration can be determined by various types of calorimeters, which can be classified into three types: adiabatic (no loss or heat gain through system), semi-adiabatic

(known heat loss through the system), and isothermal calorimetry (constant temperature in the system) [38-40]. In this research, two types of semi-adiabatic calorimeter (iQdrum and Heat-Box) were used to measure the generated heat of hydration in different admixed concrete [32]. Semi-adiabatic calorimetry is commonly used to provide an estimate of the heat generation characteristics of a concrete mixture. Semi-adiabatic calorimeters differ from adiabatic calorimeters in that they allow a small amount of heat loss from the system. Insulation is used to slow down the rate of heat loss. The amount of heat loss is measured, and the measured temperature values of the concrete are corrected to account for this loss.

The general shape of degree of hydration curve (shown in Figure 4-1) can be accurately represented by the exponential formulation shown in Eqn. (4).

$$\alpha(t_e) = \alpha_u e^{-\left(\frac{\tau}{t_e}\right)^\beta} \quad (4.4)$$

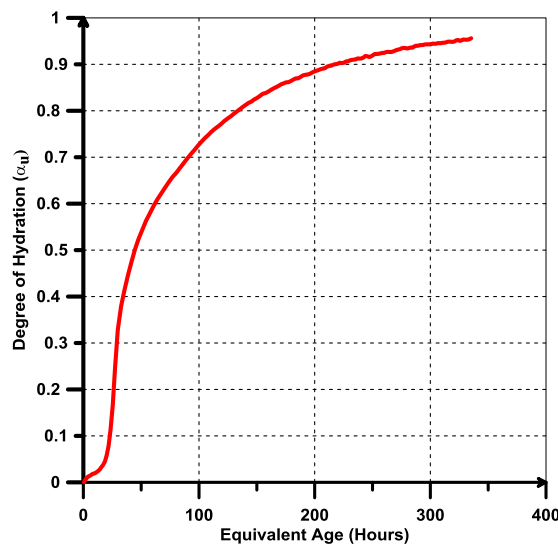


**Figure 4-1: General Shape of Adiabatic Heat of Hydration Rise Curve**

where  $\alpha_u$  represents the ultimate degree of hydration, a material-dependent parameter.  $\tau$  is the hydration time parameter (hrs), and a larger  $\tau$  implies a larger delay for hydration.  $\beta$

is the hydration shape parameter, which primarily represents the slope of the major linear portion of the hydration–time relationship.

$\alpha_u$ ,  $\tau$ , and  $\beta$  are called hydration parameter. The trend of increasing the three hydration parameters is shown in Figure 4-2 to Figure 4-4.

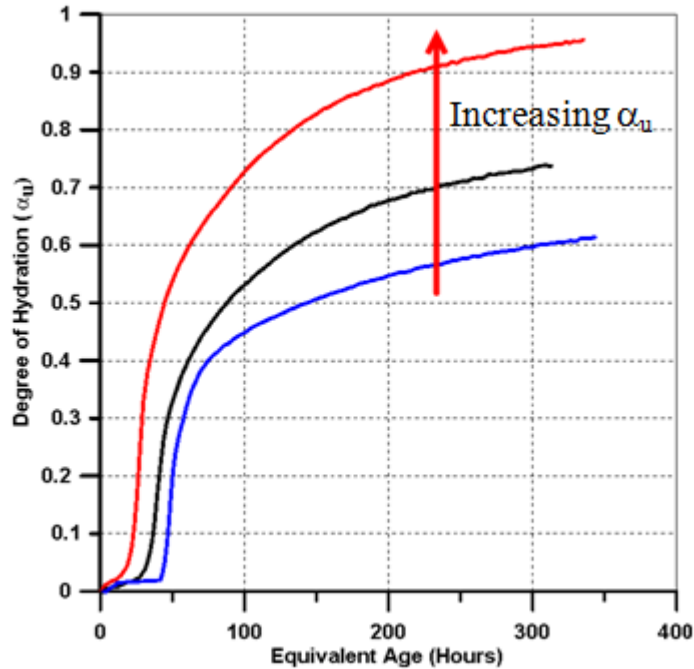


**Figure 4-2: Effect of Increasing  $\alpha_u$  on the Hydration Curve**

#### 4.2.1 Determining the Hydration Parameters from Chemical Compositions of Mix

The progress of the hydration of cementitious materials is quantified by the degree of hydration ( $\alpha$ ), which varies from 0 to 1, with a value of 1 indicating complete hydration. For this study, degree of hydration is taken as the ratio of heat evolved at time,  $t$ , to the total amount of heat available [3,4], as shown in Eqn. (4.5)

$$(\alpha_e) = \frac{H(t_e)}{H_u} \quad (4.5)$$

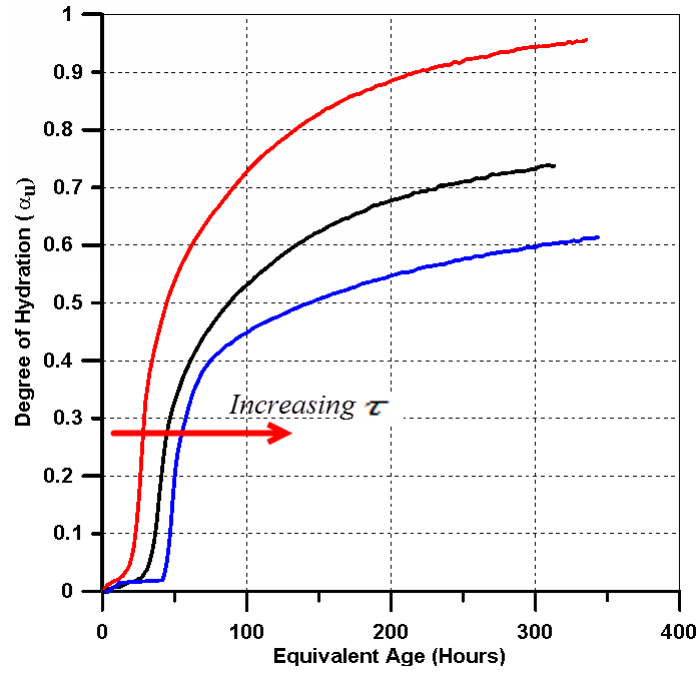


**Figure 4-3: Effect of Increasing  $\tau$  on the Hydration**

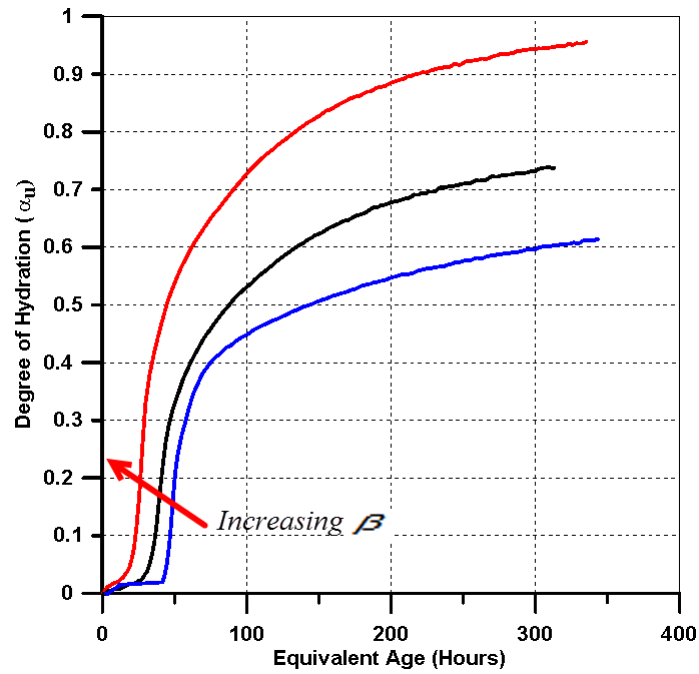


**Figure 4-4: Effect of Increasing  $\beta$  on the Hydration Curve**

where  $\alpha$  is degree of hydration at time  $t_e$ ,  $H(t_e)$  is heat generated at specific time  $t_e$  (J/gram), and  $H_u$  is total heat (J/gram).

The total heat,  $H_u$ , is dependent on material composition and amount, and type of supplementary cementing materials (SCMs).  $H_u$  can be calculated as follows [10, 41]:

$$H(u) = H_{cem} P_{cem} + 461 P_{slag} + 18000 P_{FA-Cao} \cdot P_{FA} \quad (4.6)$$

where  $P_{slag}$  is the mass ratio of slag over total cementitious content,  $P_{FA}$  is the mass ratio of fly ash over total cementitious content,  $P_{FA-CaO}$  is the mass ratio of CaO in fly ash over the total fly ash content, and  $P_{cem}$  is the mass ratio of cement over the total cementitious content.

$H_{cem}$  is the total heat of cement hydration (J/g), which can be determined as follows [10,41]:

$$H_{cem} = 500P_{C3S} + 260P_{C2S} + 866P_{PC3} + 420P_{C4AF} + 624P_{SO3} + 1186P_{Free\ Ca} + 850P_{MgO} \quad (4.7)$$

where  $P$  is the mass ratio of the component to the total cement content, which is determined from the material chemical composition test according to the ASTM C150 [42] “Standard Specification for Portland Cement” .

The hydration curve parameters ( $\alpha_u, \beta, \tau$ ) can be determined through curve fitting by minimizing the degree of hydration difference between measured degree of hydration (using Eq. (4.5)) and predicted (using Eq. (4.4))

The Hydration curve parameters can also be determined from the adiabatic test using the temperature–time history data without knowing the chemical compositions of the mix.

## 4.2.2 Determining the Hydration Parameters from Semi adiabatic Test

### 4.2.2.1 Using Degree of Hydration Curve

Hydration curve parameters can also be determined from the adiabatic test using the temperature (Heat)–time history data. Substitute Eq. (4.5) in Eq. (4.4), the generated heat of concrete at the equivalent age  $t_e$  can be determined as follows:

$$H(t_e) = \alpha(t_e) H_u = \alpha_u e^{-(\tau/t_e)^\beta} \cdot H_u \quad (4.8)$$

Then the heat generation rate ( $W/m^3$ ) can be determined as follows:

$$\rho(t) = \frac{dH(t_e)}{dt} = \frac{dH(t_e)}{dt_e} \frac{dt_e}{dt} \quad (4.9)$$

By differentiating Eqn. (4.8) with  $t_e$ , the heat generation rate at  $t_e$  can be given as follows:

$$\frac{dH(t_e)}{dt_e} = H_u \cdot \alpha_u \cdot e^{-[\tau/t_e]^\beta} \cdot \frac{\beta}{t_e} \cdot \left(\frac{\tau}{t_e}\right)^\beta \quad (4.10)$$

From Eq.(4.2)

$$\frac{dt_e}{dt} = e^{-(E_a/R)((1/T_c+273)-(1/T_r+273))}$$

(4.11)

Substitute Eqs.(4.10) and (4.11) into Eq. (4.9)

$$\rho(t) = H_u \cdot \alpha_u \cdot e^{-[\tau/t_e]^\beta} \cdot \frac{\beta}{t_e} \cdot \left(\frac{\tau}{t_e}\right)^\beta \cdot e^{-(E_a/R)((1/T_c+273)-(1/T_r+273))}$$

(4.12)

The heat rise at a time step (from time  $t_i$  to  $t_{i+1}$ ) can be determined as follows:

$$\Delta H(t) = \int_{t_i}^{t_{i+1}} p(t) \quad (4.13)$$

The temperature rise at each step can be determined as follows:

$$\Delta T = \frac{\Delta H(t)}{\rho c} \quad (4.14)$$

Where  $\rho$  the unit weight of concrete and  $c$  is the specific heat.

Thus, the accumulative temperature up to time  $t$  can be obtained as follows:

$$T(t) = \int_{t_o}^t \frac{\Delta H(t)}{\rho c} \quad (4.13)$$

A chi-square statistics  $\chi^2$  is used, as the sum of temperature difference between the measured and predicted values.

$$\chi = \sum_{i=1}^n \left( \frac{(|T_m| - |T_p|)^2}{\sigma_{T_m}^2} \right) \quad (4.15)$$

where  $T_m$  is the measured temperature,  $T_p$  is the predicted temperature,  $T_m$  is the standard deviation of the measured temperatures,  $N$  is the measured data point number.

$\chi$  in Eq. 4.15 is minimized to achieve the optimum curve fitting using solve function embedded in Microsoft Excel which determines the hydration curve parameters.

#### 4.2.2.2 Using Adiabatic Heat of Hydration Curve

The shape of adiabatic heat of hydration rise curve can be accurately represented by the exponential formulation shown in Eqn. (4.16).

$$H(t_e) = H_u e^{-\left(\frac{\tau}{t_e}\right)^\beta} \quad (4.16)$$

Where:  $H(t_e)$  is the heat of hydration at equivalent age  $t_e$ .

The parameters  $H_u$ ,  $\tau$ , and  $\beta$  model the shape of the hydration curve and  $H_u$ , the ultimate heat of hydration.  $T$ , the hydration time parameter (hours), corresponds to the time at which approximately 37% of the degree of hydration has progressed. The larger the hydration time parameter, the larger is the delay in hydration. Lower values of  $\tau$  are, therefore, anticipated for more reactive cementitious materials such as Type I cements, whereas, higher  $\tau$  values are expected for cements that contain fly ash or GGBFS.  $\beta$ , the hydration shape parameter, which represents the slope of the linear portion of the hydration-time curve. The hydration parameters,  $H_u$ ,  $\tau$ , and  $\beta$ , were determined by fitting the adiabatic heat rise curve obtained from semi- adiabatic calorimetry with the exponential function presented in Eqn.(4.16) using grapher software. The hydration parameters,  $H_u$ ,  $\tau$ , and  $\beta$ , for all mixes are summarized in Tables 4-1 to 4-10.

**Table 4-1 : Hydration Parametrs for The Mixes in The Group #1**

Mix #	Cement (kg)	SCM* Type	SCM* (%)	W/CM	$H_u$ KJ/Kg	$\tau$ (Hour)	$\beta$
1	480	-	-	0.28	300.5	24.95	1.31
2	384	Fly Ash	20%	0.28	269.64	25.1	1.26
3	336	Fly Ash	30%	0.28	239.13	28.21	1.23
4	288	Fly Ash	40%	0.28	265.97	37.7	1.17
5	240	Fly Ash	50%	0.28	203.04	33.72	0.954
6	192	Fly Ash	60%	0.28	192.89	50.77	0.931
7	240	Fly Ash+Ret.	50%	0.28	223.26	49.66	1.129

**Table 4-2: Hydration Parameters for The Mixes in The Group #2**

Mix #	Cement Content (kg)	SCM* Type	SCM* (%)	W/CM	$H_u$ KJ/kg	$\tau$ Hours	$\beta$
8	384	GGBFS	20%	0.28	300.15	27.66	1.11
9	336	GGBFS	30%	0.28	279.4	22.88	1.042
10	288	GGBFS	40%	0.28	282.95	29.85	1.19
11	240	GGBFS	50%	0.28	296.02	30.84	1
12	192	GGBFS	60%	0.28	237.05	19.93	1.082
13	144	GGBFS	70%	0.28	235.88	32.22	1.655
14	240	GGBFS+Ret.	50%	0.28	296.02	30.84	1

**Table 4-3: Hydration Parameters for The Mixes in The Group #3**

Mix #	Cement Content (kg)	SCM* Type	SCM* (%)	W/CM	$H_u$ KJ/kg	$\tau$ Hours	$\beta$
15	384	FA+GGBFS	20%	0.28	311.26	26.96	1.118
16	336	FA+GGBFS	30%	0.28	307.07	28.67	0.861
17	288	FA+GGBFS	40%	0.28	279.05	19.78	0.87
18	240	FA+GGBFS	50%	0.28	273.42	25.76	0.971
19	192	FA+GGBFS	60%	0.28	255.05	31.54	0.8185



**Table 4-4: Hydration Parameters for The Mixes in The Group #4**

Mix #	Cement Content (kg)	SCM* Type	SCM* (%)	W/CM	$H_u$ KJ/kg	$\tau$ Hours	$\beta$
20	350	-	-	0.38	333.3	19.58	0.863
21	280	Fly Ash	20%	0.38	242.3	12.41	1.087
22	245	Fly Ash	30%	0.38	229.3	16.59	1.164
23	210	Fly Ash	40%	0.38	227.5	29.92	0.872
24	175	Fly Ash	50%	0.38	313.7	95.53	0.328

**Table 4-5: Hydration Parameters for The Mixes in The Group #5**

Mix #	Cement Content (kg)	SCM* Type	SCM* (%)	W/CM	$H_u$ KJ/kg	$\tau$ Hours	$\beta$
25	280	GGBFS	20%	0.38	362.5	22.36	0.723
26	245	GGBFS	30%	0.38	355.9	23.07	0.738
27	210	GGBFS	40%	0.38	356.8	27.2	0.719
28	175	GGBFS	50%	0.38	335.6	27.82	0.783

**Table 4-6: Hydration Parameters for The Mixes in The Group #6**

Mix #	Cement Content (kg)	SCM* Type	SCM* (%)	W/CM	$H_u$ KJ/kg	$\tau$ Hours	$\beta$
29	432	Micro silica	10	0.28	304.2	17.95	1.14
30	384	Micro silica	20	0.28	275.3	18.35	1.091
31	336	Micro silica	30	0.28	266.4	22.17	0.912
32	288	Micro silica	40	0.28	256.9	26.93	0.873

**Table 4-7: Hydration Parameters for The Mixes in The Group #7**

Mix #	Cement Content (kg)	SCM* Type	SCM* (%)	W/CM	$H_u$ KJ/kg	$\tau$ Hours	$\beta$
3	336	Fly Ash	30%	0.28	239.13	28.21	1.23
33	336	Fly Ash	30%	0.33	265.9	21.4	0.791
34	336	Fly Ash	30%	0.38	270.6	19.63	0.808

**Table 4-8: Hydration Parameters for The Mixes in The Group #8**

Mix #	Cement Content (kg)	SCM* Type	SCM* (%)	W/CM	$H_u$ KJ/kg	$\tau$ Hours	$\beta$
35	480	Fly Ash-NC	20%	0.28	291.2	23.73	0.916
36	384	Fly Ash-NC	30%	0.28	291.2	23.74	0.794
37	336	Fly Ash-NC	40%	0.28	231.8	29.26	0.84
38	480	Fly Ash-SCC	20%	0.28	287.4	24.21	0.928
39	384	Fly Ash-SCC	30%	0.28	289.8	28.47	0.876
40	336	Fly Ash-SCC	40%	0.28	250.9	29.12	0.818

**Table 4-9: Hydration Parameters for The Mixes in The Group #9**

Mix #	Cement Content (kg)	SCM* Type	SCM* (%)	W/CM	$H_u$ KJ/kg	$\tau$ Hours	$\beta$
1	480	-	-	0.28	300.5	24.95	1.31
41	700	-	-	0.28	269.2	16.19	0.987
42	900	-	-	0.28	266.2	16.1	0.97

**Table 4-10: Hydration Parameters for The Mixes in The Group #10**

Mix #	Cement Content (kg)	SCM* Type	SCM* (%)	W/CM	$H_u$ KJ/kg	$\tau$ Hours	$\beta$
4	480	Fly Ash	40%	0.28	239.12	28.22	1.26
43	480	Fly Ash	40%	0.28	272.2	33.58	0.682
44	480	Fly Ash	40%	0.28	249.89	26.34	0.71
45	480	Fly Ash	40%	0.28	221.04	34.049	0.892
46	480	Fly Ash	40%	0.28	217.02	30.917	0.87

## CHAPTER 5

### FINITE ELEMENT SIMULATION

The finite element method provides a powerful numerical tool which is able to simulate thermal and structural behavior if the appropriate modeling approach and material models are effectively utilized. The major aim of this study is to develop a finite element model which can provide reliable predictions of mass concrete behavior at early age.

In this chapter, the detailed formulation of the proposed numerical models of mass concrete structures subjected to thermal load and shrinkage are presented, including the finite element formulation and the iterative numerical solution procedures.

#### 5.1 Temperature Evolution Simulation

An accurate heat transfer analysis needs accurate input of thermal properties to determine the temperature distribution. Three main factors to be considered in heat transfer analysis are heat of hydration, thermal conductivity and specific heat capacity of the materials. Due to the difficulties in determining early age thermal properties accurately, constant values have been used for most of thermal modeling. The temperature distribution was carried out, and then followed by stress analysis.

##### 5.1.1 Thermal conductivity and Specific heat

Thermal conductivity of a material is its ability to transmit heat. The heat transfer through a finite area can be expressed by the Fourier law of conduction:

$$q_x = -k A_x \frac{\partial T}{\partial x} \quad (5.1)$$

where,

$q_x$  = heat flow, J  
 $k$  = thermal conductivity, J/m-hr- $C^\circ$   
 $A$  = the surface area,  $m^2$ .  
 $T$  = temperature,  $C^\circ$   
 $x$  = coordinate, m

The minus sign denotes that the heat flows in the direction of decreasing temperature.

In case of three-dimensional heat transfer, the Fourier equation for heat transfer becomes:

$$q_n = -k \nabla T = -k \left( i \frac{\partial T}{\partial x} + j \frac{\partial T}{\partial y} + k \frac{\partial T}{\partial z} \right) \quad (5.2)$$

where,

$x, y, z$  are the axes of the coordinate system

$i, j, k$  are the vectors directions in the coordinate system.

The equation that represents a volumetric heat balance which must be satisfied at each point in the body is given as follows:

$$\rho c \frac{dT}{dt} = \left( \frac{\partial}{\partial x} \left( k \frac{\partial T}{\partial x} \right) + \frac{\partial}{\partial y} \left( k \frac{\partial T}{\partial y} \right) + \frac{\partial}{\partial z} \left( k \frac{\partial T}{\partial z} \right) \right) + Q \quad (5.3)$$

Where  $\rho$  is the density ( $kg/m^3$ ),  $c$  is the specific heat ( $kJ/kg.C^\circ$ ), and  $Q$ , is the internal heat sources (heat of hydration in case of mass concrete structures).

Heat conduction in the concrete is dependent on the moisture content, density, specific heat, and thermal conductivity of the concrete. The specific heat and thermal conductivity of concrete is dependent on the mixture proportions, temperature, and degree of hydration of the concrete (van Breugel [43]).

The conductivity and heat capacity values of the concrete, plywood, water, and polystyrene foam in this research were obtained from the manufacturer's sheets and from the literature.

### 5.1.2 Thermal Expansion of Concrete

Most of solids, liquids and gases change its size or density due to effect of heat. When the materials are subjected to change in temperature, it may expand or contract. Most of

the materials expand when they are heated, and contract when they are cooled. Temperature changes in concrete may be caused by environmental conditions or by cement hydration. As the temperature drops, the concrete tends to be shortened. Concrete has generally positive coefficient of thermal expansion at ambient conditions but this value mainly depends on concrete mixing ingredients. Theoretically, coefficient of thermal expansion (CTE) is defined as change in unit length per degree change of temperature. It is expressed as follows:

$$\alpha = \frac{\Delta l}{l_0 \Delta t} \quad (5.4)$$

Aggregate type and its mineralogical compositions has shown the greatest influence on the expansion coefficient of concrete because of the large differences in thermal properties of various types of aggregates, modulus of deformation of the aggregate and also concrete contains aggregate constituting from 70 to 85 % of the total solid volume of the concrete. The CTE of various aggregates is shown in Table 5.1.

Some researchers have studied the coefficient of thermal expansion of concrete [44, 45]; however, no reliable formula has been developed related to the degree of hydration or maturity. A constant value for the coefficient of thermal expansion  $1.716 \times 10^{-5} \text{ (}^\circ\text{C}^{-1}\text{)}$  is used in this study , since the coarse aggregates utilized in concrete by the construction industry in the Eastern Province of the Kingdom of Saudi Arabia are mostly of limestone.

### 5.1.3 Convection Coefficient

Heat is transferred from the concrete surface to the surrounding fluid (usually air or water) by convection. Convection is the energy transport from a surface to a surrounding fluid by diffusion (random fluid particle motion contacting the surface) and bulk motion

**Table 5-1: Influences of Aggregates on CTE (Chandra at all. [44])**

Type of Aggregates	Average CTE 1 x 10 <sup>-6</sup> per K	
	Aggregates	Concrete
Expanded shale, clay and Slate	-	6.5 - 8.1
Expanded Slag		7.0 - 11.2
Blast Furnace Slag	-	9.2 - 10.6
Pumice	-	9.4 - 10.8
Perlite	-	7.6 - 11.7
Vermiculite	-	8.3 - 14.2
Cellular concrete	-	9.0 - 12.6
Quartzite	10.3	12.1
Siliceous limestone	8.3	9.4-11.7
Basalt	6.4	8.3
Limestone	5.5	5.4-8.6
Sandstone	9.3	11.4
Marble	8.3	10.7
Granite	6.8	9.6
Dolerite	6.8	9.6
Gravel	10.3	12
Chert	11.8	13.2
Cement Paste-saturated		
w/c =0.4	-	18-20
w/c =0.5	-	18-20
w/c =0.6	-	18-20

of the fluid. Convection is governed by Newton's law of cooling, shown in Eq. (5.5) (Incropera and Dewitt [46]):

$$q_{cv} = h_c (T_s - T_\infty) \quad (5.5)$$

where,

$q_{cv}$  = the convection heat flux

$h_c$  = the convection coefficient , W/m<sup>2</sup>-°C

$T_s$  = the surface temperature of concrete, °C.

$T_\infty$  = the external environment temperature, °C

The convection coefficient may be calculated using the following equation

$$\begin{aligned}
h_{free} &= 5.6 + 3.95 v, \quad v \leq 5 \text{ m/s} \\
h_{free} &= 7.6 v^{0.78}, \quad v > 5 \text{ m/s}
\end{aligned}
\tag{5.6}$$

where  $h_{free}$  is the convection heat transfer coefficient on the free surface ( $\text{W/m}^2\text{-}^\circ\text{C}$ ), and  $v$  is the wind velocity (m/s). If there are formwork or insulation slab covered on the concrete, the convection heat transfer coefficient can be calculated by [47]:

$$h_{cv} = \left( \frac{1}{h_{free}} + \sum \frac{l_i}{k_i} \right)^{-1}
\tag{5.7}$$

where,  $h_{cv}$  is the convection heat transfer coefficient considering multi-layer covers on the surface of the concrete structure ( $\text{W/m}^2\text{-}^\circ\text{C}$ ),  $l_i$  is the thickness of the  $i_{th}$  layer cover (m), and  $k_i$  is the conductivity of the  $i_{th}$  layer cover ( $\text{W/m}\cdot^\circ\text{C}$ ).

In this study, the wind velocity was measured each hour using hand held anemometer.

#### 5.1.4 Ambient Temperature

The ambient temperature was monitored and recorded every five minutes using thermocouple Type T.

#### 5.1.5 Solar Radiation

The intensity of solar radiation is influenced by many factors such as surface orientation, surface inclination angle, surface, and declination of the sun, solar elevation, hour angle of the sun, and the earth's latitude and longitude [47].

An incident solar radiation is a radiant energy from the Sun which strikes an object or surface. The incident solar radiation consists of two parts: the direct component from the Sun itself (sunshine) and the diffuse component from the visible sky (skylight). It can also contain a reflected component from other surfaces in the model and the ground.



The Ecotect software was used in this research to obtain the direct and diffuse radiation. The Ecotect software has ability to calculate the precise amount of solar radiation incident on any surface in the model.

The incident solar radiation can be given as follows [48]:

$$E_{\text{incident}} = [(E_{\text{beam}} \times \cos(A) \times F_{\text{shad}}) + (E_{\text{diffuse}} \times F_{\text{sky}})] \times \text{Exposed Area} \quad (5.8)$$

where,  $A$  is angle of incidence of the radiation,  $E_{\text{beam}}$  the direct or beam radiation,  $E_{\text{diffuse}}$  the diffuse sky radiation,  $F_{\text{shad}}$  the fraction of the surface currently in shadow from other surrounding geometry,  $F_{\text{sky}}$  the fraction of the diffuse sky actually visible from the surface.

The solar radiation is directly calculated from the geometry of the model as well as from hourly direct and diffuse solar radiation values in weather data file as shown in Figure 5-1

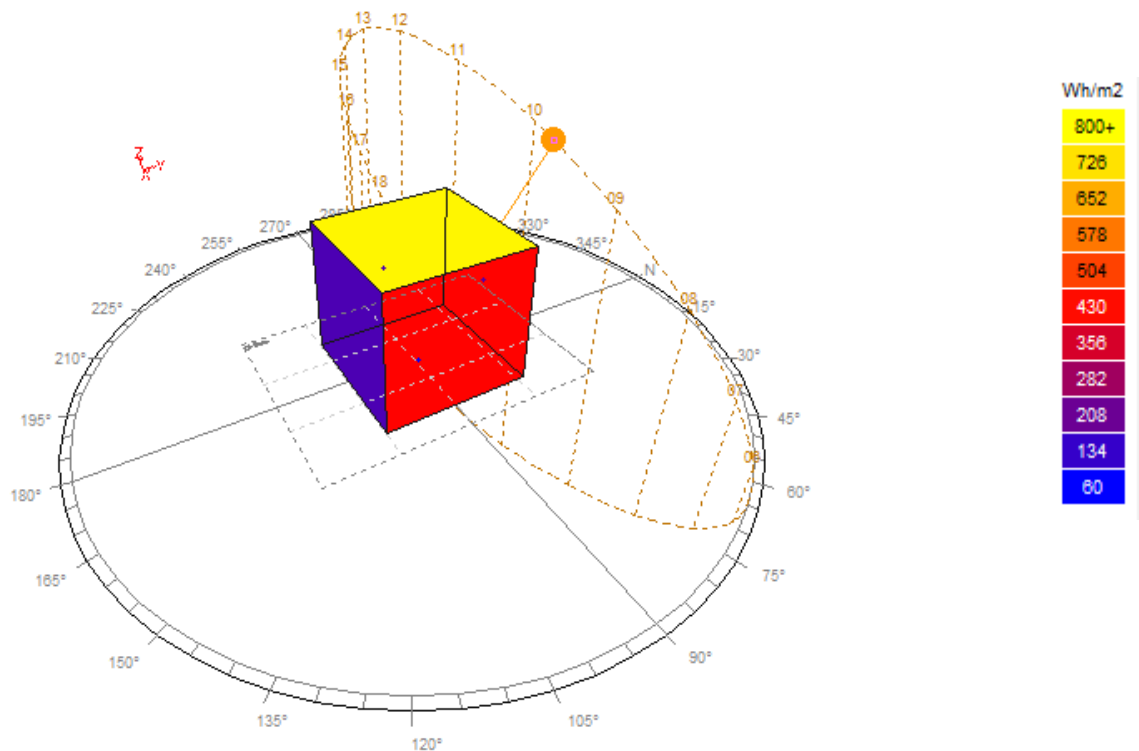


**Figure 5-1: Solar Radiation Analysis Using Ecotect Software**

### 5.1.5.1 Angle of Incidence

When radiation from the Sun strikes the surface of an object from directly front-on, the energy density per unit area will be much higher than if the radiation struck from a much greater angle. This effect can be calculated using the *cosine law*, where the radiant energy from the Sun is multiplied by the cosine of the incidence angle (as shown in Figure 5-2

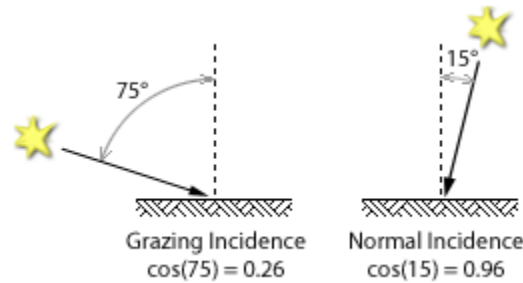


**Figure 5-2: Angle of Solar Radiation Incident**

The incidence angle is always calculated relative to the surface normal of each plane. Radiant energy density is at its maximum at *normal incidence* when the incidence angle approaches zero. It is at its minimum at *grazing incidence* when the incidence angle approaches 90°.

### 5.1.5.2 Solar – Ambient Temperature

For heat transfer analysis, it is convenient to combine the effects of ambient temperature and solar radiation intensity into a single quantity called sol–air temperature. This physical quantity can be expressed as [49, 50]:

$$T_{eq} = T_{amb} + \alpha_s G_i / h_{cv} \quad (5.9)$$

where  $T_{eq}$  is the sol–air temperature (°C),  $T_{amb}$  is the ambient temperature (°C),  $\alpha_s$  is the solar absorptivity (generally 0.55 for ordinary concrete), and  $h_{cv}$  is the convection heat coefficient (W /m<sup>2</sup>.°C).

The flow chart of the finite element analysis for the calculations of temperature field is given in Figure 5-3.

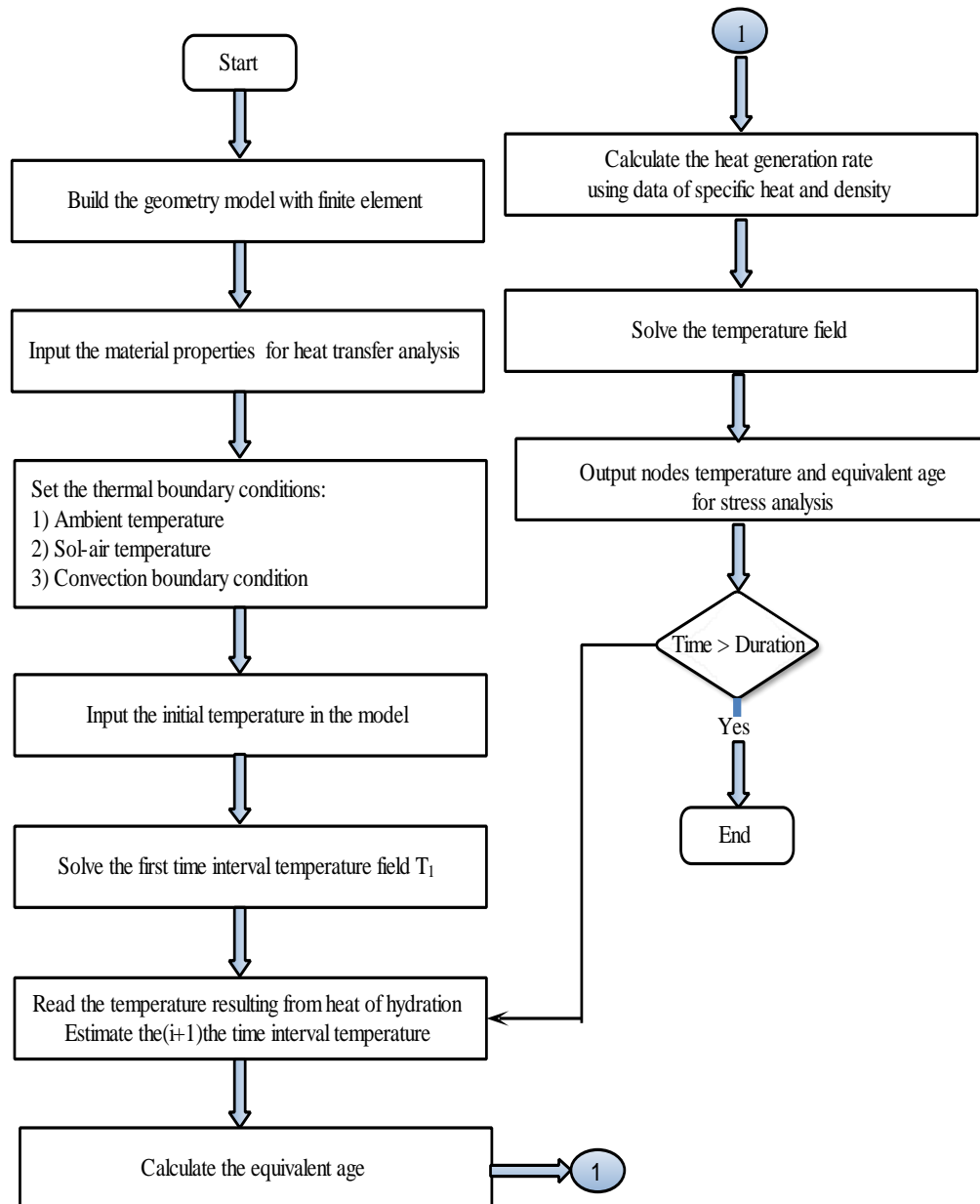


**Figure 5-3: Flow Chart For Heat Transfer Analysis**

## **5.2 Structural (Stress) Simulation**

### **5.2.1 Cracking Model**

Reinforced concrete is well known for its non-linear behavior. The non-linearity in reinforced concrete originates from the non-linear stress-strain relationship of plain concrete. The structural behavior is further complicated by cracking of concrete which causes a considerable redistribution of stresses within the intact concrete as well as the stress transfer from concrete to steel reinforcement.

The finite element method is an appropriate numerical tool to simulate the non-linear behavior of reinforced concrete structures. Rational and reliable representations of cracking of concrete must be used in conjunction with the finite element method in order to accurately describe the structural behavior. Two major approaches are available in the literature for the modeling of cracking in concrete structures, namely the discrete crack approach and the smeared crack approach. These two approaches are discussed in the subsequent sections.

### **5.2.2 Discrete Crack Approach**

In the discrete crack model, cracking is simulated as a propagation of discontinuities in a structure. Two approaches may be identified in the discrete crack model, the inter-element crack model and the intra-element crack model. In the first approach, crack propagation is modeled by means of separation of element edges and the cohesive tractions in the fracture zone are simulated using either linkage elements or interface elements as shown in Figure 5-4(a). The second approach is the intra-element discrete crack model in which the crack is allowed to propagate through the finite element as shown in Figure 5-4(b).

The discrete crack approach is most useful in structural problems with prominent localized cracking. Nevertheless, concrete structures are often dominated by randomly distributed cracking, which is resulted from thermal, shrinkage, and structural loads such as mass concrete structures. In such cases, the smeared crack approach is often considered to be advantageous compared to the discrete crack approach.

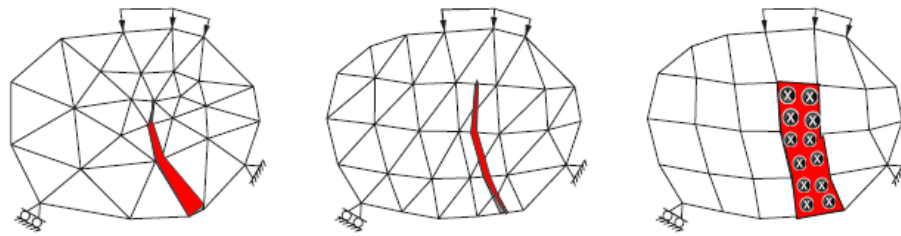


**Figure 5-4: Concrete Cracking Models: (A) Discrete Inter-Element Crack Pproach; (B) Discrete Intra-Element Crack Approach; (C) Smeared Crack Approach (Crosses The Shaded Element Are The Cracked Integration Points).**

### 5.2.3 Smeared Crack Approach

The smeared crack approach is a concept developed based upon the framework of continuum mechanics which is described in the notions of stress and strain. This approach was introduced by Rashid [51] to overcome the drawbacks of the early discrete crack models and has become the most widely adopted method for modeling cracking in structural engineering problems. The cracking in a smeared crack model is assumed to be smeared over a certain volume of material. Cracking is treated as a reduction of average material stiffness in the direction of the major principal stresses. In a finite element model, this is done at the integration point level of the element by reducing the stiffness according to a particular constitutive relationship as shown in **Figure 5-4(c)**.

Three major variants of smeared crack approach are available in the literature depending on the method of development of the crack planes: fixed crack model, rotating crack model and multi-directional fixed crack model.

### 5.2.3.1 Fixed Crack Approach

In a fixed crack model, the crack initiates normal to the major principal stress and has a fixed direction throughout the loading development. In case of two dimensional linear elastic materials, the stress may be written as:

$$\begin{bmatrix} \sigma_x \\ \sigma_y \\ \tau_{xy} \end{bmatrix} = \frac{E}{1-\nu^2} \begin{bmatrix} 1 & \nu & 0 \\ \nu & 1 & 0 \\ 0 & 0 & \frac{1}{2}(1-\nu) \end{bmatrix} \begin{bmatrix} \varepsilon_x \\ \varepsilon_y \\ \gamma_{xy} \end{bmatrix} \quad (5.10)$$

The material stiffness matrix becomes orthotropic as soon as the maximum principal stress exceeds the concrete tensile strength. The orthotropic stress-strain relationship may be written in the normal (n) and tangential (t) directions of the crack, which gives

$$\sigma_{nt} = D_{nt}^{sec} \varepsilon_{nt} \quad (5.11)$$

where  $D_{nt}^{sec}$  is the secant stiffness matrix in the directions of orthotropy .

When the stresses exceeds the tensile strength of concrete , the stiffness normal to the crack and the shear stiffness are both set to zero and the Poisson's effect vanishes immediately after cracking.

$$D_{nt}^{sec} = \begin{bmatrix} 0 & 0 & 0 \\ 0 & E & 0 \\ 0 & 0 & 0 \end{bmatrix} \quad (5.12)$$

The sudden drop of stiffness, however, gives rise to numerical difficulties. To improve this situation, a “shear retention factor”  $\beta$  was introduced (for instance, Suidan and Schnobrich, [52]) for a smooth transition from uncracked to completely cracked states. It

may also be conceived as a way to account for the aggregate interlock. The shear component is retained in the stiffness matrix as

$$D_{nt}^{sec} = \begin{bmatrix} 0 & 0 & 0 \\ 0 & E & 0 \\ 0 & 0 & \beta G \end{bmatrix} \quad (4.13)$$

in which the shear retention factor  $\beta$  is in the range  $0 \leq \beta \leq 1$ .

In real structures, the direction of principal stresses is constantly changing during the loading process. Because of the fixed crack direction, the rotation of the principal stresses causes the development of shear stress on the crack surface. A large shear stress may be induced if the rotation of the principal stresses is significant. Consequently, the fixed crack model often predicts a stiffer response than experimental results.

### 5.2.3.2 Rotating Crack Approach

The rotating crack model was proposed by Cope et al. [53], in which the crack direction rotates with the principal stress directions during the entire loading process. Consequently, the orthotropic constitutive relationship of the cracked concrete changes accordingly with the crack directions. Eq. (5.14) may now be written in the principal 1-2 axes instead of the local crack  $n-t$  axes as

$$\sigma_{12} = D_{12}^{sec} \varepsilon_{12} \quad (5.14)$$

### 5.2.3.3 Multiple Fixed Crack Model

The concept of a smeared crack model with strain decomposition was probably first proposed by Litton [54]. The basic concept of multiple fixed crack model is identical to the fixed crack model in which rotation of crack is not permitted. However, new cracks are allowed to develop at different orientations (As shown in Figure 5-5), if the angle

between two consecutively formed cracks exceeds a threshold angle. Each crack is free to open in any direction and remains fixed after the formation. This approach involves the strain decomposition of total strain into concrete and crack strain as follows.

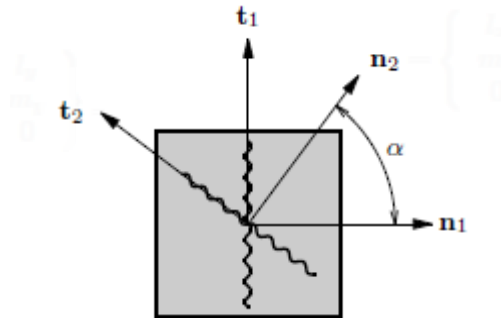


**Figure 5-5: Multi-Directional Fixed Crack Model**

$$\Delta \varepsilon = \Delta \varepsilon_e + \Delta \varepsilon_{cr} \quad (5.15)$$

where the cracking strain increment  $\Delta \varepsilon_{cr}$  is made up of the cracking strains of all cracks at different orientations, which can be written as:

$$\Delta \varepsilon_{cr} = \Delta \varepsilon_{cr1} + \Delta \varepsilon_{cr2} + \Delta \varepsilon_{cr3} + \dots \quad (5.16)$$

In this study the smeared crack approach is implemented.

The linear tension softening approach is adopted in the FE Simulation depending on the change of maturity with time.

The behavior of concrete in tension was modeled as linear up to the concrete tensile strength ( $f_t$ ). A linear tension cut-off governed crack initiation. A crack forms according to the linear cut-off criterion if the principle tensile stress exceeds the tensile strength of concrete. The post-cracking behavior of concrete modeled by a linear softening model ( see Eq. (5.17) which relates the ultimate concrete tensile strain ( $\varepsilon_{c,ult}$ ) to the concrete tensile strength, concrete fracture energy ( $G_f$ ) , crack bandwidth ( $h_b$ ) .



$$\varepsilon_{c,ult} = \frac{2G_f}{h_b f_t} \quad (5.17)$$

The concrete fracture energy ( $G_f$ ) was calculated using the formulations of Philips and Binsheng (1993):

$$G_f = 43.2 + 1.13 f_{cu} \quad (5.18)$$

In Eq.(5.18),  $G_f$  is given in N/m whereas the ultimate compressive strength ( $f_{cu}$ ) must be in N/mm<sup>2</sup>. The crack bandwidth ( $h_b$ ) is a parameter used to regulate the value  $\varepsilon_{c,ult}$  in order to achieve mesh-independent predictions. It was taken as the cube root of the concrete finite element volume recommended by DIANA [55].

#### 5.2.3.4 Cracking Index

Cracking in concrete develops when the tensile stresses exceed the tensile strength of concrete. The probability of cracking is determined according to the following equation:

$$I_{cr}(t) = \frac{F_t(t)}{F_u(t)} \quad (5.19)$$

Where:  $I_{cr}$  = the crack index,  $F_t(t)$  = thermal stresses and  $F_u(t)$  = the tensile strength of concrete. When the tensile stresses exceed the tensile strength of concrete, the crack index approaches and subsequently exceed 1.

#### 5.2.4 Strain Analysis

The total increment strain developed in mass concrete structures can be expressed as follows:

$$\Delta \varepsilon_t = \Delta \varepsilon^e + \Delta \varepsilon^{cr} + \Delta \varepsilon^{th} + \Delta \varepsilon^{sh} \quad (5.20)$$

where  $\Delta \varepsilon_t$  is the total increment strain, and  $\Delta \varepsilon^e, \Delta \varepsilon^{cr}, \Delta \varepsilon^{th}, \Delta \varepsilon^{sh}$  are the increments of elastic strain, creep strain, thermal strain, and shrinkage strain, respectively. The elastic

strain and creep strain are load dependent, whereas thermal strain, shrinkage strain are load-independent. In the 3D space, each strain is a column matrix with six component in

the form of :  $\begin{bmatrix} \varepsilon_x & \varepsilon_y & \varepsilon_z & \gamma_{xy} & \gamma_{yz} & \gamma_{zx} \end{bmatrix}^T$

, where  $\varepsilon_x, \varepsilon_y, \varepsilon_z$  are the normal strain and  $\gamma_{xz}, \gamma_{yz}, \gamma_{zx}$  are the shear strains.

#### 5.2.4.1 Elastic Strain

According to the Hook law, elastic strain increment can expressed as:

$$\{\Delta \varepsilon^e\} = \frac{1}{E_n(t)} [Q] \{\Delta \sigma_n\} \quad (5.21)$$

Where  $\frac{1}{E_n(\tau)}$  is the elastic compliance matrix, which is a function of concrete age, and

$[Q]$  is a matrix in terms of Poisson's ratio  $\nu$  :

$$[Q] = \begin{bmatrix} 1 & -\nu & -\nu & 0 & 0 & 0 \\ & 1 & -\nu & 0 & 0 & 0 \\ & & 1 & 0 & 0 & 0 \\ & & & 2(1+\nu) & 0 & \\ sym. & & & & 2(1+\nu) & \\ & & & & & 2(1+\nu) \end{bmatrix}$$

It can be assumed that  $\nu$  doesn't change with the age of concrete t.  $\{\Delta \sigma_n\}$  is the incremental stress which has six components in the form of  $\begin{bmatrix} \sigma_x & \sigma_y & \sigma_z & \tau_{xy} & \tau_{yz} & \tau_{zx} \end{bmatrix}^T$ .

#### 5.2.4.2 Creep Strain

Creep is a nonlinear time-dependent behavior. the effect of creep in this study is neglected due to its small effect at early age.

#### 5.2.4.3 Thermal Strain

Thermal strain increment is determined by the coefficient of thermal expansion and temperature difference as follows:

$$\{\Delta \varepsilon^{th}\} = [\alpha_{th} \Delta T \quad \alpha_{th} \Delta T \quad \alpha_{th} \Delta T \quad 0 \quad 0 \quad 0]^T \quad (5.22)$$

Where  $\alpha_{th}$  is the coefficient of thermal expansion, and  $\Delta T$  is the temperature difference during time step.

The flexural frame in the Heavy Equipment Laboratory at the Department of Civil Engineering was utilized for the testing of the hollow core slabs in flexure and shear

#### 5.2.4.4 Shrinkage Strain

Shrinkage of concrete is also taken into consideration in the FEM by applying the method of CEB-FIP Model Code 1990 [56]. Shrinkage is classified based on the causes of volume change to plastic shrinkage, autogenous shrinkage, drying shrinkage at early age [57, 58]. The method of CEB-FIP Model Code 1990 [56] allows a prediction of the development of shrinkage strain over time as well as a prediction of the final shrinkage strain. According to this method, the total shrinkage strain is estimated by:

$$\varepsilon_s(t, t_s) = \varepsilon_{s0} \beta_s(t - t_s) \quad (5.23)$$

where  $\varepsilon_{s0}$  is the notational shrinkage coefficient, given by following eqn.

$$\varepsilon_{s0} = \varepsilon_s(f_{cm28}) \beta_{RH} \quad (5.24)$$

$\beta_s(t - t_s)$  is the coefficient to predict the development of shrinkage with time, given by

$$\beta_s(t - t_s) = \left( \frac{(t - t_s)}{350 \left( \frac{h}{h_0} \right) + (t - t_s)} \right)^{1/2} \quad (5.25)$$

Where  $\varepsilon_s(f_{cm28})$  the strain at 28 days age

$\beta_{RH}$  Function describe the effect of humidity

$h$  is the notational size of concrete member in mm

$$h_0 = 100 \text{ mm}$$

$t_s$  is the age of concrete in days at the beginning of shrinkage

In order to simplify the computations, the shrinkage in the mass concrete structures is assumed to be uniform and isotropic . The shrinkage deformation can thus be treated similar to thermal expansion as:

$$\begin{aligned} \{\Delta \varepsilon^{sh}\} = & \begin{bmatrix} \Delta \varepsilon^{sh} & \Delta \varepsilon^{sh} & \Delta \varepsilon^{sh} & 0 & 0 & 0 \end{bmatrix}^T \\ & \begin{bmatrix} \alpha_{th} \Delta T^{sh} & \alpha_{th} \Delta T^{sh} & \alpha_{th} \Delta T^{sh} & 0 & 0 & 0 \end{bmatrix}^T \end{aligned} \quad (5.26)$$

Where  $\alpha_{th} \Delta T^{sh}$  is the equivalent thermal strain corresponding to the shrinkage deformation.

### 5.2.5 Stress Analysis

The incremental stress can be expressed as follows:

$$\begin{aligned} \{\Delta \sigma\} = & [D] \{\Delta \varepsilon^e\} \\ = & [D] \left[ \{\Delta \varepsilon\} - \{\Delta \varepsilon^{cr}\} - \{\Delta \varepsilon^{th}\} - \{\Delta \varepsilon^{sh}\} \right] \end{aligned} \quad (5.27)$$

Where  $[D]$  is the elastic material stiffness matrix of Hook's law. It is known from finite element formulations:

$$\{\Delta \varepsilon\} = [B] \{\Delta \delta\} \quad (5.28)$$

where  $[B]$  is the product of the differential operator matrix and the shape function matrix, and  $\{\Delta \delta\}$  is the incremental nodal displacements at the  $n$ th step.

By substituting Eq. (5.28) in Eq. (5.27)

$$\{\Delta \sigma\} = [D] \left[ [B] \{\Delta \delta\} - \{\Delta \varepsilon^{cr}\} - \{\Delta \varepsilon^{th}\} - \{\Delta \varepsilon^{sh}\} \right] \quad (5.29)$$

In the finite element method, the governing equation can finally be converted to

$$\int [B]^T \{\Delta\sigma\} dV = \{\Delta R\} \quad (5.30)$$

where  $\{\Delta R\}$  is the incremental equivalent nodal forces. Substituting Eq.(5.29) in Eq.(5.30)

$$\begin{aligned} [K]\{\Delta\delta\} &= \{\Delta R\} + \{\Delta R^{th}\} + \{\Delta R^{sh}\} \\ \{\Delta R^{th}\} &= \int [B][D]\{\Delta\varepsilon^{th}\} dV \\ \{\Delta R^{sh}\} &= \int [B][D]\{\Delta\varepsilon^{sh}\} dV \end{aligned} \quad (5.31)$$

where  $[K]$  is the stiffness matrix which is calculated by :  $[K] = \int [B]^T [D][B] dV$

,  $\{\Delta R^{th}\}$ , and  $\{\Delta R^{sh}\}$  are the incremental equivalent nodal forces due to thermal and shrinkage, respectively.

By solving Eq. (5.31), increment displacement vector  $\{\Delta\delta\}$  can be calculated and then  $\{\Delta\sigma\}$  can be determined from Eq. (5.29)

The flow chart of the finite element analysis for the calculations of stress field is given in Figure 5-6.

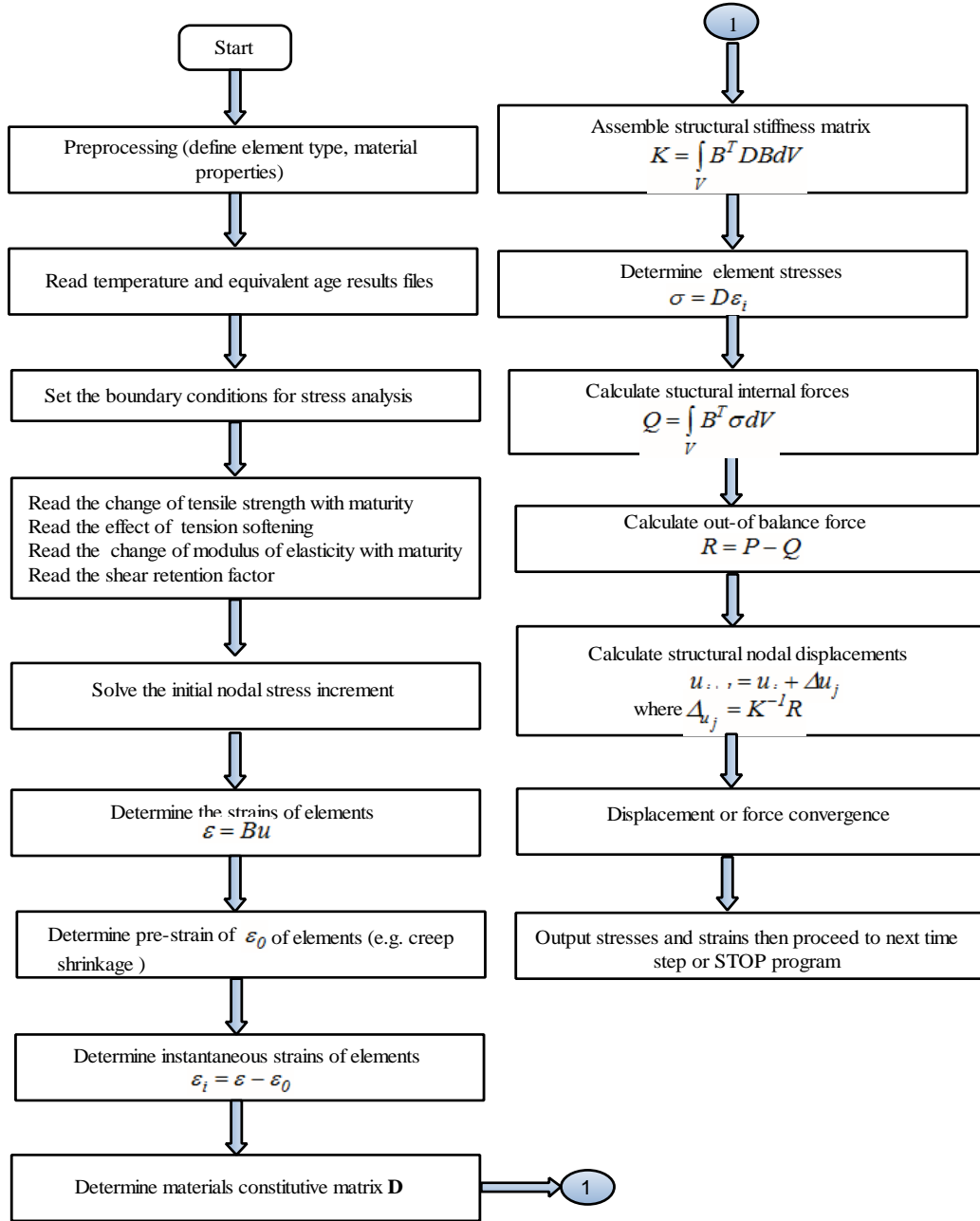


**Figure 5-6: Flow Chart for Stress Analysis**

### 5.2.6 Interaction between soil and concrete

When large localized strains are involved between construction and soil, special elements are needed to describe the interface behavior correctly. Two mechanisms can be distinguished at the interface: the contact-gapping mechanism and the frictional shearing mechanism.

Basically two kinds of interface constitutive equations are used to model these mechanisms in numerical simulations [59].

- The soil-structure interface is considered as a thin continuum layer.
- The continuum equations are degenerated in such a way that the interface zone is replaced by a bi-dimensional constitutive relation [60].

The second approach is adopted in this contribution. The interface behavior is described in terms of a relation between the normal and shear tractions,  $t_n$  and  $t_s$  and the normal and shear relative displacements across the interface,  $\Delta u_n$  and  $\Delta u_s$ . In geomechanics, when the stresses are within the elastic region, the normal and shear relations are generally assumed to be independent:

$$\begin{bmatrix} t_n \\ t_s \end{bmatrix} = \begin{bmatrix} D_{nn} & 0 \\ 0 & D_{tt} \end{bmatrix} \begin{bmatrix} \Delta u_n \\ \Delta u_s \end{bmatrix} \quad (5.32)$$

The component  $D_{nn}$  stands for the relation between normal traction and normal relative displacement: the contact-gapping mechanism.  $D_{nn}$  resembles an elastic spring stiffness, a very stiff spring to simulate contact up to a specified maximum normal traction. If the normal traction exceeds this maximum value a discrete "gap" arises between the construction and the soil and the normal traction reduces to zero: instantaneous, linear or nonlinear.

Generally the friction mechanism,  $D_{tt}$ , is described as follows: up to a specified shear stress level, depending on the normal stress at the interface, "elastic" shearing-behavior is assumed. If the shear stress exceeds this threshold, plastic slip deformation occurs at the interface. In that case the shear stress  $\tau$  can be defined by the Coulomb friction model as shown in Figure 5-7:

$$\tau = c + \sigma \tan \phi \quad (5.33)$$

where  $c$  is the cohesion of soil ,  $\sigma$  is the normal stress at the interface , and  $\phi$  is the interface friction angle.

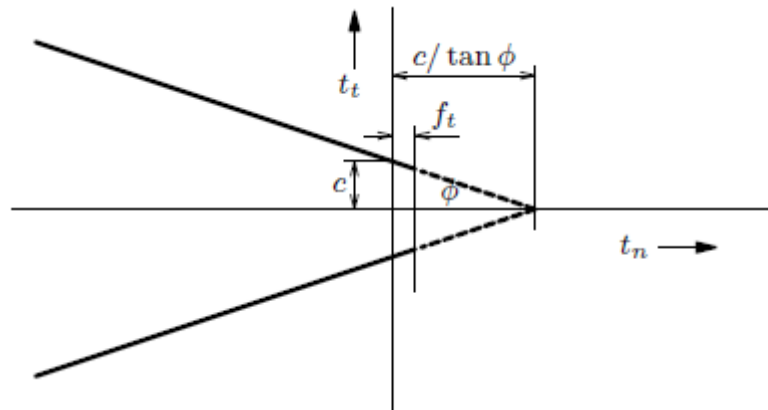


**Figure 5-7: Coulomb Friction Criterion**

In this study, The tangential and normal stiffness of interface element can be given as follows [55]:

$$D_{tt} = \frac{A^2}{t} \left( \frac{E_{soil}}{2(1+\nu_{soil})} \right) \quad (5.34)$$

$$D_{nn} = f \times D_{tt} \quad (5.35)$$

Where  $D_{tt}$  is the tangential stiffness,  $D_{nn}$  the normal stiffness,  $E_{soil}$  is the Young's modulus of the soil and  $\nu$  its Poisson's ratio.  $A$  is a reduction factor to depends on the type of soil ( $A$  may range from 0.5 to 1.0), Factor  $t$  is a small length representing the virtual thickness of the interfaces;  $f$  is a multiplication factor that can vary from 10 to 100.

The nonlinear interface behavior can be modeled with the Coulomb friction model. Two different surface types are considered: smooth and rough interface. The smooth surface is applied for a very low degree of restraint between the concrete and soil; however, the rough surface presents a high degree of restraint. The maximum restraint condition is assumed in case of the perfect bond between the two surfaces; either slips or detachment are not allowed in that case.



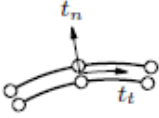
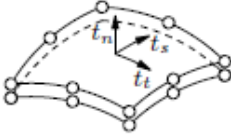
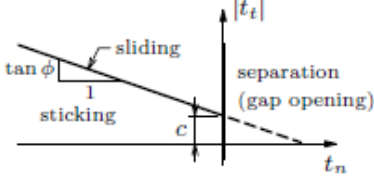
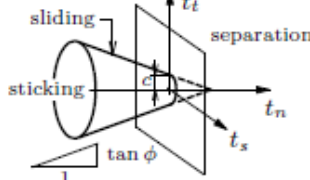
Constitutive behavior of the interface is described in DIANA in terms of relationships between normal and shear relative displacements across the interface, and the normal and shear effective stresses (also known as ‘tractions’).

The constitutive law for frictional behavior of interface elements in FE simulation is summarized in Table 5-2.

### **5.3 Types of Elements Used in FEM Simulation**

The finite element method was used to simulate the temperature evolution and associated thermal stresses. The feature of staggered flow-stress analysis in TNO DIANA software was utilized, in which the temperature distribution was calculated by heat flow analysis, followed by structural analysis. An eight-noded isoparametric brick element (HX8HT) was used to simulate the heat flow in formwork, water layer and polystyrene foam. The outer surfaces of the block which are subjected to convections (formwork and top surface of mock-up) were modeled using the BQ4HT element which is a four-node isoparametric quadrilateral element specially used to describe boundaries in three-dimensional thermal analyses. The concrete was modeled with twenty-node isoparametric solid brick element (CHX60). The sandy soil was modeled with a quadratically interpolated structural element (HX24L) that is converted during thermal analysis to a linearly interpolated flow element. The

**Table 5-2: Constitutive law for frictional behavior of interface [55]**

	Analysis type	
	Plane Strain Axisymmetric	Three-dimensional
		
Stresses	$\mathbf{t} = \{t_n, t_t\}^T$	$\mathbf{t} = \{t_n, t_t, t_s\}^T$
Elasticity matrix	$\mathbf{D}_{el} = \begin{bmatrix} K_n & 0 \\ 0 & K_t \end{bmatrix}$	$\mathbf{D}_{el} = \begin{bmatrix} K_n & 0 & 0 \\ 0 & K_t & 0 \\ 0 & 0 & K_s \end{bmatrix}$
Natural parameters	$c$ – cohesion $\phi$ – friction angle $\psi$ – dilatancy angle	
Stress conditions	Slip activated when	
	$f_1 = t_t + \tan \phi t_n - c > 0$	$f_1 = \sqrt{t_t^2 + t_s^2} + \tan \phi t_n - c > 0$
	No tension ('cut-off') activated when	
	$f_2 = t_n > 0$	
		

interface between the concrete and soil was modeled by 8-nodes element (Q24IF), having zero-thickness. The types of elements used in FE simulation is shown in Figure 5-8.

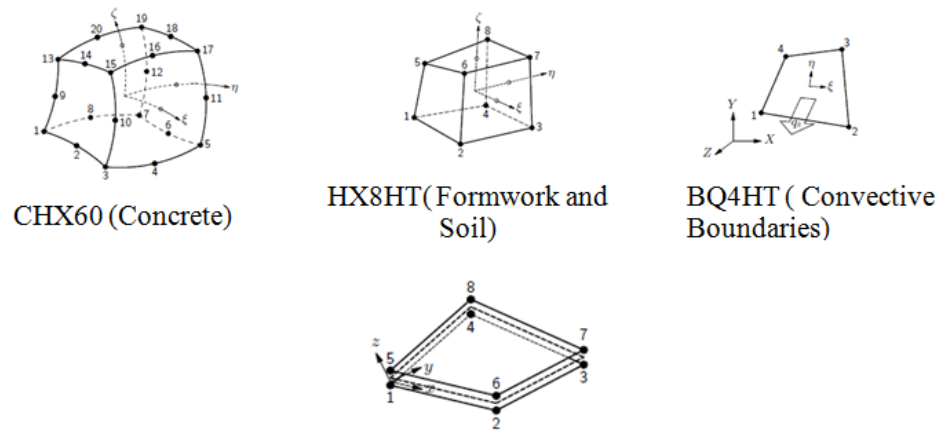


**Figure 5-8: Types of Elements Used in FE Simulation**

Due to symmetry, only the quarter of the mock-up specimens and piles-cap was simulated. The quarter portion of mockup geometry and the different types of elements used in the model are shown in Figure 5-9.

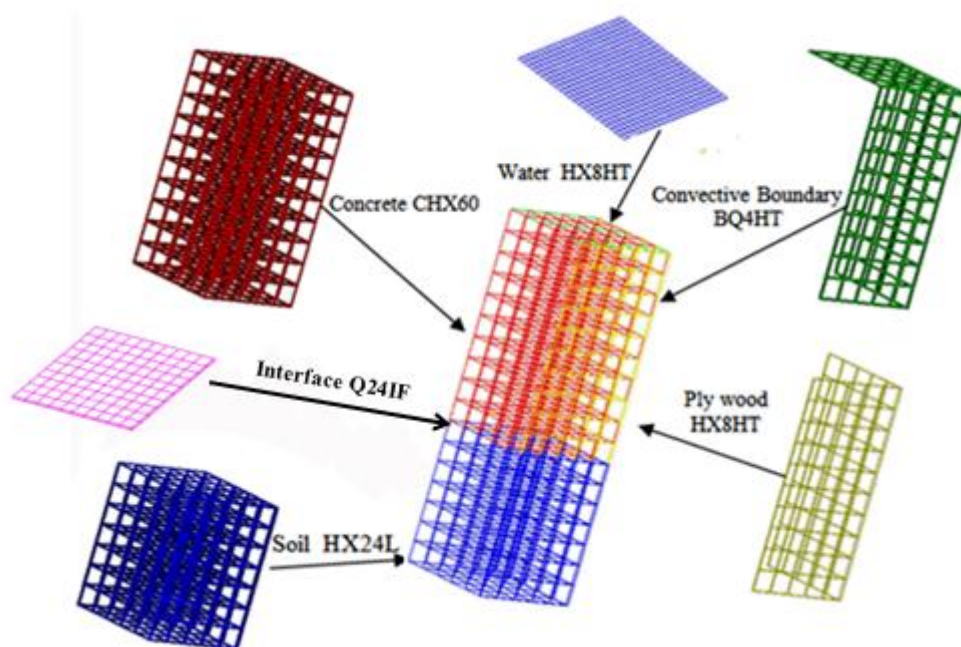


**Figure 5-9: Geometry of Quarter of Mockup Specimen**

## **CHAPTER 6**

### **EXPERIMENTAL RESULTS**

#### **6.1 Experimental Results**

The results of laboratory tests and field monitoring tests will be given and discussed in this chapter.

##### **6.1.1 Lab. Tests Results**

##### **6.1.1.1 Heat of Hydration Results**

The heat of hydration of various 46 concrete mixes was measured using the semi adiabatic calorimeter (iQdrum and Heat Box). The heat loss was measured and added back to the measured heat to obtain the adiabatic heat of hydration. In the group#1, the Portland cement is replaced with different percentages (20%, 30%, 40%, 50%, 60%, and 50% with retarder) of Fly Ash.

The heat of hydration evolution versus equivalent age for the mixes in the group# 1 is shown in Figure 6-1.

It is noticed from Figure 6-1 that the heat generated from control mix (OPC) is the highest when it compared with other mixes in the group. The heat of hydration decreases with an increase of the Fly Ash replacement percentage. The fly ash has a significant effect in reducing the heat of hydration.

The three hydration parameters ( $H_u$ ,  $\tau$  and  $\beta$ ) of the mixes in the group#1 were determined and plotted in Figure 6-2.

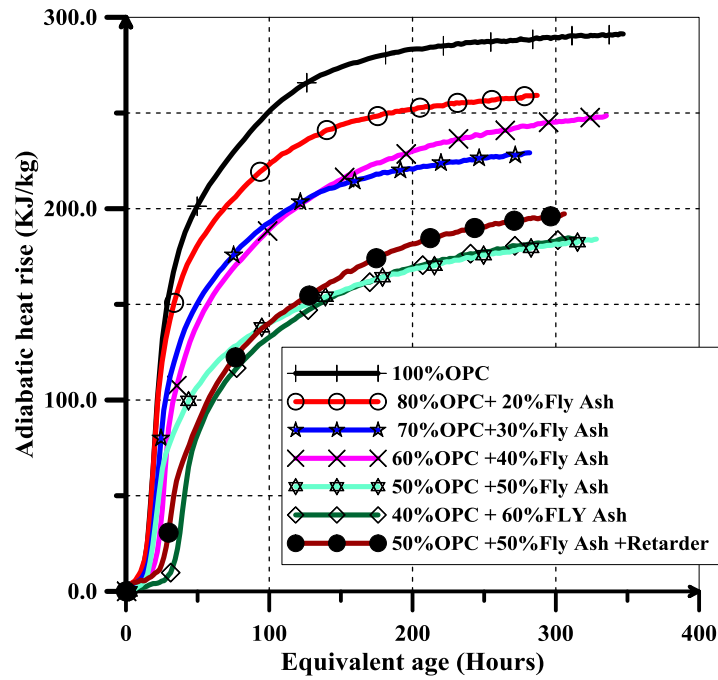
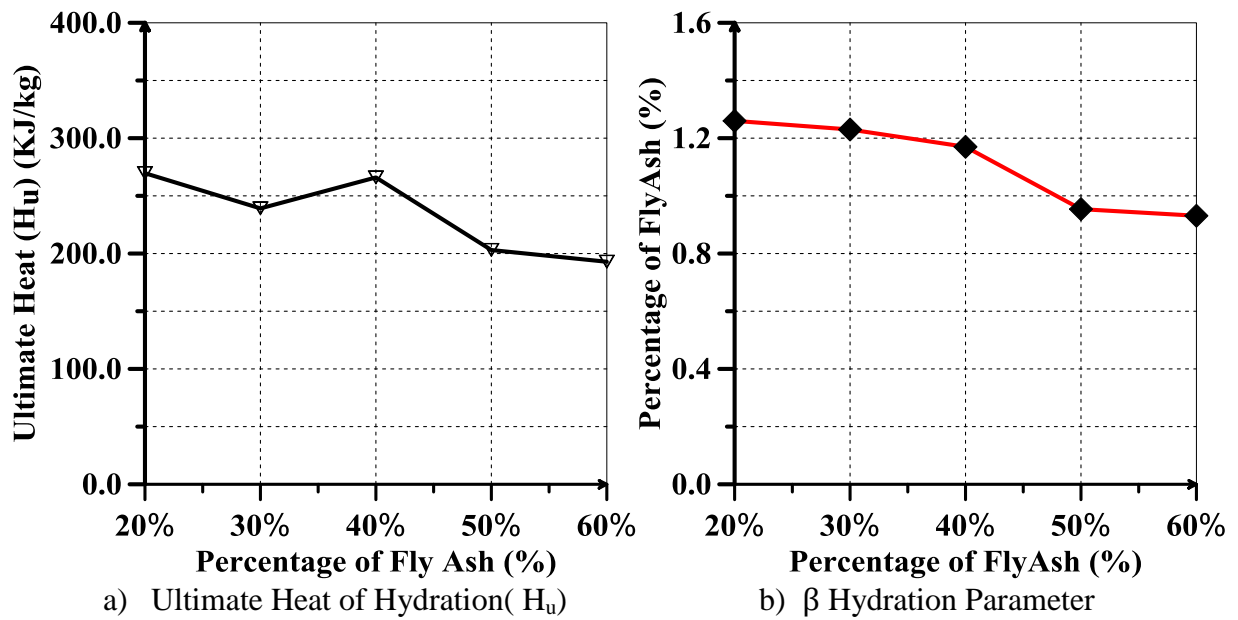
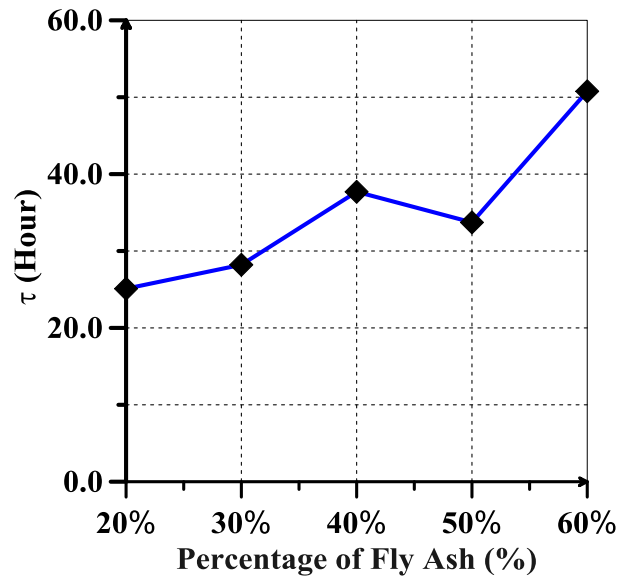


Figure 6-1: Adiabatic Heat of Hydration Rise for the Mixes of Group#1





c)  $\tau$  Hydration Parameter

**Figure 6-2: Hydration Parameters of Mixes in the Group#1; A) Ultimate Heat of Hydration (Hu); B)  $\beta$  Hydration Parameter; and C)  $\tau$  Hydration Parameter**

The ultimate heat of hydration decreases with an increase of the replacement percentage of Fly Ash except for 40% (see Figure 6-2, a)). The higher replacement percentage of Fly Ash, the higher reduction of generated heat of hydration. The slope of linear part of adiabatic heat of hydration curve declines with an increase of replacement percentage of Fly Ash ( Figure 6-2 (b)) . This means, the rate of heat evolution is decreasing with an increase of percentage of Fly Ash. Figure 6-2(c) shows that increasing the replacement Percentage of Fly Ash in the cement will generally retard the hydration of the mixture. The retarder (warda 8) delays the heat evolution, although they don't reduce the total adiabatic heat rise (see Figure 6-3).

In the group#2, the Portland cement is replaced with different percentages (20%, 30%, 40%, 50%, 60%, 70, and 50% with retarder) of GGBFS.

Figure 6-3 shows the effects of different replacement percentages of GGBFS on the heat evolution of mixtures of the group#2.

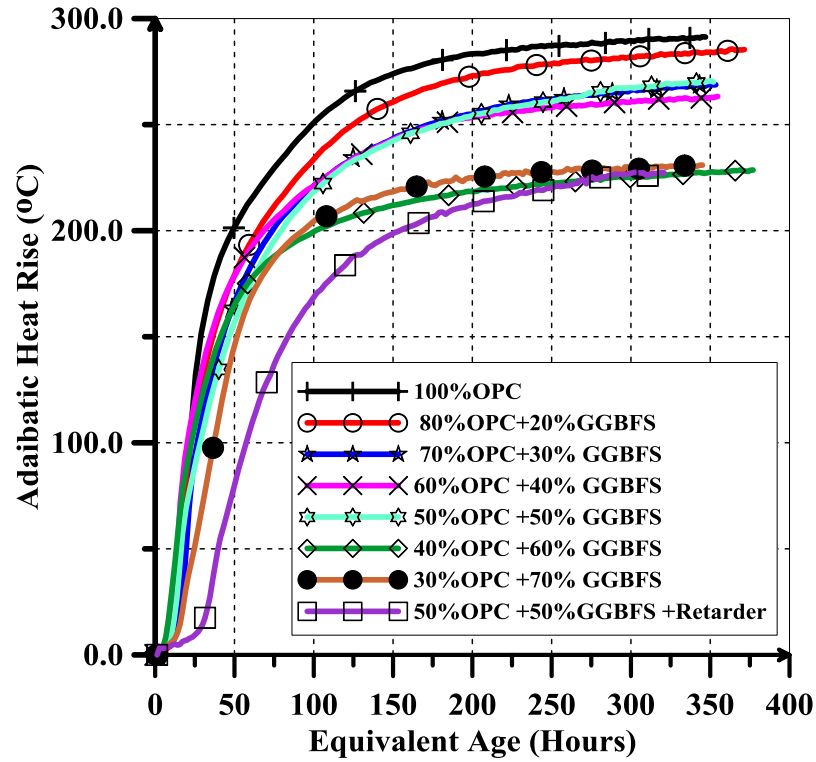
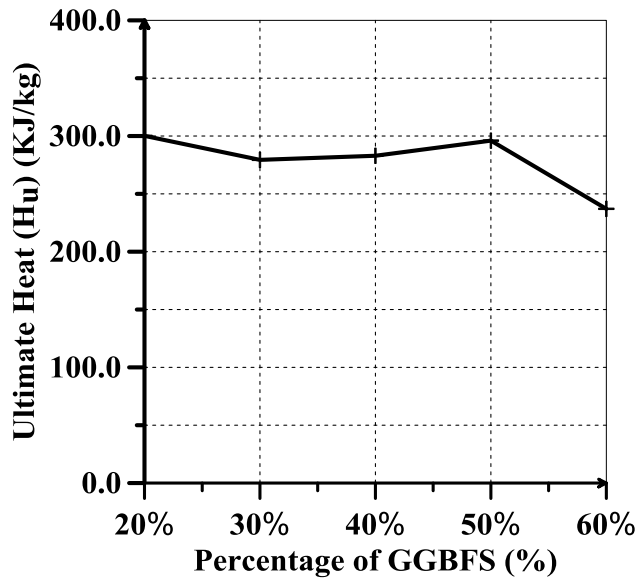


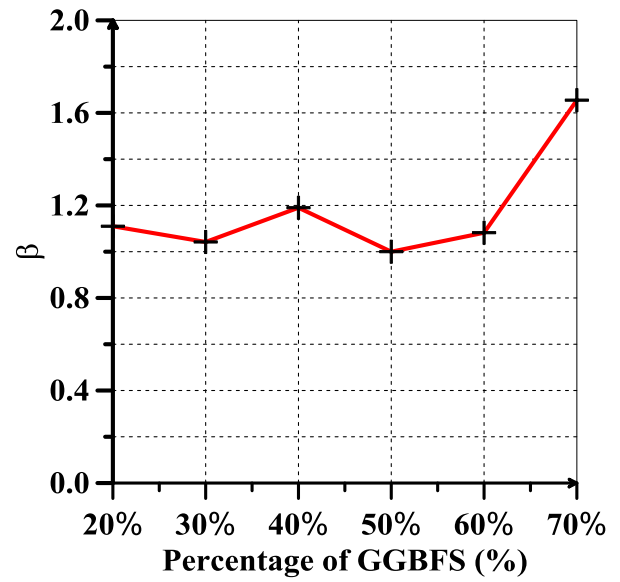
**Figure 6-3: Adiabatic Heat of Hydration Rise for the Mixes of Group#2**

Replacing cement with GGBFS up to approximately 50 % slightly reduces the heat of hydration evolution as shown in Figure 6-3. Increasing the replacement percentage of GGBFS up to 70% or more can lead to reduction in heat of hydration evolution. Figure 6-3 shows that the heat evolution is delayed with the addition of Warda 8 retarder (1.5 liter/m<sup>3</sup>).

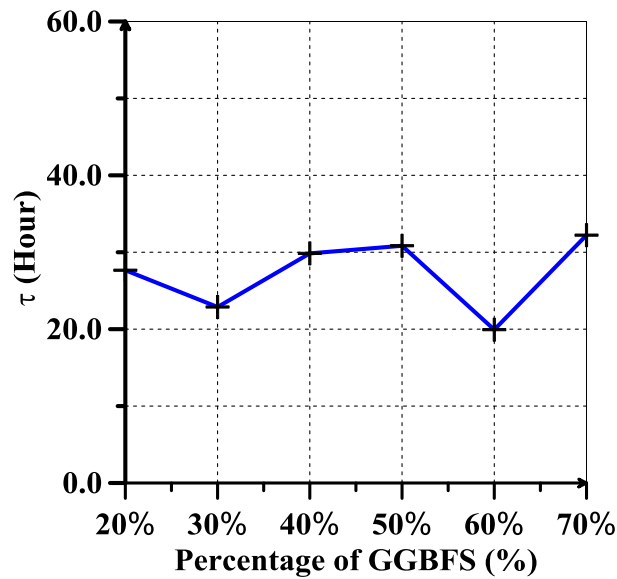
The three hydration parameters ( $H_u$ ,  $\tau$  and  $\beta$ ) of the mixes in the group#2 were determined and plotted in Figure 6-4.



a) Ultimate Heat of Hydration(  $H_u$ )



b)  $\beta$  Hydration Parameter



c)  $\tau$  Hydration Parameter

**Figure 6-4: Hydration Parameters of Mixes in the group #2; a) Ultimate Heat of Hydration ( $H_u$ ); b)  $\beta$  Hydration Parameter ; and c)  $\tau$  Hydration Parameter.**

Figure 6-4 (a) shows that there is a slight reduction in heat of hydration evolution when the replacement percentage of GGBFS is in the range of 20%-30%, then it remains almost constant until reaches 50%. The significant reduction in heat evolution has noticed



when the replacement percentage of GGBFS exceeds 50%. The hydration parameters ( $\beta, \tau$ ) is fluctuating between 20% and 60% replacement percentage of GGBFS, then they increase after exceeding the replacement percentage of 60% as shown in Figure 6-4(a)&(b).

The increase of replacement percentage of GGBFS doesn't necessarily lead to either slow the rate of hydration or to delay the heat of hydration evolution.

In the group#3, the Portland cement is replaced with equal different percentages of Fly Ash and GGBFS (20% (10%FA+10GGBFS), 30%, 40%, 50%, and 60%).

The semi-adiabatic results of heat adiabatic rise for the mixes in the group#3 are shown in Figure 6-5.

The heat evolution is decreasing with an increasing the replacement percentage of Fly Ash and GGBFS as shown in Figure 6-5. The 20% replacement percentage has a slight effect on reducing the heat evolution. The decrease on heat evolution is much more noticeable for the 60% replacement percentage of Fly Ash and GGBFS as shown in Figure 6-5.

The three hydration parameters ( $H_u, \tau$ , and  $\beta$ ) of the mixes in the group#3 were determined and plotted in Figure 6-6.

It is clear from Figure 6-6 (a) that the ultimate heat of hydration decreases with an increase of replacement percentage of Fly Ash and GGBFS.

Figure 6-6 (b) shows that there is a slight reduction in rate of heat evolution when the replacement percentage of FA and GGBFS is in the range of 20%-30%, then it remains almost constant until reaches 40%. Then, the rate of heat evolution is decreased as the replacement percentage of GGBFS and FA exceeds 50%.

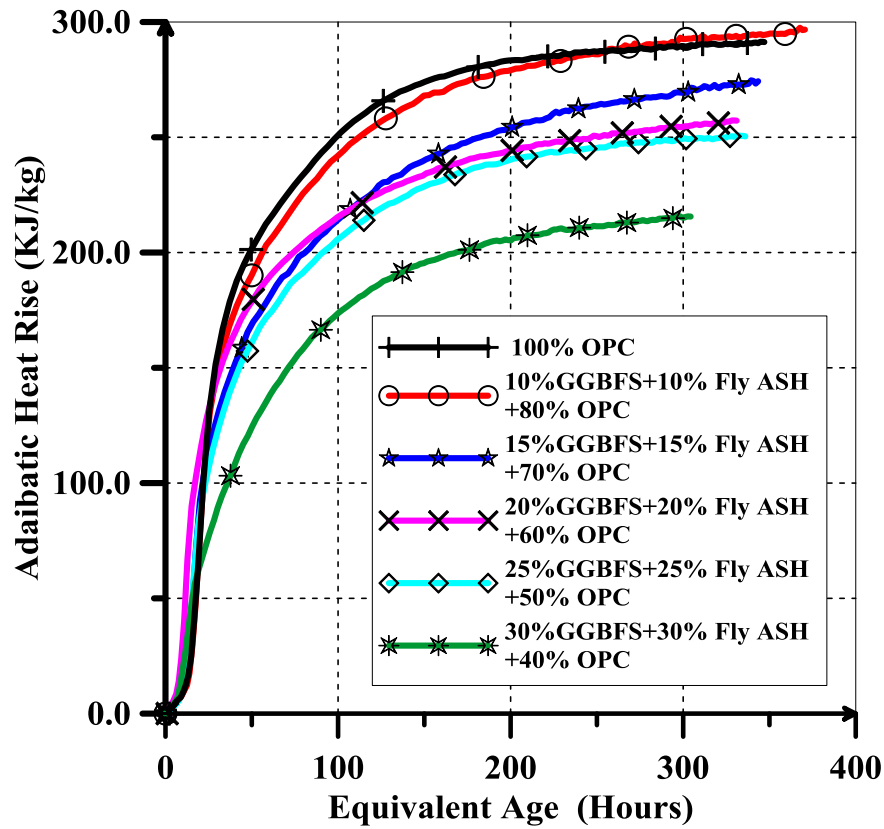
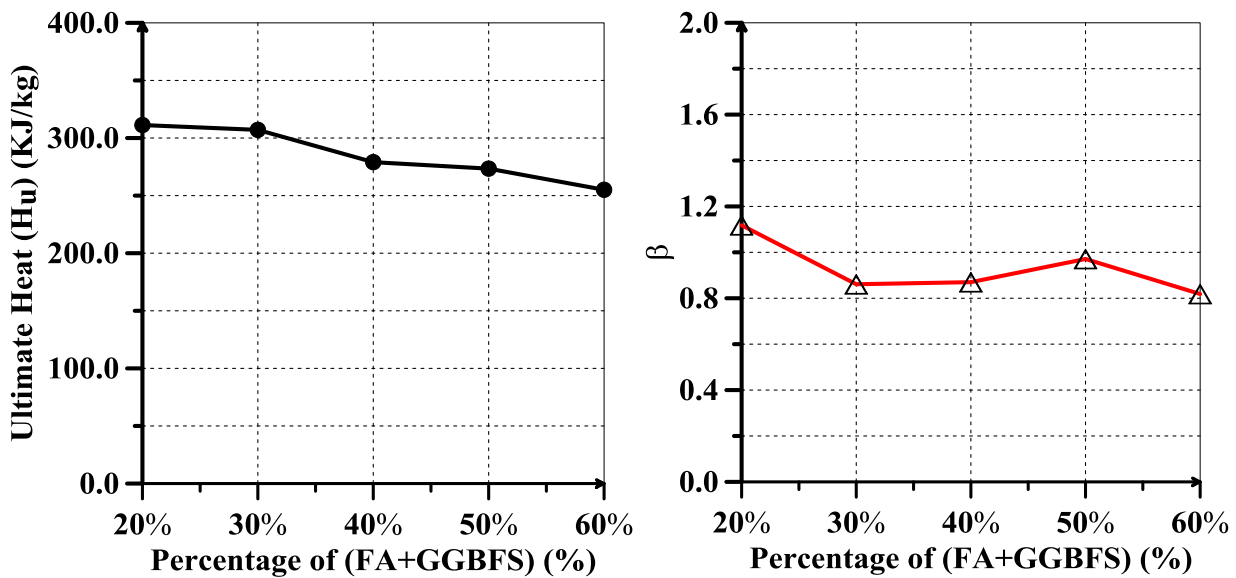
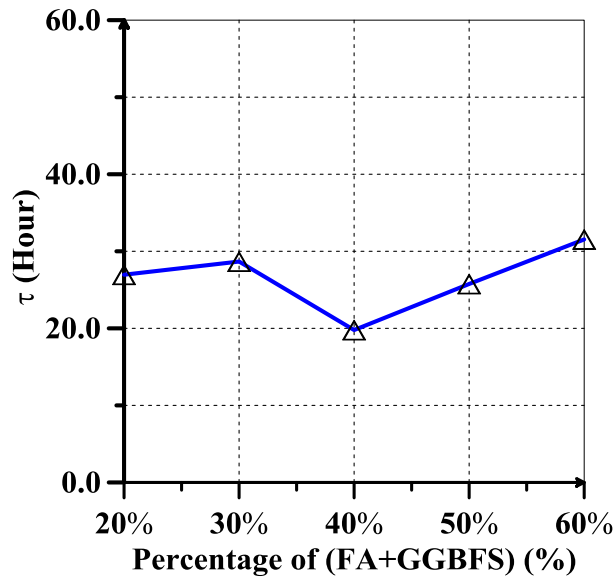


Figure 6-5: Adiabatic Heat of Hydration Rise for the Mixes of Group#3



a) Ultimate Heat of Hydration(  $H_u$ )

b)  $\beta$  Hydration Parameter



c)  $\tau$  Hydration Parameter

**Figure 6-6: Hydration Parameters of Mixes in The Group #3: A) Ultimate Heat of Hydration ( $H_u$ ); B)  $B$  Hydration Parameter; And C)  $T$  Hydration Parameter**

It can be noticed from Figure 6-6(c), the heat evolution is retarded when the percentage of GGBFS and FA is between 20% and 30%, and then It is accelerated when the percentage of GGBGS and FA is between 30% and 40%. After that, the retardation continues when the replacement percentage of GGBFS and FA exceeds 40%.

In the fourth group, the total cementitious materials content is  $350 \text{ kg/m}^3$  and the water/binder ratio is 0.38. Portland cement is replaced with different percentages (20%, 30%, 40%, and 50%) of Fly Ash. This group differs from the group#1 in the cementitious materials content and in water/binder ratio.

The heat of hydration evolution versus equivalent age of the mixtures in the group# 4 is shown in Figure 6-7.

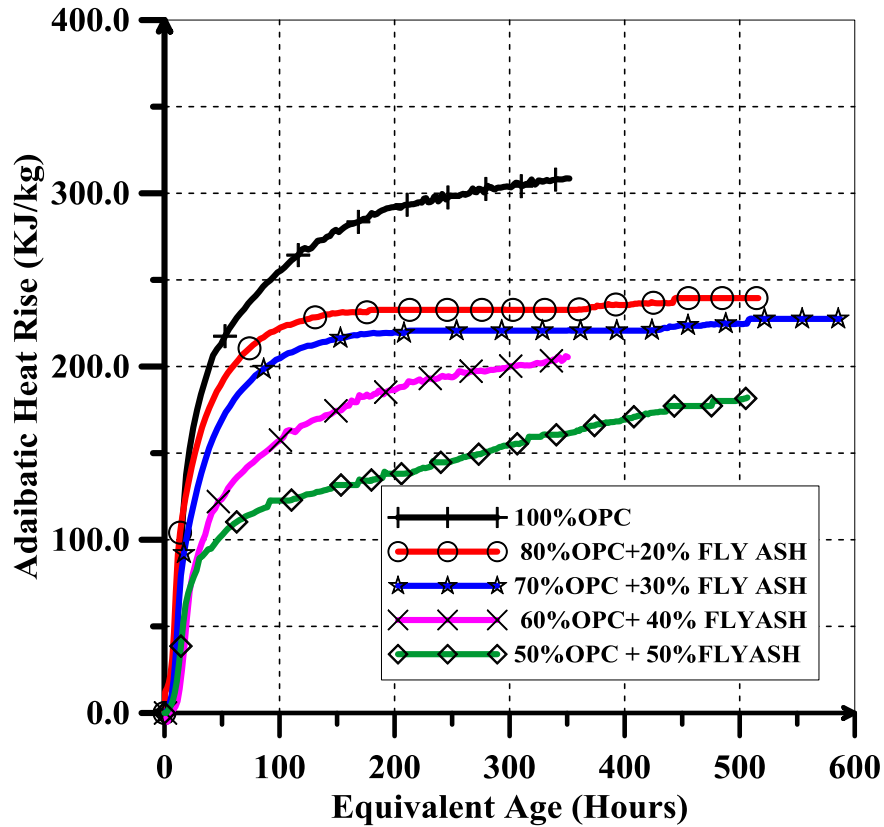


**Figure 6-7: Adiabatic Heat of Hydration Rise for the Mixes in Group#4**

It is noticed from Figure 6-7 that the heat generated from control mix (OPC) is the highest when it compared with other mixes in the group. The heat of hydration decreases with an increase of the Fly Ash replacement percentage. The fly ash has a significant effect in reducing the heat of hydration.

The higher replacement percentage of Fly Ash, the higher reduction in the heat of hydration as shown in Figure 6-7. Replacing cement with Fly Ash delays the hydration process.

In the fifth group, the total cementitious materials content is  $350 \text{ kg/m}^3$  and the water/binder ratio is 0.38. Portland cement is replaced with different percentages (20%, 30%, 40%, and 50%) of GGBFS. This group differs from the group#2 in the cementitious materials content and in water/binder ratio.

The heat of hydration evolution versus equivalent age of the mixtures in the group# 5 is shown in Figure 6-8.

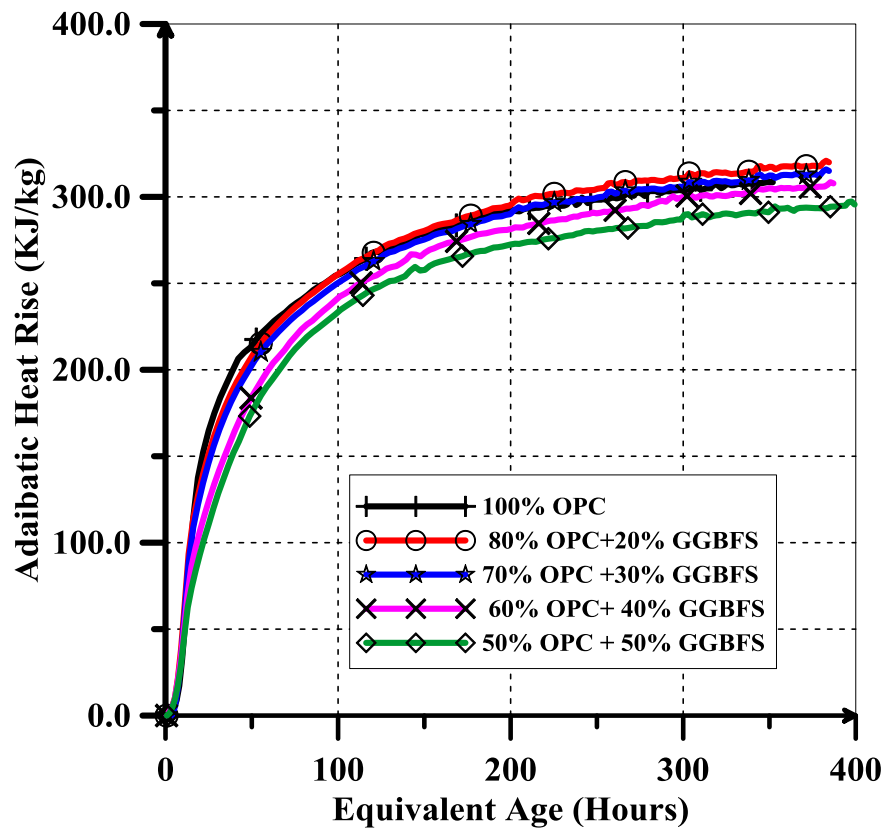


**Figure 6-8: Adiabatic Heat of Hydration Rise for the Mixes of Group#5**

Replacing cement with GGBFS up to 50 % causes a slight decrease in heat evolution as shown in Figure 6-8. The reduction of heat evolution using GGBFS can be achieved by increasing the replacement percentage to 70% or even 80%.

In the Sixth group, the total cementitious materials content is  $480 \text{ kg/m}^3$  and the water/binder ratio is 0.28. Portland cement is replaced with different percentages (10%, 20%, 30%, and 40%) of Micro-silica.

The semi-adiabatic results of heat adiabatic rise for the mixes in the group#6 are shown in Figure 6-9.

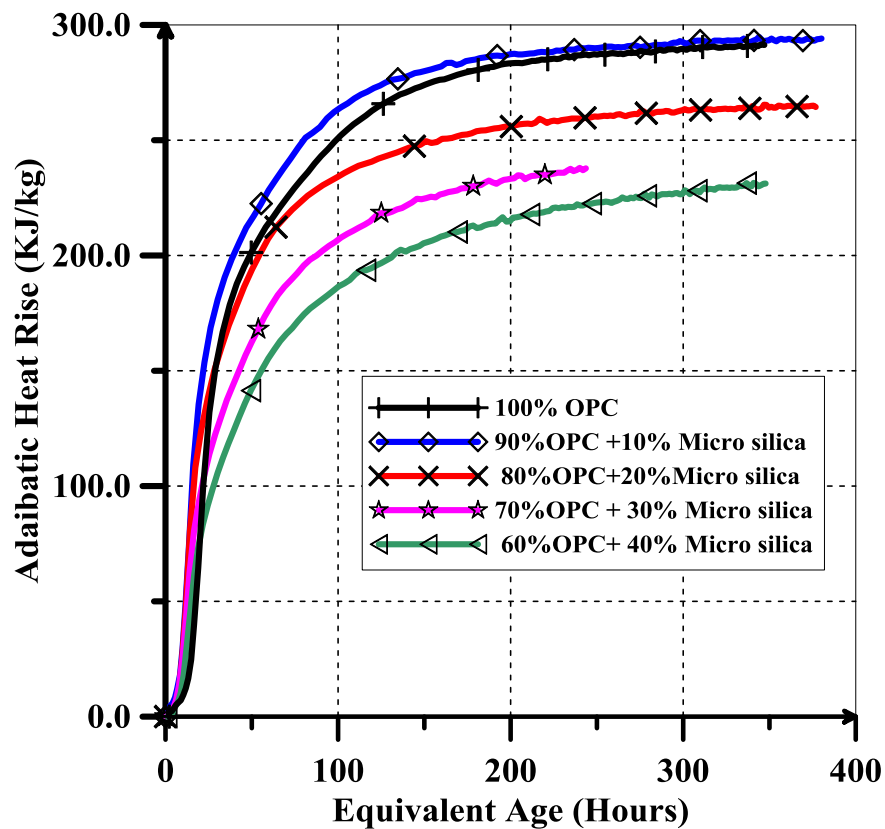
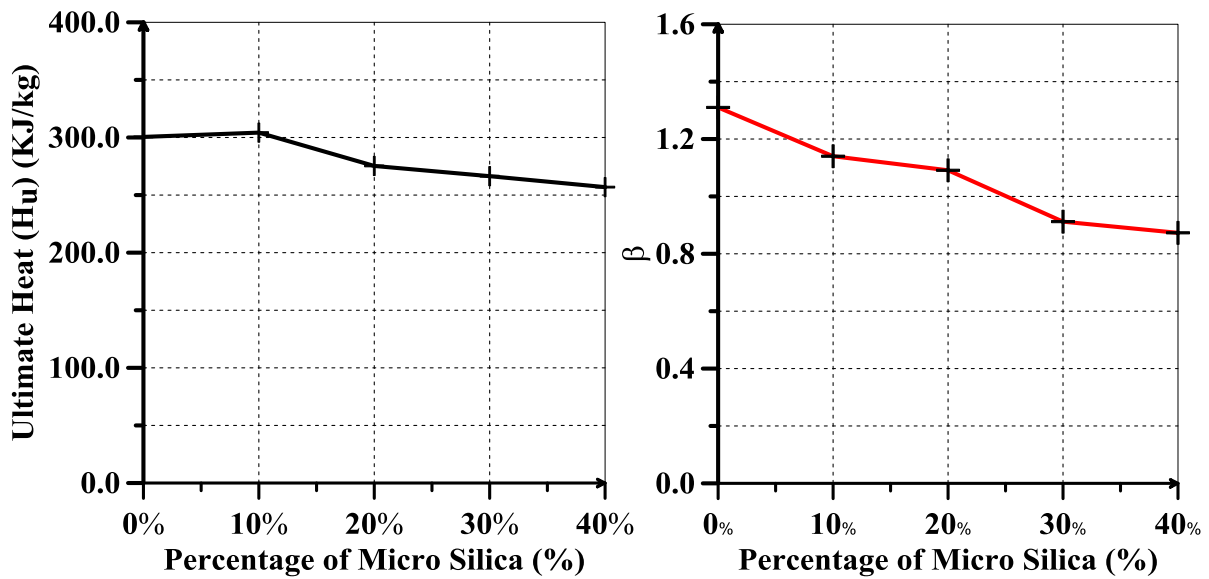


**Figure 6-9: Adiabatic Heat of Hydration Rise for the Mixes of Group#6**

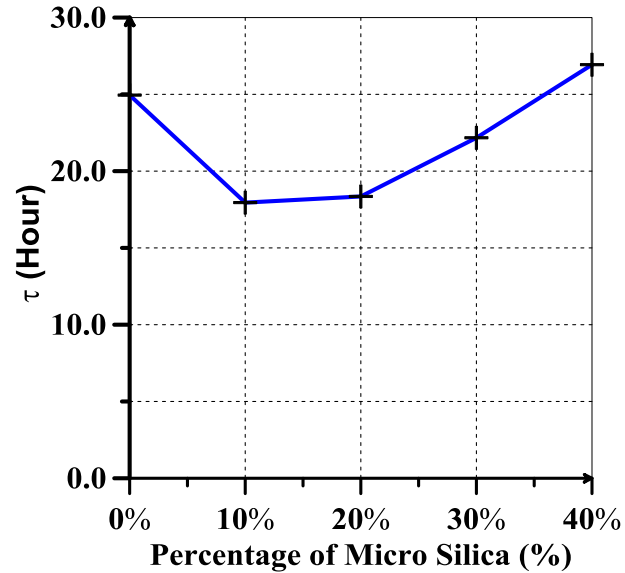
Figure 6-9 shows that there is an increase in the heat of hydration evolution when the replacement percentage of Micro-Silica is 10%. The increase of replacement percentage of Micro-Silica from 10% to 40% leads to a decrease in the heat of hydration evolution.

Figure 6-10 shows that the effects of different replacement percentages of Micro-Silica in the hydration parameters ( $H_u$ ,  $\tau$ , and  $\beta$ ) of the mixes in the group#6 .



a) Ultimate Heat of Hydration(  $H_u$ )

b)  $\beta$  Hydration Parameter



c)  $\tau$  Hydration Parameter

**Figure 6-10: Hydration Parameters of Mixes In The Group #6; A) Ultimate Heat of Hydration ( $H_u$ ); B)  $\beta$  Hydration Parameter; And C) Hydration Parameter**

It is observed that the ultimate heat of hydration increases as the Micro-Silica replacement percentage increases up to 10%. When the replacement percentage of Micro-Silica is greater than 10%, the heat evolution decreases. As long as the replacement percentage of Micro-Silica is less than 10%, the time parameter  $\tau$  drops (there is an acceleration in heat evolution) . The delay in the heat evolution is noticed when the replacement percentage of Micro-Silica is larger than 10% as shown in Figure 6-10(c). The rate of hydrating decreases with an increase of replacement percentage of Micro-Silica as shown in Figure 6-10(b).

In the group#7, the effect of w/cm ratio in the heat of hydration evolution was investigated. The heat evolution versus equivalent age for the mixes in the group# 7 is shown in Figure 6-10.

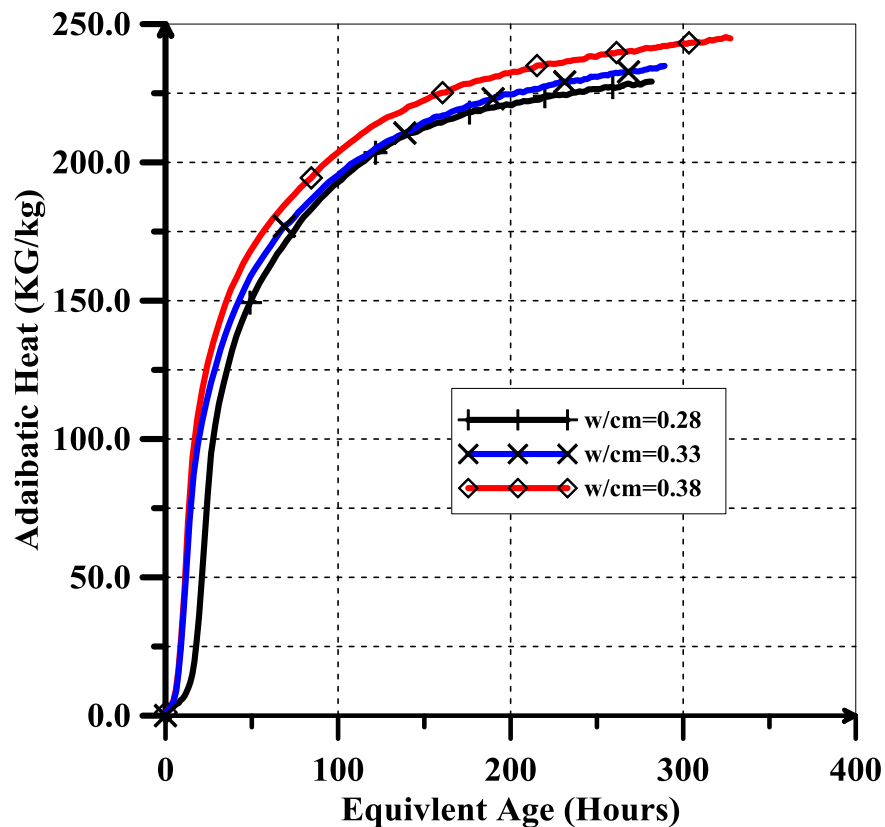


**Figure 6-11: Adiabatic Heat of Hydration Rise for The Mixes of Group#7**

Figure 6-11 shows the effect of varying w/cm from 0.28 to 0.33 on the adiabatic



heat of hydration rise . Clearly, an increase in the water cementitious material (w/cm) ratio leads to an increase in the heat evolution. When more water is available to solubilize and react with the cement, the rate of heat evolution generally increases.

In the group#8, the generation of heat of hydration from different type of concrete: normal, flowing, and self-compacting concretes using iQdrum heat signature calorimeter has been investigated.

The mixes proportions of the concrete mixes are shown in Table 3-8. Mix 1 (REF) is a reference mix with only OPC Type I at 480 (kg/m<sup>3</sup>) and water/binder ratio of 0.28. The water/binder ratio was kept constant in all mixes. Three mixes (Mixes 2 to 4) are flowing concrete with OPC replaced by 20%, 30% and 40% of Class-F fly ash, which has high slump flow but does not pass the self-compatibility tests. Mixes 35 to 37 are high slump (150 mm to 200 mm) normal concrete in which OPC was replaced by 20%, 30% and 40% of Class-F fly ash. Mixes 38 to 40 with 20%, 30% and 40% replacement of OPC with fly ash are self-compacting concrete designed to achieve flowability, passing ability and segregation resistance. The content of coarse aggregate in SCC mixes is lower than those of flowing or conventional concrete. Therefore, SCC has higher quantity of fine aggregates in order to avoid gravity segregation of larger aggregates in the fresh mix. The dosage of super plasticizer was adjusted to achieve the required levels of flow ability. The measured properties of the FC and SCC mixes are summarized in Table 6-1.

**Table 6-1: Results of Self Compactability Tests on Fresh Concrete**

<b>Mix</b>	<b>Slump flow (mm)</b>	<b>T50 (s)</b>	<b>V. Funnel (s)</b>	<b>L-Box (mm/mm)</b>	<b>Slump (mm)</b>
<b>Mix 1</b>	665	13	80	-	-
<b>Mix 2</b>	690	12	75	-	-
<b>Mix 3</b>	720	10.5	60	-	-
<b>Mix 4</b>	780	9.2	50	-	-
<b>Mix 35</b>	-	-	-	-	165
<b>Mix 36</b>	-	-	-	-	200
<b>Mix 37</b>	-	-	-	-	220
<b>Mix 38</b>	680	4.5	12	0.912	-
<b>Mix 39</b>	750	3.5	11	0.908	-
<b>Mix 40</b>	780	3	10	0.906	-

Figure 6-12 shows the adiabatic heat of hydration rise curve for all concrete mixes investigated in the group#8. The adiabatic heat for the reference mix is significantly higher as compared to other mixes. The adiabatic heat rise and the rate of heat rise are significantly reduced with an increase in Class F fly ash replacement level. At early ages fly ash content does not have significant effect on heat rise, however, at later ages the adiabatic heat rise decreases with increased fly ash percentages. It is also observed that at 20% and 30% fly ash replacement, there is no significant difference between flowing, self-compacting and normal concrete. However, at 40% fly ash replacement, the adiabatic heat rise for flowing concrete is substantially higher.

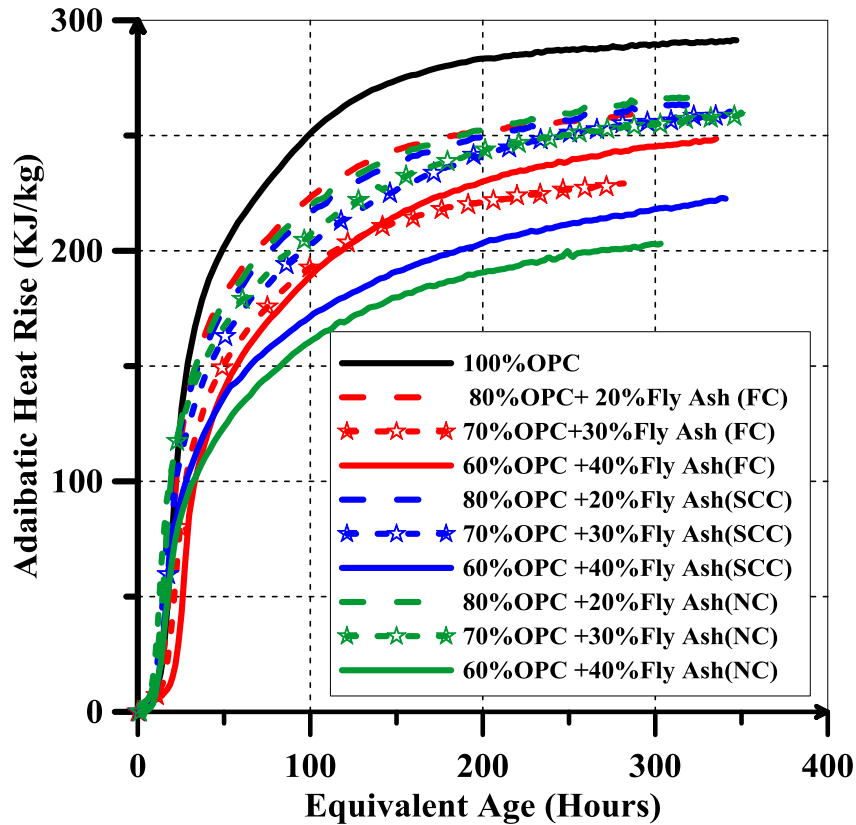


**Figure 6-12: Adiabatic Heat of Hydration Rise for the Mixes of Group#8**

In the group #9, the effect of high content of cement on the heat of hydration of concrete mixtures has been investigated. To test the effects of different amounts of cement content in a mixture, mixtures 41, 42, and 43 were run at a w/cm of 0.28 with 480, 700 and 900 kg/m<sup>3</sup>. The difference in adiabatic temperature rise associated with different cement contents (Mixtures 41, 42, and 43) is shown in Figure 6-13.

By reducing the cement content from 900 kg/m<sup>3</sup> to 480 kg/m<sup>3</sup>, the adiabatic temperature rise is reduced by 25 °C. One of the easiest ways to reduce the adiabatic temperature rise is to reduce the cement content in a concrete mixture. If the mixture with 900 kg cement is used in mass concrete structures, the placement temperature (e.g. 30°C) will be added to the adiabatic temperature rise of 900 kg mixture (e.g. 92°C) which results in a very high temperature (122°C).

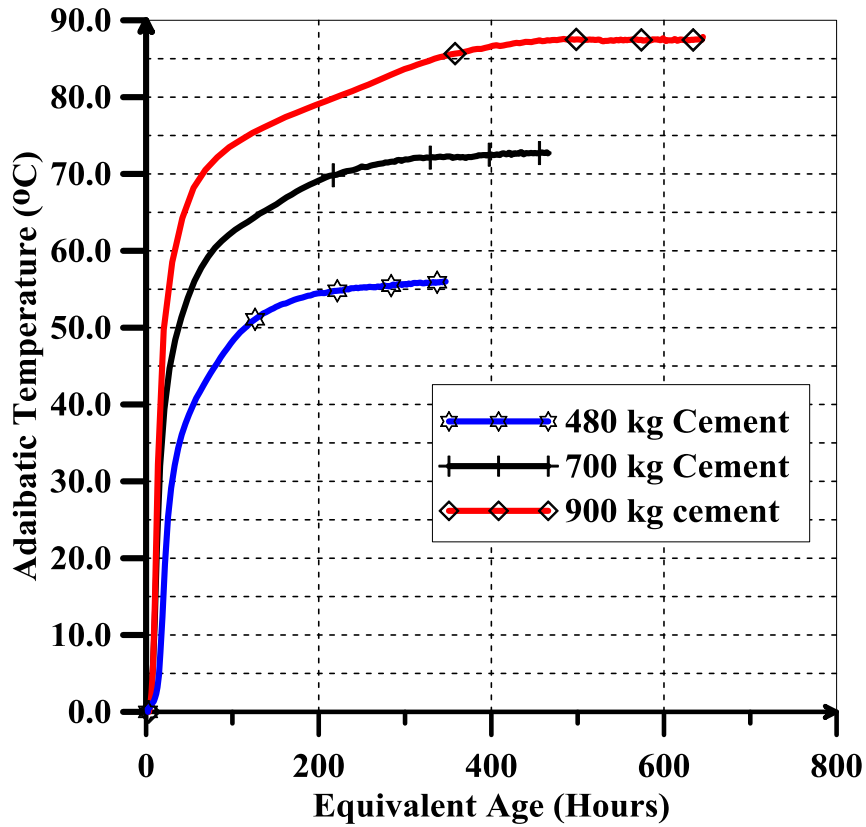


**Figure 6-13: Adiabatic Temperature Rise for the Mixes of Group#9**

In the group #10, the effect of steel and Polypropylene fibers in heat evolution was investigated. Fibers are generally used to strengthen the concrete against cracking. They also reduce the permeability of concrete and thus reduce bleeding of water.

The mixes proportions of the concrete mixes of Group#10 are shown in Table 3-10. Mix 4 (REF) is a reference mix with 60 % OPC Type I (288 (kg/m<sup>3</sup>)), 40% Fly Ash Type F, and water/binder ratio of 0.28. The water/ binder ratio remains the same for the mixes of this group. Mix43 and mix44 contains steel fibers with 0.3% and 0.5% volume fractions respectively whereas Mix45 and mix46 contains Polypropylene fibers with 0.3% and 0.5% volume fractions respectively. The adiabatic temperature rise curves for the mixes in group#9 are shown in Figure 6-14.

The addition of polypropylene fibers to concrete mixes significantly decreases the heat evolution compared to the decrease obtained by adding the steel fibers. At early ages

(about 2 days from casting) steel or polypropylene fibers does not have significant effect on heat rise, however, at later ages the adiabatic heat rise decreases with increased fibers percentages as shown in Figure 6-14.

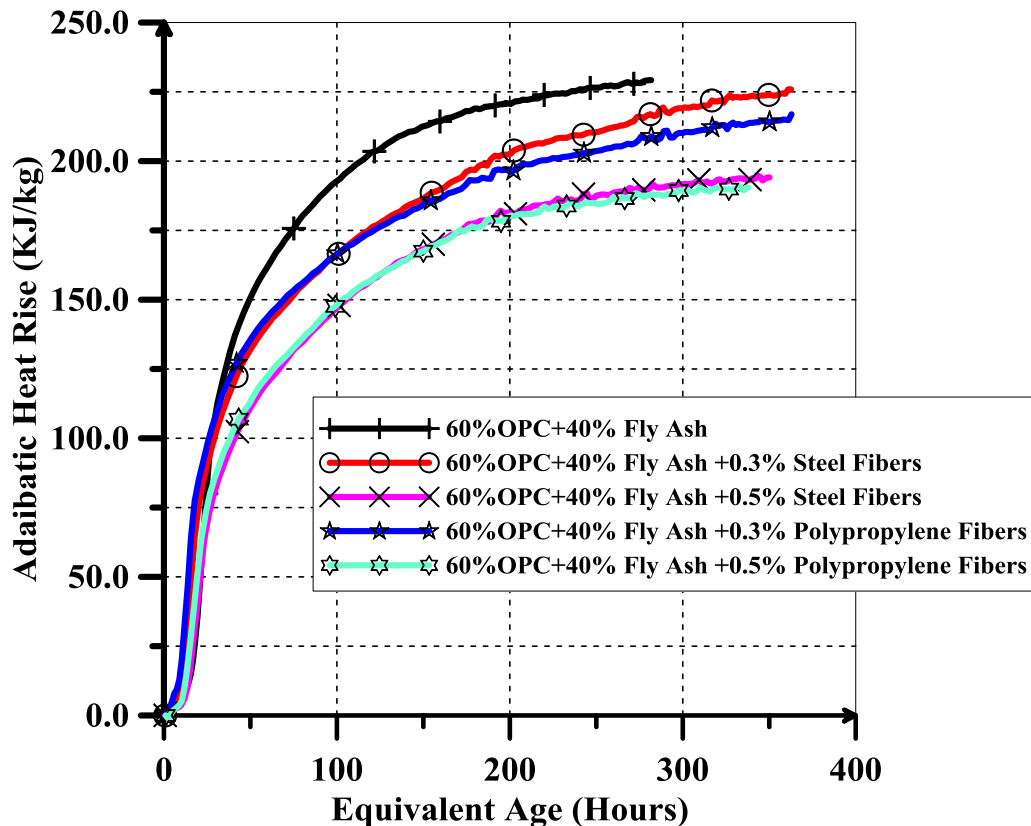


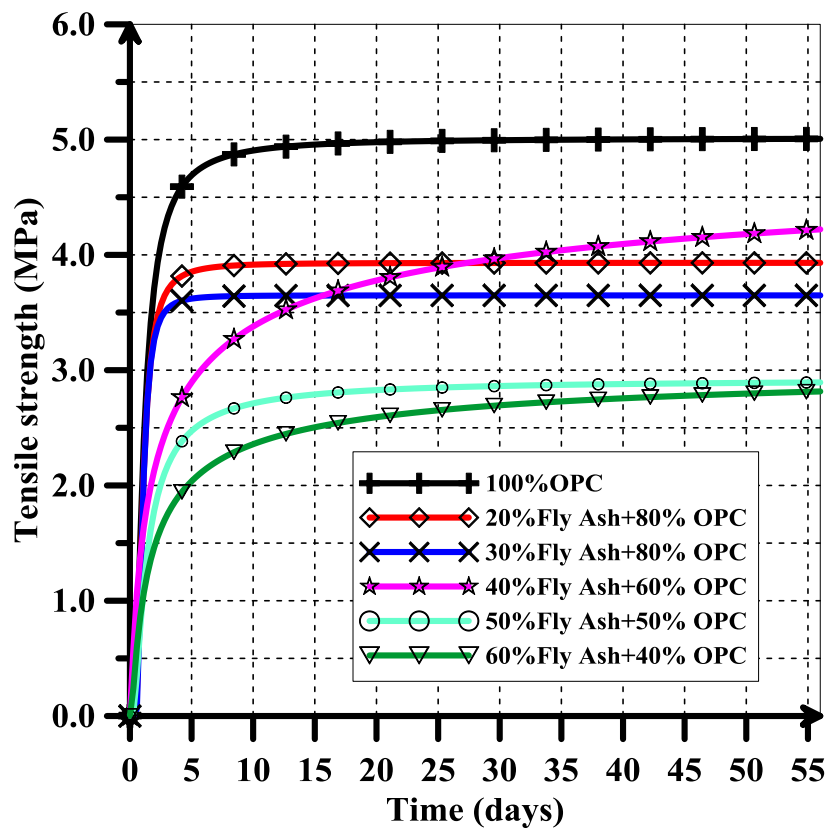
**Figure 6-14: Adiabatic Temperature Rise for the Mixes of Group#10**

It is noticed that the workability (slump) is impacted only slightly for the mixtures with steel fibers, but was reduced more significantly for the mixtures with polypropylene fibers. It is likely that the reduction of the heat evolution caused by polypropylene fibers is a result of the decrease in the workability of concrete mixtures.

#### **6.1.1.2 Results of Tensile Strength**

The splitting tensile strength has been determined for all mixes at ages 2, 4, 7, 28, and 56 days. The development of tensile strength with time for the mixes of group#1 is

shown in 6-15. It is noticed from Figure 6-15 that the tensile strength development for control mix (OPC) is the highest when it compared with other mixes in the group. The tensile strength decreases with an increase of the Fly Ash replacement percentage. The Fly Ash has a significant effect in reducing the tensile strength of concrete. Increasing the replacement percentage of fly ash more than 40% leads to a reduction in a tensile strength to about 50% compared to control mix. For the mixes with 100% OPC, 20% Fly Ash, and 30% Fly Ash, the tensile strength after 7days changed slightly. As the percentage of Fly Ash increases, the change of tensile strength with time becomes higher.



**6-15: Development of Tensile Strength with Time for the Mixes in Group#1**

Replacing cement with GGBFS up to approximately 50 % slightly reduces the tensile strength of concrete as shown in Figure 6-16. Increasing the replacement percentage of

GGBFS up to 70% or more doesn't lead to reduction in tensile strength of concrete. It is notice from Figure 6-16 that the tensile strength of the mixes with 60% and 70% of GGBFS is higher than that of control mix (100% OPC) at later ages.

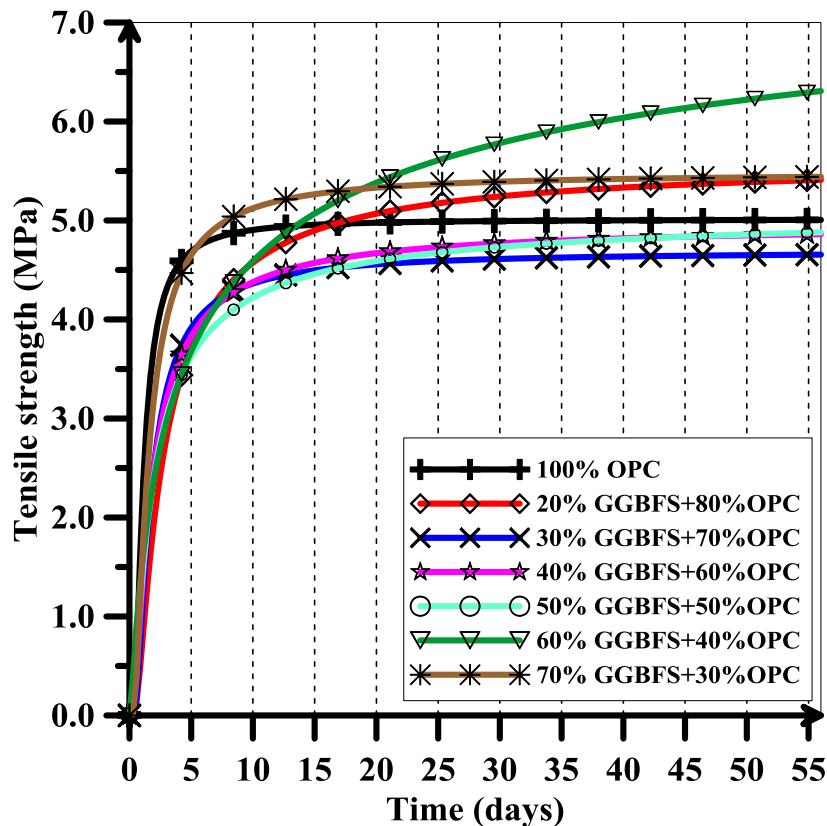


**Figure 6-16: Development of Tensile Strength with Time for the Mixes in Group#2**

In the group#3, the Portland cement is replaced with equal different percentages of Fly Ash and GGFS (20% (10%FA+10GGBFS), 30%, 40%, 50%, and 60%).

The development of tensile strength with time for the mixes in the group#3 is shown in Figure 6-17. The increase in the replacement percentage of Fly ash and GGBFS doesn't necessarily lead to the decrease in the development of tensile strength as shown in Figure 6-17. The mix with 20% replacement percentage of Fly Ash and GGBFS has a higher tensile strength than that of control mix (100% OPC) at later ages.

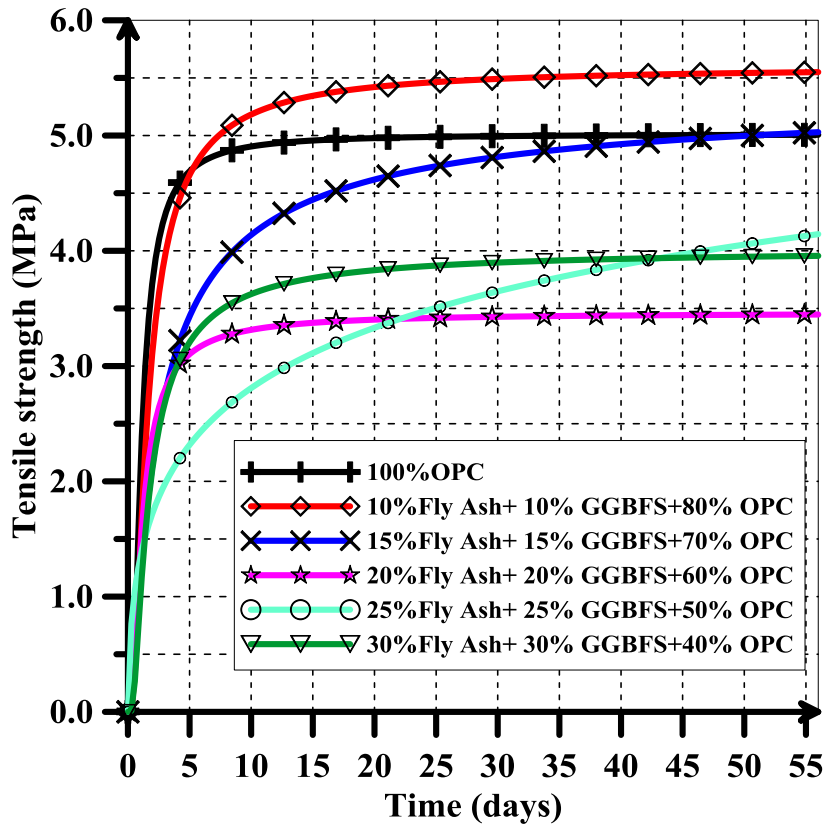


**Figure 6-17: Development of Tensile Strength with Time for the Mixes in Group#3**

In the fourth group, the total cementitious materials content is  $350 \text{ kg/m}^3$  and the water/binder ratio is 0.38. Portland cement is replaced with different percentages (20%, 30%, 40%, and 50%) of Fly Ash. This group differs from the group#1 in the cementitious materials content and in water/binder ratio.

The development of tensile strength with time for the mixtures in the group# 4 is shown in Figure 6-18.

The Figure 6-18 shows that the tensile strength development of control mix (OPC) is the highest when it compared with other mixes in the group#4. The tensile strength decreases



with an increase of the Fly Ash replacement percentage. As the replacement percentage of Fly Ash increases, the development of tensile strength decreases.

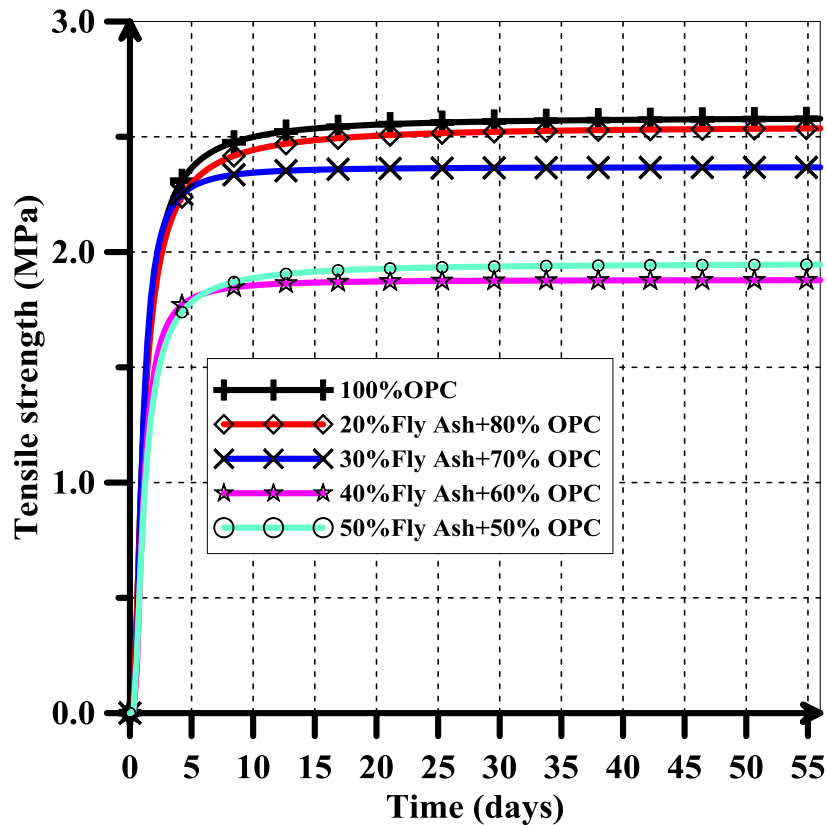


**Figure 6-18: Development of Tensile Strength with Time for the Mixes in Group#4**

In the fifth group, the total cementitious materials content is  $350 \text{ kg/m}^3$  and the water/binder ratio is 0.38. Portland cement is replaced with different percentages (20%, 30%, 40%, and 50%) of GGBFS. This group differs from the group#2 in the cementitious materials content and in water/binder ratio.

The development of tensile strength with time for the mixtures of the group# 5 is shown in Figure 6-19. It is clear from Figure 6-19 that the increase in the replacement percentage of GGBFS up to 50 % slightly reduces the tensile strength of concrete. The tensile strength of the mixes with 40% and 50% GGBFS is higher than that of the mixes with 20% and 30% percentage replacement of GGBFS.

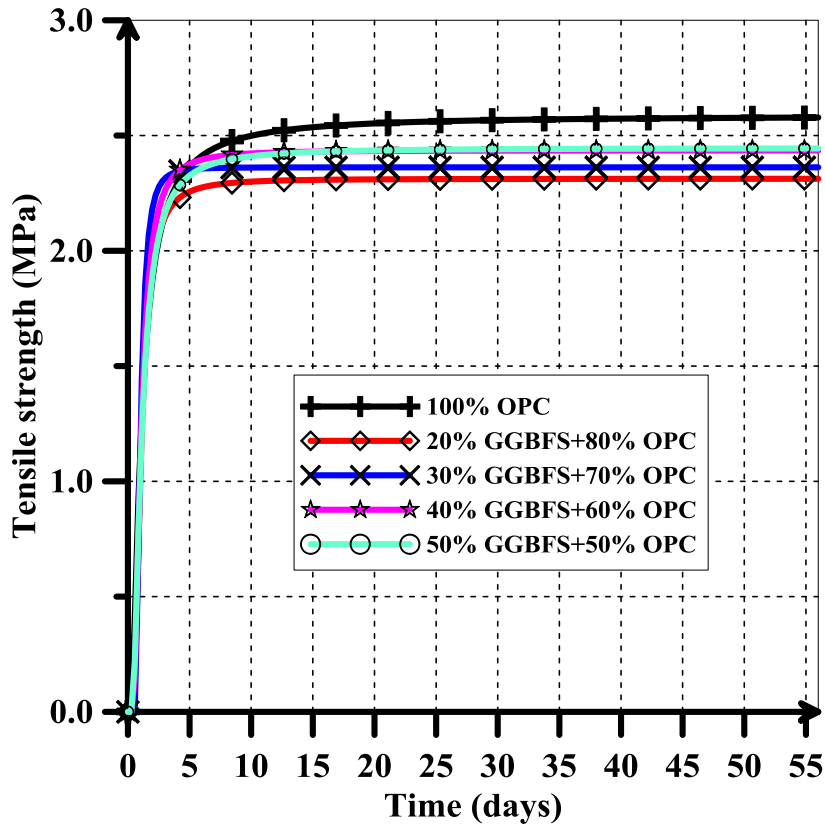


**Figure 6-19: Development of Tensile Strength with Time for the Mixes in Group#5**

In the Sixth group, the total cementitious materials content is  $480 \text{ kg/m}^3$  and the water/binder ratio is 0.28. Portland cement is replaced with different percentages (10%, 20%, 30%, and 40%) of Micro-Silica.

The change of tensile strength with time for the mixes in the group#6 is shown in Figure 6-20.

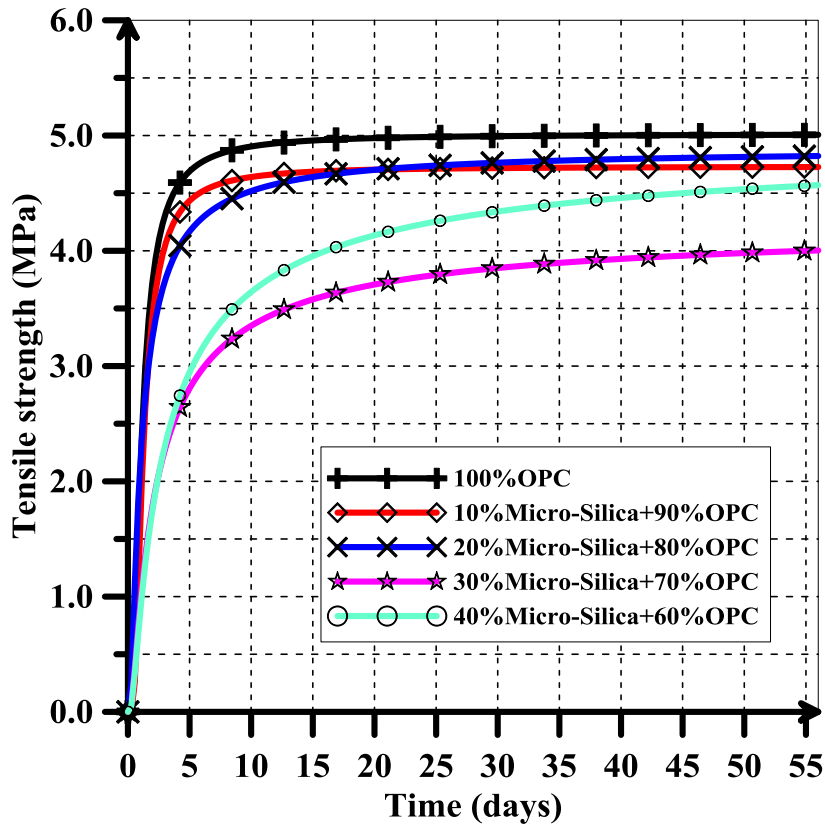


**Figure 6-20: Development of Tensile Strength with Time for the Mixes in Group#6**

Figure 6-20 shows that there is a decrease in the tensile strength development with an increase of replacement percentage of Micro-Silica at early age. At later ages, the development of tensile strength for the mix with 40% Micro-Silica is higher than the tensile strength of the mix with 30% of Micro-Silica.

In the group#7, the effect of w/cm ratio in the tensile strength was investigated. The development of tensile strength with time for the mixes in the group# 7 is shown in Figure 6-21.

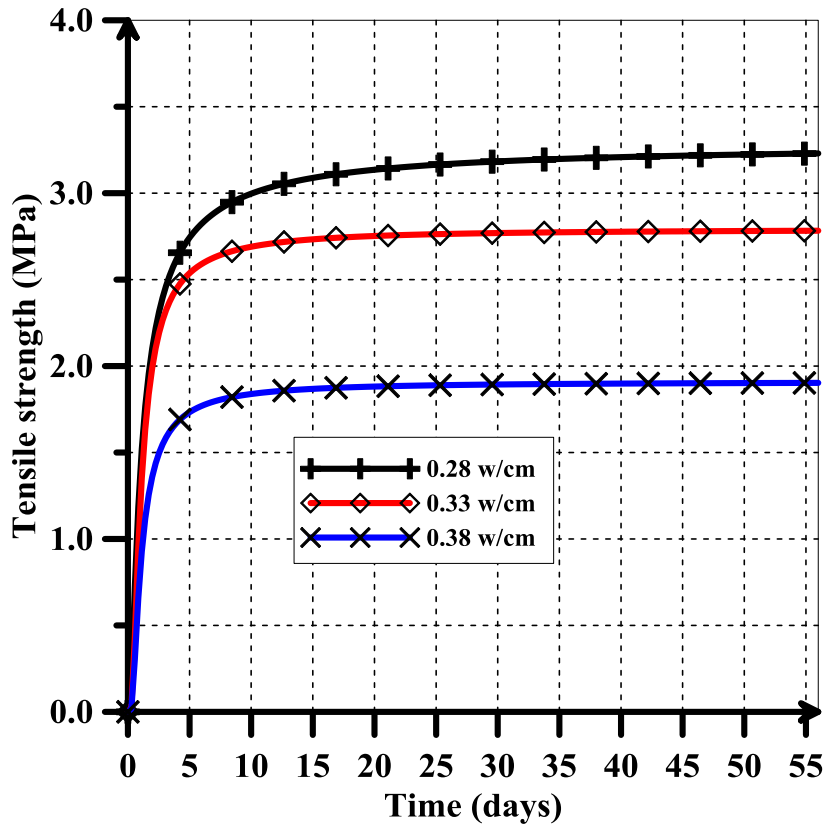


**Figure 6-21: Development of Tensile Strength with Time for the Mixes in Group#7**

Figure 6-21 shows the effect of varying the w/cm from 0.28 to 0.33 on the tensile strength of concrete. As the water cementitious material (w/cm) ratio increases, the tensile strength of concrete decreases. A higher water/cement ratio decreases the gel/space ratio increasing the porosity thereby decreasing the tensile strength of concrete.

Figure 6-22 shows the change of tensile strength with time for the concrete mixes investigated in the group#8. The tensile strength for the reference mix is significantly higher as compared to other mixes. The tensile strength is significantly reduced with an increase in Class F fly ash replacement level. At early ages fly ash content does not have a significant effect on tensile strength, however, at later ages the effect is more noticeable. It is also observed that the tensile strength for flowing concrete is higher than that of self-compacting and normal concrete. At 40% fly ash replacement, the development of tensile strength for flowing concrete is substantially higher.

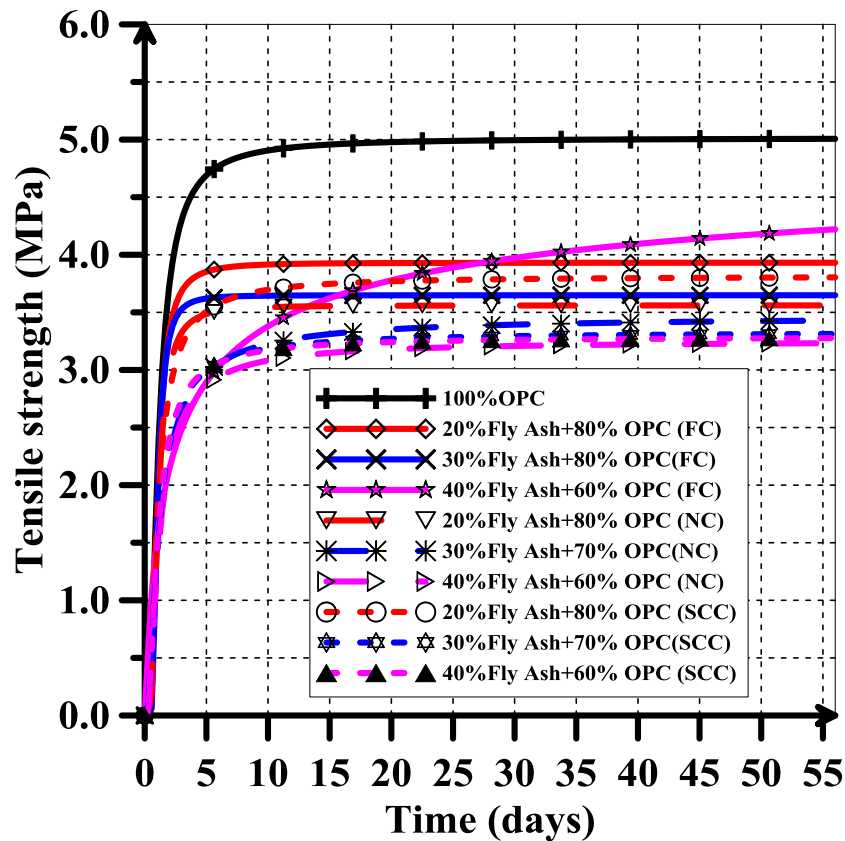


**Figure 6-22: Development of Tensile Strength with Time for the Mixes in Group#8**

In the group #9, the effect of high content of cement in concrete mixtures has been investigated. Three different contents of cement (480, 700 and 900 kg/m<sup>3</sup>) with constant water cement ratio (0.28) were considered. The difference in tensile strength between the three mixes is shown in Figure 6-23. When the cement content increases, the tensile strength decreases.

The maximum limit of cement content in the concrete may also have to be specified. This is because concrete mixes having high cement content may give rise to shrinkage, cracking and creep of concrete. In mass concrete structures, high cement content may give rise to excessive cracking caused by differential thermal stresses due to hydration of cement in young concretes.

This decrease is also probably occurred due to the reduction in aggregate content in the concrete mix. The increase in the cement content doesn't necessarily leads to an increase

of mechanical properties of concrete. The effect of aggregate in gaining strength is significant.

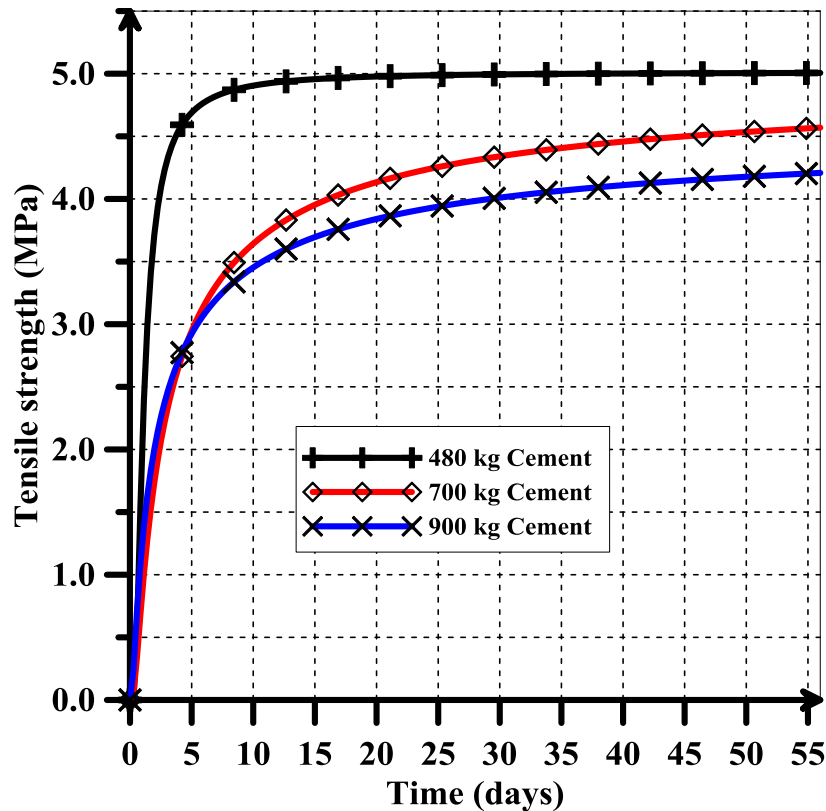


**Figure 6-23: Development of Tensile Strength with Time for the Mixes in Group#9**

In the group #10, the effect of steel and Polypropylene fibers in the development of tensile strength was investigated. The mixes proportions of the concrete mixes of Group#10 are shown in Table 3-10. The change of tensile strength with time for the mixes in group#10 is shown in Figure 6-24.

At early ages (about 2 days from casting), the tensile strength of the mixes with steel or polypropylene fibers are less than that of the mix without fibers. At 7 days age, the mixes with steel or polypropylene fibers significantly have higher tensile strength than that of control mix. At later ages, the steel and polypropylene fibers significantly increase the tensile strength as shown in Figure 6-24.

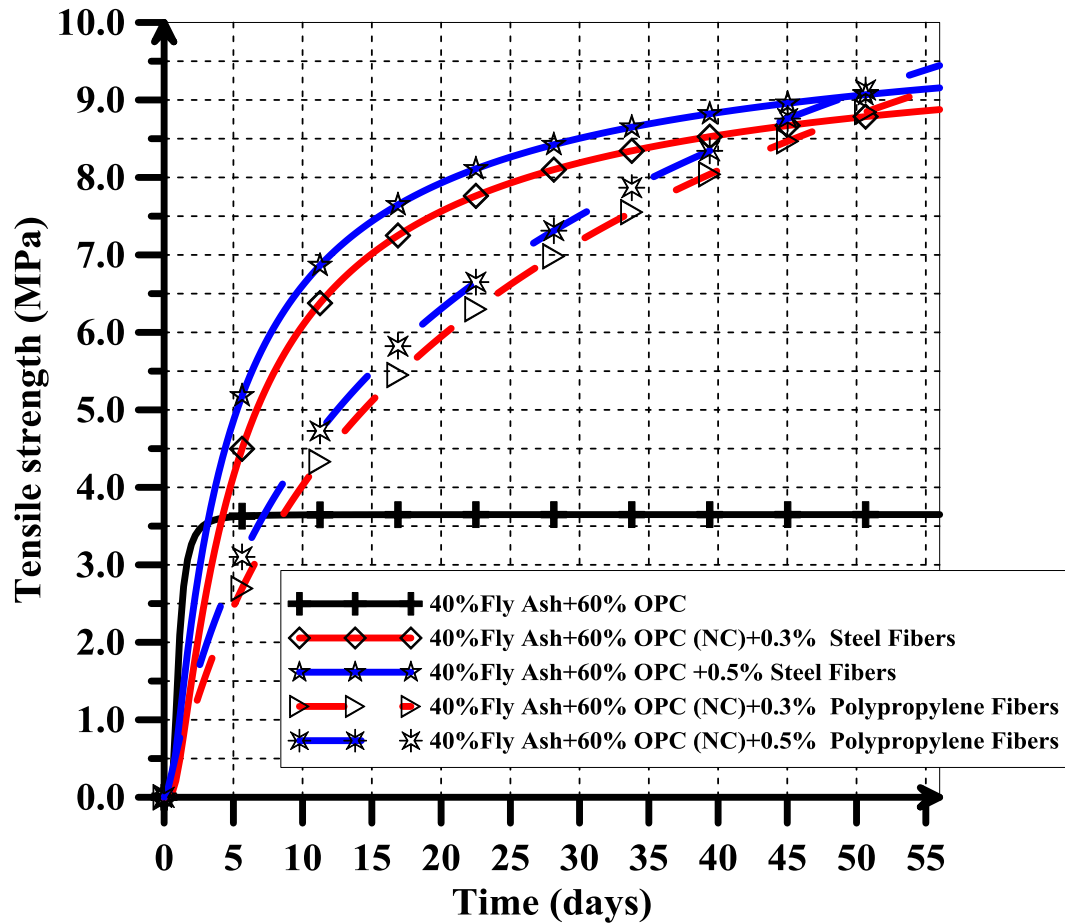


**Figure 6-24: Development of Tensile Strength with Time for the Mixes in Group#10**

#### 6.1.1.3 Results of Modulus of Elasticity

The modulus of elasticity has been determined for all mixes at ages 2, 4, 7, 28, and 56 days. The development of modulus of elasticity with time for the mixes of group#1 is shown in Figure 6-25. It is noticed from Figure 6-25 that the development of modulus of elasticity for the control mix (OPC) is the highest when it compared with other mixes in the group. The modulus of elasticity decreases with an increase of the Fly Ash replacement percentage. The Fly Ash has a significant effect in reducing the modulus of elasticity of concrete.

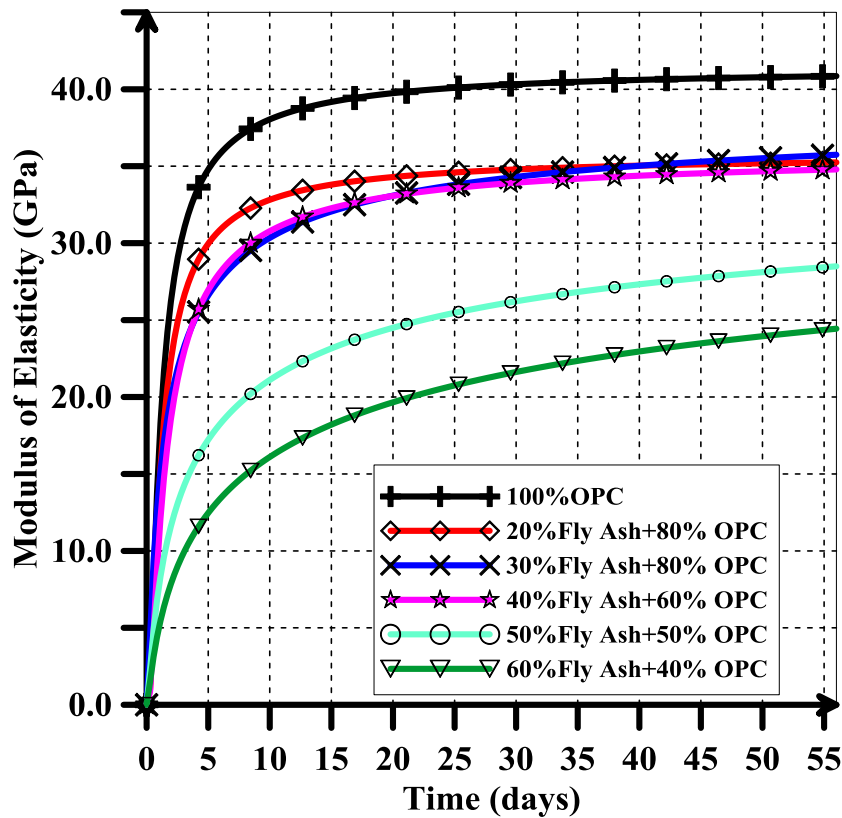


**Figure 6-25: Development of Modulus of Elasticity with Time for the Mixes in Group#1**

No general rule can be drawn for the effect of replacing cement with GGBFS in the modulus of elasticity. Replacing cement with different percentages of GGBFS causes fluctuations in the development of elasticity modulus. The development of modulus of elasticity with time for the mixes of group#2 is shown in Figure 6-26. It can be noticed from Figure 6-26 that the developments of modulus of elasticity with time for the mixes of 100% OPC, and 30% replacement percentages of GGBFS are very close. Even if the replacement percentage of GGBFS reaches 70%, the modulus of elasticity remains high.

In the group#3, the Portland cement is replaced with equal different percentages of Fly Ash and GGBFS (20% (10%FA+10GGBFS), 30%, 40%, 50%, and 60%).



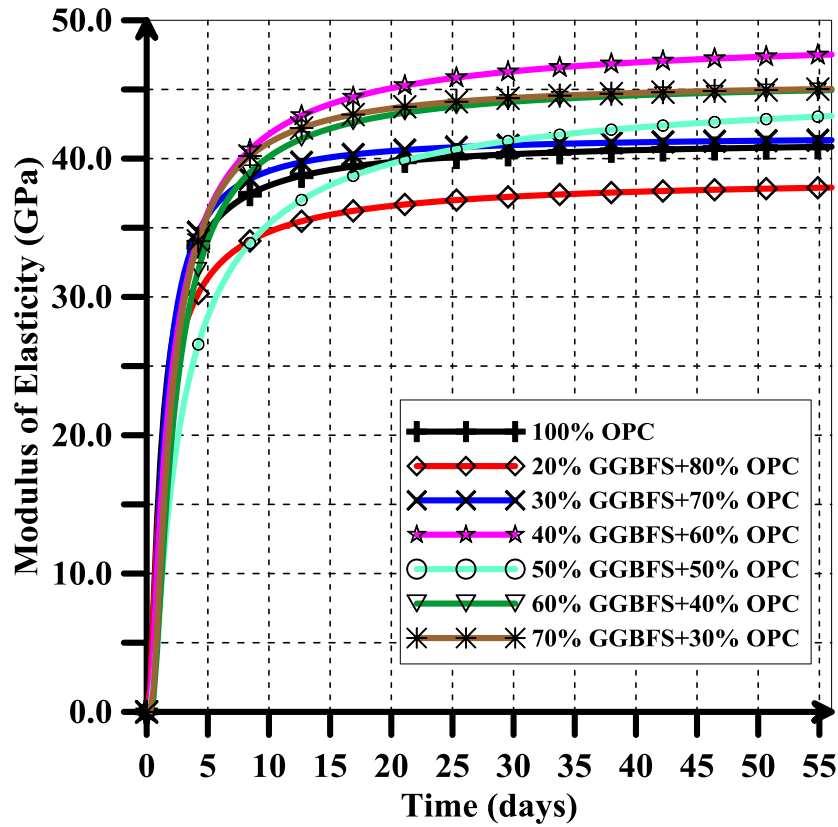


**Figure 6-26: Development of Modulus of Elasticity with Time for the Mixes in Group#2**

The development of modulus of elasticity with time for the mixes in the group#3 is shown in Figure 6-27. At early ages (1 to 7 days), the increase in the replacement percentage of Fly ash and GGBFS leads to the decrease in the development of modulus of elasticity as shown in Figure 6-27. At later ages, the development of modulus of elasticity with time for the mixes of 30% , 40% ,50, and 60% replacement percentage of Fly Ash and GGBFS is increasing rapidly more than that of mixes with 100% OPC and 20% Fly Ash and GGBFS.

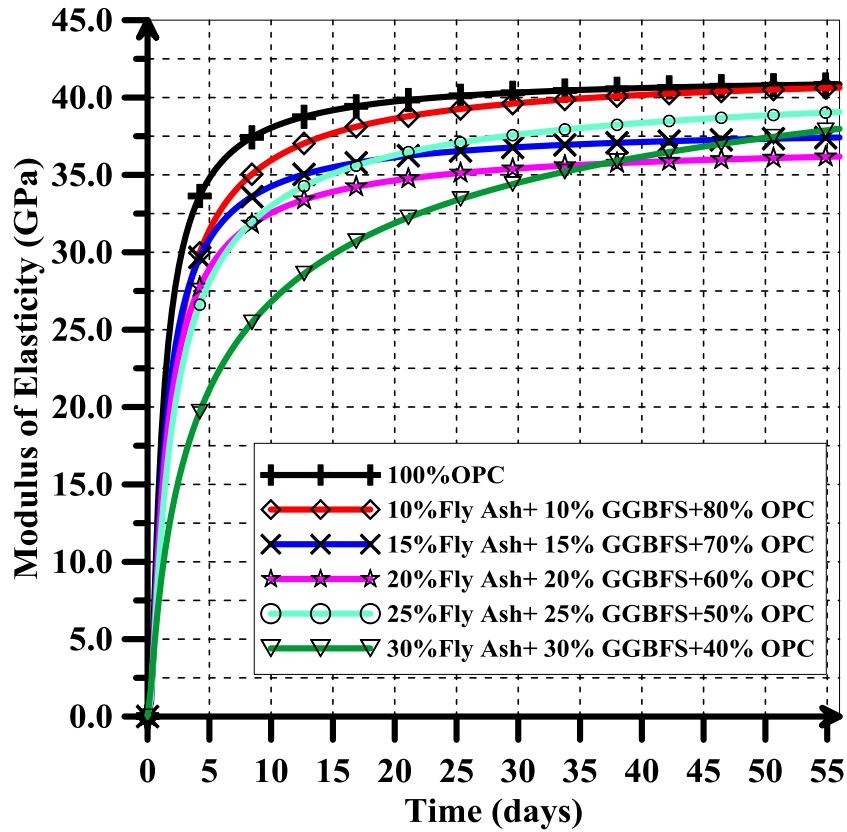


**Figure 6-27: Development of Modulus of Elasticity with Time for the Mixes in Group#3**

In the fourth group, the total cementitious materials content is  $350 \text{ kg/m}^3$  and the water/binder ratio is 0.38. Portland cement is replaced with different percentages (20%, 30%, 40%, and 50%) of Fly Ash.

The development of tensile strength with time for the mixtures in the group# 4 is shown in Figure 6-28.

The Figure 6-28 shows that the modulus of elasticity of control mix (100% OPC) is the highest when it compared with other mixes in the group#4. The modulus of elasticity decreases with an increase of the Fly Ash replacement percentage.

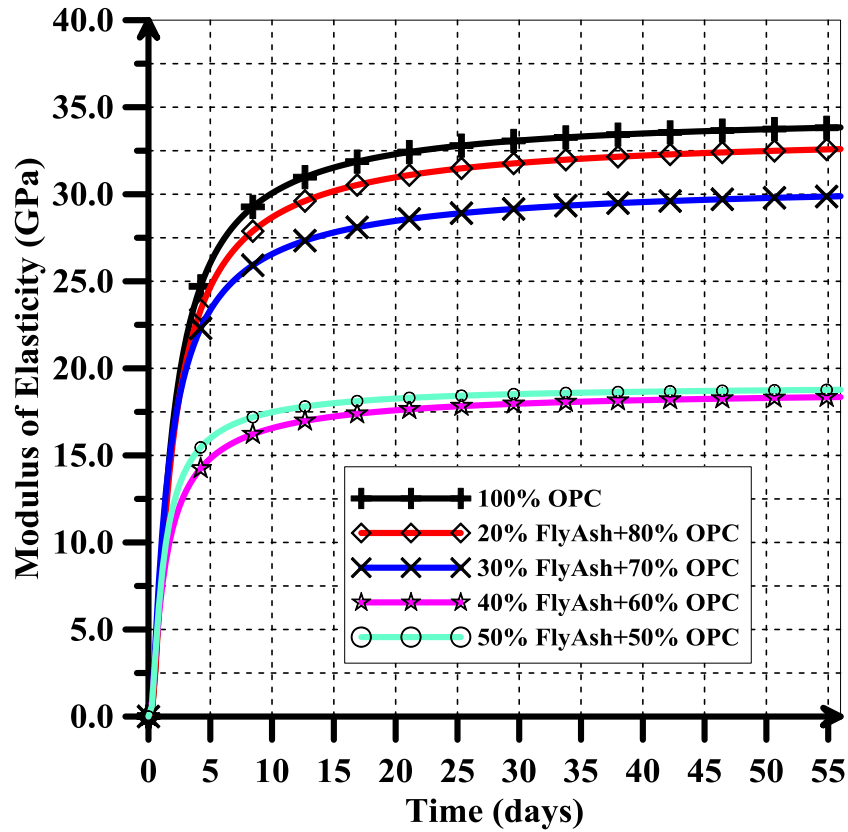


**Figure 6-28: Development of Modulus of Elasticity with Time for the Mixes in Group#4**

In the fifth group, the total cementitious materials content is  $350 \text{ kg/m}^3$  and the water/binder ratio is 0.38. Portland cement is replaced with different percentages (20%, 30%, 40%, and 50%) of GGBFS. The development of modulus of elasticity with time for the mixtures of the group# 5 is shown in Figure 6-29.

Replacing cement with different percentages of GGBFS causes fluctuations in the development of elasticity modulus. It can be noticed from Figure 6-29 that the developments of modulus of elasticity with time for the mixes of 20%, 40% and 50% replacement percentages of GGBFS are very close.

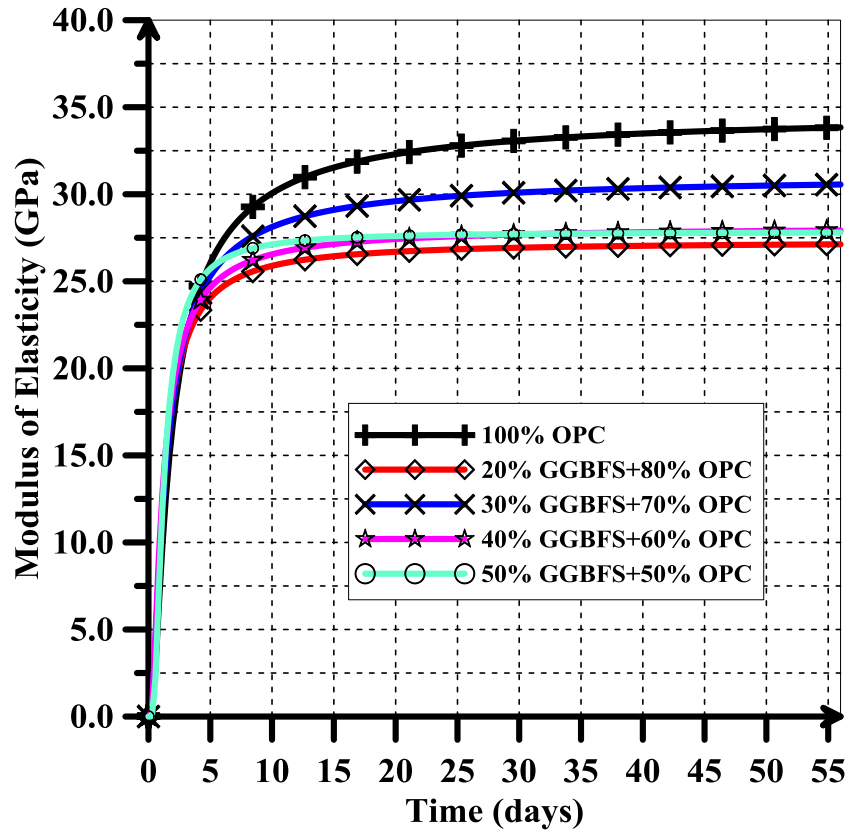


**Figure 6-29: Development of Modulus of Elasticity with Time for the Mixes in Group#5**

In the Sixth group, the total cementitious materials content is  $480 \text{ kg/m}^3$  and the water/binder ratio is 0.28. Portland cement is replaced with different percentages (10%, 20%, 30%, and 40%) of Micro-Silica.

The change of modulus of elasticity with time for the mixes in the group#6 is shown in Figure 6-30. Figure 6-30 shows that the modulus of elasticity for the mixes with 10% and 20% of Micro-Silica is slightly larger compared to the mix without Micro-Silica (100% OPC). Replacing cement with 30% and 40% Micro-Silica leads to a decrease in the modulus of elasticity, compared to the mix without Micro-Silica (100% OPC).

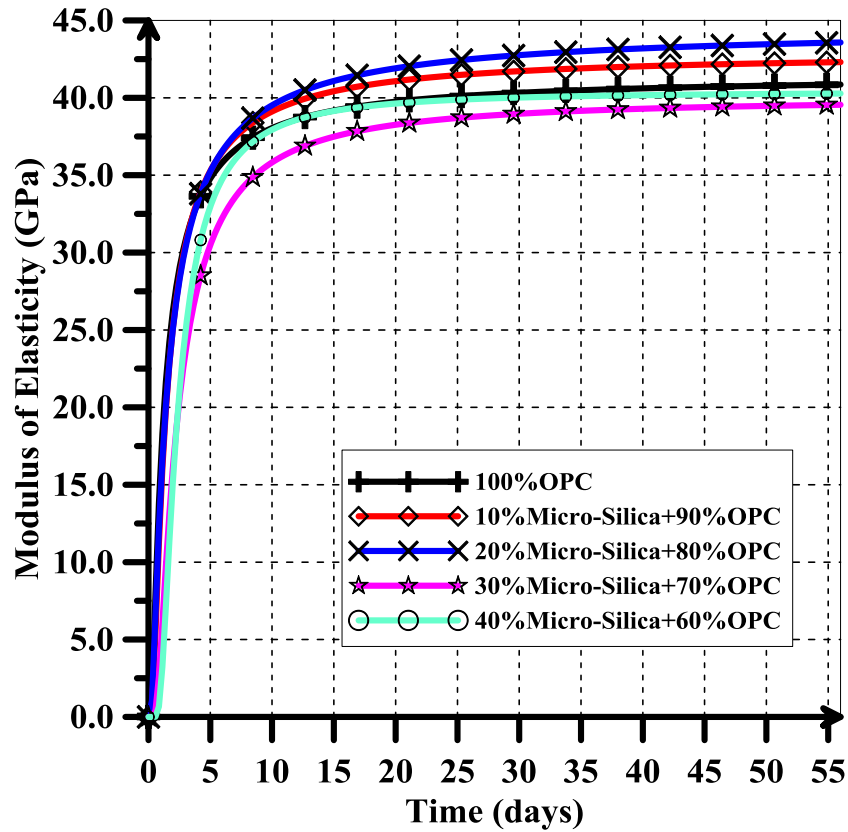


**Figure 6-30: Development of Modulus of Elasticity with Time for the Mixes in the Group#6**

The development of modulus of elasticity with time for the mixes in the group# 7 is shown in Figure 6-31. As the water cementitious material (w/cm) ratio increases, the modulus of elasticity decreases as shown in Figure 6-31.

Figure 6-32 shows the change of modulus of elasticity with time for all concrete mixes investigated in the group#8. The modulus of elasticity for the reference mix (100% OPC) is significantly higher as compared to other mixes. The modulus of elasticity is reduced with an increase in Class F fly ash replacement level.

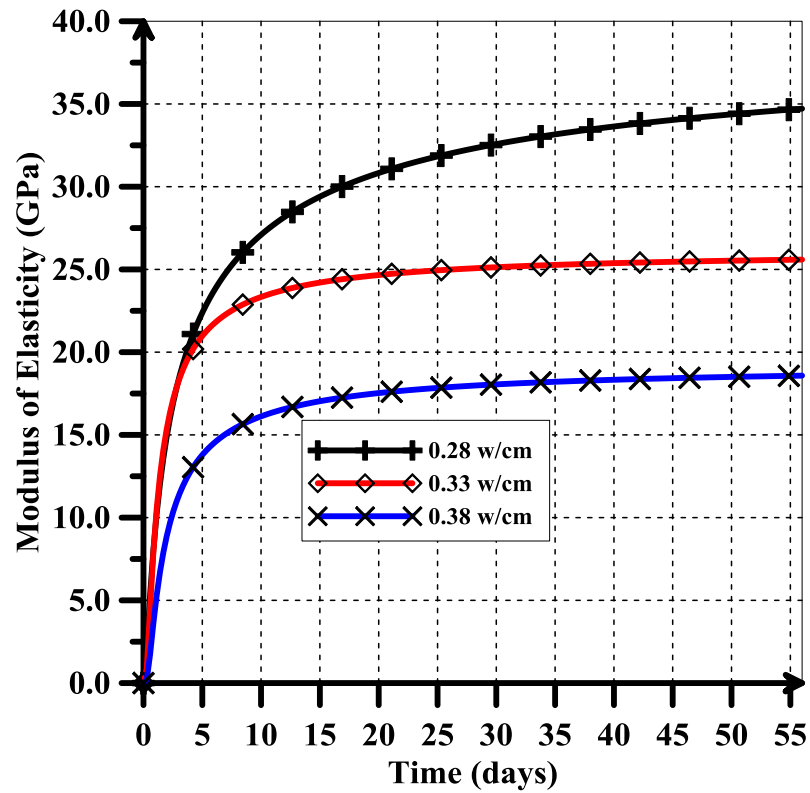


Figure 6-31: Development of Modulus of Elasticity with Time for the Mixes in the Group#7

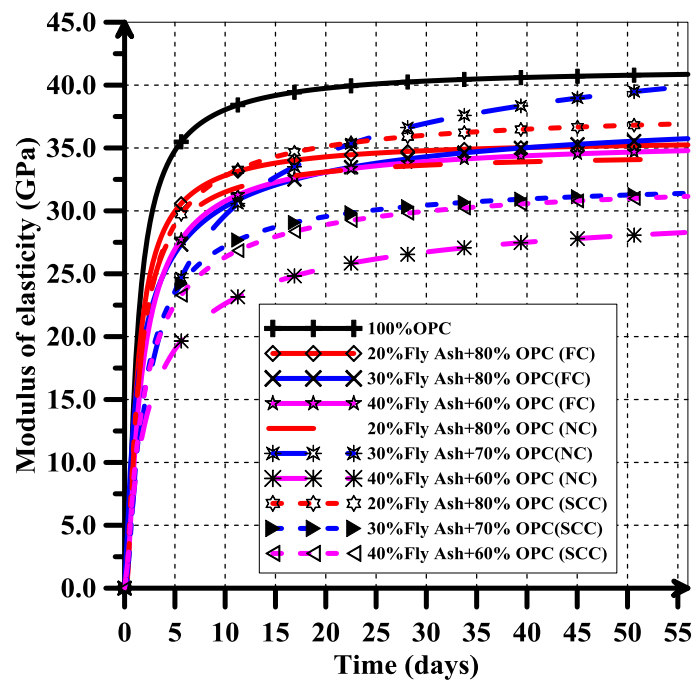


Figure 6-32: Development of Modulus of Elasticity with Time for the Mixes in the Group#8

It is also observed that at 20% fly ash replacement, there is no significant difference between flowing, self-compacting and normal concrete. At 40% fly ash replacement, the modulus of elasticity for flowing concrete is higher than that of self-compacting and normal concrete.

In the group #9, the effect of high content of cement in concrete mixtures has been investigated. Three different contents of cement (480, 700 and 900 kg/m<sup>3</sup>) with constant water cement ratio (0.28) were considered. The difference in modulus of elasticity between the three mixes is shown in Figure 6-33.

As the cement content increases, the modulus of elasticity decreases. This is because concrete mixes having high cement content may give rise to shrinkage, cracking and creep of concrete also increases with the cement paste content. This decrease is also probably occurred due to the reduction in aggregate content in the concrete mix. The increase in the cement content doesn't necessarily leads to an increase of mechanical properties of concrete.

In the group #10, the effect of steel and Polypropylene fibers in the development of modulus of elasticity was investigated. The mixes proportions of the concrete mixes of Group#10 are shown in Table 3-10 .The change of modulus of elasticity with time for the mixes in group#10 is shown in Figure 6-34.

At early ages (from 1 day to 14 days), the modulus of elasticity of the mixes with steel or polypropylene fibers are less than that of the mix without fibers. At later ages, the mix with 0.5% steel fibers has the largest increase in modulus of elasticity whereas the modulus of elasticity of the mixes with polypropylene fibers or with 0.3% steel fibers remains less than that of the mix without fibers as shown in Figure 6-34.

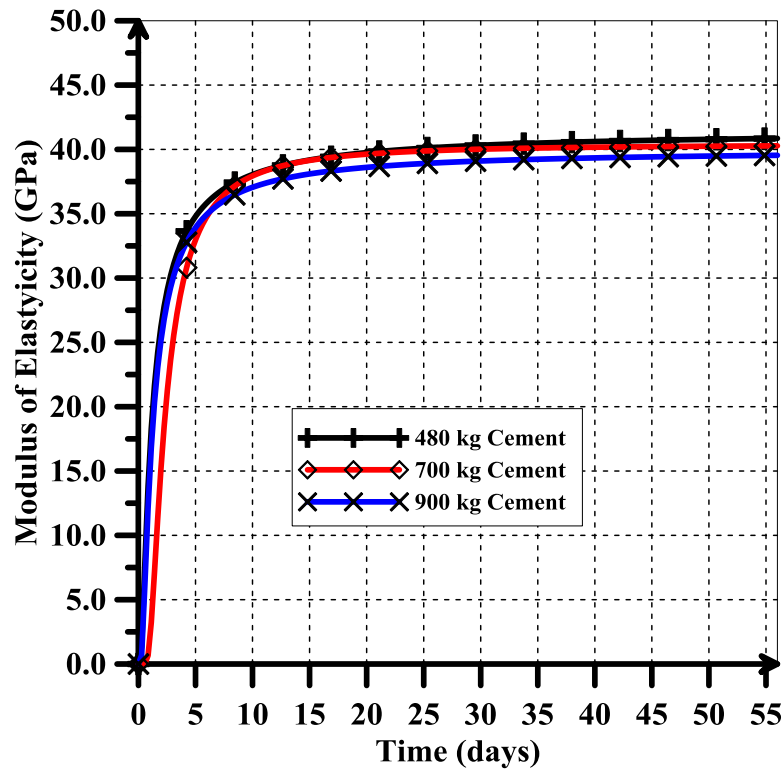


Figure 6-33: Development of Modulus of Elasticity with Time for the Mixes in the Group#9

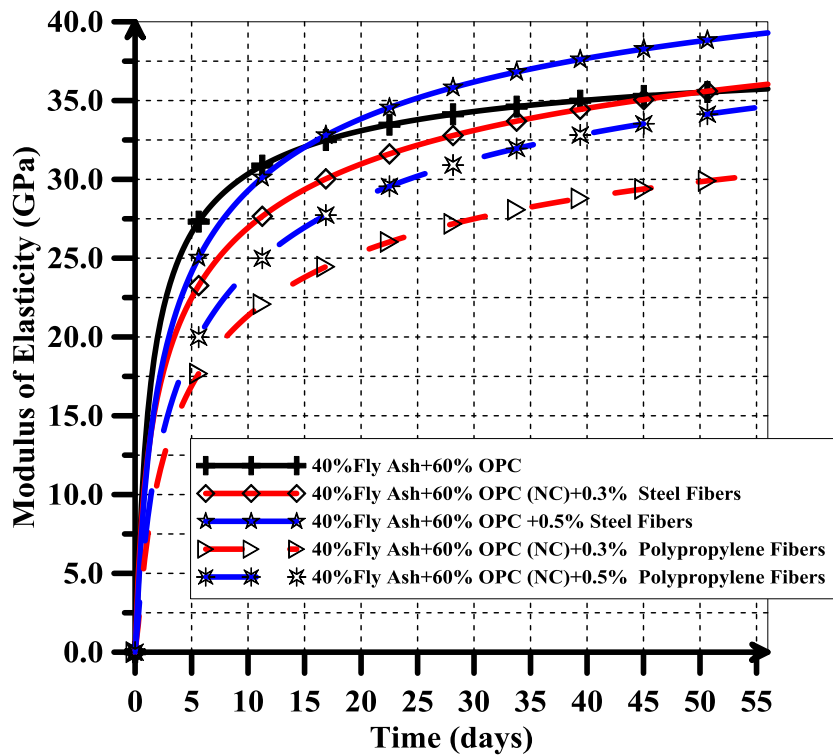
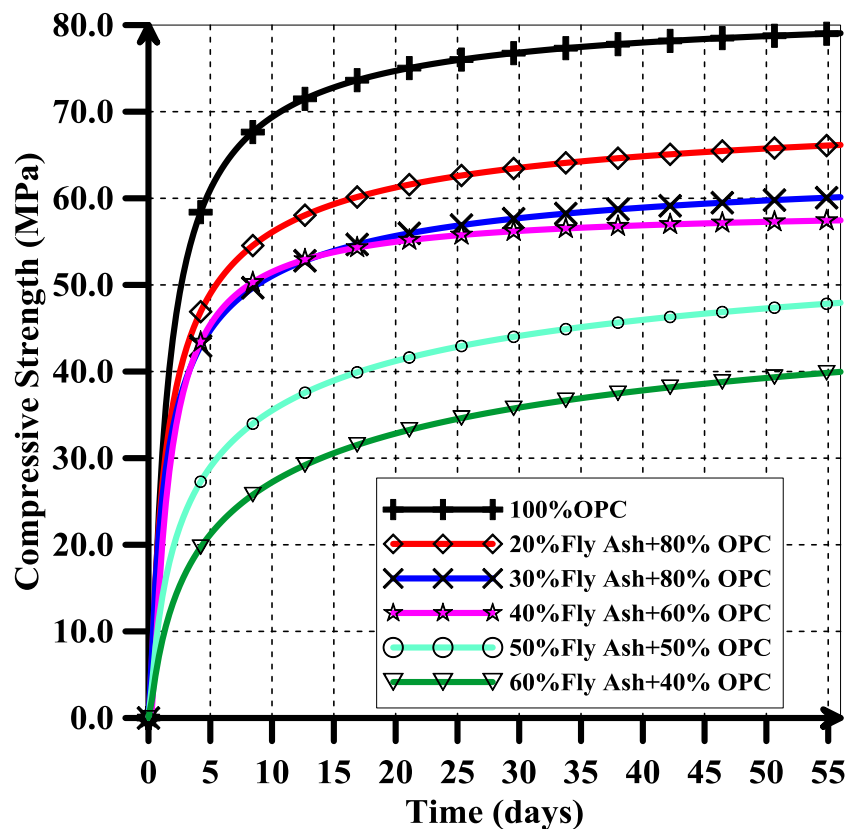


Figure 6-34: Development of Modulus of Elasticity with Time for the Mixes in the Group#10



#### 6.1.1.4 Results of Compressive Strength

The compressive strength has been determined for all mixes at ages 2, 4, 7, 28, and 56 days. The development of compressive strength with time for the mixes of group#1 is shown in Figure 6-35. It is noticed from Figure 6-35 that the development of compressive strength for the control mix (OPC) is the highest when it compared with other mixes in the group. The compressive strength decreases with an increase of the Fly Ash replacement percentage. The fly ash has a significant effect in reducing the concrete compressive strength.



**Figure 6-35: Development of Compressive Strength with Time for the Mixes in the Group#1**

Replacing cement with different percentages of GGBFS causes fluctuations in the development of compressive strength. The compressive strength development with time for the mixes of group#2 is shown in Figure 6-36. It can be noticed from Figure 6-36 that

the compressive strength development with time for the mixes of 30% 40% and 70% replacement percentages of GGBFS are higher than the mix with 100% OPC. The compressive strength development for the mixes with 20% and 60% replacement of GGBFS is very close. Even if the replacement percentage of GGBFS reaches 70%, the compressive strength remains high.

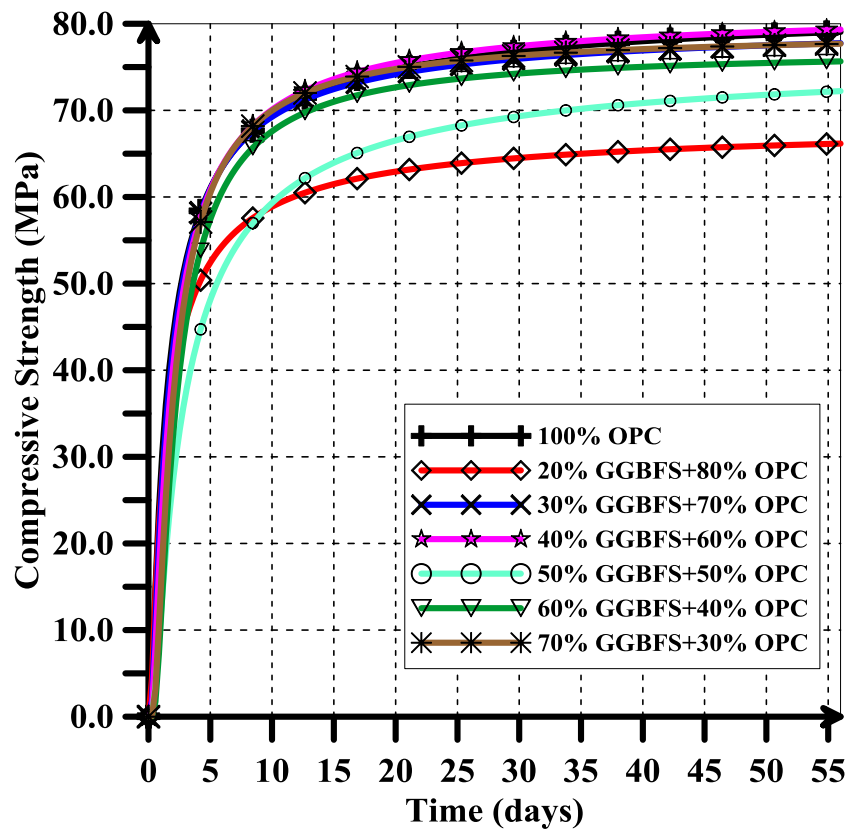


**Figure 6-36: Development of Compressive Strength with Time for the Mixes in the Group#2**

The development of compressive strength with time for the mixes in the group#3 is shown in Figure 6-37. Increasing the replacement percentage of Fly ash and GGBFS leads to decreased in the development of compressive strength as shown in Figure 6-37. The mix with 60% (30% GGBFS+30% Fly Ash) replacement percentage has the lowest compressive strength in the group#3.

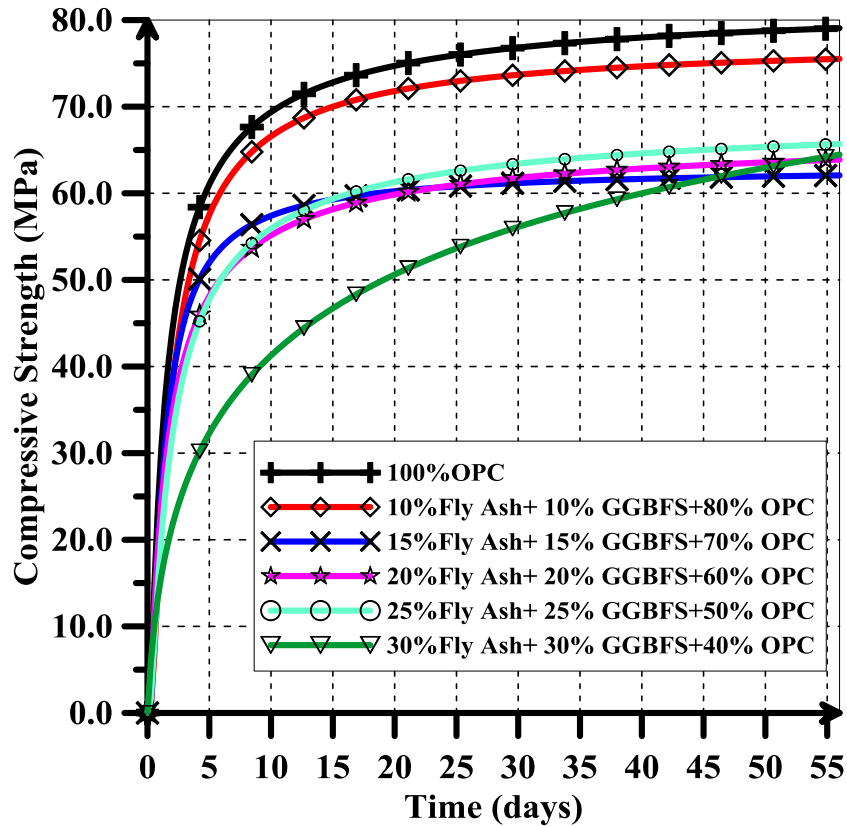


**Figure 6-37: Development of Compressive Strength with Time for the Mixes in the Group#3**

In the fourth group, the total cementitious materials content is  $350 \text{ kg/m}^3$  and the water/binder ratio is 0.38. Portland cement is replaced with different percentages (20%, 30%, 40%, and 50%) of Fly Ash.

The development of compressive strength with time for the mixtures in the group# 4 is shown in Figure 6-38. The Figure 6-38 shows that the compressive strength of control mix (100% OPC) is the highest when it compared with other mixes in the group#4. The compressive strength decreases with an increase of the Fly Ash replacement percentage.

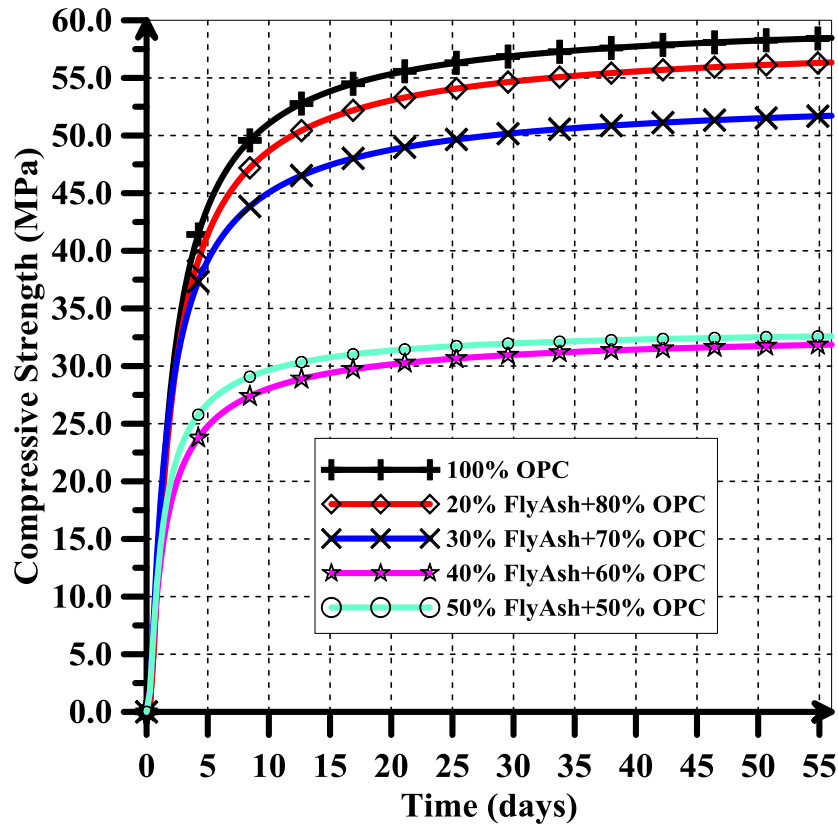


**Figure 6-38: Development of Compressive Strength with Time for the Mixes in the Group#4**

In the fifth group, the total cementitious materials content is  $350 \text{ kg/m}^3$  and the water/binder ratio is 0.38. Portland cement is replaced with different percentages (20%, 30%, 40%, and 50%) of GGBFS. The development of compressive strength with time for the mixtures of the group# 5 is shown in Figure 6-39.

Replacing cement with different percentages of GGBFS causes fluctuations in the development of compressive strength. It can be noticed from Figure 6-39 that the mix with 100% OPC has the highest compressive strength. The developments of compressive strength with time for the mixes of 20%, 40% and 50% replacement percentages of GGBFS are very close.

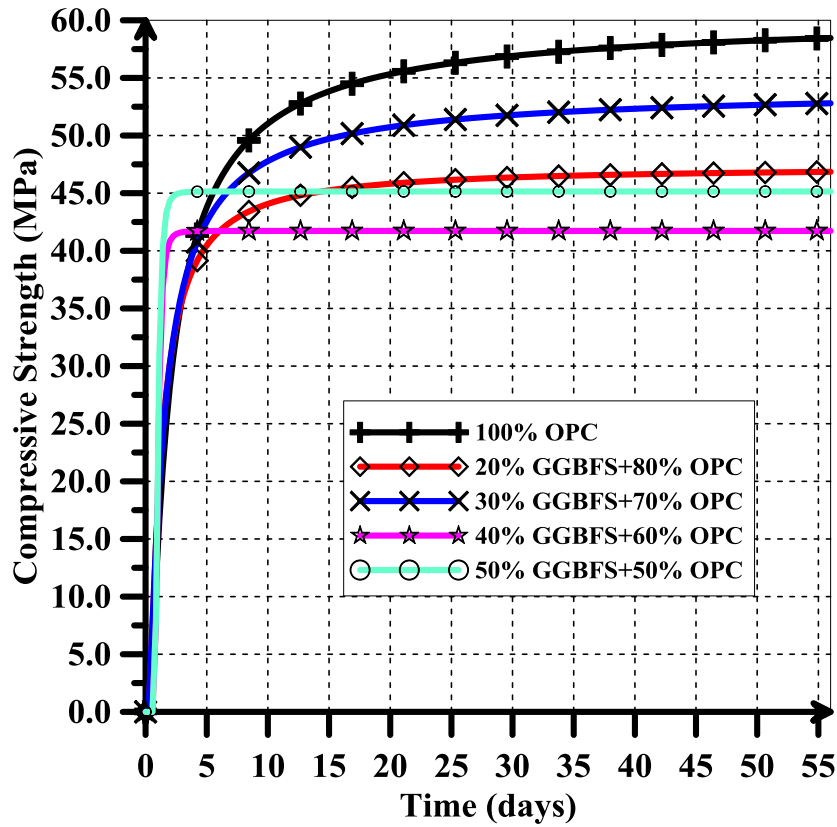


**Figure 6-39: Development of Compressive Strength with Time for the Mixes in the Group#5**

In the Sixth group, the total cementitious materials content is  $480 \text{ kg/m}^3$  and the water/binder ratio is 0.28. Portland cement is replaced with different percentages (10%, 20%, 30%, and 40%) of Micro-Silica.

The change of compressive strength with time for the mixes in the group#6 is shown in Figure 6-40. Figure 6-40 shows that the compressive strength development for the mix with 10% Micro-Silica replacement is slightly larger than the mix without Micro-Silica (100% OPC). Replacing cement with 20%, 30% and 40% Micro-Silica leads to a decrease in the compressive strength, compared to the mix without Micro-Silica (100% OPC).

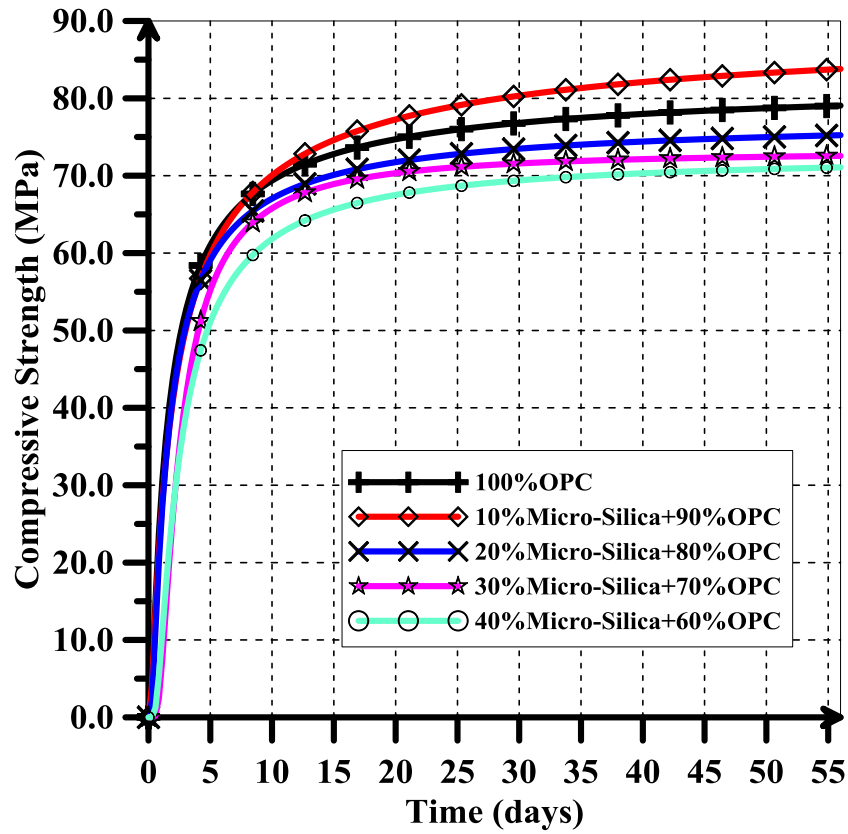


**Figure 6-40: Development of Compressive Strength with Time for the Mixes in the Group#6**

The development of compressive strength with time for the mixes in the group# 7 is shown in Figure 6-41. As the water cementitious material (w/cm) ratio increases, the compressive strength decreases as shown in Figure 6-41.

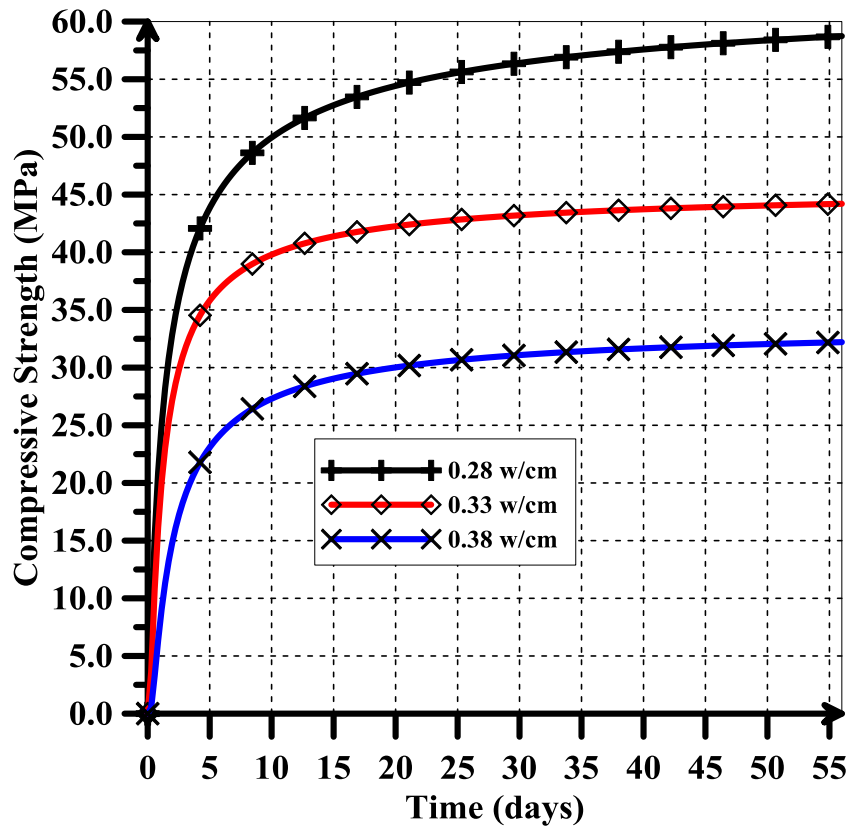


**Figure 6-41: Development of Compressive Strength with Time for the Mixes in the Group#7**

Figure 6-42 shows the change of compressive strength with time for all concrete mixes investigated in the group#8. The compressive strength for the reference mix (100% OPC) is significantly higher as compared to other mixes. The compressive strength is reduced with an increase in Class F fly ash replacement level. The development of compressive strength with time for flowing concrete is higher than the self-compacting and normal concrete. The normal concrete has lower compressive strength compared to flowing and normal concrete as shown in Figure 6-42.

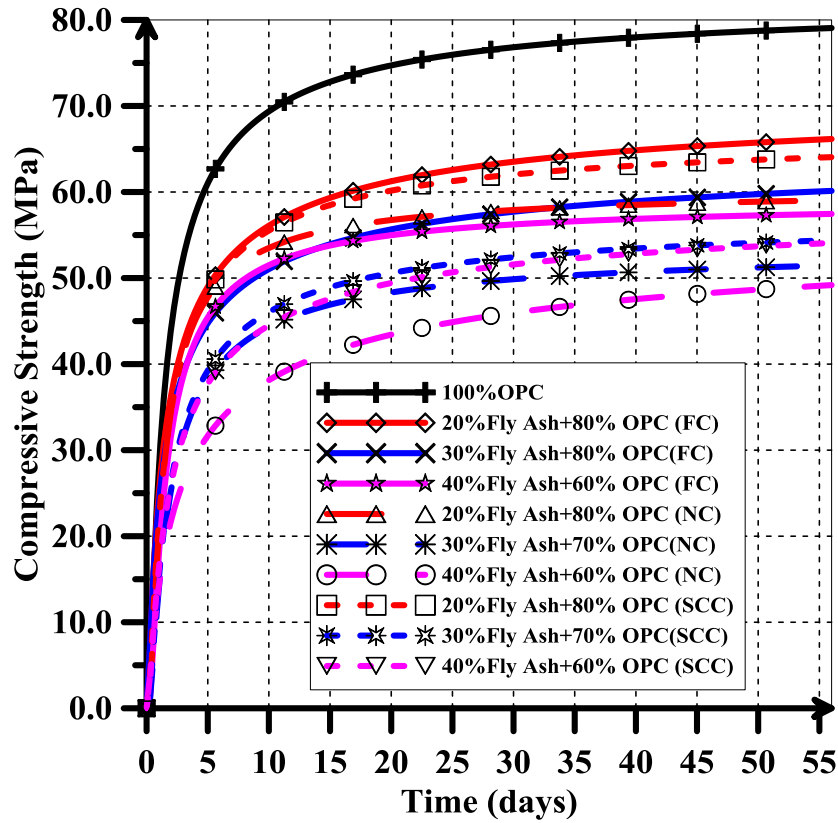


**Figure 6-42: Development of Compressive Strength with Time for the Mixes in the Group#8**

In the group #9, the effect of high content of cement in concrete mixtures has been investigated. Three different contents of cement (480, 700 and 900 kg/m<sup>3</sup>) with constant water cement ratio (0.28) were considered. The difference in the compressive strength development between the three mixes is shown in Figure 6-43.

It is noticed that, as the cement content increases, the compressive strength decrease.

The cause of this decrease is likely occurred due to the reduction in aggregate content in the concrete mix. The increase in the cement content doesn't necessarily leads to an increase of mechanical properties of concrete.



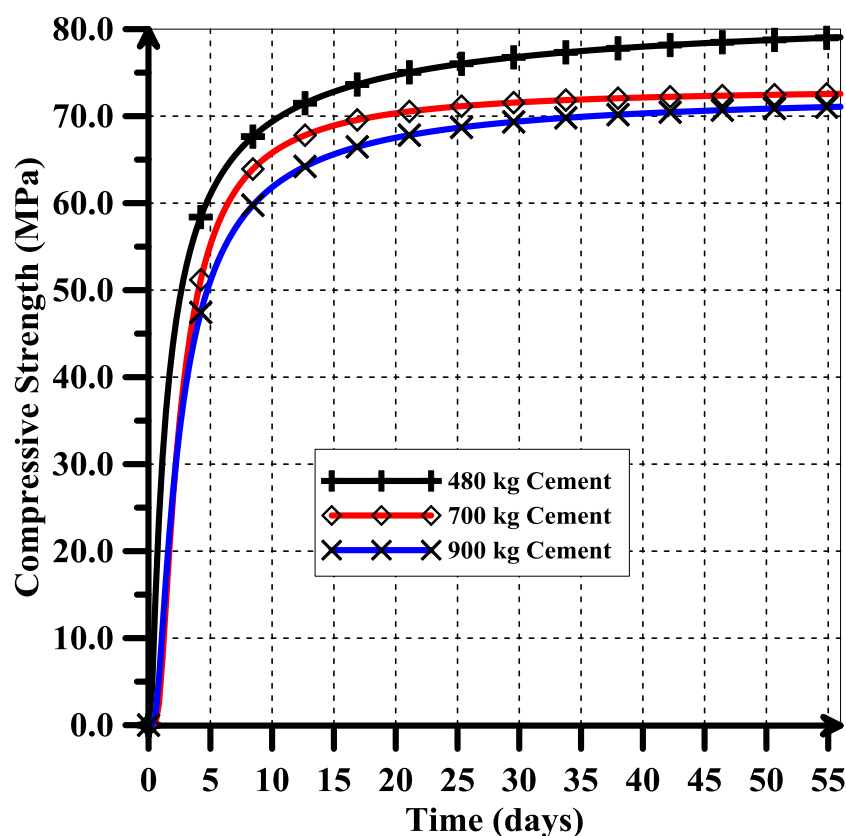


**Figure 6-43: Development of Compressive Strength with Time for the Mixes in the Group#9**

In the group #10, the effect of steel and Polypropylene fibers in the development of compressive strength was investigated. The mixes proportions of the concrete mixes of Group#10 are shown in Table 3-10 .The change of compressive strength with time for the mixes in group#10 is shown in Figure 6-44.

At early ages, the compressive strength of the mixes with steel or polypropylene fibers is less than that of the mix without fibers. At later ages, the mixs with 0.5% and 0.3% steel fibers has the largest increase in compressive strength whereas the modulus of elasticity of the mixes with polypropylene fibers remains less than that of the mix without fibers as shown in Figure 6-44.

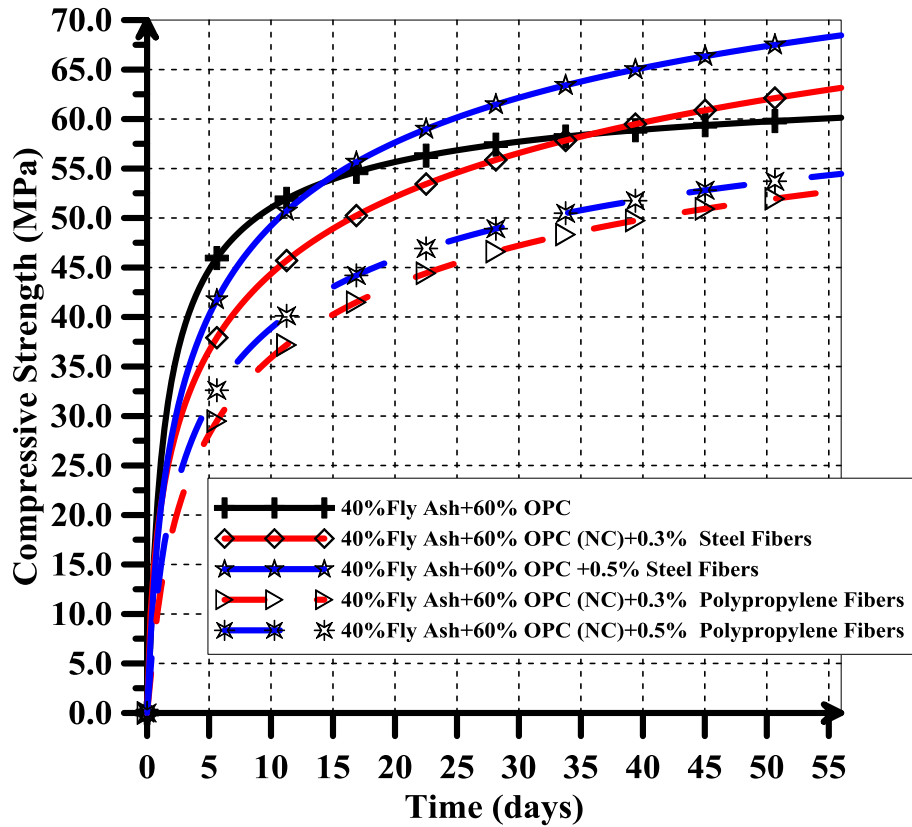


**Figure 6-44: Development of Compressive Strength with Time for the Mixes in the Group#10**

## 6.2 Field Monitoring Results

The temperature rise and strains were monitored for seven mockup specimens. These mockup specimens are divided into three categories (King Fahd University Mock-up Specimens (KMUS), Dammam Mock-up Specimens DMUS, and Jeddah Mock-up Specimens (JDMUS)) depending on their locations.

### 6.2.1 Field Monitoring Results of KMUS

#### 6.2.1.1 Temperature Monitoring Results of KMUS

Three mock-up specimens with dimensions of 2m×2m×2m were cast inside the campus of KFUPM in July 2013. The maximum ambient temperature during the day of concrete placement was 46 °C. The wind velocity was ranging from 3m/s to 6 m/s. The mix with

100% OPC and 0.28 w/c ratio was in the mock-up #1. The results of temperature rise for the six locations in the Mockup #1 are shown in Figure 6-45 to Figure 6-50.

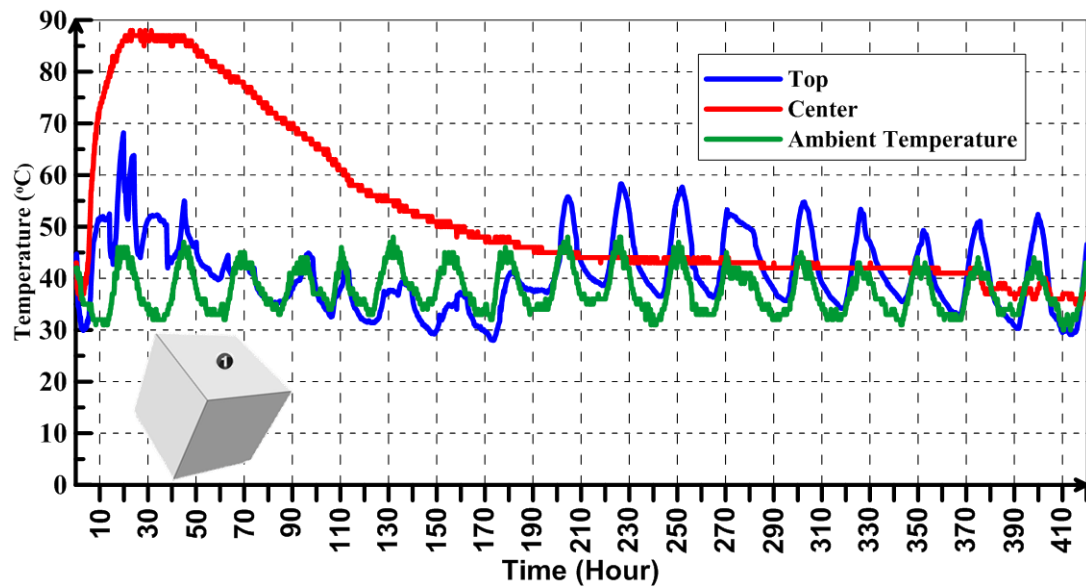


**Figure 6-45: Temperature rise at Location 1 (Top, Center, and Bottom)**

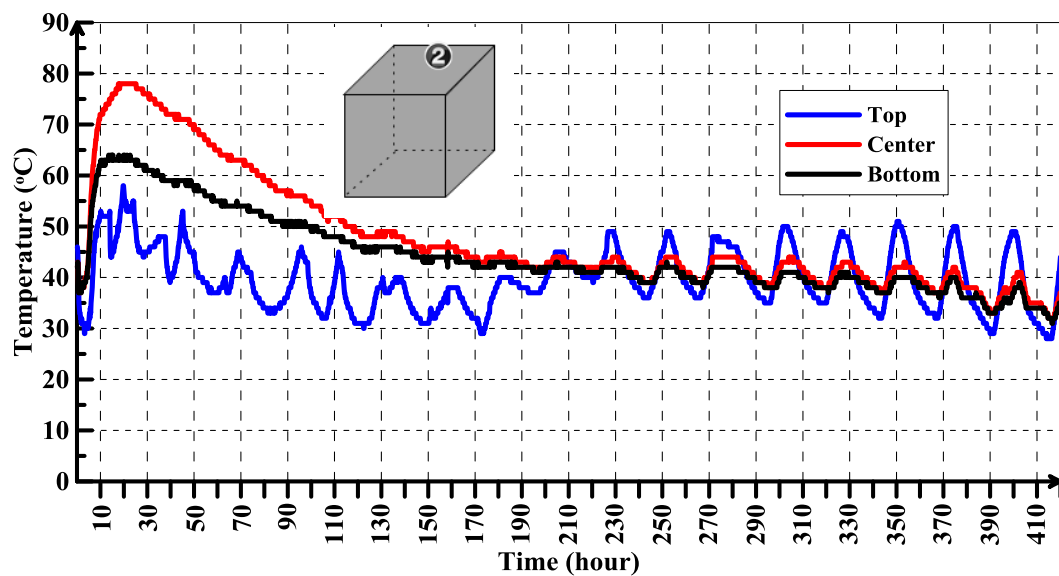


**Figure 6-46: Temperature rise at Location 2 (Top, Center, and Bottom)**

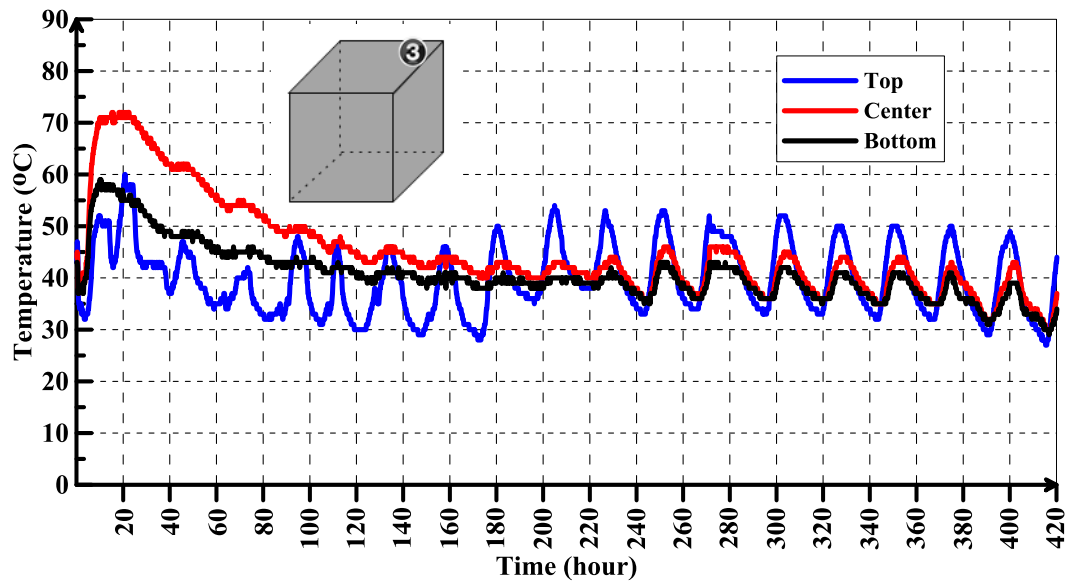


Figure 6-47: Temperature rise at Location 3 (Top, Center, and Bottom)

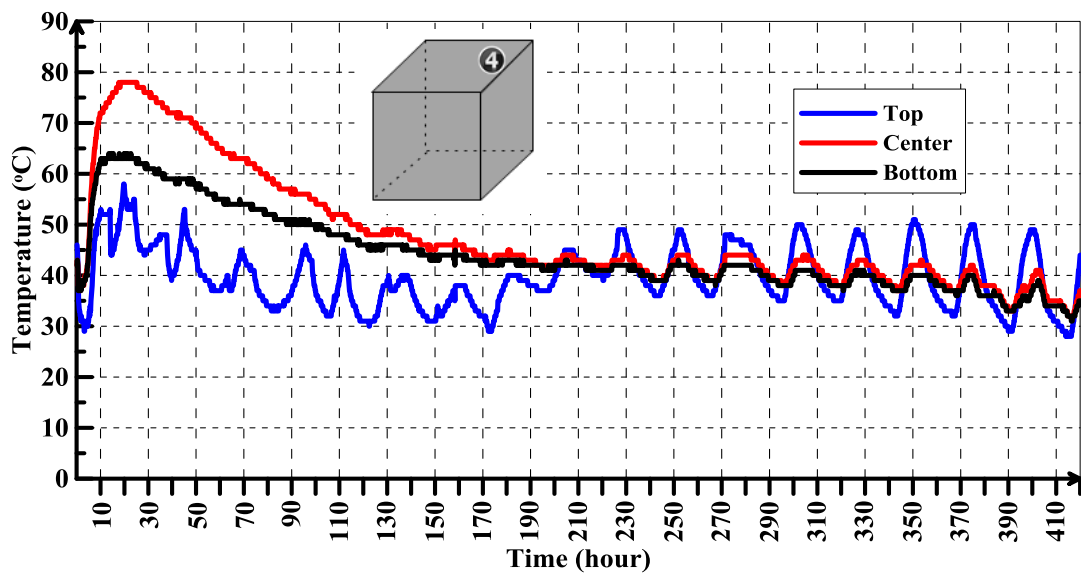
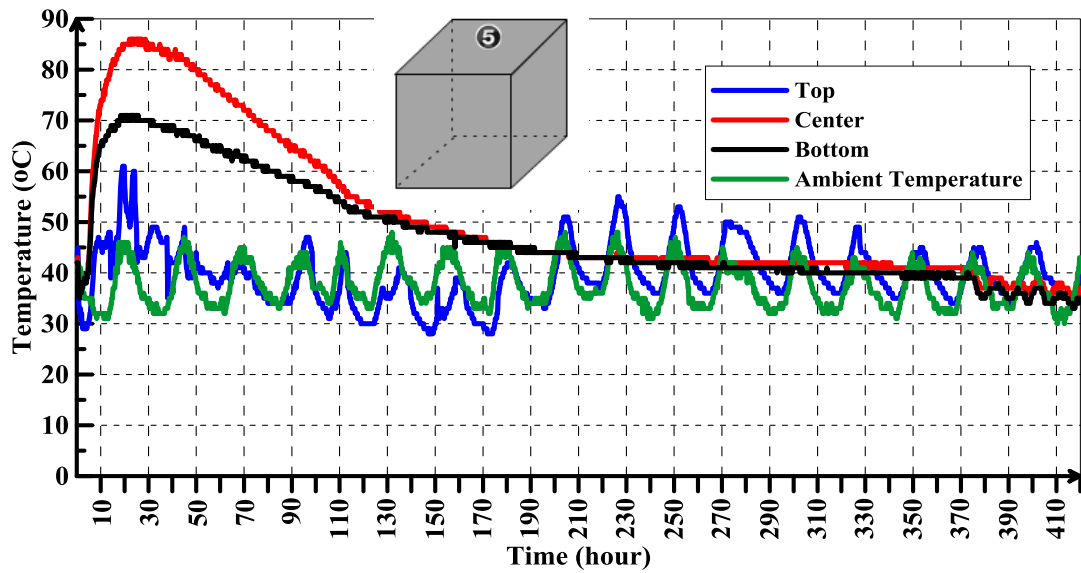
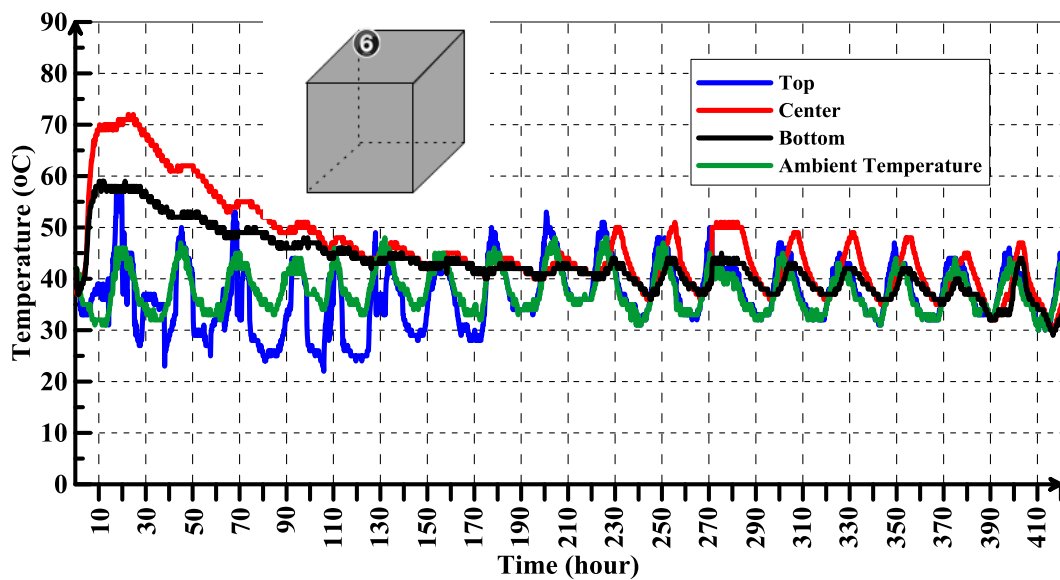


Figure 6-48: Temperature rise at Location 4 (Top, Center, and Bottom)



**Figure 6-49: Temperature rise at Location 5 (Top, Center, and Bottom)**



**Figure 6-50: Temperature rise at Location 6 (Top, Center, and Bottom)**

The peak temperatures recorded and the maximum differences monitored between the center of mock-up#1 and its surface for the six locations are listed in Table 6-2. It can be seen, the highest peak temperature is (88°C) at the core and the maximum temperature difference between the core of mockup#1 and its surface 44 °C.

**Table 6-2: Summary of Peak Temperatures and Max. Differences for the Mock-Up Specimen #1**

Mockup No.	Location No.						
<b>Mockup#1 (100%OPC)</b>		<b>1</b>	<b>2</b>	<b>3</b>	<b>4</b>	<b>5</b>	<b>6</b>
	Peak Temp. (°C)	88	78	72	77	86	72
	Time (Hour)	22.71	17.71	19.04	18.37	22.55	22.55
	Max. difference(°C)	44	33	30	35	43	30
	Time (Hour)	38.24	25.55	15.7	15.36	38.2	15.6

In the Mock-up specimen #2, the cement Type I was replaced with 40% Fly Ash. The total content of cementitious materials was  $480 \text{ kg/m}^3$ . The water cement cementitious materials ratio was 0.28. The results of temperature rise with time for the six locations (Shown in Figure 3-13) are shown in Figure 6-51 to Figure 6-56

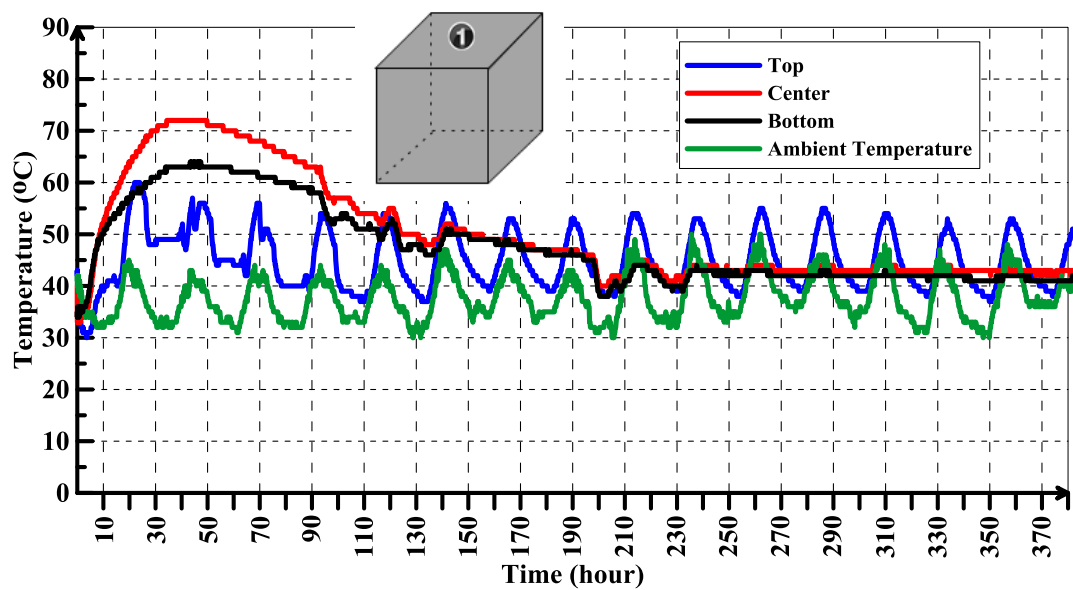


**Figure 6-51: Temperature rise at Location 1 (Top, Center, and Bottom)**

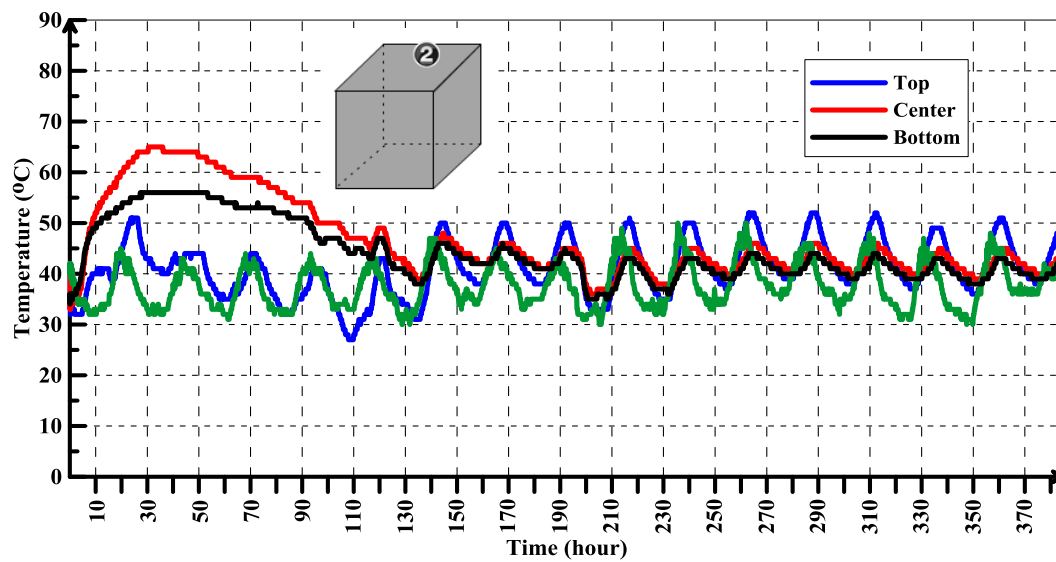


**Figure 6-52: Temperature rise at Location 2 (Top, Center, and Bottom)**

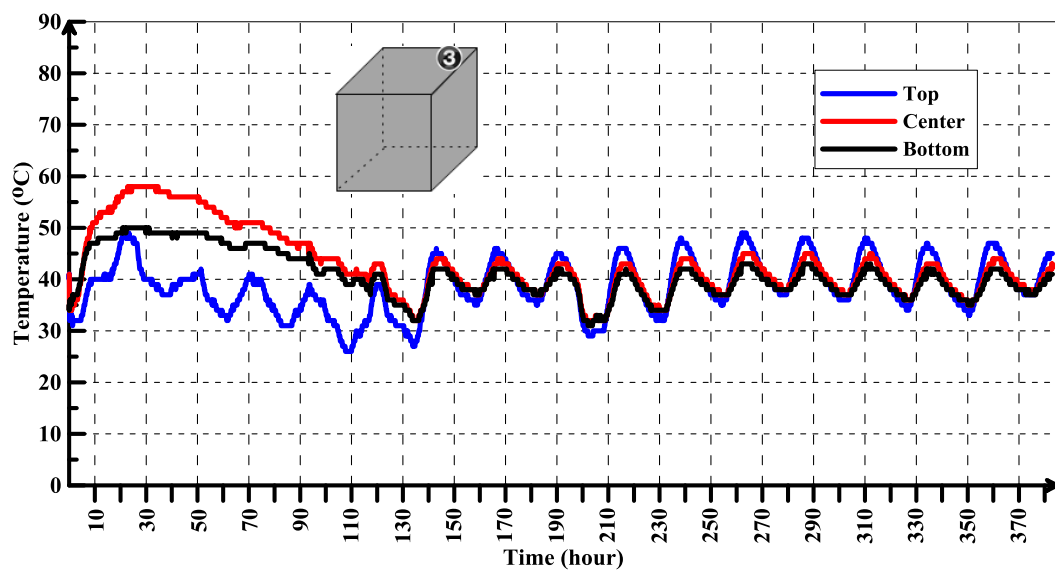


**Figure 6-53: Temperature rise at Location 3 (Top, Center, and Bottom)**

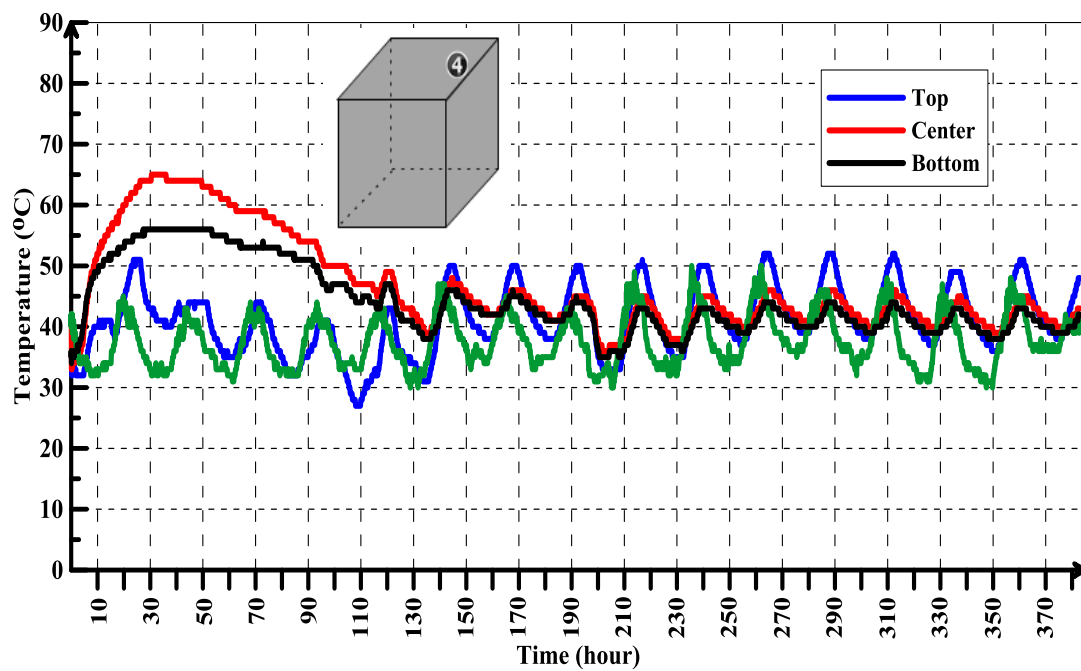


**Figure 6-54: Temperature rise at Location 4 (Top, Center, and Bottom)**

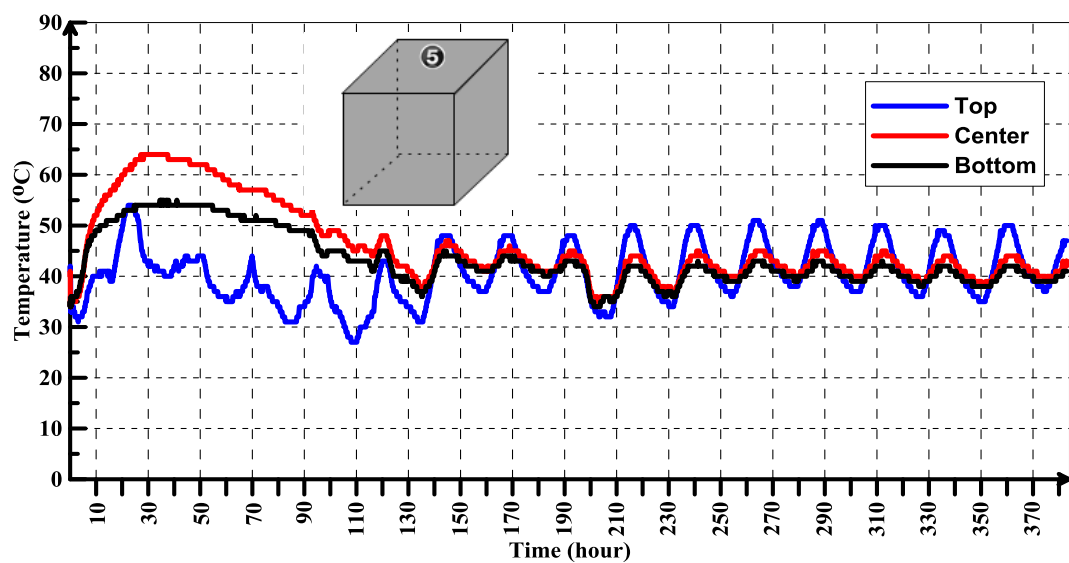


**Figure 6-55: Temperature rise at Location 5 (Top, Center, and Bottom)**



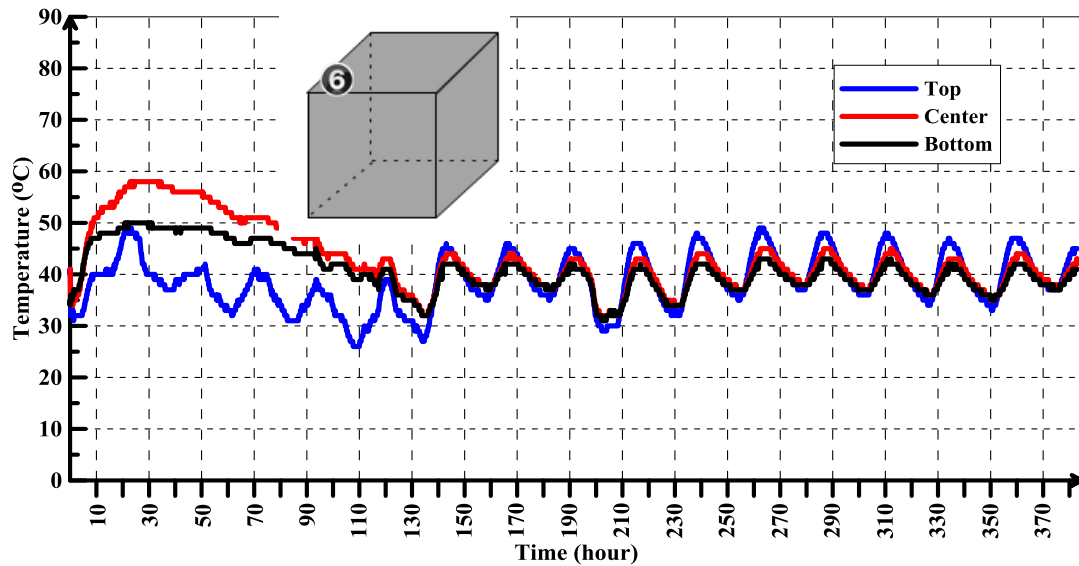


**Figure 6-56: Temperature rise at Location 6 (Top, Center, and Bottom)**

The peak temperatures recorded and the maximum differences monitored between the center of mock-up#2 and its surface for the six locations are listed in Table 6-3. It can be seen, the highest peak temperature is (72°C) at the core and the maximum temperature difference between the core of mockup#2 and its surface 27 °C.

**Table 6-3: Summary of Peak Temperatures and Max. Differences for the Mock-Up Specimen #2**

Mockup No.	Location No.						
		1	2	3	4	5	6
<b>Mockup#2 (40%OPC)</b>	Peak Temp. (°C)	72	65	58	64	70	59
	Time (Hour)	43.33	30.49	24.31	27.98	31.16	21.307
	Max. difference(°C)	27	26	20	24	27	22
	Time (Hour)	53.37	57.88	61.38	60.39	54.7	60.4

In the Mock-up specimen #3, the cement Type I was replaced with 60% GGBFS. The total content of cementitious materials was 480 kg/m<sup>3</sup>. The water cement cementitious materials ratio was 0.28. The results of temperature rise with time for the six locations (Shown in Figure 3-13) are shown in Figure 6-57 to Figure 6-62.

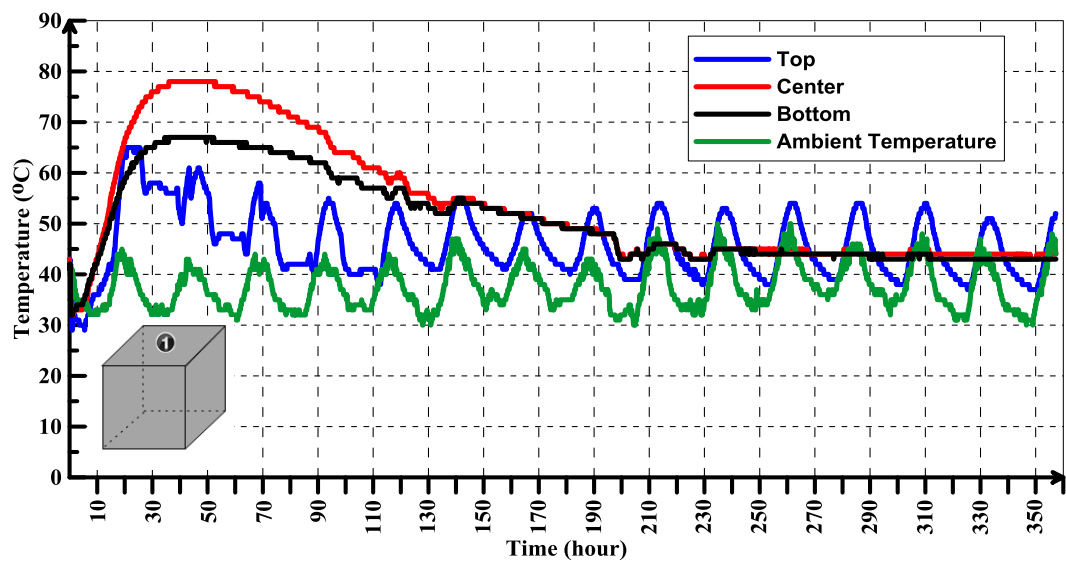


**Figure 6-57: Temperature rise at Location 1 (Top, Center, and Bottom)**

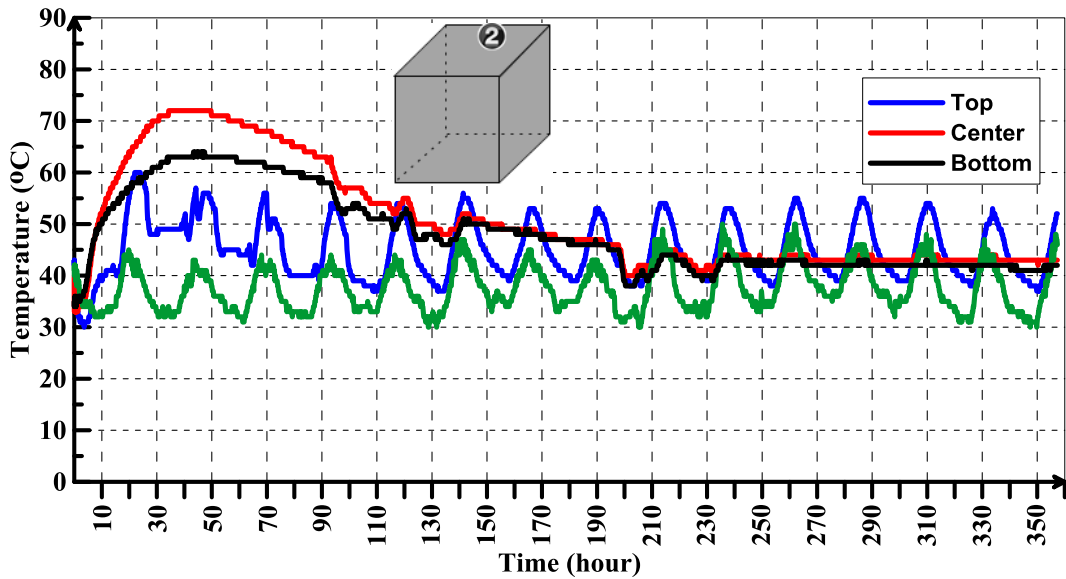


**Figure 6-58: Temperature rise at Location 2 (Top, Center, and Bottom)**

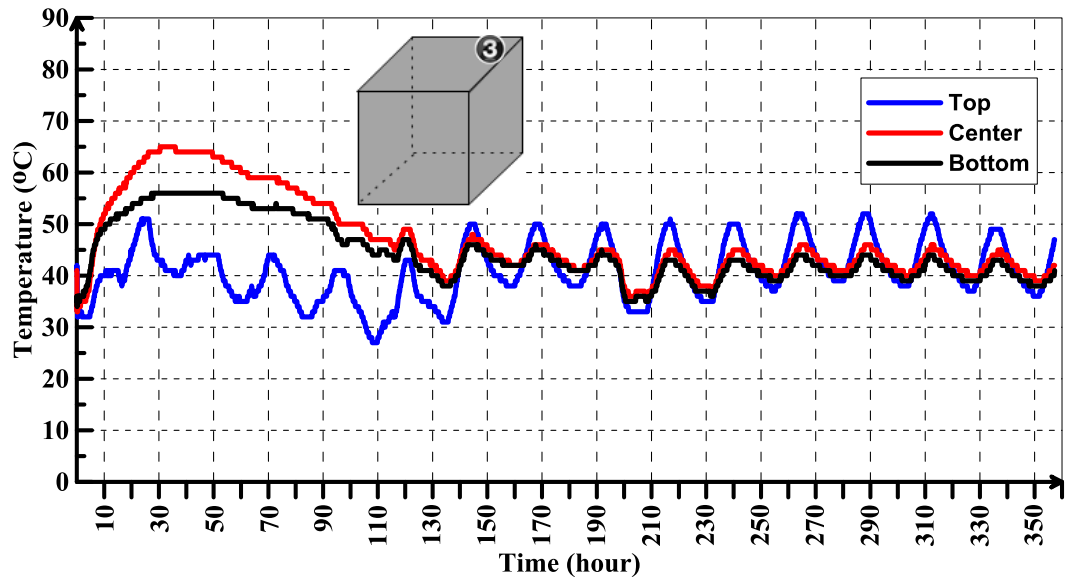


**Figure 6-59: Temperature rise at Location 3 (Top, Center, and Bottom)**

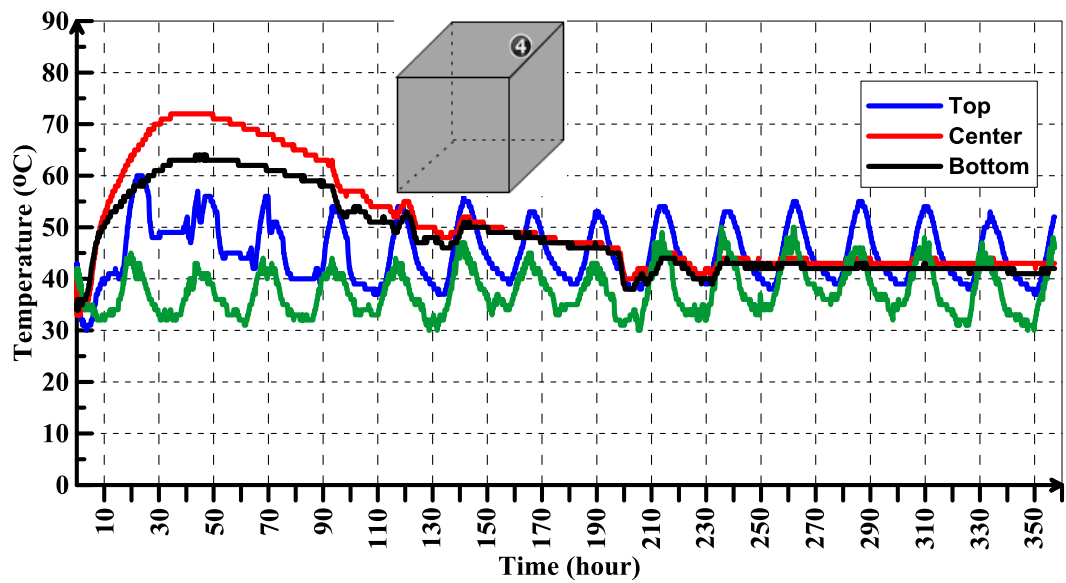


**Figure 6-60: Temperature rise at Location 4 (Top, Center, and Bottom)**

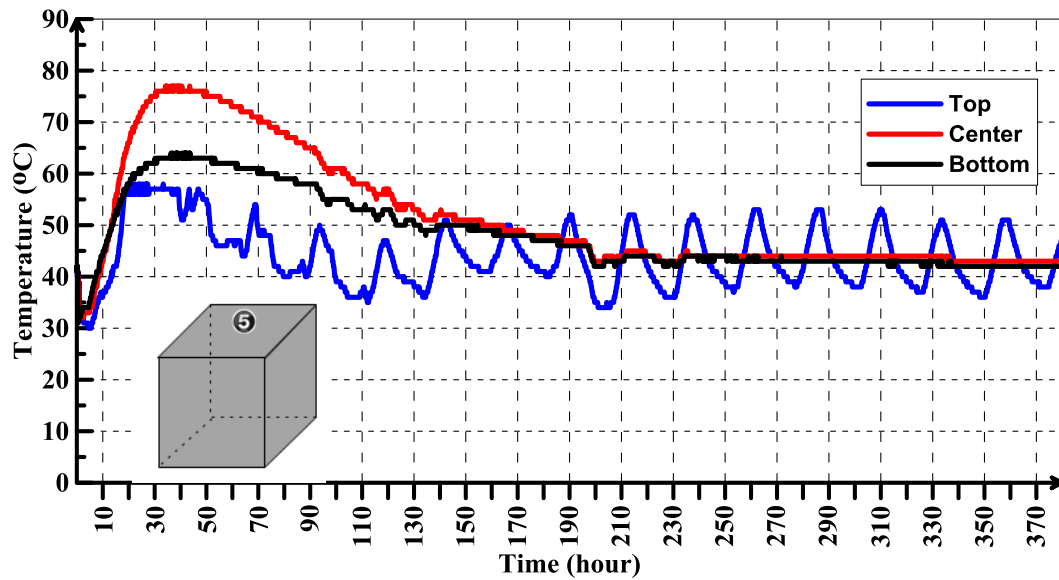


**Figure 6-61: Temperature rise at Location 5 (Top, Center, and Bottom)**

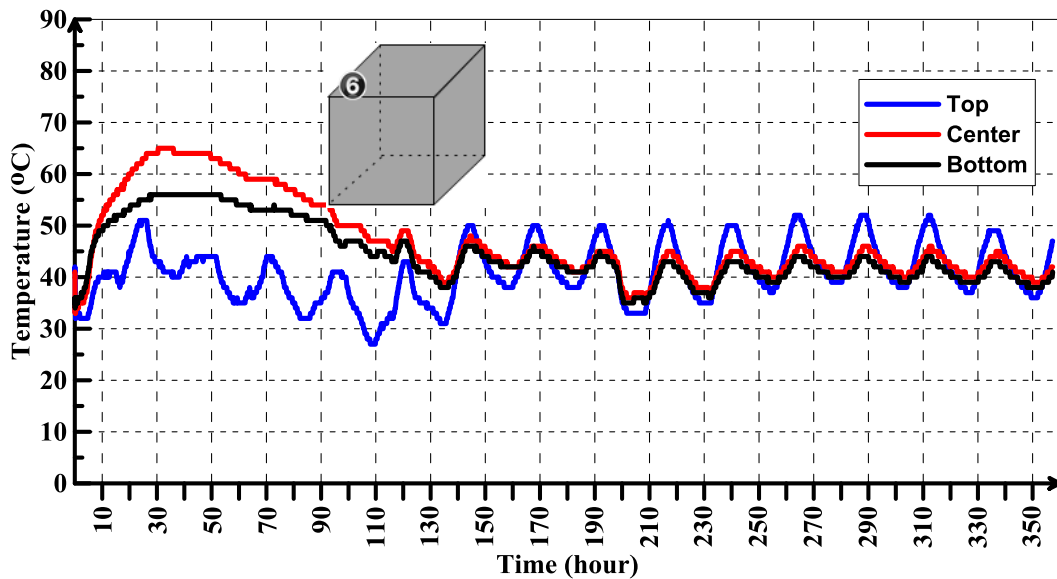


**Figure 6-62: Temperature rise at Location 6 (Top, Center, and Bottom)**

The peak temperatures recorded and the maximum differences monitored between the center of mock-up#3 and its surface for the six locations are listed in Table 6-4. It can be seen, the highest peak temperature is (78°C) at the core and the maximum temperature difference between the core of mockup#2 and its surface 32 °C. It is also shown, as expected, that the lowest temperatures were recorded in the thermocouples located nearest to the exposed top surface of the concrete block.

**Table 6-4: Summary of Peak Temperatures and Max. Differences for the Mock-Up Specimen #2**

Mockup No.	Location No.						
<b>Mockup#2 (40%OPC)</b>		<b>1</b>	<b>2</b>	<b>3</b>	<b>4</b>	<b>5</b>	<b>6</b>
	Peak Temp. (°C)	78	70	67	68	77	67
	Time (Hour)	36.03	25.14	24.48	24.14	36.17	25.48
	Max. difference(°C)	32	26	21	25	29	22
	Time (Hour)	36.72	55.37	56.37	52.1	38	53

#### 6.2.1.2 Strains Monitoring Results of KMUS

The strains were monitored using PMFL-50-5LT strain gauges (Manufactured by Tokyo Sokii Company). The mock-up #1 is instrumented with 12 strain gauges. The locations of strain gauges are shown in Figure 3-13 (1, 2, 3, and 4). The recorded strains include the elastic, thermal, shrinkage, and creep strains. The elastic strain will be considered in the calculation of stresses and cracking index. The results of monitored strains are shown in Figure 6-63 to Figure 6-66.

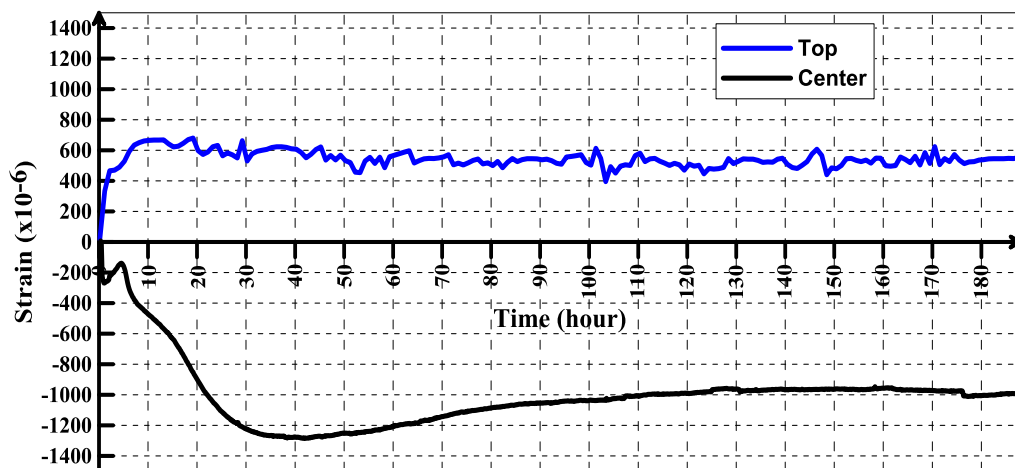


**Figure 6-63: Strain Evolution with Time at Location#1 (Top and Center)**

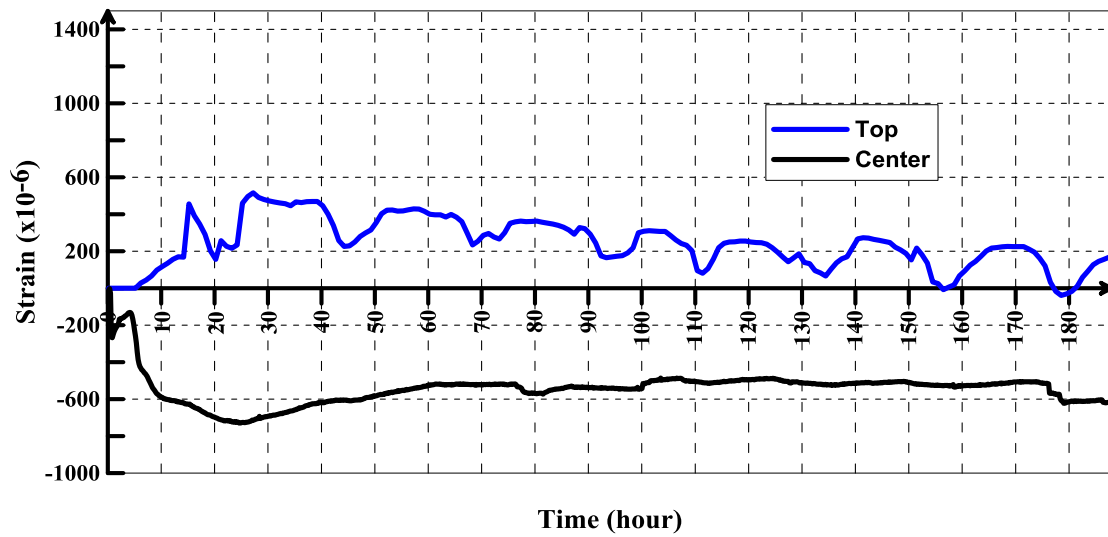


Figure 6-64: Strain Evolution with Time at Location#2 (Top and Center)

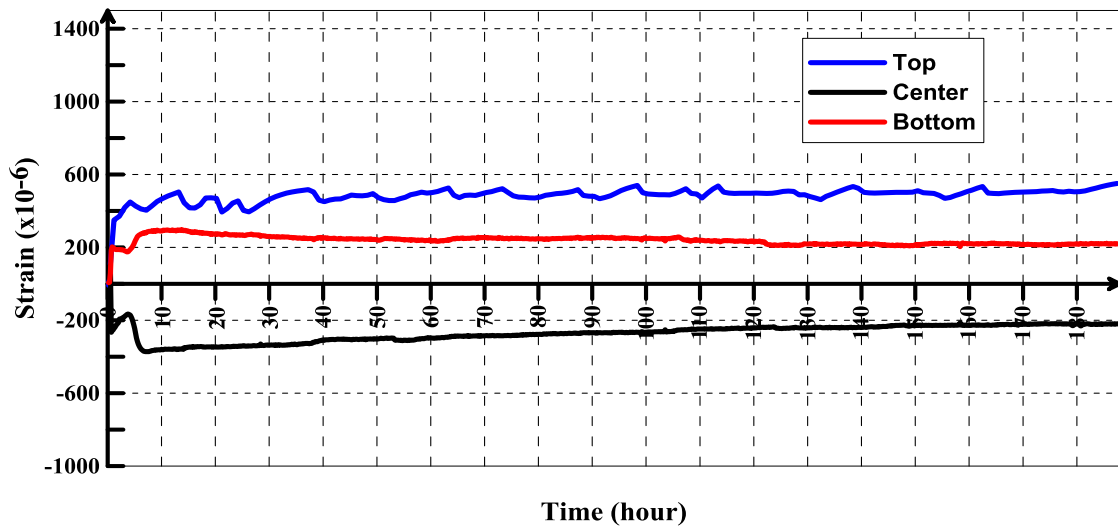
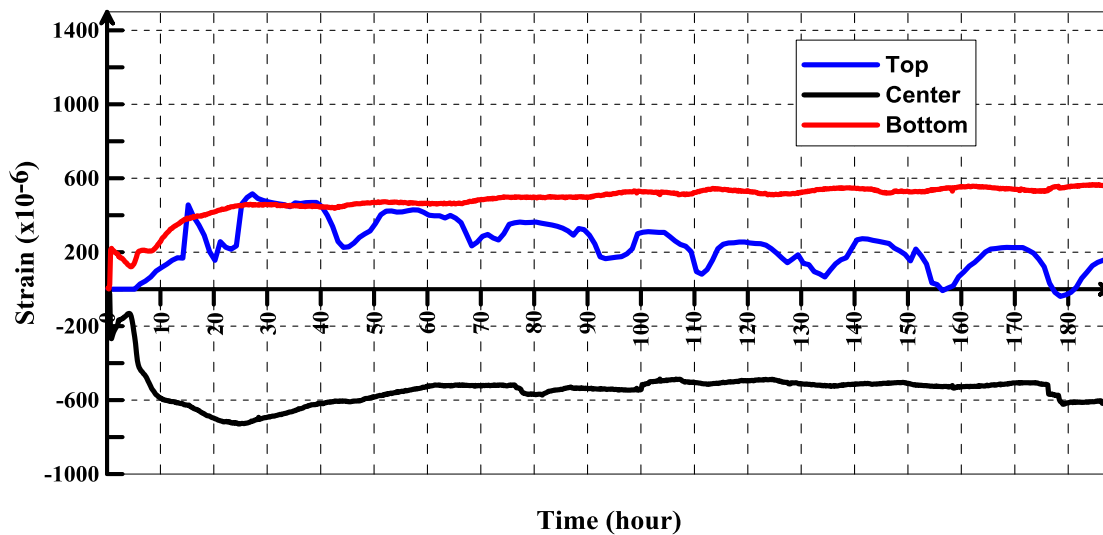


Figure 6-65: Strain Evolution with Time at Location#3 (Top, Center, and Bottom)



**Figure 6-66: Strain Evolution with Time at Location#4 (Top, Center, and Bottom)**

## **6.2.2 Monitoring Results of DMUS**

### **6.2.2.1 Temperature Monitoring Results of DMUS**

In these three mockup specimens, the steel formwork was used instead of plywood formwork. The mock-up specimens were reinforced with only two layers of epoxy steel reinforcement at top and bottom ( $7\phi 12/m$ ). The polystyrene foam was used to insulate the top surfaces of Dammam Mockup Specimens. First Mock-up specimen in the DMUS was cast with a mix containing 50% cement Type II and 50% GGBFS. The water cementitious materials ratio was 0.34. The results of temperature rise with time for the four locations (See Figure 3-20) are shown in Figure 6-67 to Figure 6-70

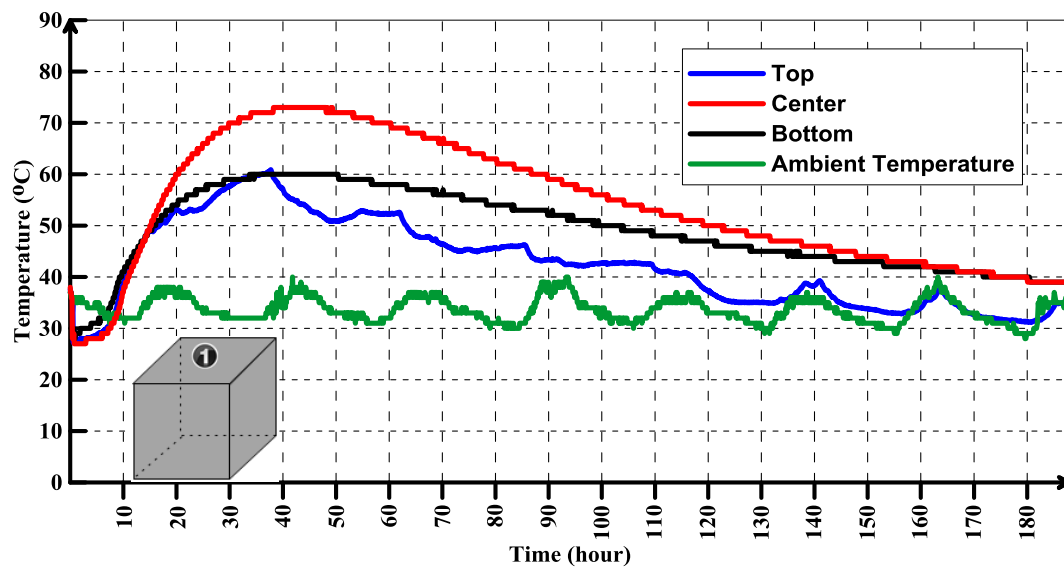


**Figure 6-67: Temperature rise at Location 1 (Top, Center, and Bottom)**

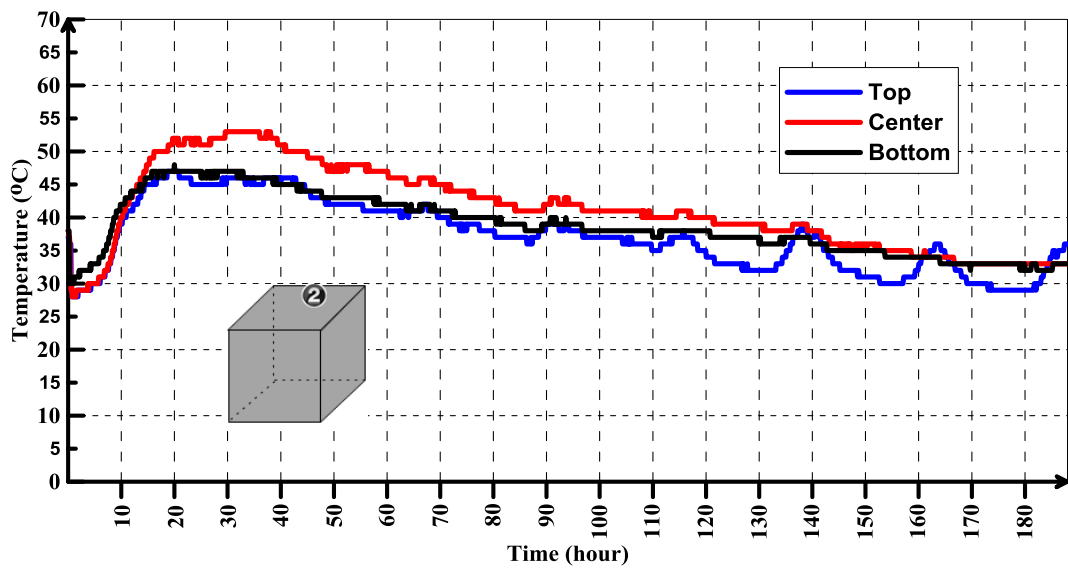


Figure 6-68: Temperature rise at Location 2 (Top, Center, and Bottom)

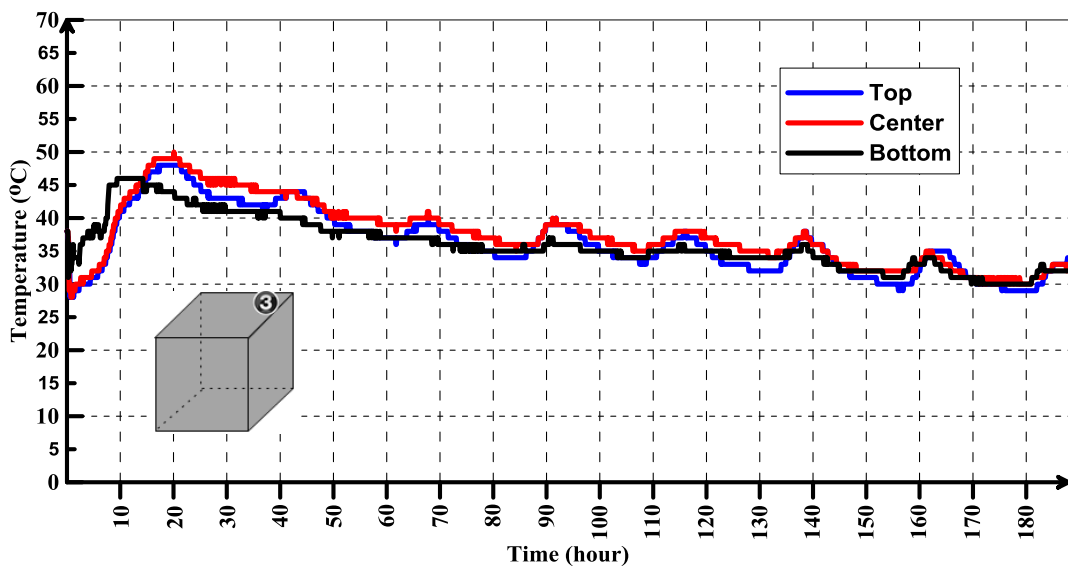
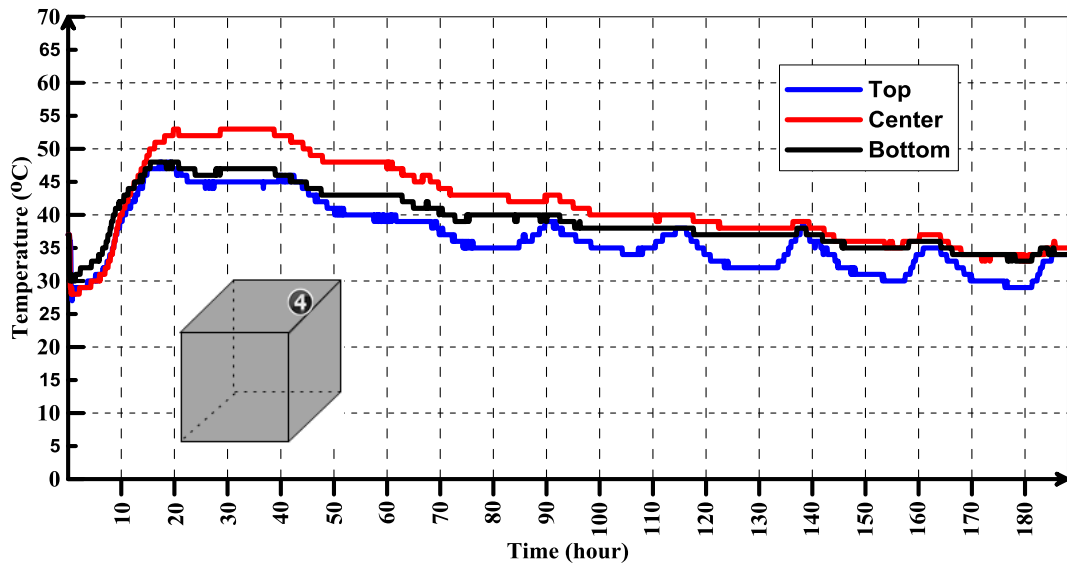


Figure 6-69: Temperature rise at Location 3 (Top, Center, and Bottom)





**Figure 6-70: Temperature rise at Location 4 (Top, Center, and Bottom)**

The second Mock-up specimen in the DMUS was cast with a mix containing 35% cement Type II and 65% GGBFS. The water cementitious materials ratio was 0.34. The results of temperature rise with time for the four locations are shown in Figure 6-71 to Figure 6-74

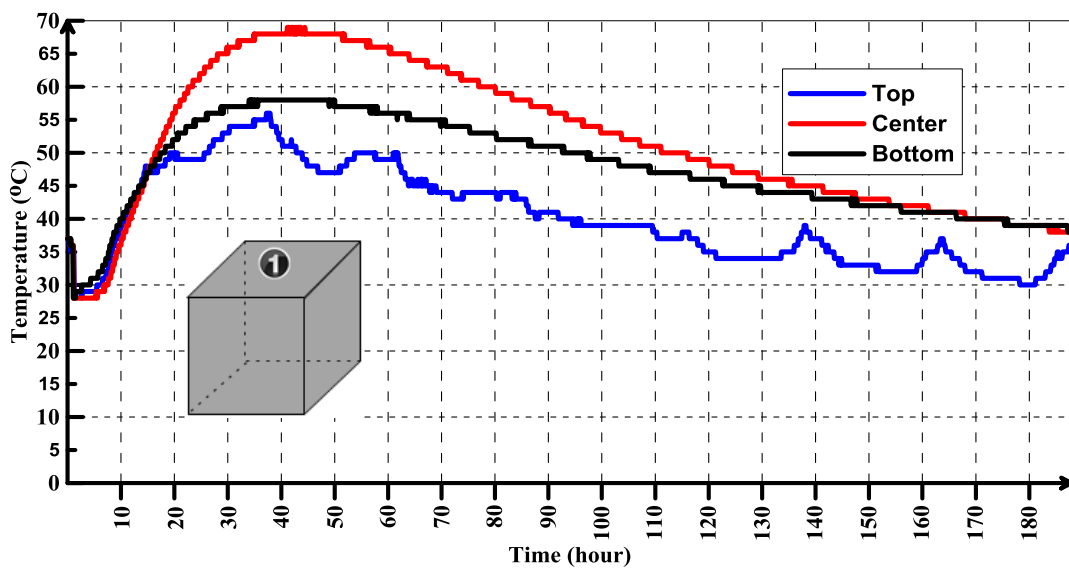


**Figure 6-71: Temperature rise at Location 1 (Top, Center, and Bottom)**

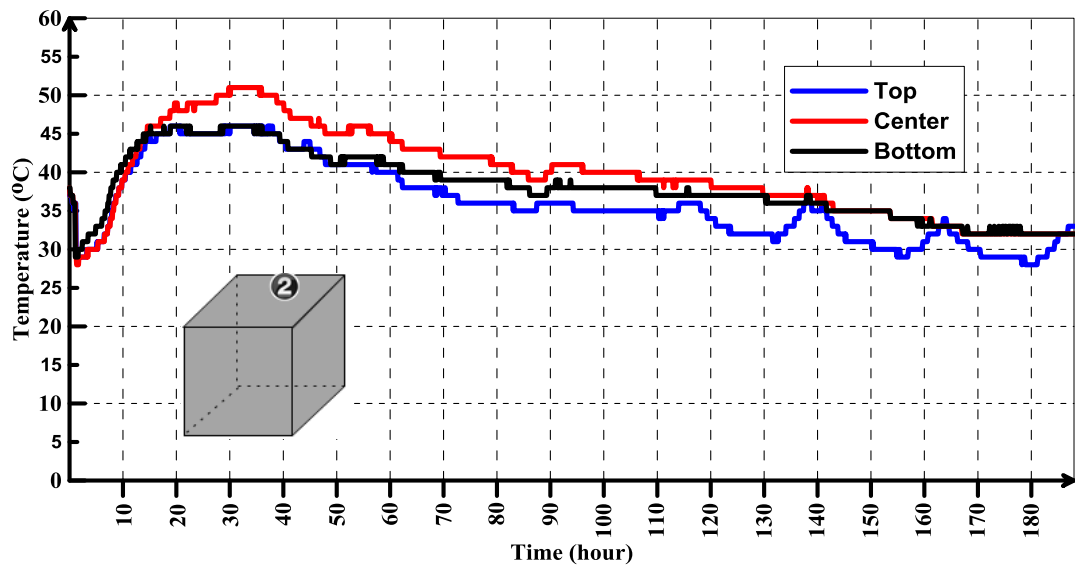


Figure 6-72: Temperature rise at Location 2 (Top, Center, and Bottom)

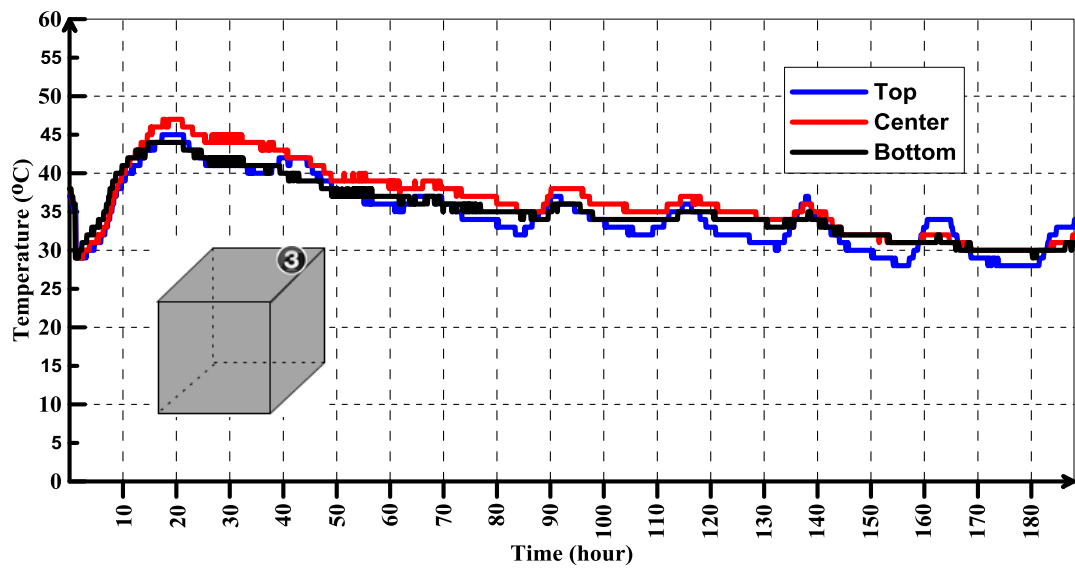
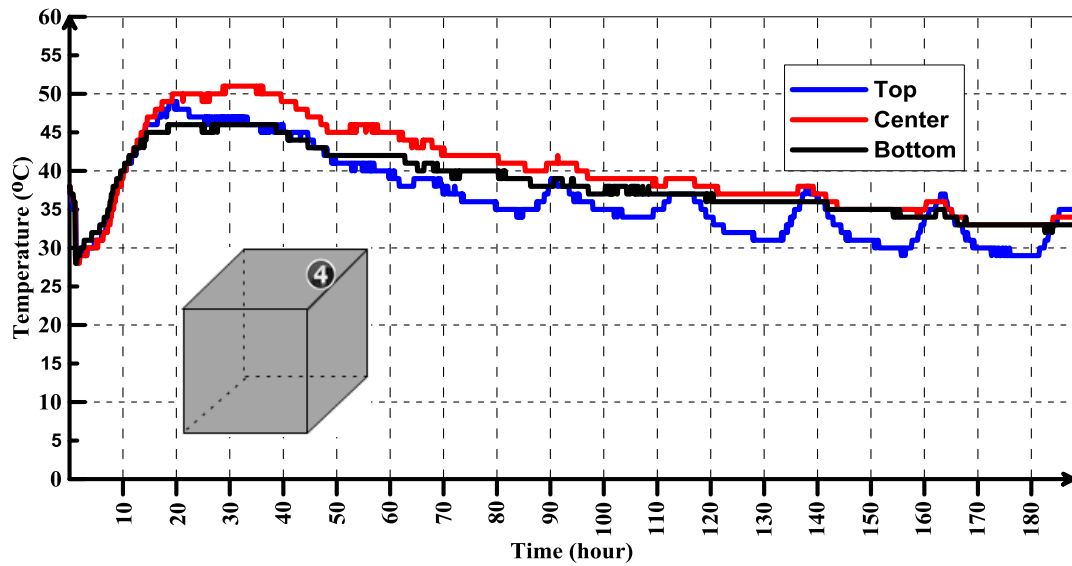
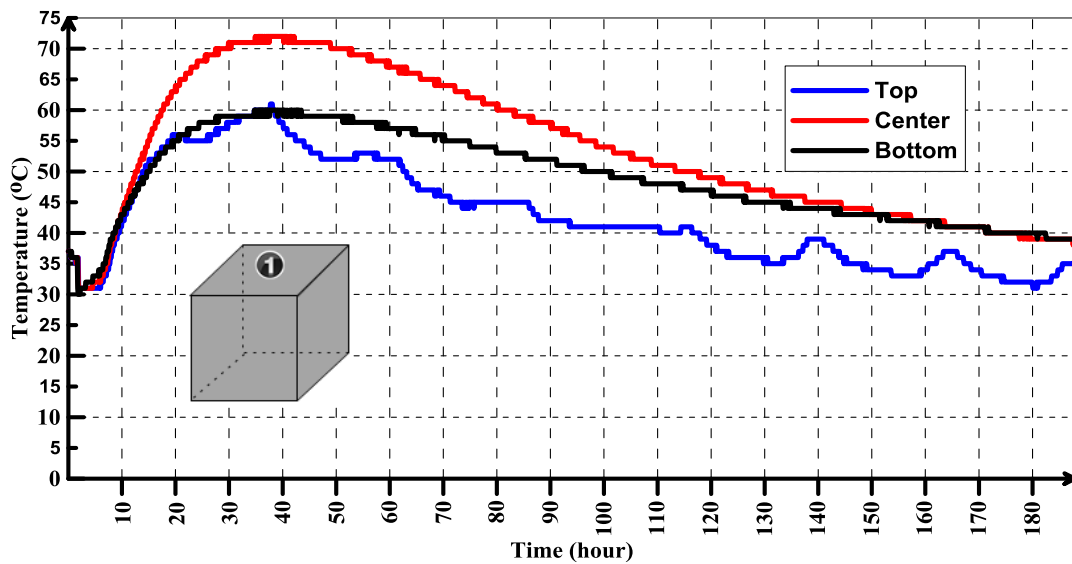


Figure 6-73: Temperature rise at Location 3 (Top, Center, and Bottom)



**Figure 6-74: Temperature rise at Location 4 (Top, Center, and Bottom)**

In the third mock-up specimen in the DMUS, The Mix with 30% cement Type II and 70% GGBFS was used. The water cementitious materials ratio was 0.34. The results of temperature rise with time at the four locations are shown in Figure 6-75 to Figure 6-78.



**Figure 6-75: Temperature rise at Location 1 (Top, Center, and Bottom)**

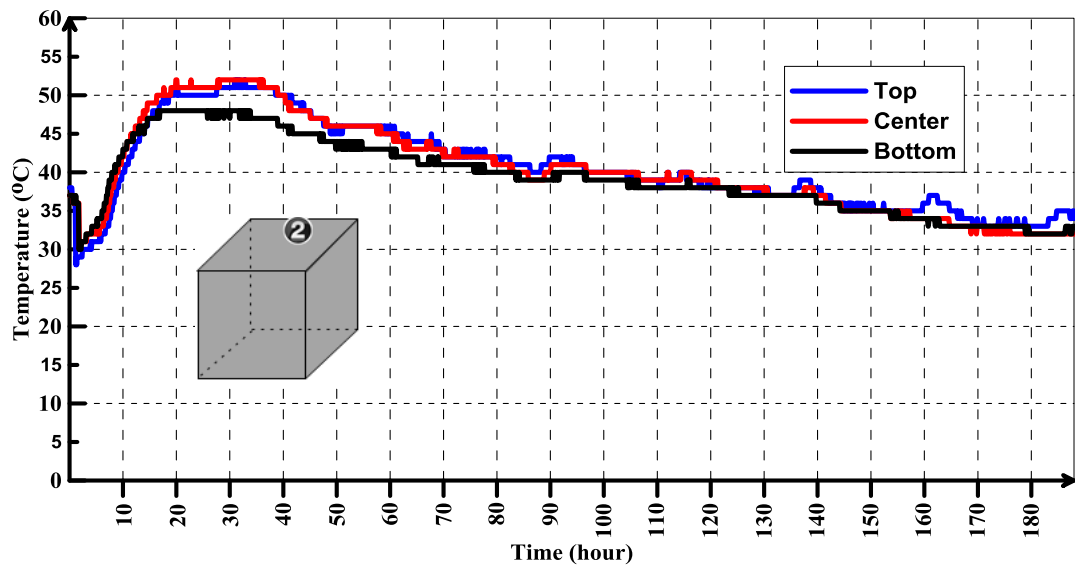


Figure 6-76: Temperature rise at Location 2 (Top, Center, and Bottom)

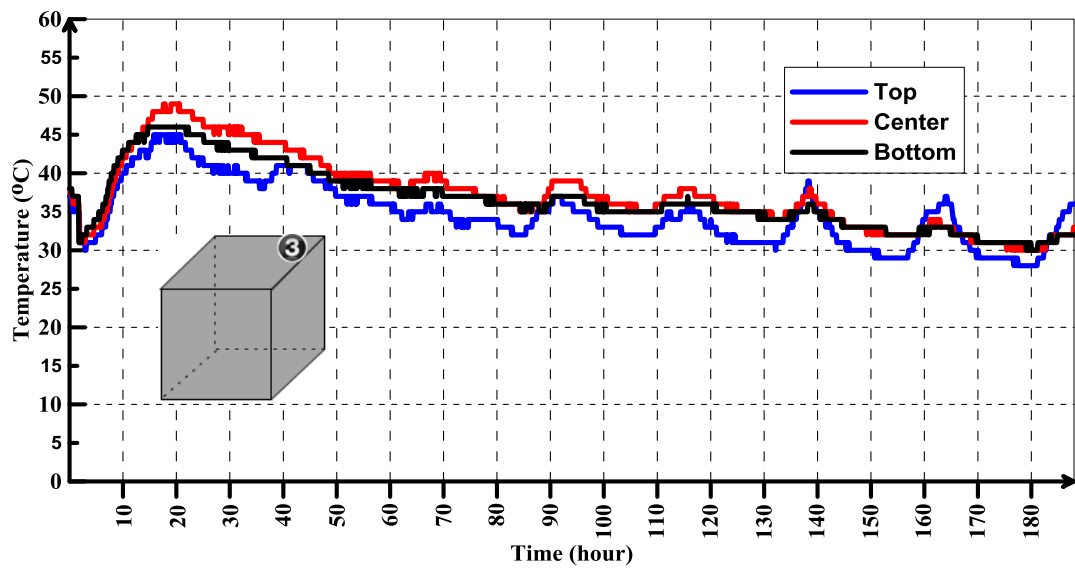
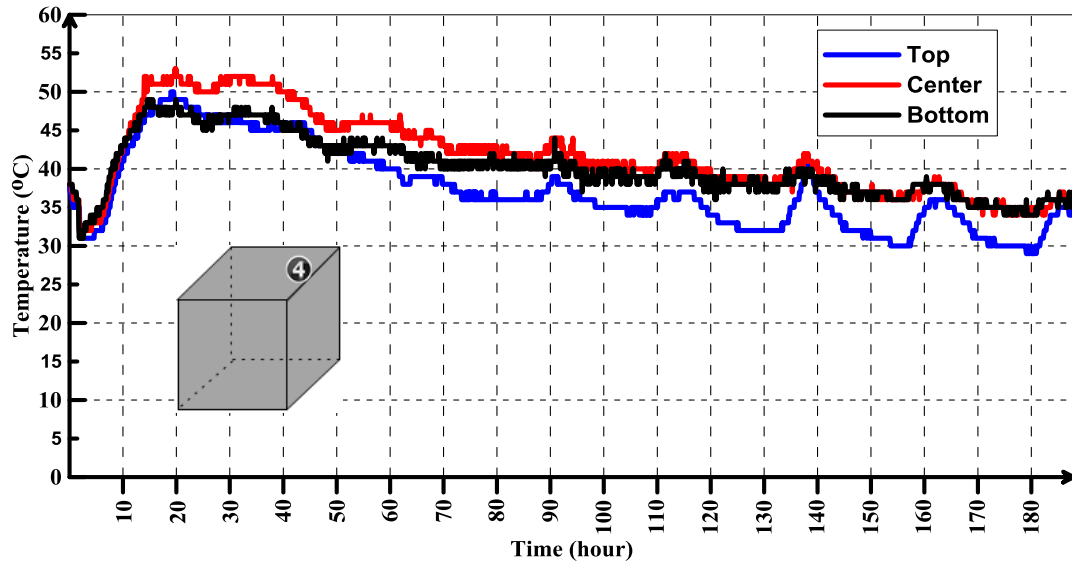


Figure 6-77: Temperature rise at Location 3 (Top, Center, and Bottom)



**Figure 6-78: Temperature rise at Location 4 (Top, Center, and Bottom)**

It is clear from the results of temperature rise for the DMUS, The temperature rise at location#1 (Center) is always higher than other locations. Since, the location#1 is far from the surfaces subjected to heat convection, the temperature rise of it is high especially at the core. The location#3 is located near to the corner of the mock-up specimen in which the heat loss is high. Therefore, the temperature rise at location #3 (Top, center, and bottom) is generally lower than other locations

The maximum temperatures at the four locations for DMUS are summarized in Table 6-5 .

**Table 6-5: Maximum Temperatures at varying locations in DMUS**

Mock-Up No.	Location#1			Location#2			Location#3			Location#4		
	Top	Center	Bottom	Top	Center	Bottom	Top	Center	Bottom	Top	Center	Bottom
<b>Mockup#1</b>	60.9	73	60	47	53	48	48	50	56	48	53	48
<b>Mockup#2</b>	56	69	58	46	51	46	45	47	44	49	51	46
<b>Mockup#3</b>	61	72	60	52	52	48	45	49	46	50	53	49

It can be noticed from Table 6-5; the peak temperature in the mockup#1 is 73 °C at the core . The difference between the peak temperature of mockup#1 and mockup#2 is 4°C. Increasing the replacement percentage of GGBFS from 50% to 70%

leads to a decrease in the maximum temperature to only 1°C. The temperature difference between the core and the surface of DMUS in the four locations are shown in Table 6-6

**Table 6-6: Temperature Differences between the Core and the Top Center of Surface**

Mock-Up No.	Max. Difference			
	Location#1	Location#2	Location#3	Location#4
Mockup#1	22	8	3	9
Mockup#2	21	6	4	7
Mockup#3	19	8	6	8

Table 6-6 shows that the maximum difference in the temperature between the core and the surface in the three mock-up specimens was at location #1. The increase in the replacement parentage of GGBFS from 50% to 65% results in the decrease in the maximum difference from 22 °C to 21°C. The maximum difference is also decreased by 1 °C when the replacement percentage increases from 65% to 70%.

It is clear from the temperature rise charts in the locations 2,3 and 4 , the heat losses from sides is large which results in high temperature difference between the core of mockup specimen and the sides. This loss is due to the high thermal conductivity of steel formwork. It is noticed from the charts of temperature rise, the temperature difference between the core and sides is higher the temperature difference between the core and the top surface. The temperature differences between the core and sides are summarized in Table 6-7.

**Table 6-7: Temperature Differences between the Core and the Sides**

Mock-Up No.	Max Diff. between core and sides		
	Side1	Corner	Side2
Mockup#1	26	32	25
Mockup#2	25	31	26
Mockup#3	23	29	23

### 6.2.3 Monitoring Results of JMUS

This mock-up specimen was located in Jeddah City and monitored by Saudi Ready Mix Company. The mock-up specimen had dimensions of 3×3×3 m. The concrete mix used in the mock up consisted of 65% cement (330 kg/m<sup>3</sup>), 35% fly ash (180 kg/m<sup>3</sup>) and 0.29 water/binder ratio. The temperature rise was monitored by 9 thermocouples. The results of field monitoring in the mockup specimen at three locations are shown in Figure 6-79 to Figure 6-81

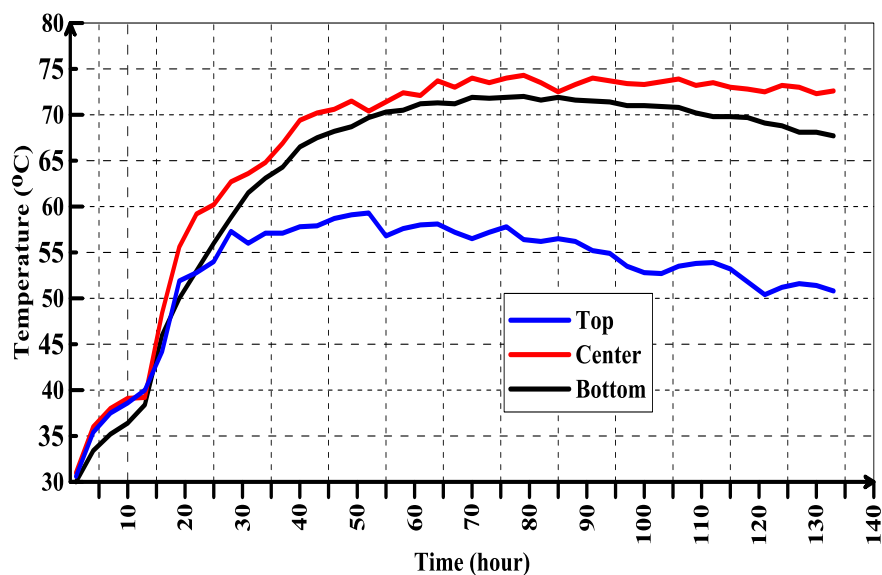


**Figure 6-79: Temperature rise at Location 1 (Top, Center, and Bottom)**

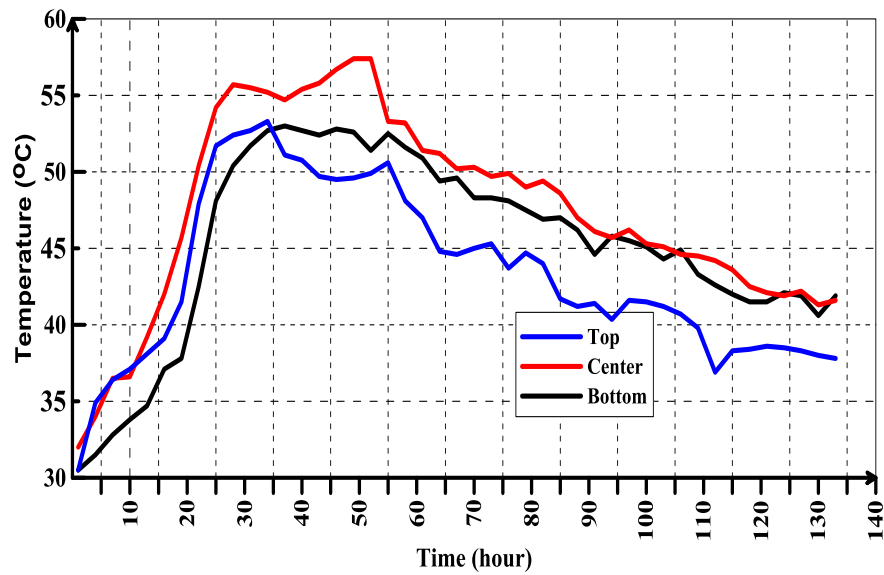


**Figure 6-80: Temperature rise at Location 2 (Top, Center, and Bottom)**

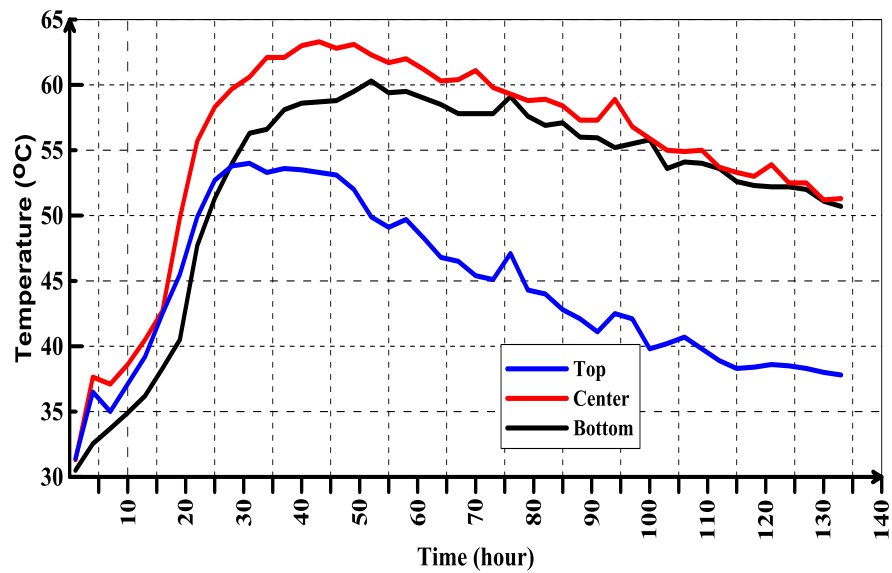


**Figure 6-81: Temperature rise at Location 3 (Top, Center, and Bottom)**

The maximum temperatures and temperature differences between the core and the surface of JMUS for the three locations are shown in Table 6-8

**Table 6-8: Max. Temperatures and Temperature Differences for the JMUS**

JMUS	Location#1	Location#2	Location#3
Max. Temperature	74.5	57.4	63.6
Max. Difference	22.7	8.8	9.3



#### 6.2.4 Monitoring Results of Bridge Piles- Cap

The temperature rise due to the heat of hydration in the concrete piles cap was monitored by using 15 thermocouples installed in the pile cap at various locations and depth as shown in Figure 3-30. The thermocouples were installed and embedded in the concrete at the top, middle, and bottom of the piles cap. The formwork on sides was plywood supported by steel stiffeners. The results of temperature rise at the selected locations are shown in Figures Figure 6-82 to Figure 6-86.

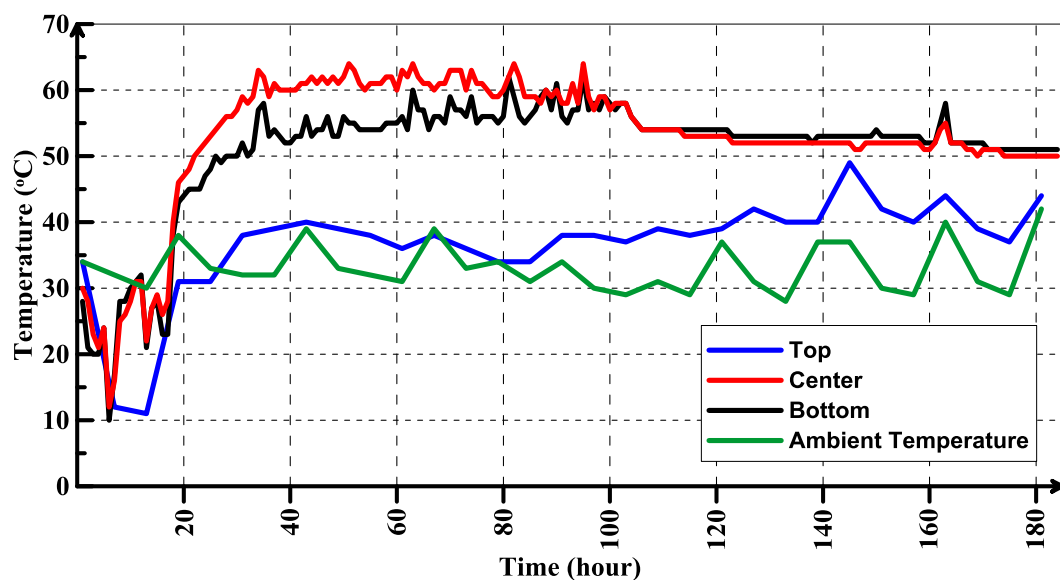
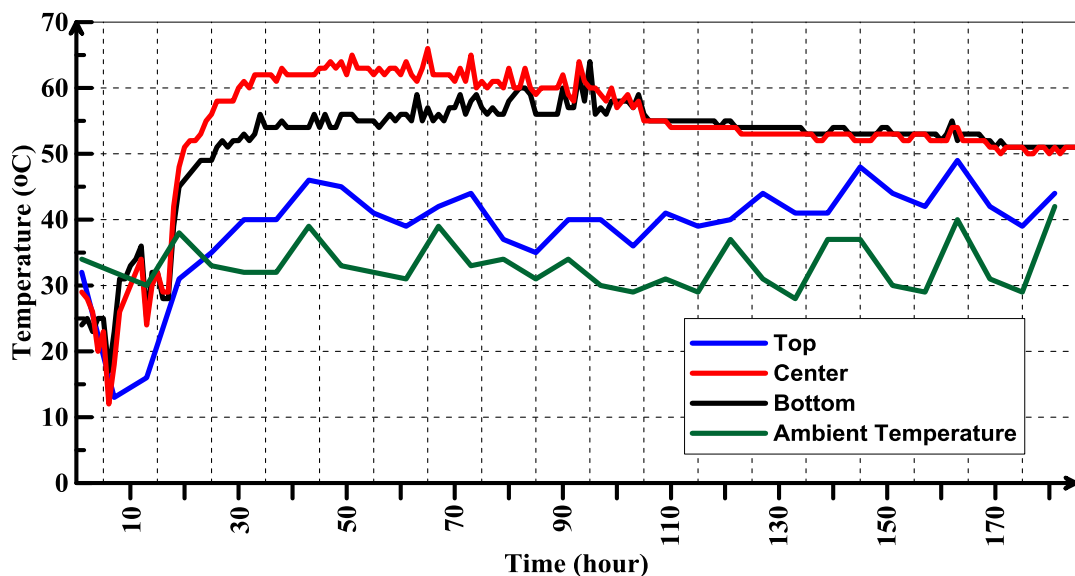
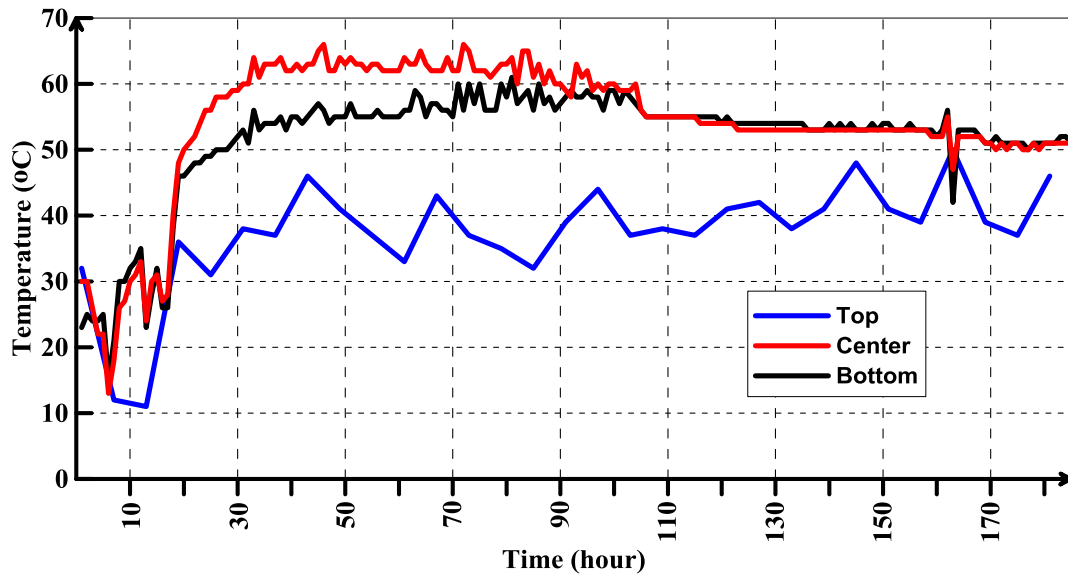


Figure 6-82: Temperature rise at Location 1 (Top, Center, and Bottom)



**Figure 6-83: Temperature rise at Location 2 (Top, Center, and Bottom)**



**Figure 6-84: Temperature rise at Location 3 (Top, Center, and Bottom)**

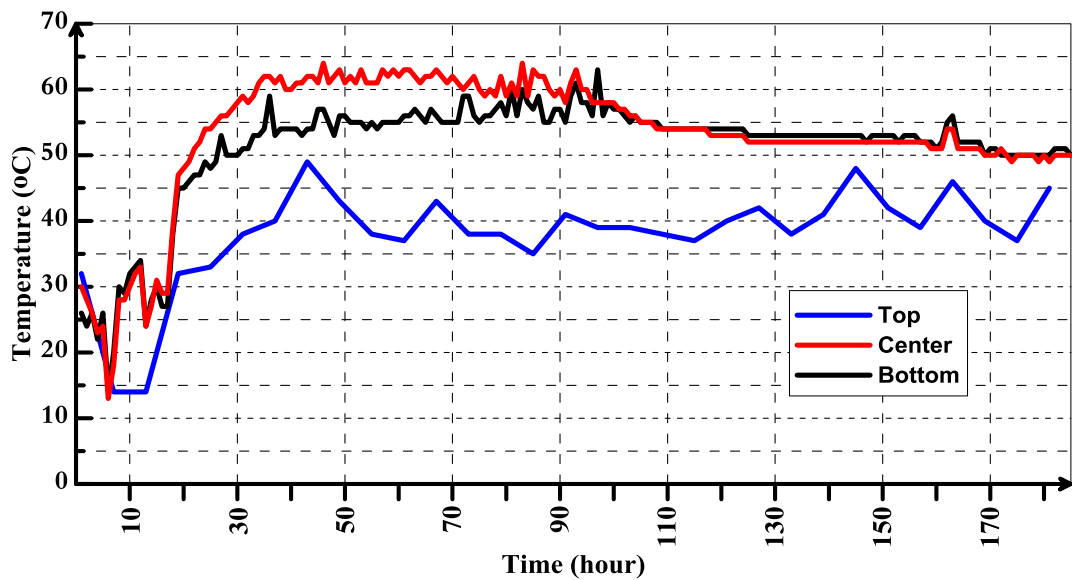


**Figure 6-85: Temperature rise at Location 4 (Top, Center, and Bottom)**

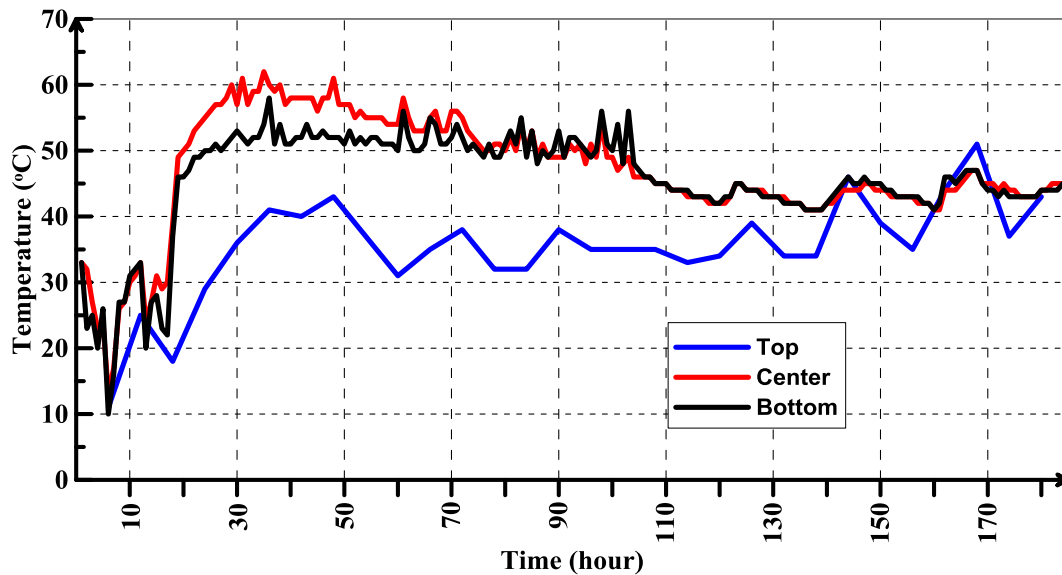


**Figure 6-86: Temperature rise at Location 5 (Top, Center, and Bottom)**

The maximum temperatures and temperature differences between the core and the top surface of Piles-Cap for the three locations are shown in Table 6-9

**Table 6-9: Max. Temperatures and Temperature Differences for the Piles-Cap**

JMUS	Location#1	Location#2	Location#3	Location#4	Location#5
Max. Temperature	65	66	66	66	62
Time (hour)	55	50	50	50	35
Max. Difference	29	31	31	30	29
Time (hour)	77	80	78	78.5	23

The peak temperature recorded in the pile cap was 66°C at the central core of pile cap at location 2,3 and 4. The recorded peak temperature was less than 70°C which can be considered as a safe value in terms of a delayed ettringite formation problem (DEF). The maximum difference of temperature between the center of pile cap and its surface was observed to be about 31°C at location#2 and 3. The recorded temperature difference however, exceeded the value of 20°C recommended by ACI.

## **CHAPTER 7**

### **FINITE ELEMENT SIMULATION RESULTS**

#### **7.1 Introduction**

Finite element simulation of the early age thermal behavior of mass concrete was conducted using the commercially available software package TNO DIANA. The TNO DIANA feature of staggered flow- stress analysis was utilized, in which the temperature distribution is calculated by flow heat analysis, then the temperature distribution used as a load in the subsequent structural analysis. In this chapter the results of heat transfer analysis and stresses analysis will be presented.

#### **7.2 Heat Transfer Analysis Results**

There are several factors which can affect the heat transfer and temperature distribution in the mass concrete structures including ambient temperatures, heat convection, placement temperature of concrete, solar radiation, and thermal properties of concrete and formwork. The comparison between the temperature rise from heat transfer analysis and the monitored temperature rise will be shown in the following sections.

##### **7.2.1 Temperature Simulation Results of KMUS**

The change of ambient temperature with time was measured using thermocouple Type T each ten minutes. The wind velocity was measured using hand held anemometer. The solar radiation effect was carried out using Echotect software. The thermal properties of concrete, plywood, steel, water, and soil which is used in the model are summarized in Table 7-1

**Table 7-1: Thermal Properties of Materials Used in FE Simulation**

Material	Concrete	Ply wood	Steel	Water	Soil
Density ( $\text{kg/m}^3$ )	2300-2450		7850	1000	1700
Heat conduction coefficient ( $\text{J/hour.m.}^\circ\text{C}$ )	7.92E+03	5.4E+02	15.480E+04	2.08E+03	1.91E+02
Convection coefficient ( $\text{J/hour.m}^2.^\circ\text{C}$ )	2.016 E+04 to 9.12E+04	2.016 E+04 to 9.126E+04	-	-	-
Thermal expansion Coefficient	7.16E-06 to 10E-06	-	10E-06	-	7.0E-06
Poisson Ratio	0.2	-	0.2	-	0.3
Volumetric Thermal Capacity ( $\text{J/m}^3.^\circ\text{C}$ )*	2.53 E+06 to 2.68E+06	8.54E+05	3.82E+06	7.05E+05	1.42E+06

\* Volumetric Thermal Capacity = specific heat  $\times$  density

Due to symmetry, only one-quarter of the mockup specimen was modeled as shown in Figure 7-1.

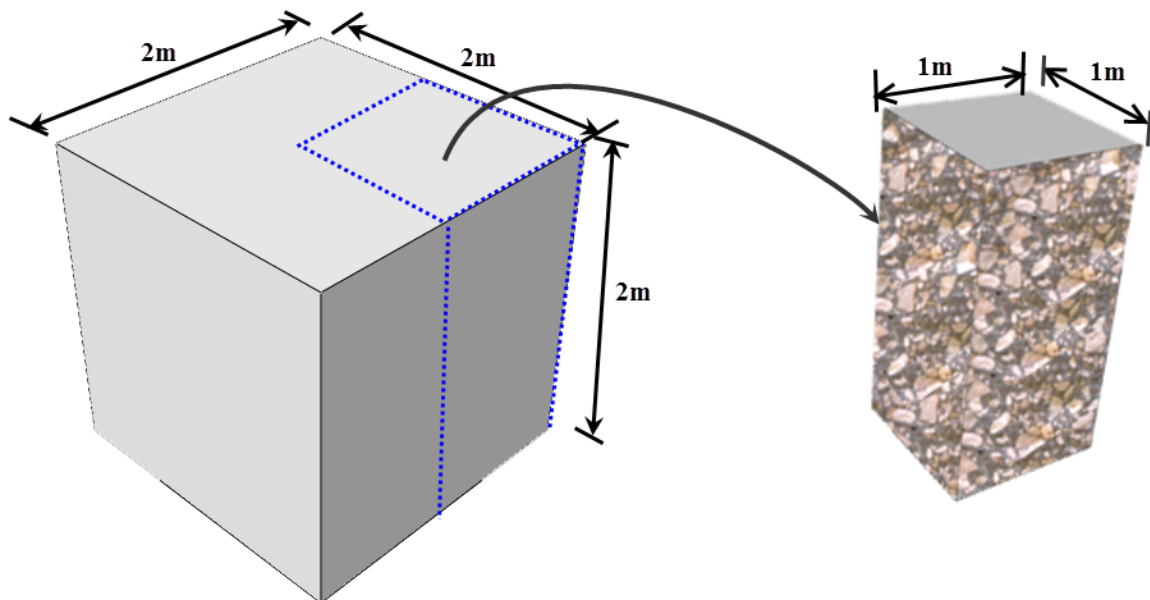


**Figure 7-1: Dimensions of Quarter of Mock-Up Specimen used in Simulation**

The geometry of finite element model with element types is shown in Figure 7-2.

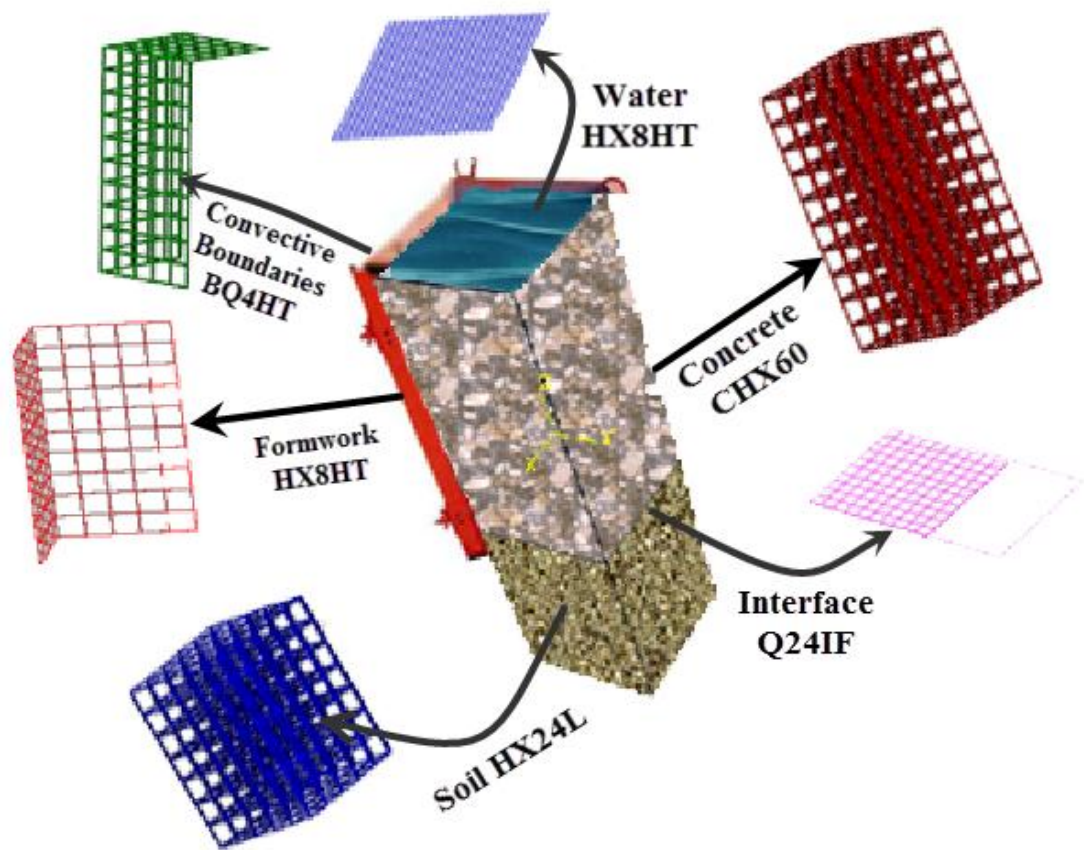


**Figure 7-2: Geometry of FEM with Element Types**

The mock-up Specimen #1 was cast with a mix containing 100% OPC ( $480 \text{ kg/m}^3$ ). The plywood was used as formwork in the KMUS. The top surface of mockup specimens were Cured with water and burlap for one week. The comparison between the results of field monitoring and the results of finite element simulation in the mock-up specimen#1 are shown in Figure 7-3 to Figure 7-5.

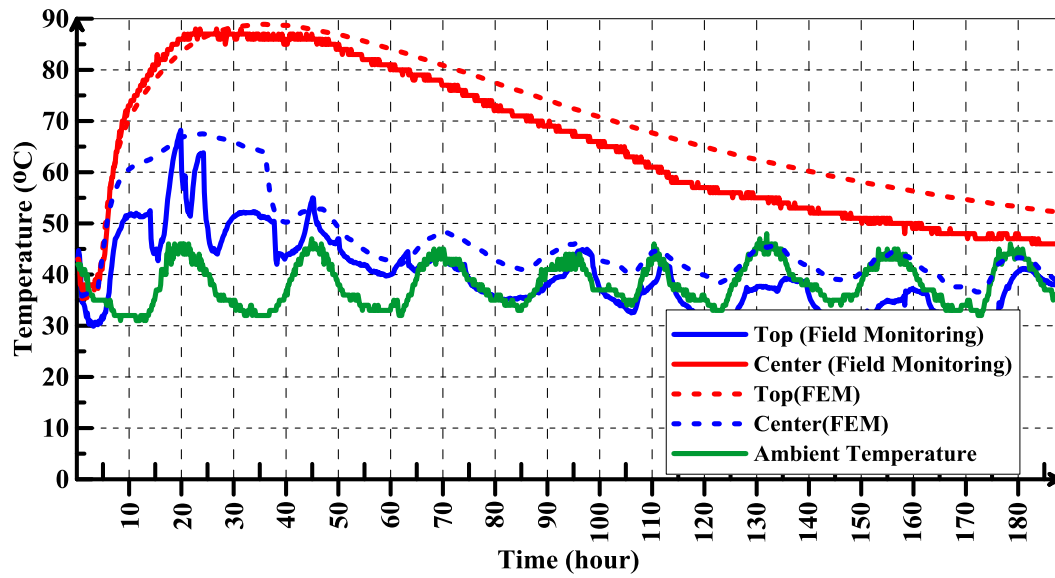


Figure 7-3: Temperature Rise at Location 1 for Mockup#1 in KMUS (100% OPC)

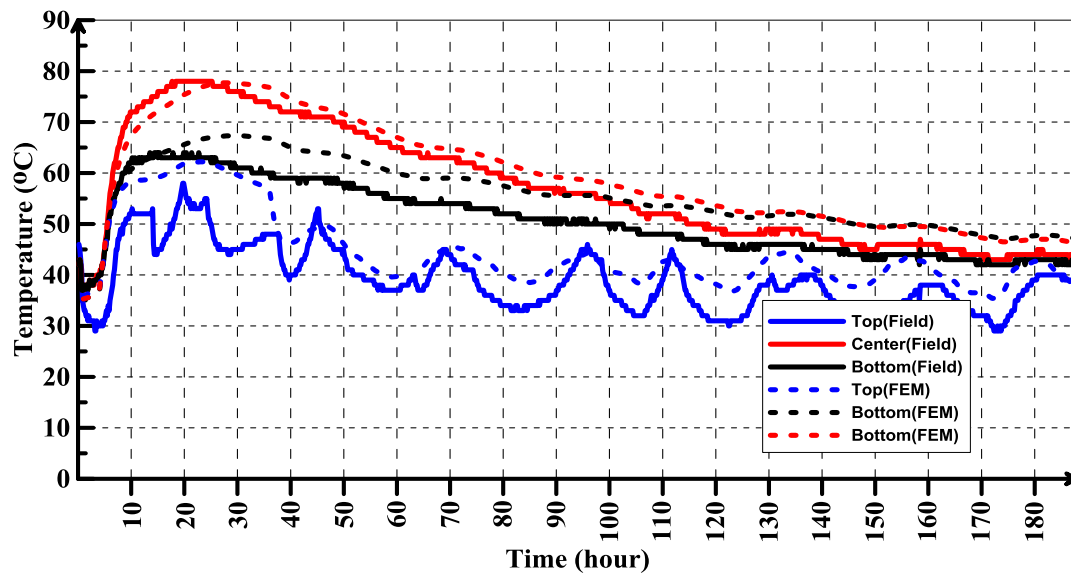
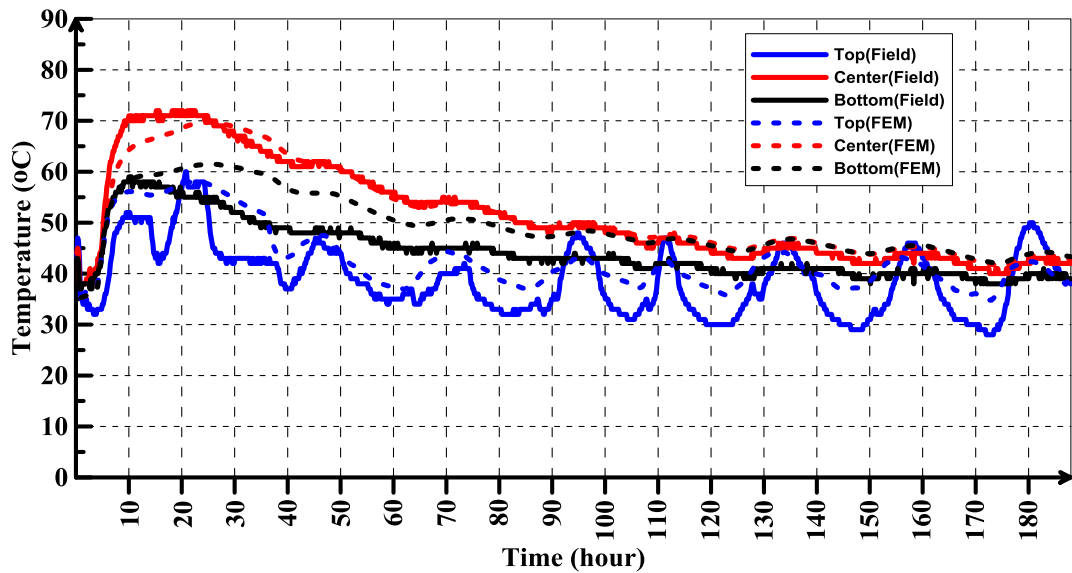
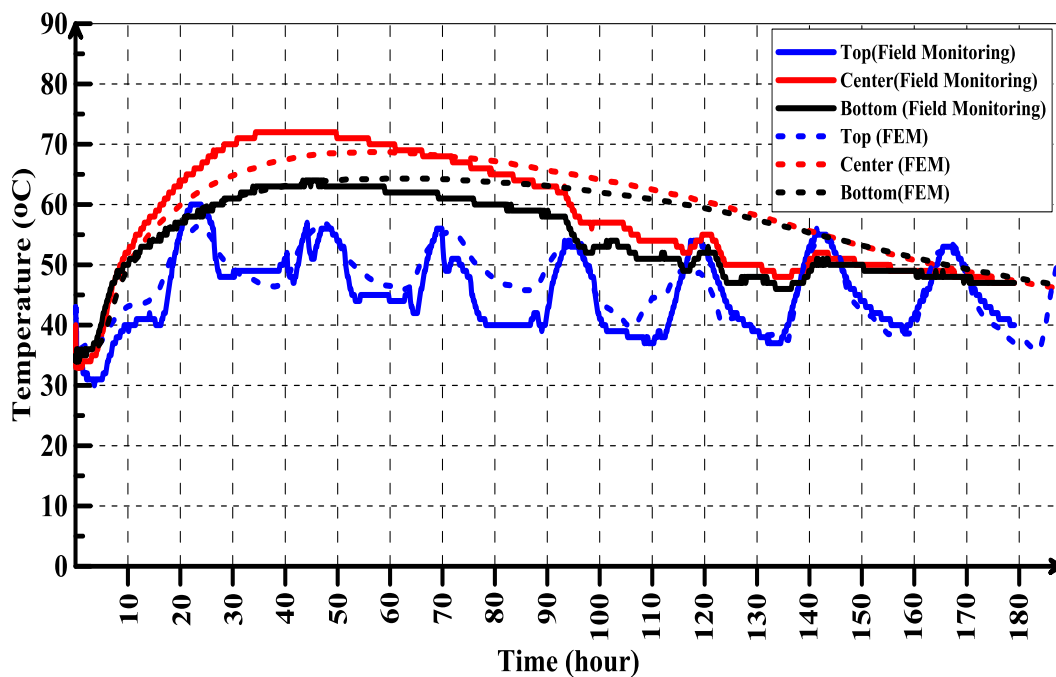


Figure 7-4: Temperature Rise at Location 2 for Mockup#1 in KMUS (100% OPC)



**Figure 7-5: Temperature Rise at Location 3 for Mockup#1 in KMUS ( 100% OPC)**

In the mock-up specimen #2, OPC was replaced with 40% Fly Ash. The comparison between the results of field monitoring and the results of finite element simulation in the mock-up specimen#1 are shown in Figure 7-6 to Figure 7-8.



**Figure 7-6: Temperature Rise at Location 1 for Mockup#2 in KMUS (40% Fly Ash)**



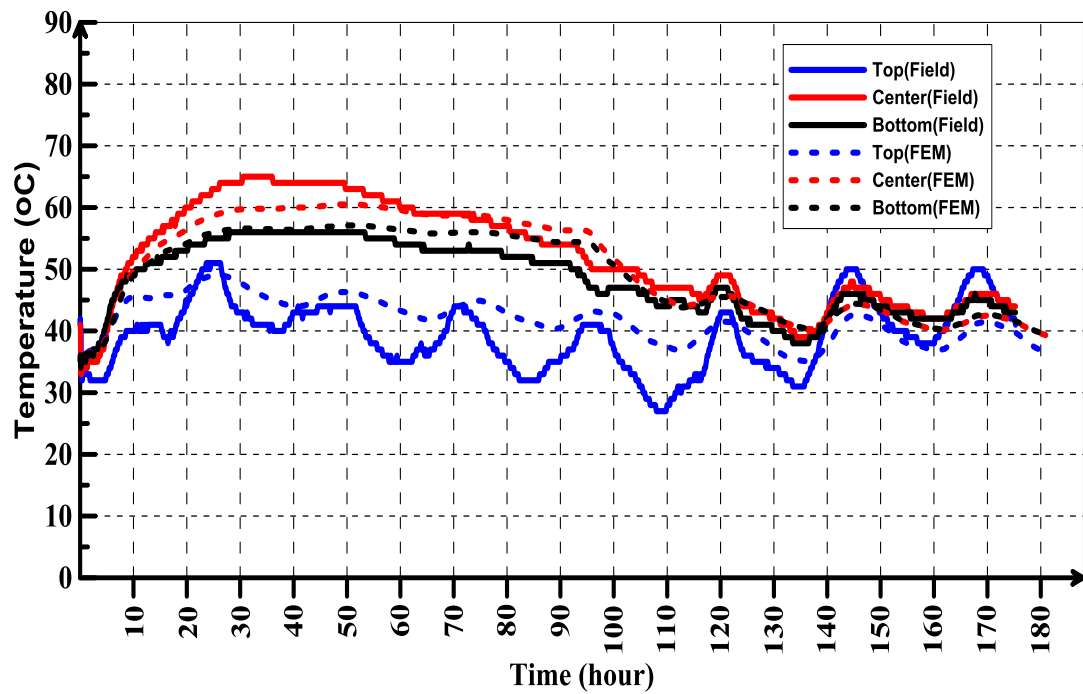


**Figure 7-7: Temperature Rise at Location 2 for Mockup#2 (40% Fly Ash)**

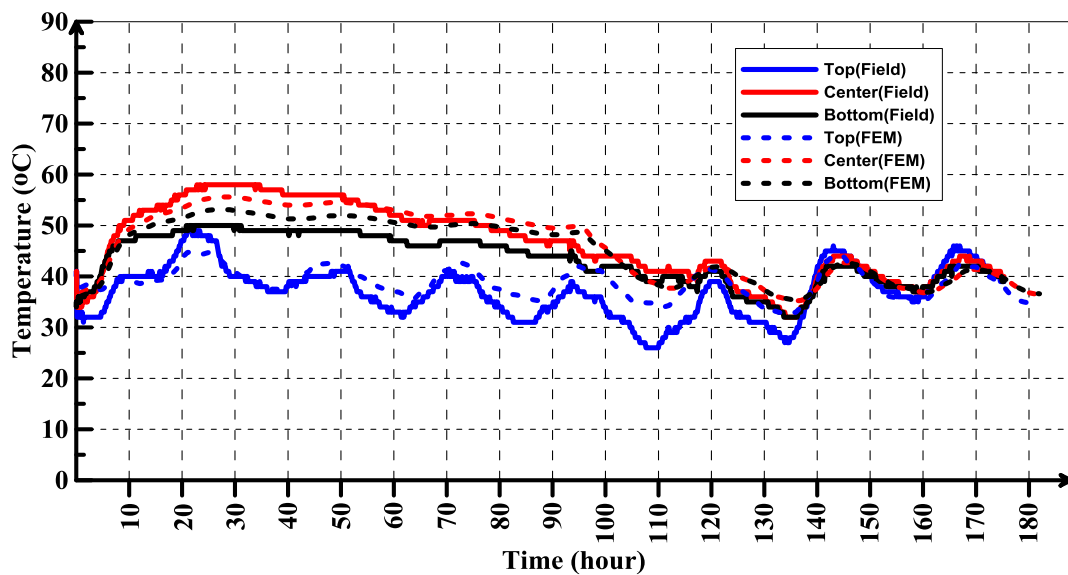


**Figure 7-8: Temperature Rise at Location 3 for Mockup#2 in KMUS (40% Fly Ash)**

In the mock-up specimen #3, OPC was replaced with 60% Fly Ash. The comparison between the results of field monitoring and the results of finite element simulation in the mock-up specimen#3 are shown in Figure 7-9 to Figure 7-11.

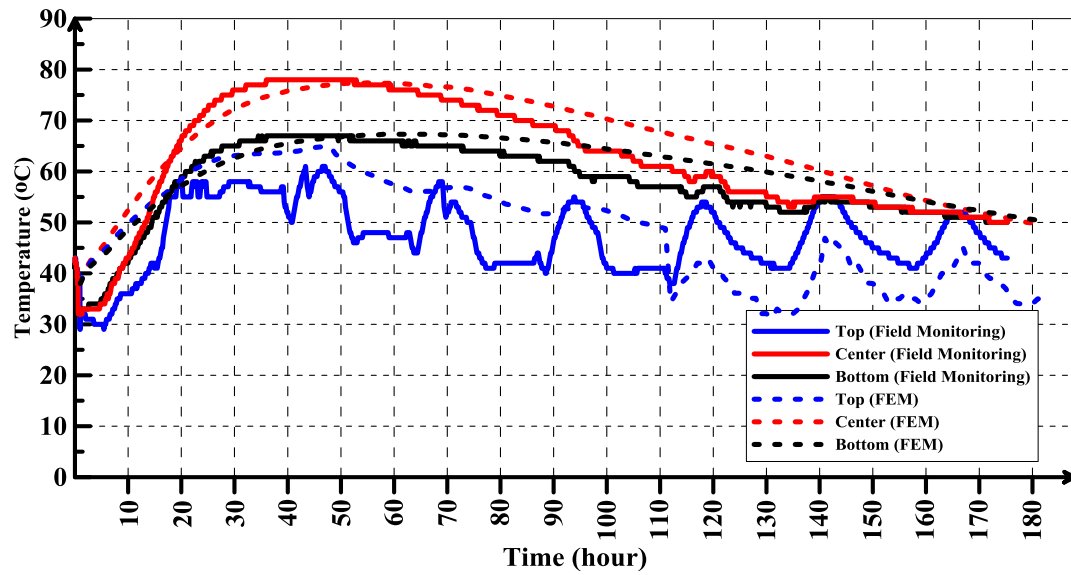


**Figure 7-9: Temperature Rise at Location 1 for Mockup#3 in KMUS (60% GGBFS)**

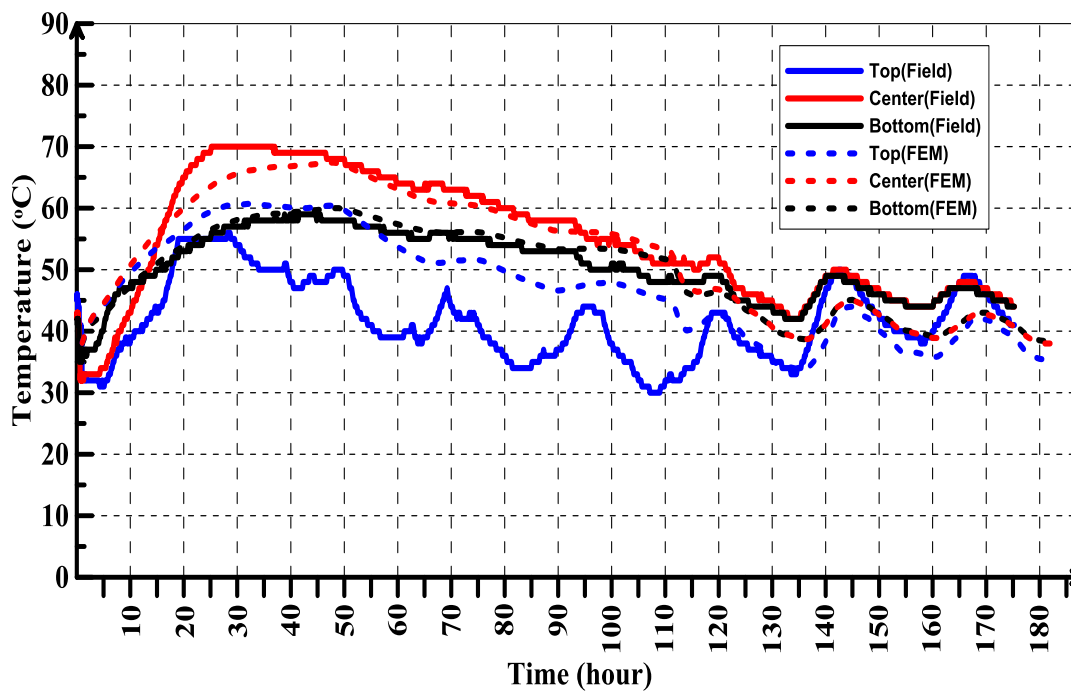


**Figure 7-10: Temperature Rise at Location 2 for Mockup#3 in KMUS (60% GGBFS)**

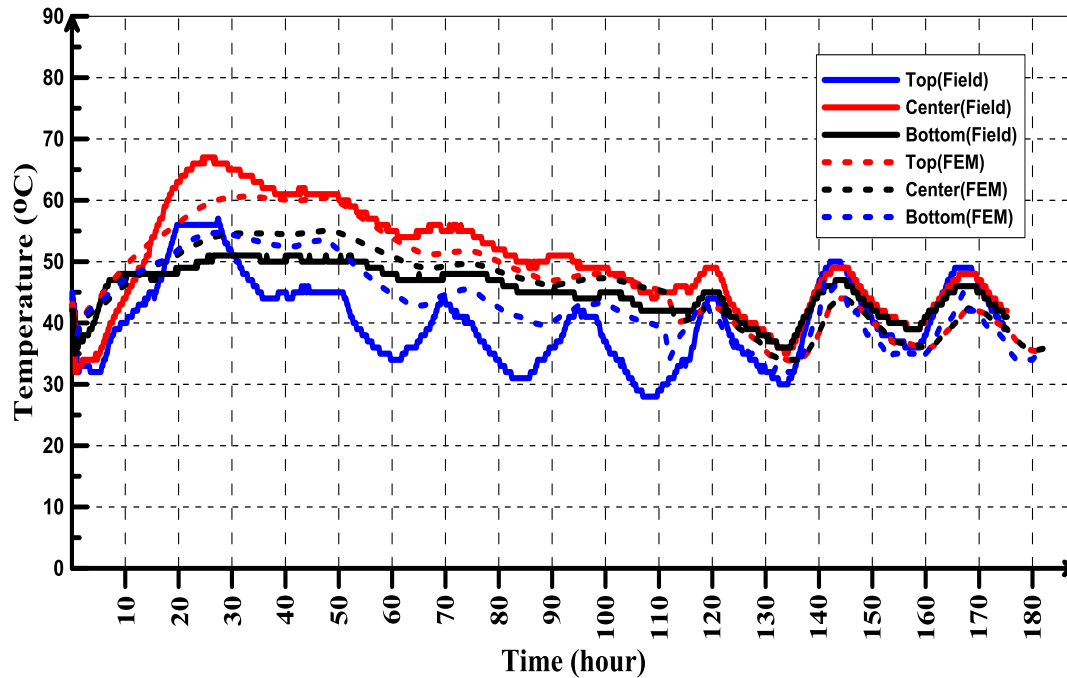


**Figure 7-11: Temperature Rise at Location 3 for Mockup#3 in KMUS (60% GGBFS)**

### 7.2.2 Temperature Simulation Results of DMUS

In the DMUS, the steel formwork was used instead of plywood formwork. The Polystyrene foam was used to insulate the top surfaces of mockup specimens for reducing the temperature difference. The DMUS were slightly reinforced with two layers of steel reinforcement ( $7\phi 12/m$ ). The total content of cementitious materials in the mixes used for casting the DMUS was  $400 \text{ Kg/m}^3$ . The concrete mixture used in the first mock-up specimen of DMUS contains 50% of cement Type II and 50% GGBFS. The measured slump was 220mm. The placement temperature was  $29^\circ\text{C}$ . The comparison between the results of field monitoring and the results of finite element simulation in the mock-up specimen#1 are shown in Figure 7-12 to Figure 7-14.

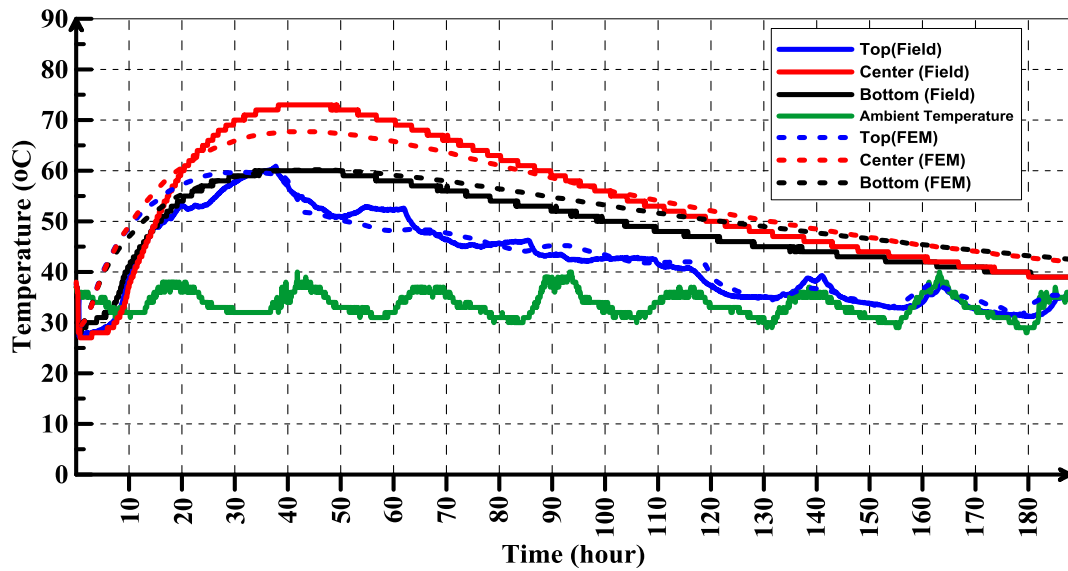


**Figure 7-12: Temperature Rise at Location#1 for Mockup#1 in DMUS (50% GGBFS)**

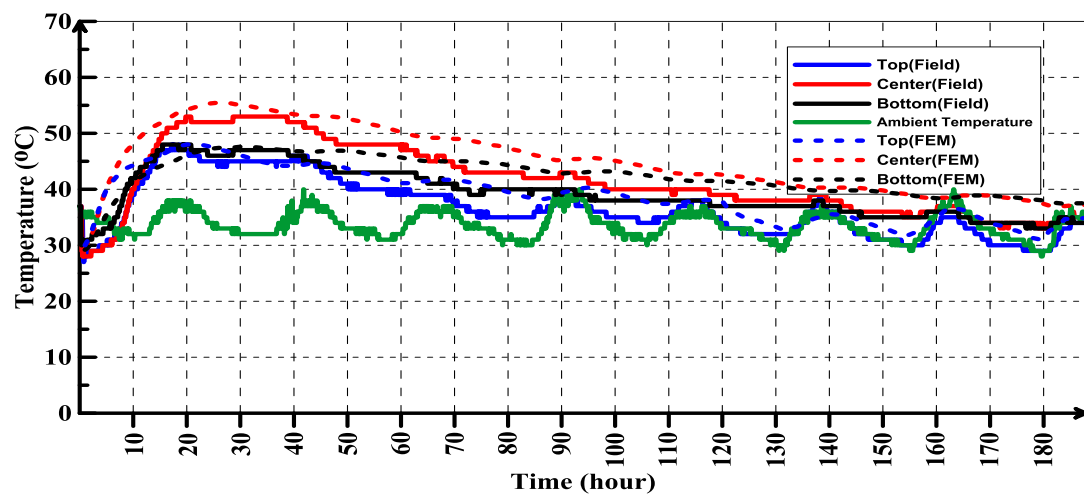


**Figure 7-13: Temperature Rise at Location#2 for Mockup#1 in DMUS (50% GGBFS)**

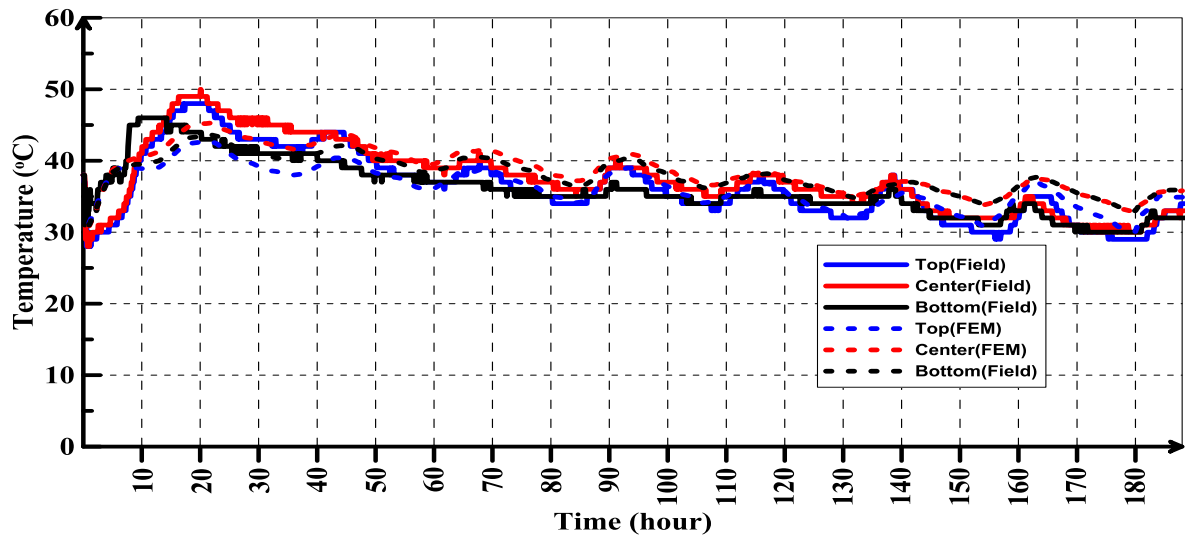


**Figure 7-14: Temperature Rise at Location#3 for Mockup#1 in DMUS (50% GGBFS)**

The concrete mixture used in the second mock-up specimen in DMUS contains 35% of cement Type II and 65% GGBFS. The measured slump was 180mm. The placement temperature was 29 °C. The comparison between the results of field monitoring and the results of finite element simulation in the mock-up specimen#2 are shown in Figure 7-15 to Figure 7-17.

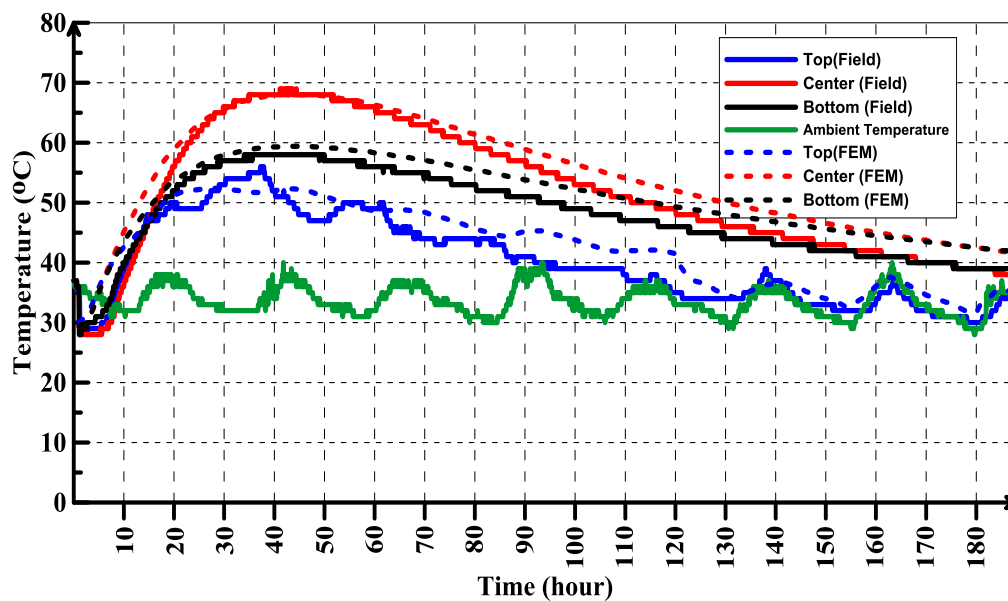


**Figure 7-15: Temperature Rise at Location#1 for Mockup#2 in DMUS (65% GGBFS)**

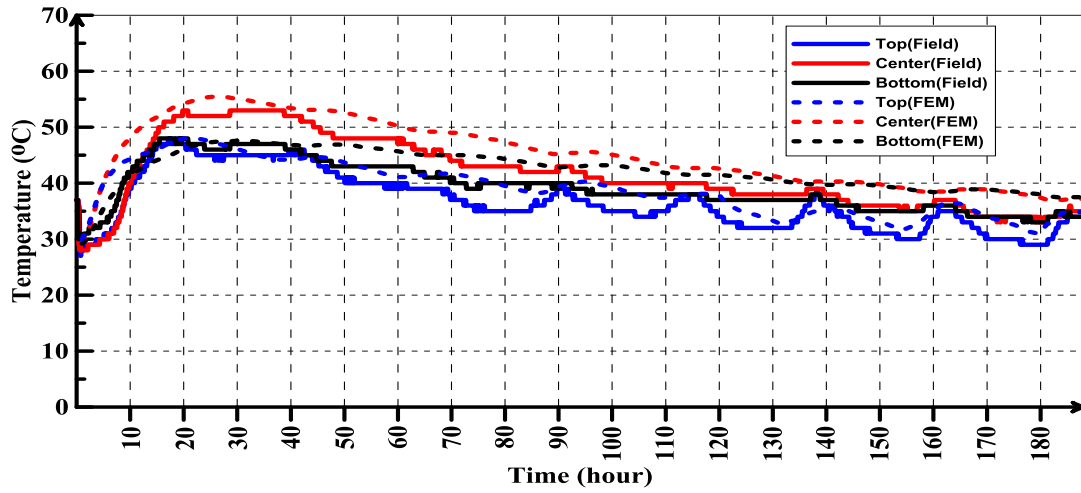


**Figure 7-16: Temperature Rise at Location#2 for Mockup#2 in DMUS (65% GGBFS)**

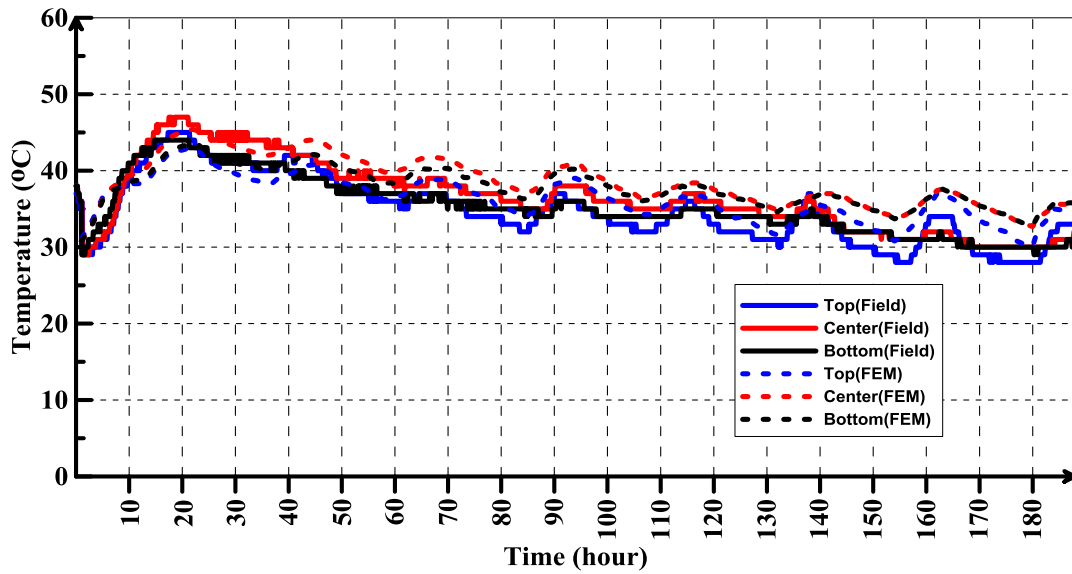


**Figure 7-17: Temperature Rise at Location#3 for Mockup#2 in DMUS (65% GGBFS)**

The mix used in the mock-up #3 in DMUS contains 30% of cement Type II and 60% GGBFS. The measured slump was 150mm. The placement temperature was 28 °C.

The comparison between the results of field monitoring and the results of finite element simulation in the mock-up specimen#2 are shown in Figure 7-18 to Figure 7-20.

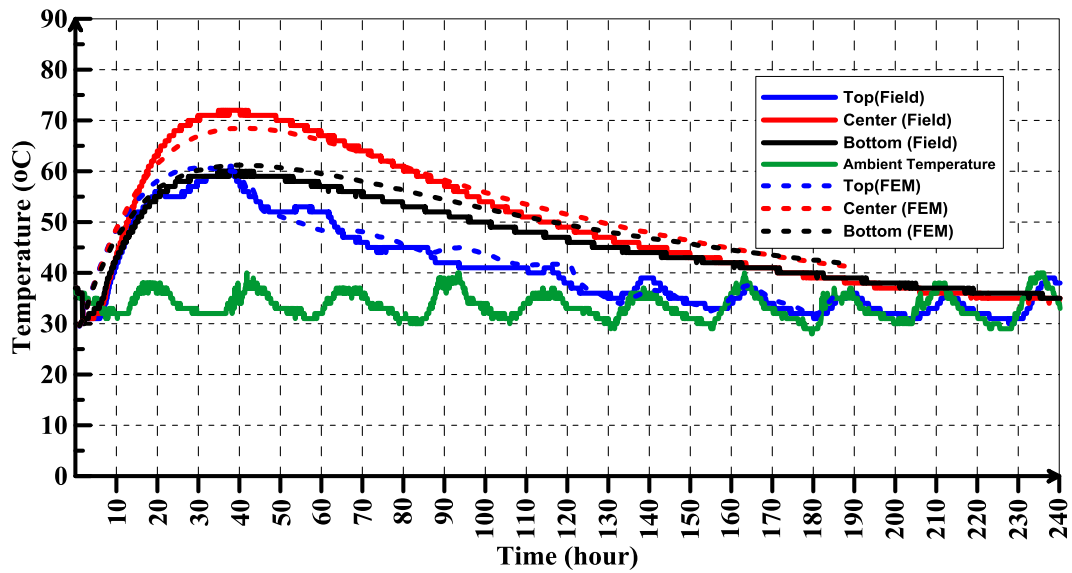


**Figure 7-18: Temperature Rise at Location#1 for Mockup#3 in DMUS (70% GGBFS)**

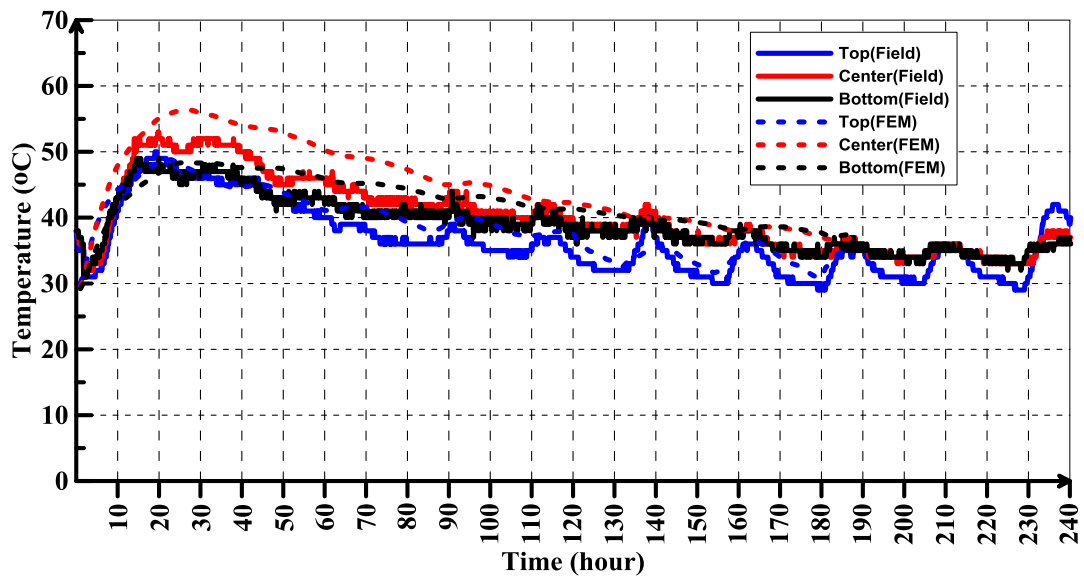


**Figure 7-19: Temperature Rise at Location#2 for Mockup#3 in DMUS (70% GGBFS)**

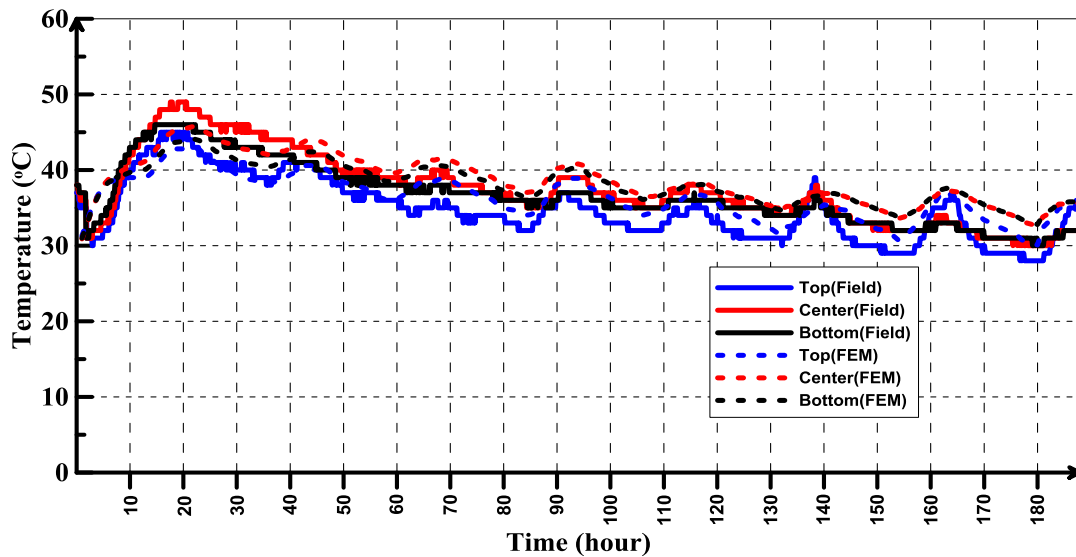


**Figure 7-20: Temperature Rise at Location#3 for Mockup#3 in DMUS (70% GGBFS)**

### 7.2.3 Temperature Simulation Results of JMUS

The heat transfer analysis was carried out for the JMUS. The locations of thermocouples are shown in Figure 3-28. Figure 7-20 to Figure 7-22 show the comparison between the results of field monitoring and the results of finite element simulation in the JMUS at locations 1, 2 and 3.

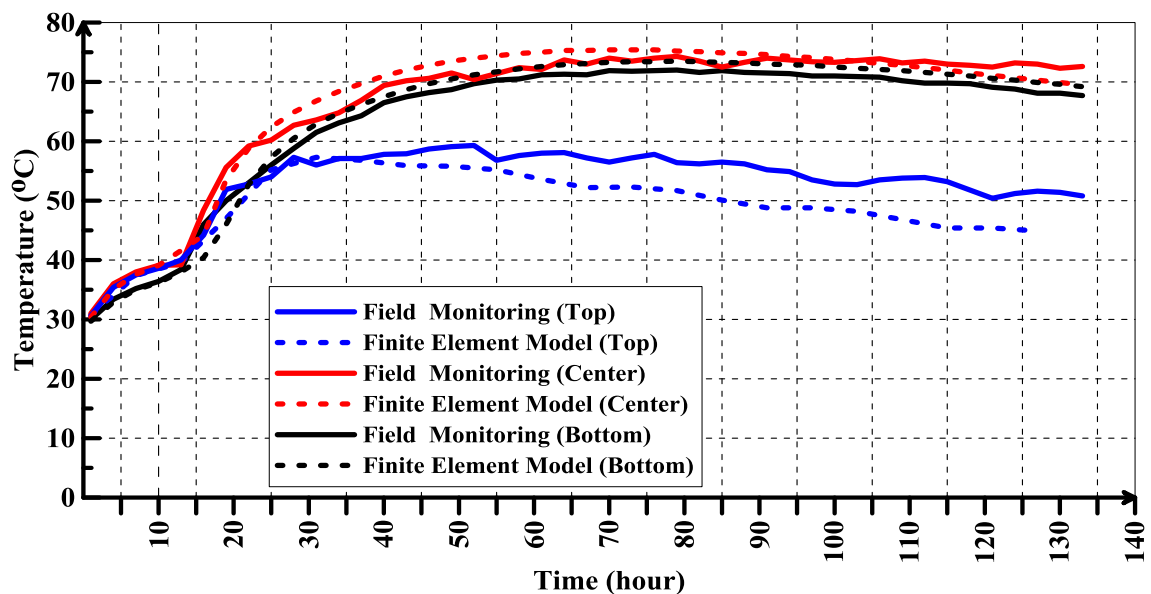


**Figure 7-21: Temperature Rise at Location#1 for JMUS**



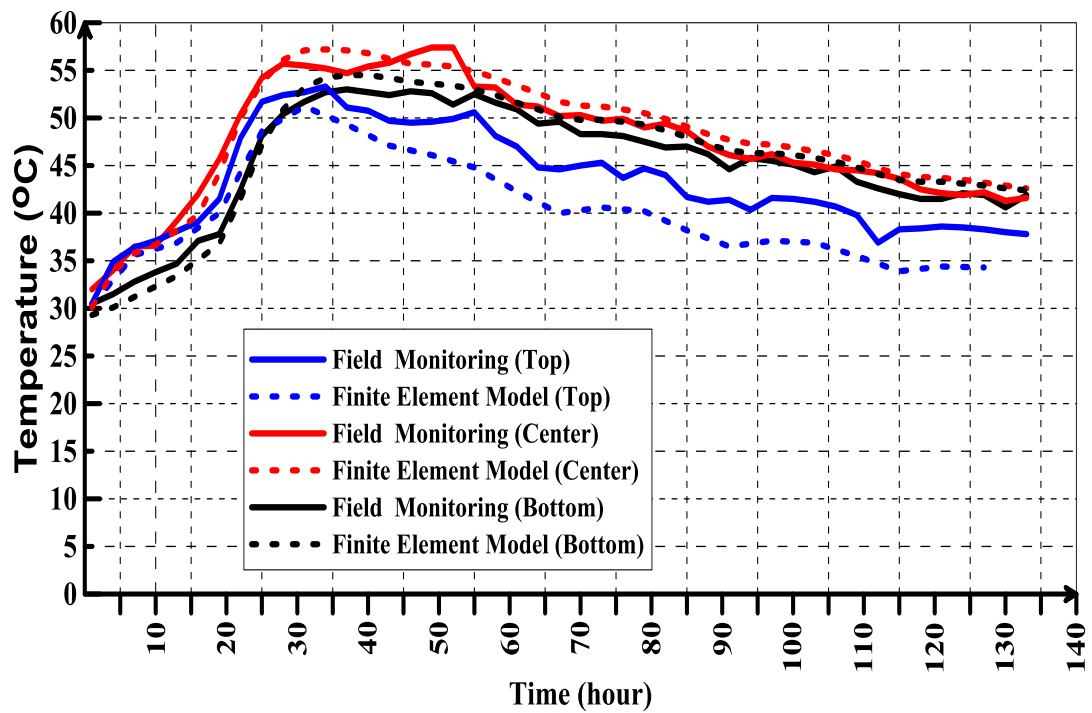


Figure 7-22: Temperature Rise at Location#2 for JMUS

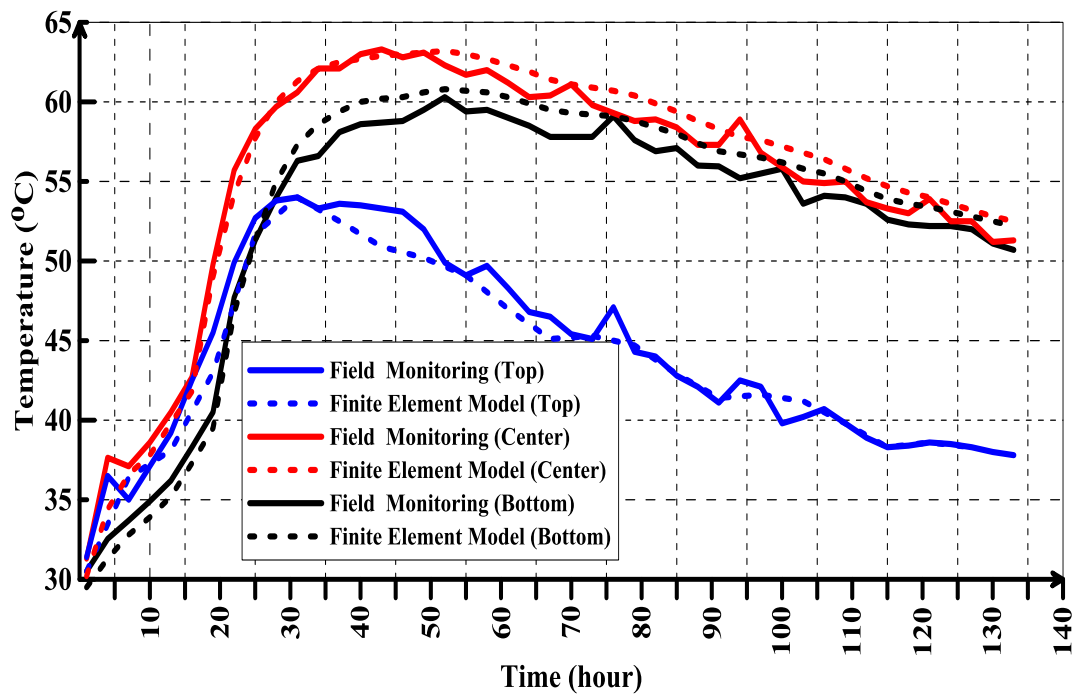
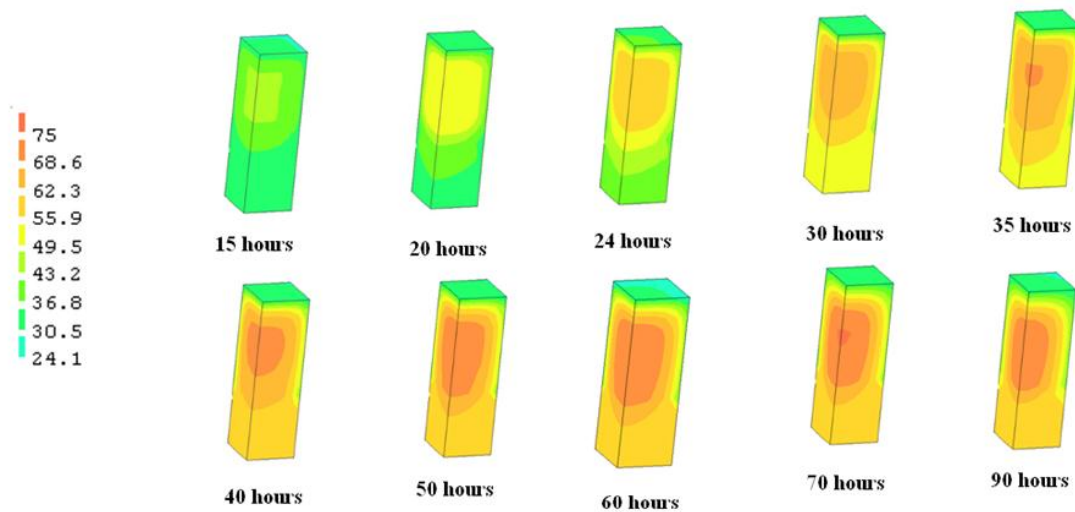


Figure 7-23: Temperature Rise at Location#3 for JMUS

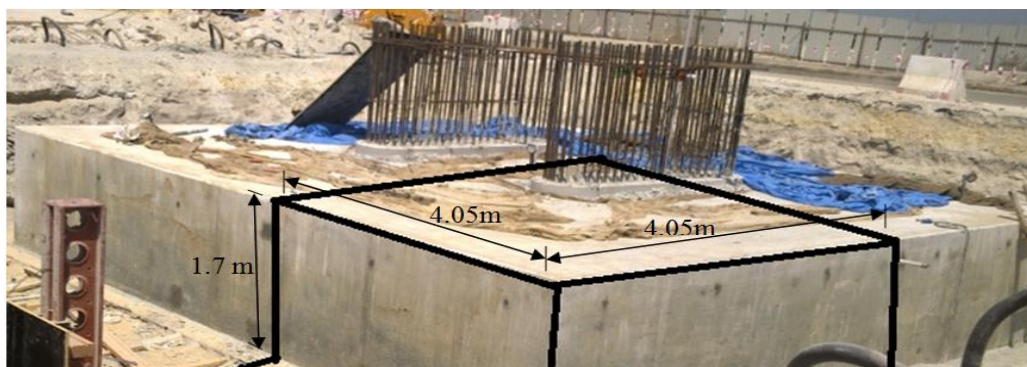
The evolution of temperature distribution at different ages in the mock-up concrete is shown in Figure 7-24, where it can be observed that the peak temperature at the core of mock-up reaches around 74 °C at age 70 hours.



**Figure 7-24: Contours of Temperature Distribution at Different Ages**

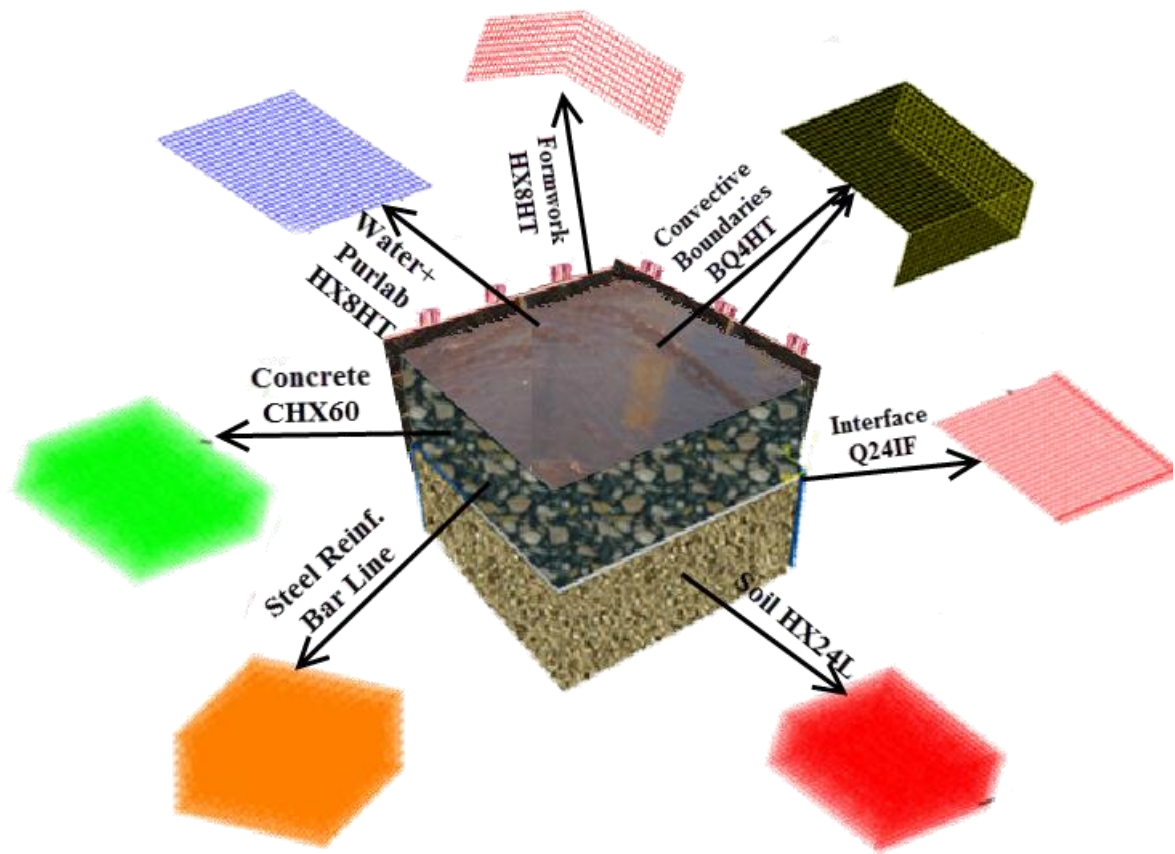
#### 7.2.4 Temperature Simulation Results of Piles-Cap

The simulation of the early age thermal behavior of the piles-cap was conducted using Finite Element Method. Due to symmetry, only quarter of piles cap is modeled as shown in Figure 7-25.



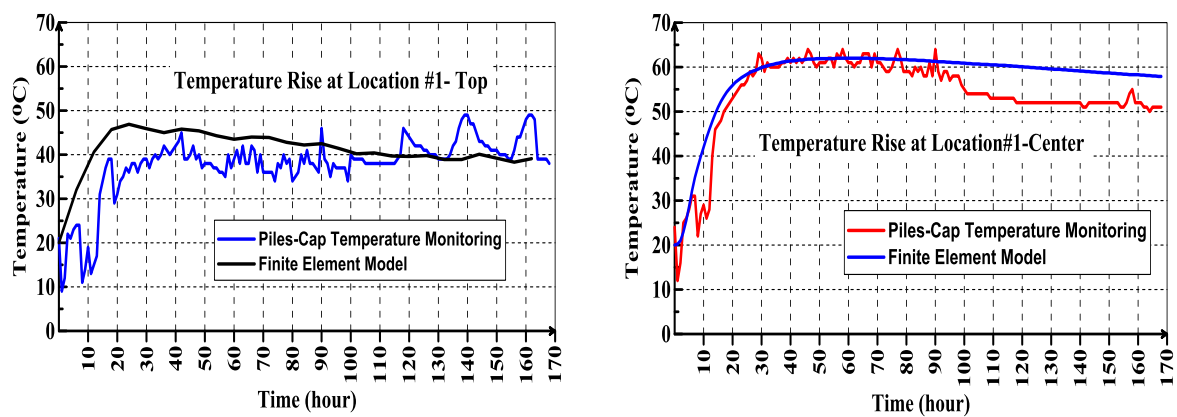
**Figure 7-25: Dimensions of Quarter of Pile Cap Used in Simulation**

The plywood formwork and the water curing layer were explicitly modeled in the finite element simulation. Since only the effect of curing water and formwork on the convection of the thermal energy generated in the concrete is of interest, these materials were modeled using the flow elements (HX8HT) in DIANA. The flow elements are active only during the thermal analysis of the pile cap. The blinding concrete layer of the piles cap with a thickness of 10 cm and the sandy soil were modeled using the quadratically interpolated structural element (HX24L) for the finite element analysis. The HX24L element is converted during the thermal analysis to a linearly interpolated flow element. The concrete was modeled using the 20-noded isoperimetric solid brick element (CHX60) in DIANA. The outer surfaces which are subjected to convections (plywood and water curing layer) were modeled using the BQ4HT element which is a four-noded isoperimetric quadrilateral element specially used to describe boundaries in three-dimensional thermal analyses. Figure 7-26 shows all types of element which used in simulating the temperature distribution in the piles cap.



**Figure 7-26: Element Types in finite Element Simulation of Piles-Cap**

The comparison between the results of field monitoring and the results of finite element simulation in the Piles-cap at locations #1,2, and 5 are shown in Figure 7-27.



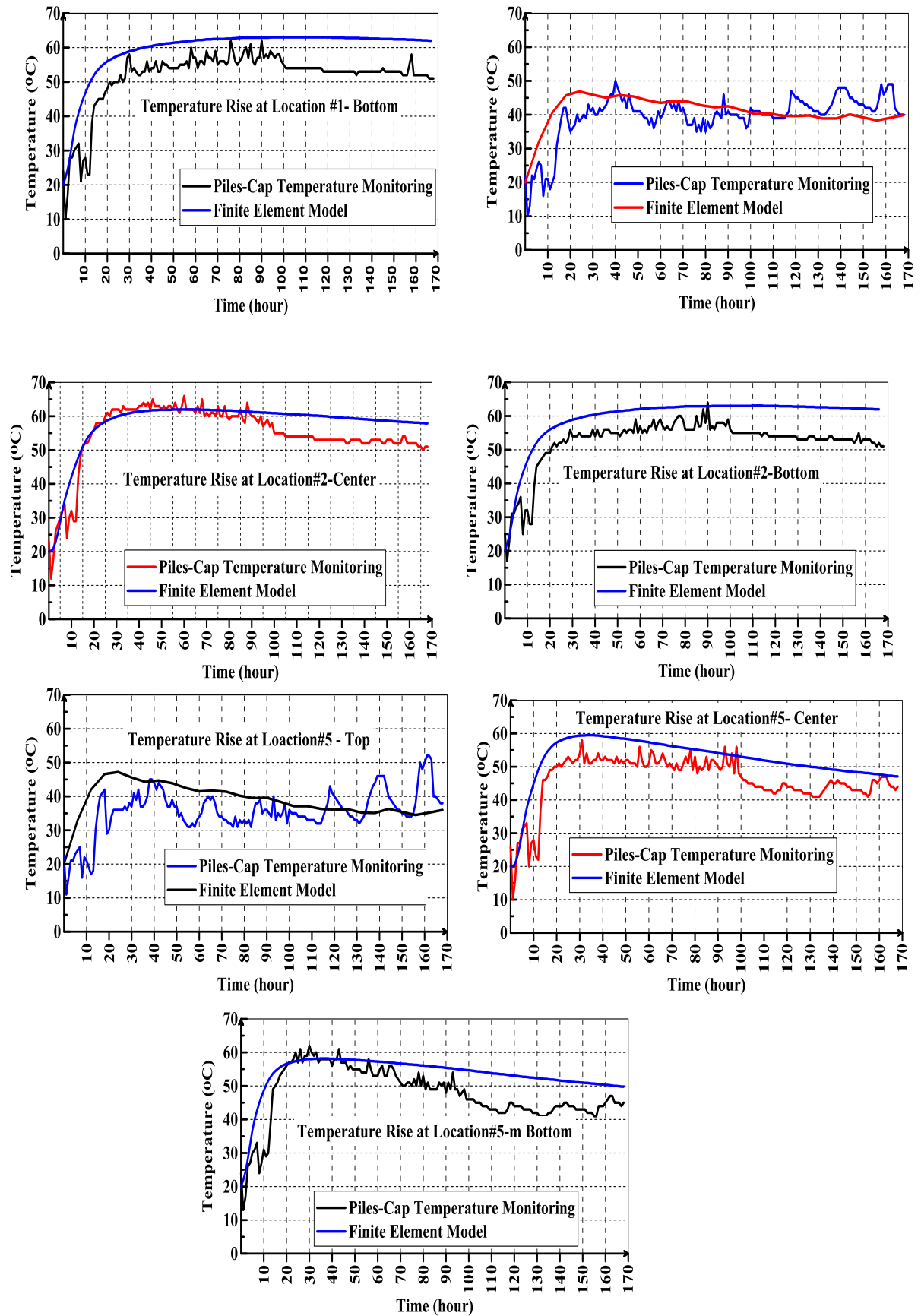


**Figure 7-27: Comparison of Measured and Finite Element Results of Evolution of Temperature at Various Locations in Piles Cap.**

The evolution of contour temperature distribution at different times is shown in Figure 7-28. It can be observed that the temperature at the core of piles-cap reaches around 65 °C after 30 hours from casting.

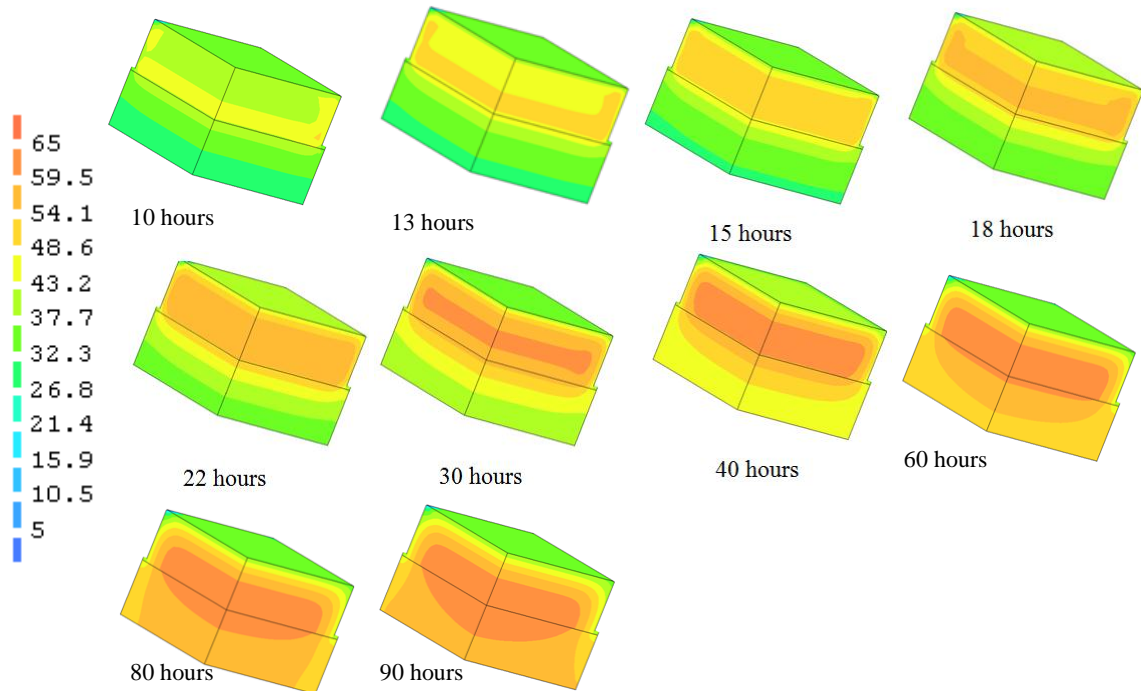


**Figure 7-28: Contours of Temperature Distribution in the Piles-Cap at Different Ages**

### 7.3 Stress Analysis Results

In this section, results of stress analysis using finite element method are presented. The evolution of mechanical properties of concrete (Tensile strength and modulus of elasticity) is used as input. As sated earlier, the cracking behavior is simulated using a smeared cracking concept, in which the cracked material is treated as continuous, and the discontinuity of the displacement field caused by the crack is spread across the element by changing the constitutive equation. A constant shear retention factor  $\beta$  for the cracked concrete is assumed equal to 0.2 in the finite element simulation. The tension softening criterion is applied depending on the maturity. The behavior of concrete in tension was modeled as

linear up to the concrete tensile strength ( $f_t$ ) . A linear tension cut-off governed crack initiation. A crack forms according to the linear cut-off criterion if the principle tensile stress exceeds the tensile strength of concrete. The post-cracking behavior of concrete modeled by a linear softening model. The required inputs for the FE simulation are summarized in Appendix A.

The elements located at the top, middle, and bottom of the central line AB of mock-up specimens and piles-cap (as shown in Figure 7-29) were chosen for analyzing their stresses during the hydration process. These locations were chosen because the largest tensile and compressive actions will be experienced at the top and central region of the concrete respectively.

### **7.3.1 Stresses Results of KMUS**

The stresses in x direction ( $S_{xx}$ ) are predicted by finite element model. Figure 7-30 shows the predicted stresses in x direction for the element located at the top center of surface (see Figure 7-29) of the three mock-up specimens of KMUS group. It can be observed from Figure 7-30 that the element located at the top center of surface undergoes tensile stresses. The tensile stresses in the mockup specimen #1 are higher than others. This is due to the high content of cement in the mockup specimen #1. The KMUS#2 (40%Fly Ash) has the lowest tensile stresses. This indicates that the Fly ash has a significant effect in reducing the heat of hydration .Consequently, the tensile stresses decreases.



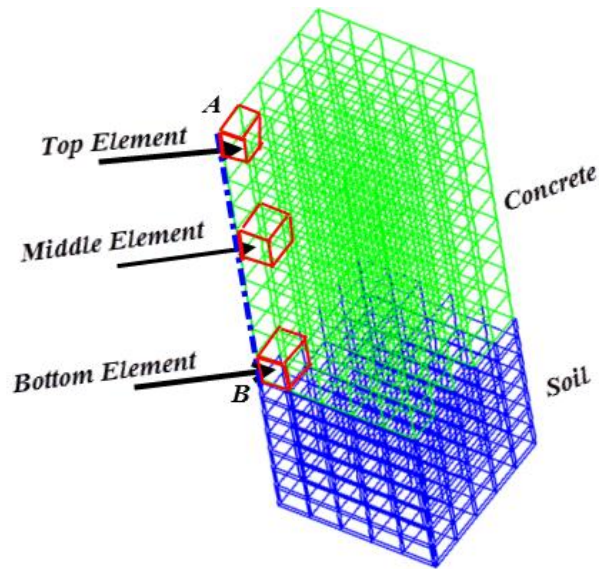


**Figure 7-29: Locations of Elements for Stress Analysis**

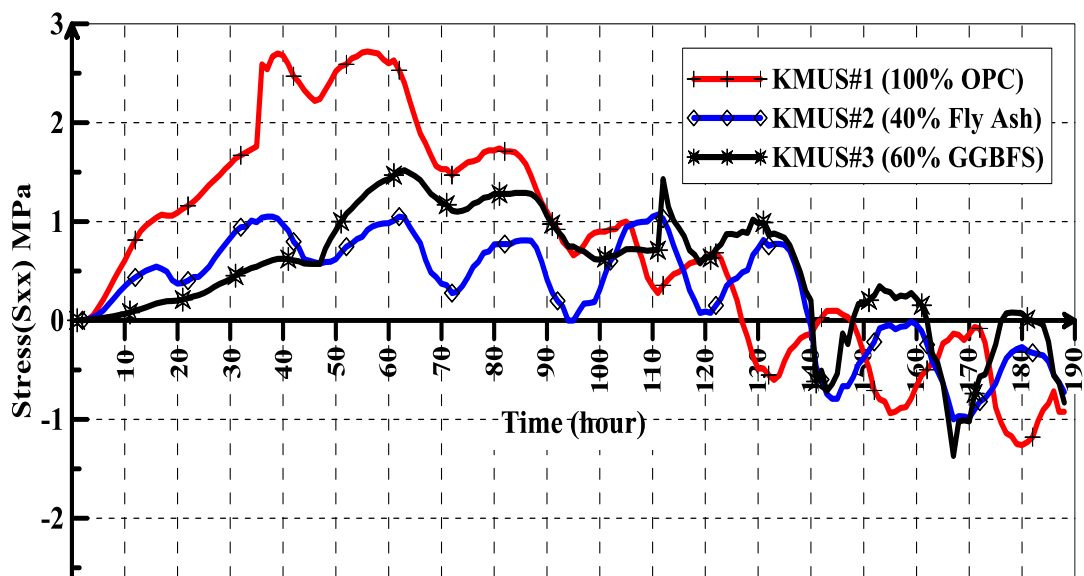


**Figure 7-30: Stresses in X Direction ( $S_{xx}$ ) for the Element Located at Top Surfaces of KMUS**

It is clear from Figure 7-30 that the use of OPC without addition of mineral admixture leads to develop high tensile stresses which increases the potential of cracking.

The developed stresses in the element located at the center of KMUS (see Figure 7-29) are shown in the Figure 7-31.



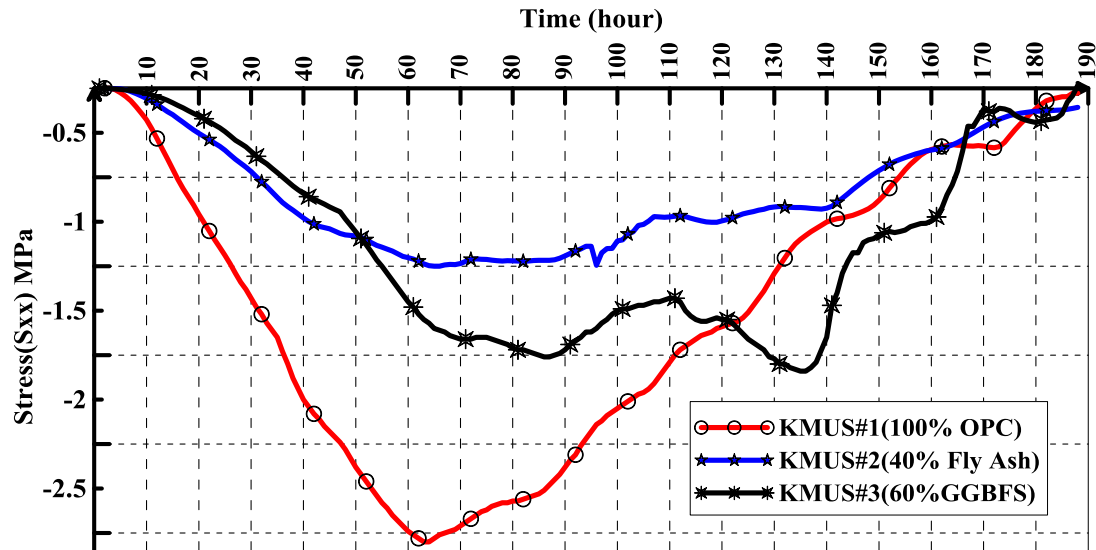


**Figure 7-31: Stresses in X Direction ( $S_{xx}$ ) for the Element Located at Core of KMUS**

Figure 7-31 shows that the element located at the core of KMUS is under compressive stresses. The heat of hydrating at the core of mockup specimens is higher than the heat of regions that in contact with the environmental conditions. This makes the core is under expansion but this expansion is restricted by the less mature concrete around it. Consequently, the compressive stresses are developed at the core of mockup specimens. The compressive stresses in the mockup specimen #1 are higher than other two mockup specimens. The compressive stresses in the mockup specimen#2 (40% Fly Ash) are lower than in the mockup specimen#3 (60% GGBFS).

The development of stresses in the element located at the bottom of KMUS is shown in Figure 7-32.

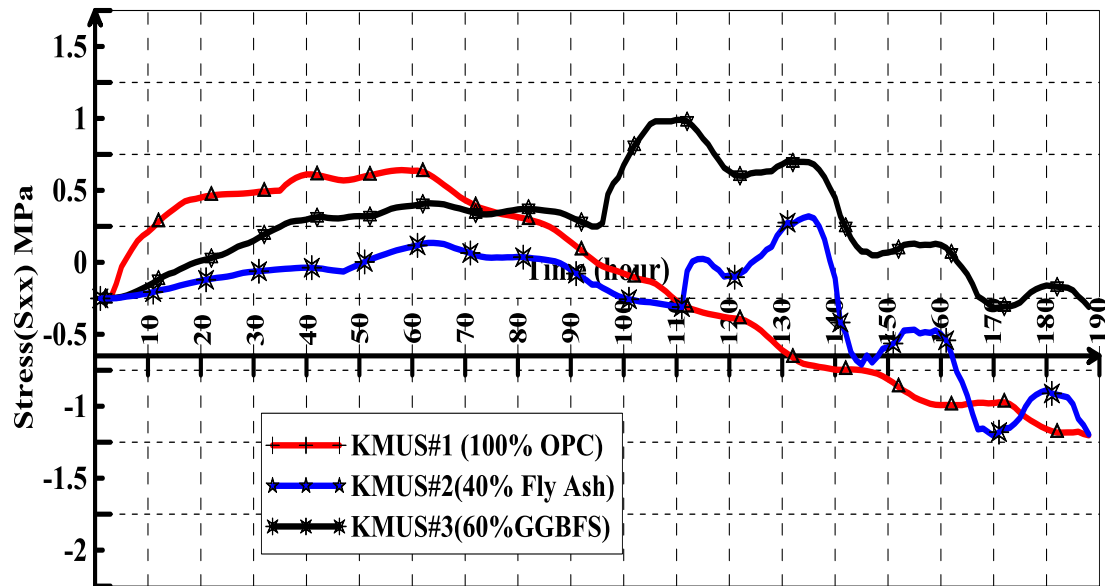


**Figure 7-32: Stresses in X Direction ( $S_{xx}$ ) for the Element Located at Bottom of KMUS**

Figure 7-32 shows that the Element located at the bottom of central line of KMUS is subjected to tensile stresses. The plywood formwork of the two mockup specimens #2 and #3 was removed after about 4 days from casting. Therefore, the increase in tensile stresses for the mockup specimens #2 and #3 after about 4 days from casting (96 hours) is resulting from the removal of plywood formwork of these two mockups earlier than of mockup specimen #1.

At age of 30 hours from casting, the evolution of temperature, cracking index and stresses in x direction ( $S_{xx}$ ) across the central line AB of the three mockup specimens are shown in Figure 7-33.

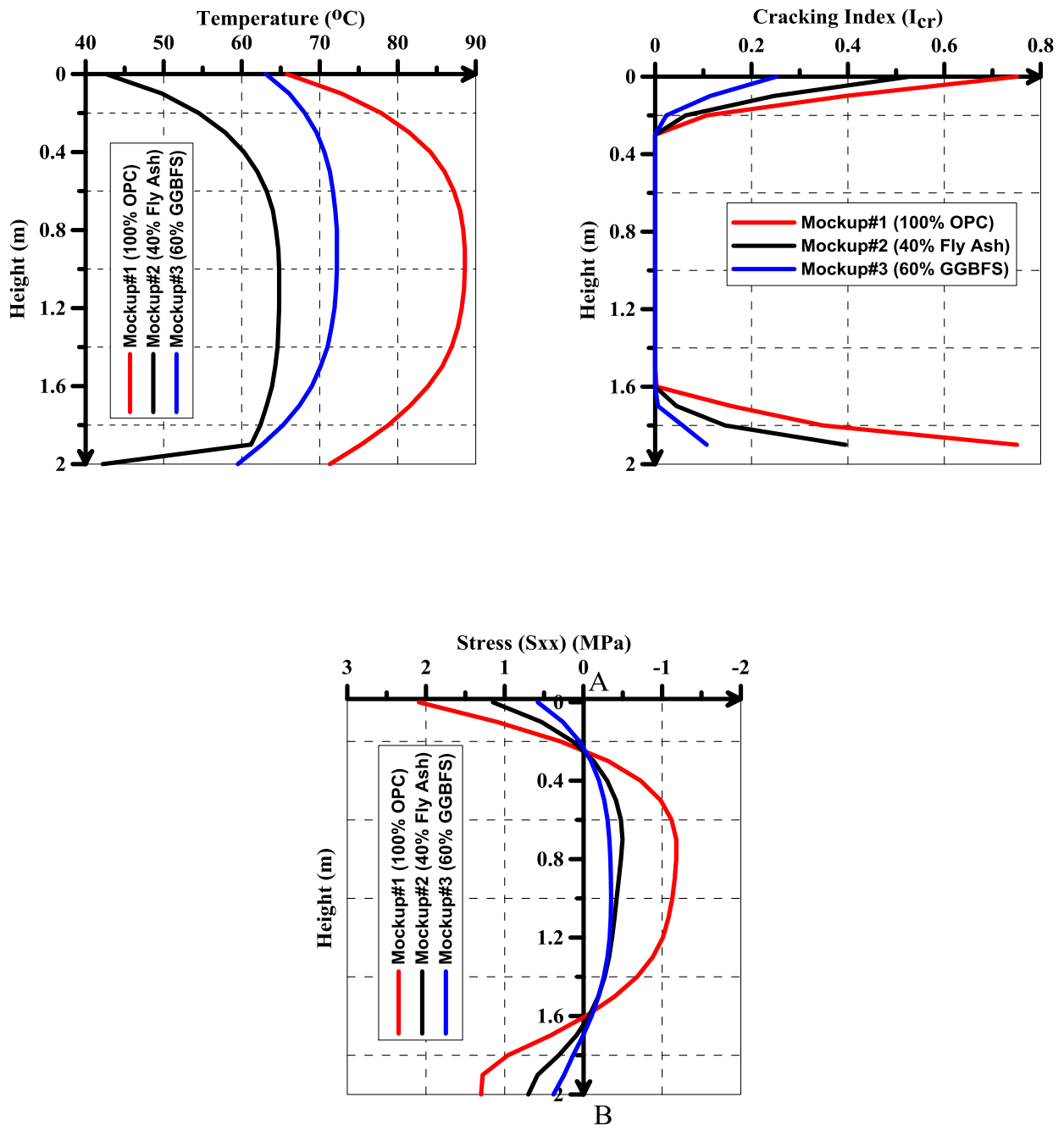


**Figure 7-33: Evolution of Temperature, Cracking Index, and Stresses ( $S_{xx}$ ) Across the Depth AB (Fig.7-34) of Mockup Specimens (After 30 Hours from Casting)**

It can be noticed from Figure 7-33, the cracking index in the mockup#1(100% OPC) is higher than cracking index of the mockup #2 and#3. Although, the temperature rise in the

mockup#3(60% GGBFS) is higher than that of mockup#2(40% Fly Ash), the cracking index in mockup#3 is less. This is due to the effect of fly ash in reducing the mechanical properties of concrete (tensile strength and compressive strength) at early age.

The crack patterns of the mockup specimens after 40 hours from casting are shown in Figure 7-34 . It is clear; the mockup specimen #1 has been cracked whereas the mockup specimens #1 and #2 are free from cracks. The cracks developed at the top surface of the mockup specimen#1..

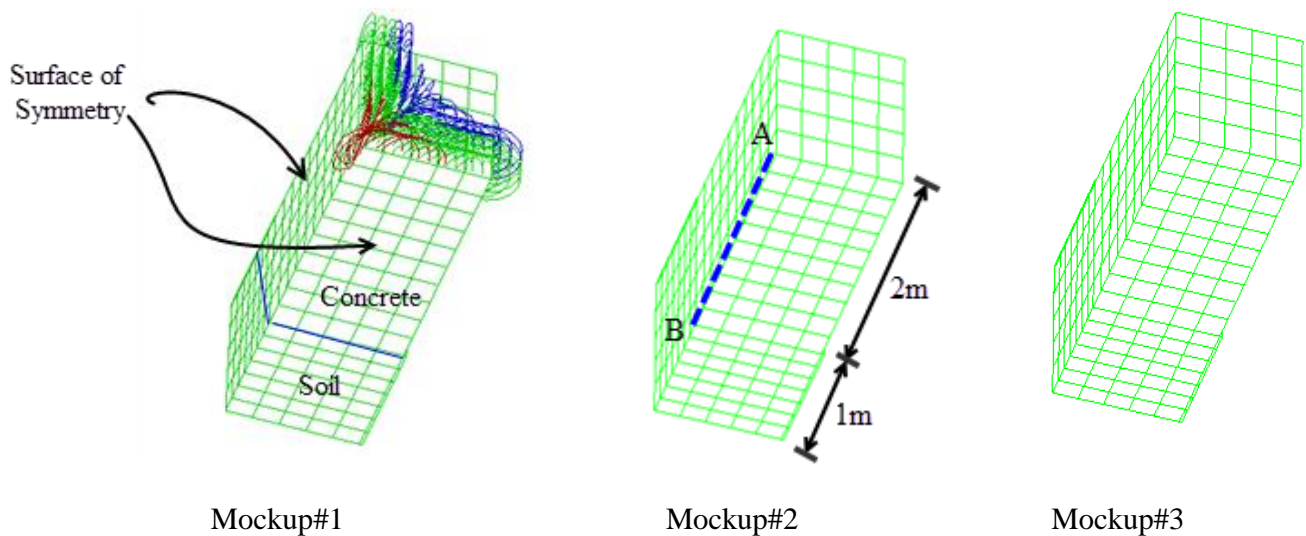


**Figure 7-34: Crack Pattern in the Mockup Specimens after 40 Hours from Casting**

The change of cracking index with time for the element located at the top center of mockups' surfaces is shown in Figure 7-35. It is noticed that the cracking index for the three mockup specimens is high at the first 60 hours from casting, and then starts to decrease. The 40% fly ash has less effect in reducing the probability of cracking during the early 45 hours when compared with the effect of 60% GGBFS. After 45 hours from casting, the mockup#2 (40% Fly Ash) became stiffer against cracking than mockup #3.

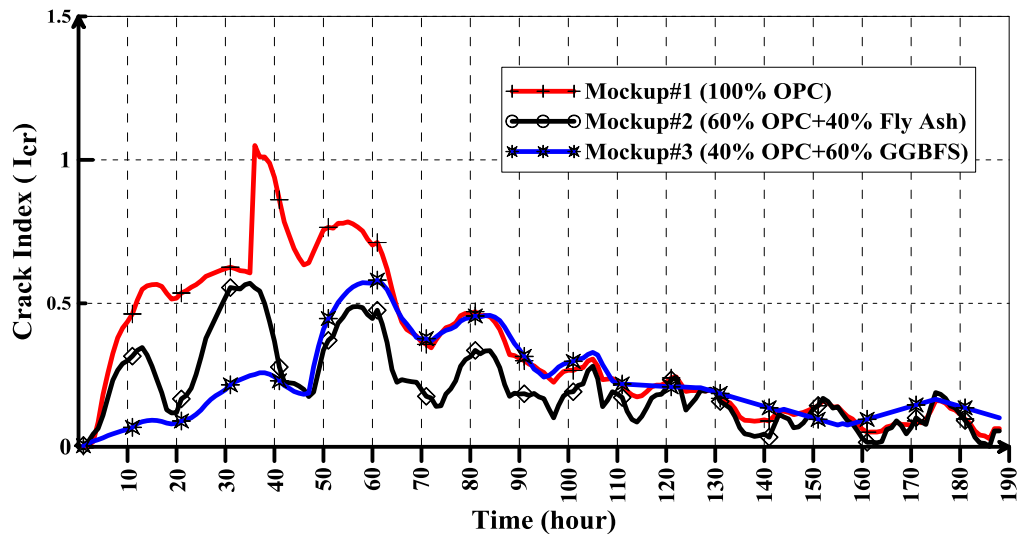


**Figure 7-35: Cracking Index of Element Located at the Top Centre of the Surface**

### 7.3.2 Stresses Results of DMUS

The stresses in x direction ( $S_{xx}$ ) are predicted by finite element model. Figure 7-36 shows the predicted stress in x direction for the element#205 located at the top center of surface (as shown in Figure 7-29) for the three mock-up specimens in DMUS group. It can be observed from Figure 7-36 that the element located at the top center of surface undergoes tensile stresses. The tensile stresses in the three mockup specimens are very close. The increase in the replacement percentage of GGBFS from 50% to 70% has a slight effect in increasing the stresses in X direction.

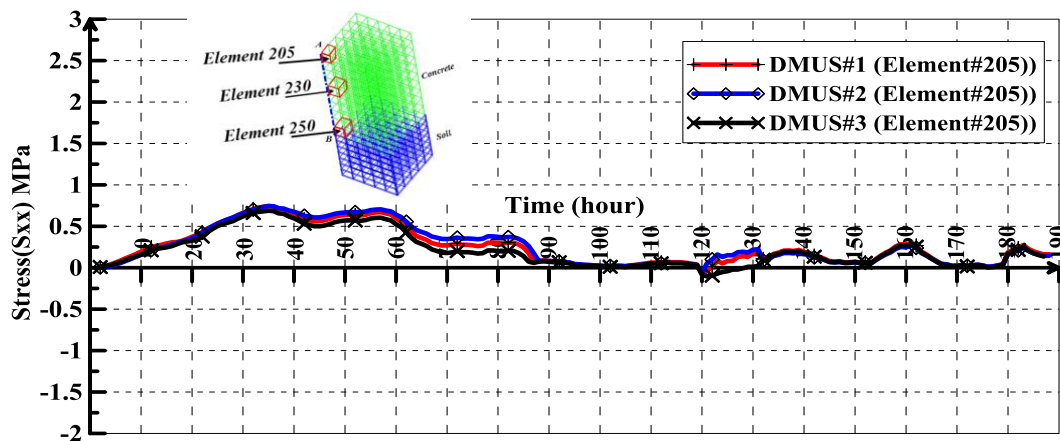


**Figure 7-36: Stresses in X Direction ( $S_{xx}$ ) for the Element Located at Top Surfaces of DMUS**

The developed stresses in the element located at the center (element#230) of DMUS ( see Figure 7-29) are shown in the Figure 7-37.

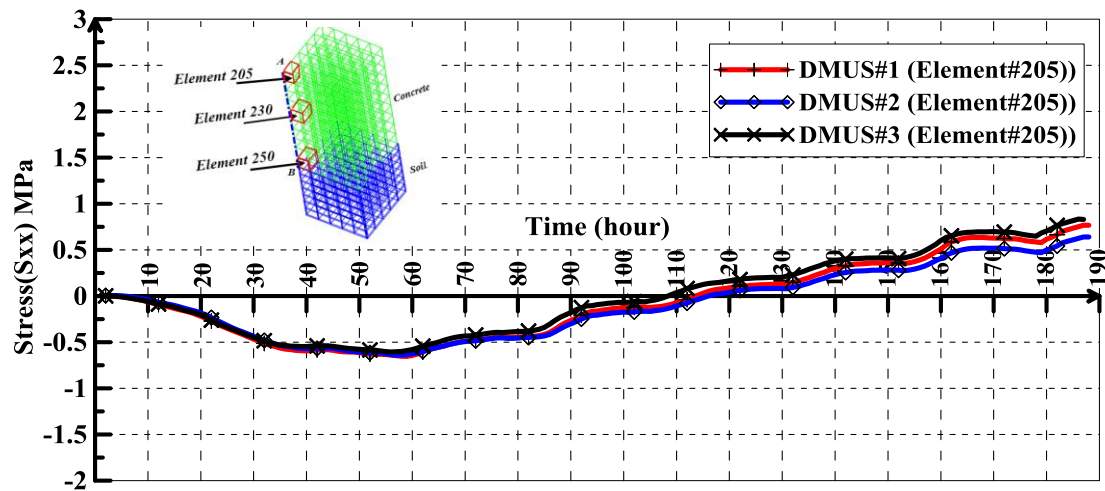


**Figure 7-37: Stresses in X Direction (Sxx ) for the Element Located at Core of DMUS**

Figure 7-37 shows that the element located at the core of KMUS is under compressive stresses. After 120 hours from casting, the stresses transition to tensile stresses. The steel formwork causes a rapid decrease in the peak temperature at the core of DMUS to become close to ambient temperature. This rapid drop in the peak temperature leads to a change in the stresses from compression to tension.

The development of stresses in the element located at the bottom of KMUS is shown in Figure 7-38. It shows that the Element located at the bottom of central line of DMUS is subjected to compressive stresses. The temperature difference between the core of DMUS and the bottom is not large. Therefore, the tensile stresses were not developed at the bottom element. At age of 30 hours from casting, the evolution of temperature, cracking index and stresses in x direction (Sxx) across the central line AB of the DMUS are shown in Figure 7-39. It can be noticed from Figure 7-39, the cracking index for the three mockups are almost the same. The effect of increasing the GGBFS from 50% TO 70% in the cracking index, temperature distribution and stresses in X direction is negligible.

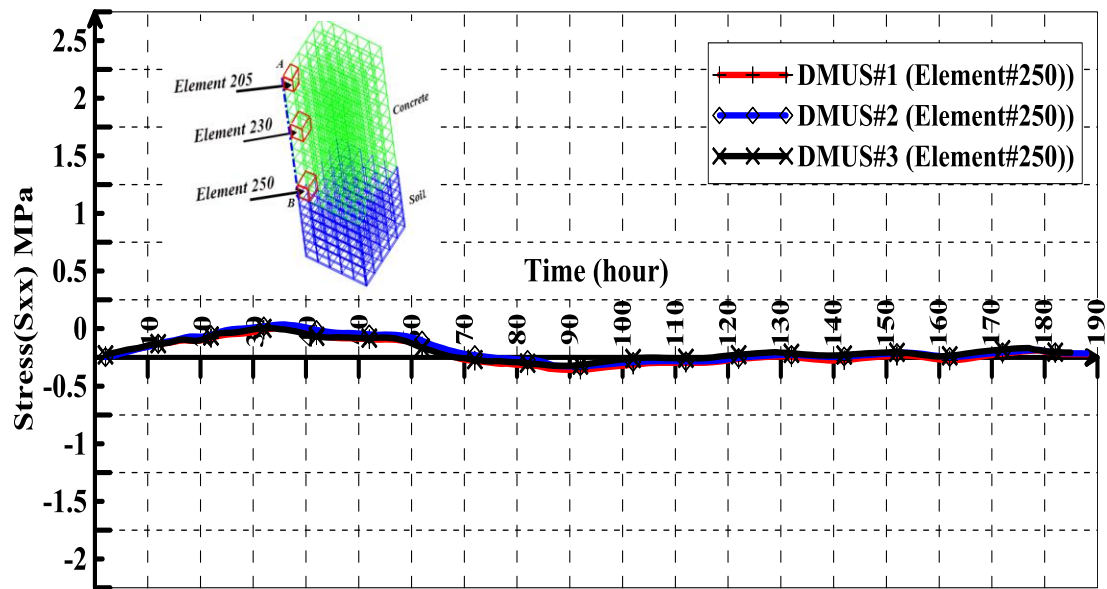


Figure 7-38: Stresses in X Direction ( $S_{xx}$ ) for the Element#250 Located at Bottom of DMUS

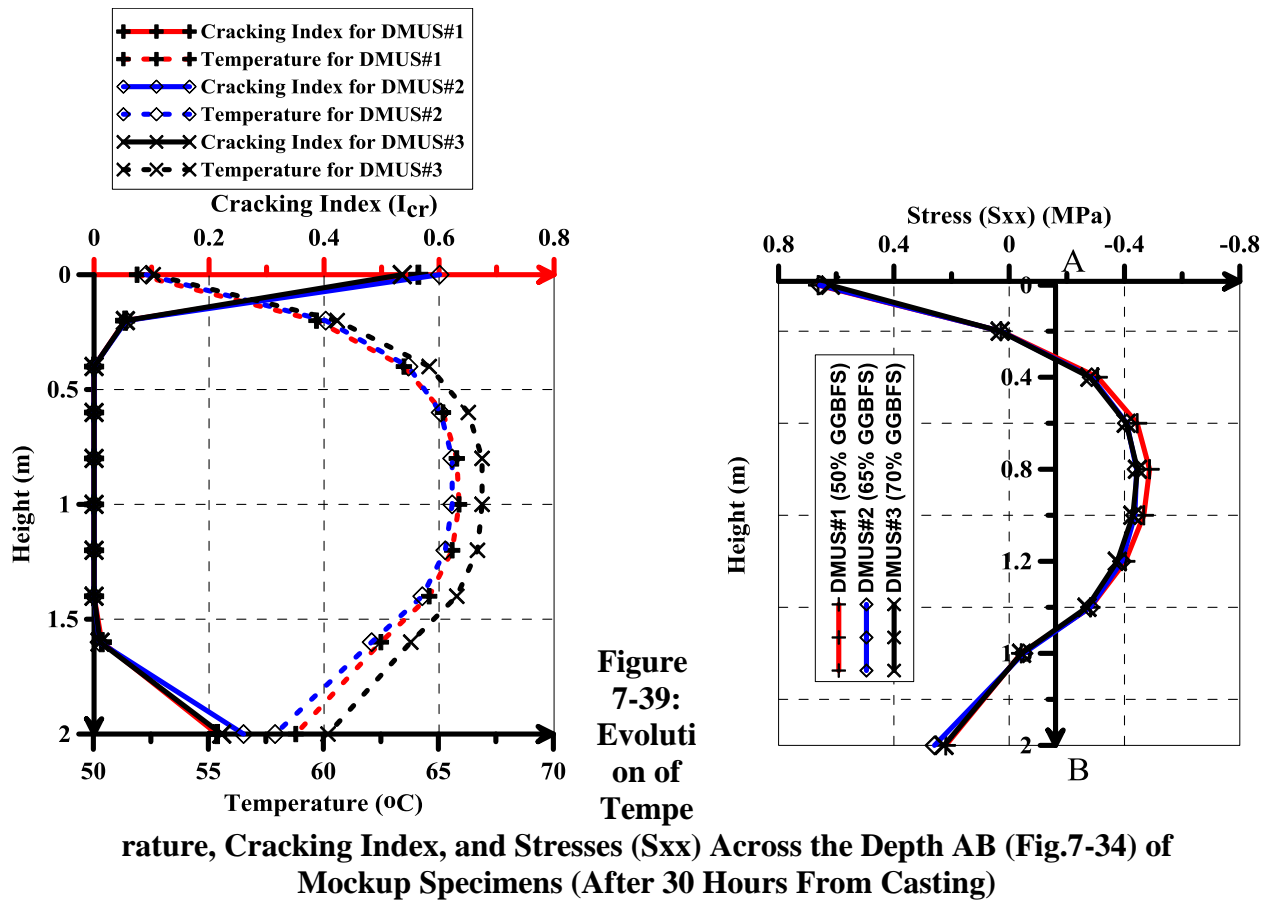
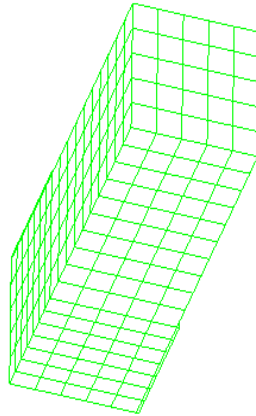


Figure 7-39:  
Evolution of Temperature, Cracking Index, and Stresses ( $S_{xx}$ ) Across the Depth AB (Fig.7-34) of Mockup Specimens (After 30 Hours From Casting)

The crack patterns of the mockup specimens after 40 hours from casting are shown in Figure 7-40. It is clear; the mockup specimens are free from cracks.



Mockup#1, 2 and 3

**Figure 7-40: Crack Pattern in the DMUS after 40 Hours from Casting**

The change of cracking index with time for the elements (205, 230, and 250) located at the top, center, and bottom of central line AB of DMUS is shown in Figure 7-41. It is noticed that the cracking index for the element #205 (located at the top surface) is less than one, which indicated that no cracks were formed in this element. After about 110 hours from casting, the cracking index for the element #230 (located at center of DMUS) starts to develop.

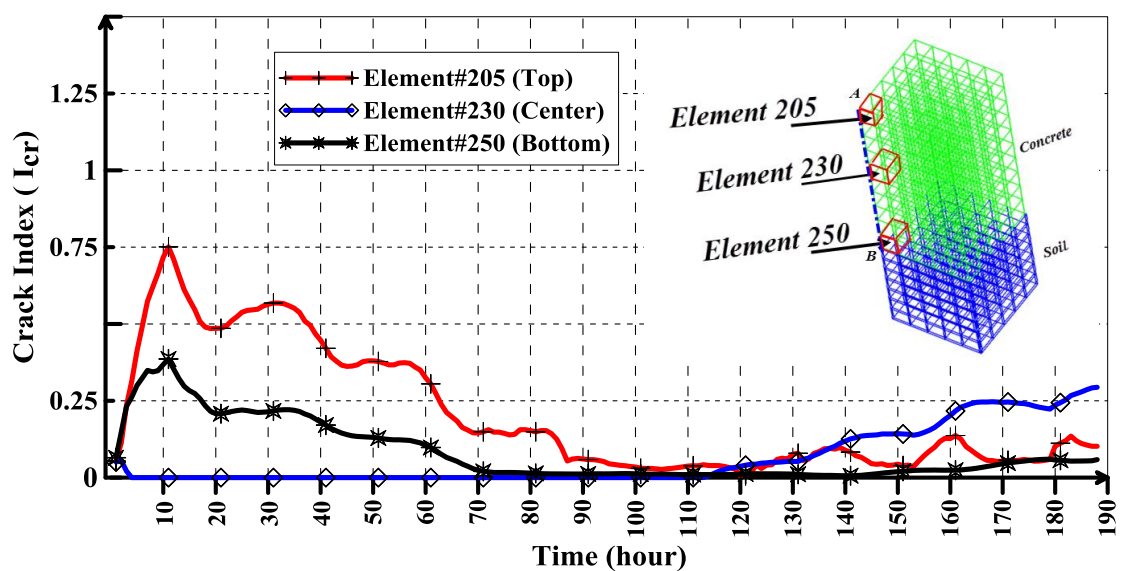


**Figure 7-41: Cracking Index of Elements 205, 230, and 250.**



### 7.3.3 Stresses Results of JMUS

The stress in x direction ( $S_{xx}$ ) is predicted by finite element model. Figure 7-42 shows the predicted stress in x direction for the elements located at the top, center and bottom of the center line of JMUS. It can be observed from Figure 7-42 that the elements located at the top and bottom are subjected to tensile stresses whereas the element located at the center is under compressive stresses. Due to the higher temperature gradient between the core and surface, the tensile stresses in the top surface element are higher than in the bottom element. After 30 hours from casting, the evolution of temperature, cracking index and stresses in x direction ( $S_{xx}$ ) across the central line AB of the JMUS are shown in Figure 7-43. It can be noticed from Figure 7-43, the cracking index in the top center of JMUS surface reached 0.82 after about 30 hours from casting. The elements located at height 0.5 m from the top to about 1.5m from bottom are subjected to compressive stresses. The zero cracking index indicated that the element is subjected to compressive stress. At 30 hours from casting, the tensile stresses in x direction reached about 1.2MPa which is close the tensile strength of concrete at this age .

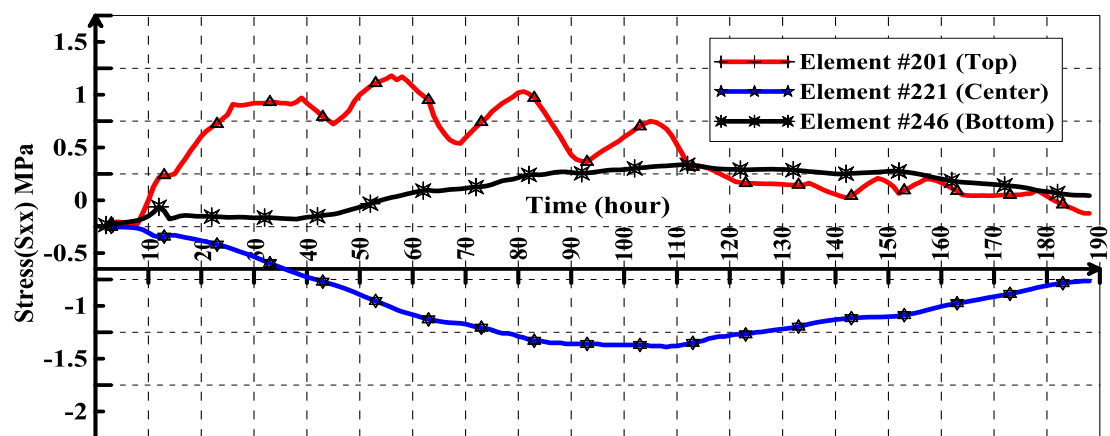


**Figure 7-42: Stresses in X Direction ( $S_{xx}$ ) for the Elements Located at Top, Center, and Bottom of Center Line of JMUS**

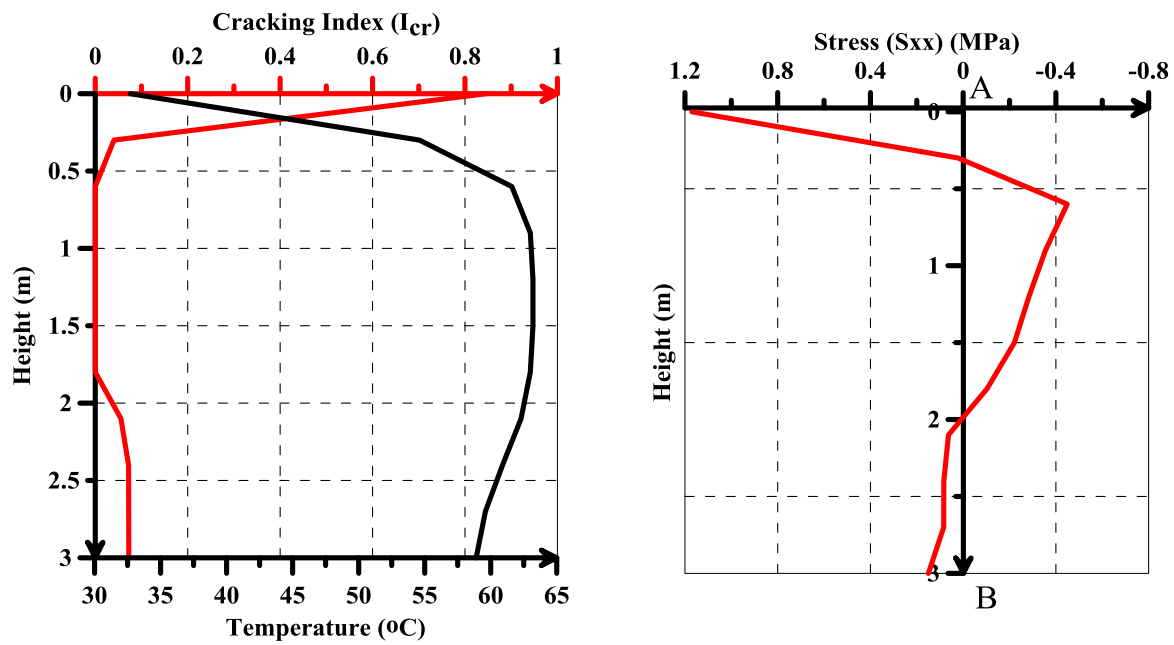


**Figure 7-43: Evolution of Temperature, Cracking Index, and Stresses ( $S_{xx}$ ) Across the Concrete Depth AB (Fig.7-29) of JMUS (After 30 Hours from Casting)**

The change of cracking index with time for the elements located at top, center, and bottom across the central depth of JMUS is shown in Figure 7-44.

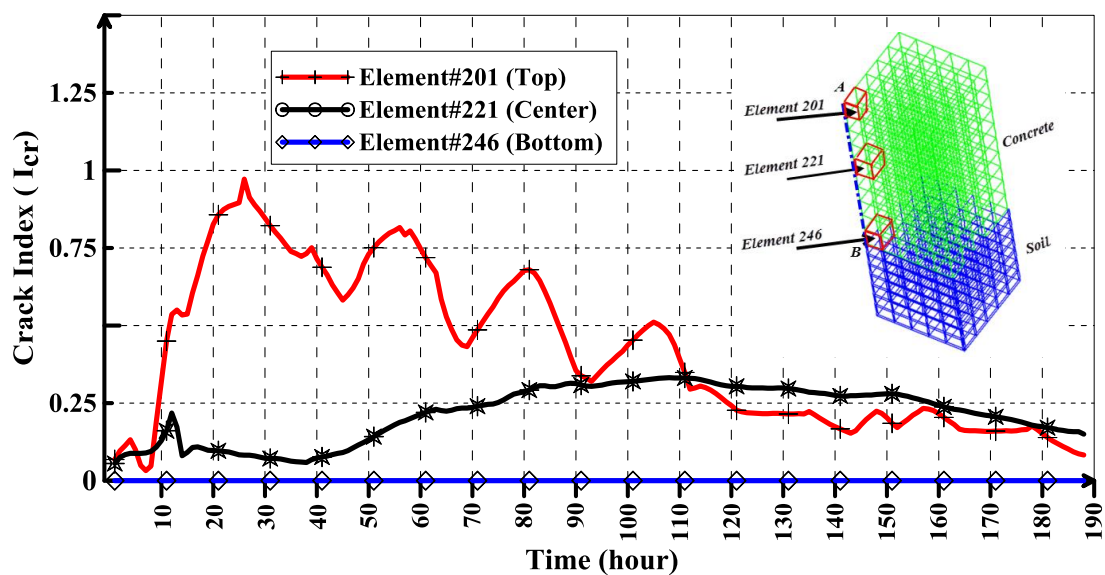


**Figure 7-44: Cracking Index of Elements 201, 221 and 246**

Figure 7-44 shows that the cracking index of the element #201 increases rapidly from 10 to 25 hours. Then, it decreases until it reaches a zero value. The cracking index for the element # 221 (located at center) equals zero all times, which indicated that the core of JMUS is subjected to compressive stresses. The element#246 undergoes tensile stresses in a less amount compared to the tensile stresses at the surface of JMUS.

The crack patterns of the mockup specimens after 30 hours from casting are shown in Figure 7-45. It is clear; the mockup specimen has been cracked at the top surface.

The evolution of contours plot for the principal stresses (S1) at different ages in JMUS is shown in Figure 7-46. The tensile stresses were developed at the top surfaces and sides whereas the compressive stresses developed in the core of JMUS.

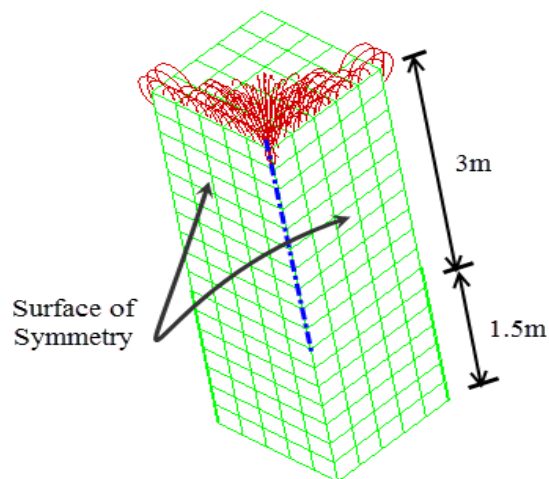


**Figure 7-45: Crack Pattern in the JMUS after 30 Hours from Casting**

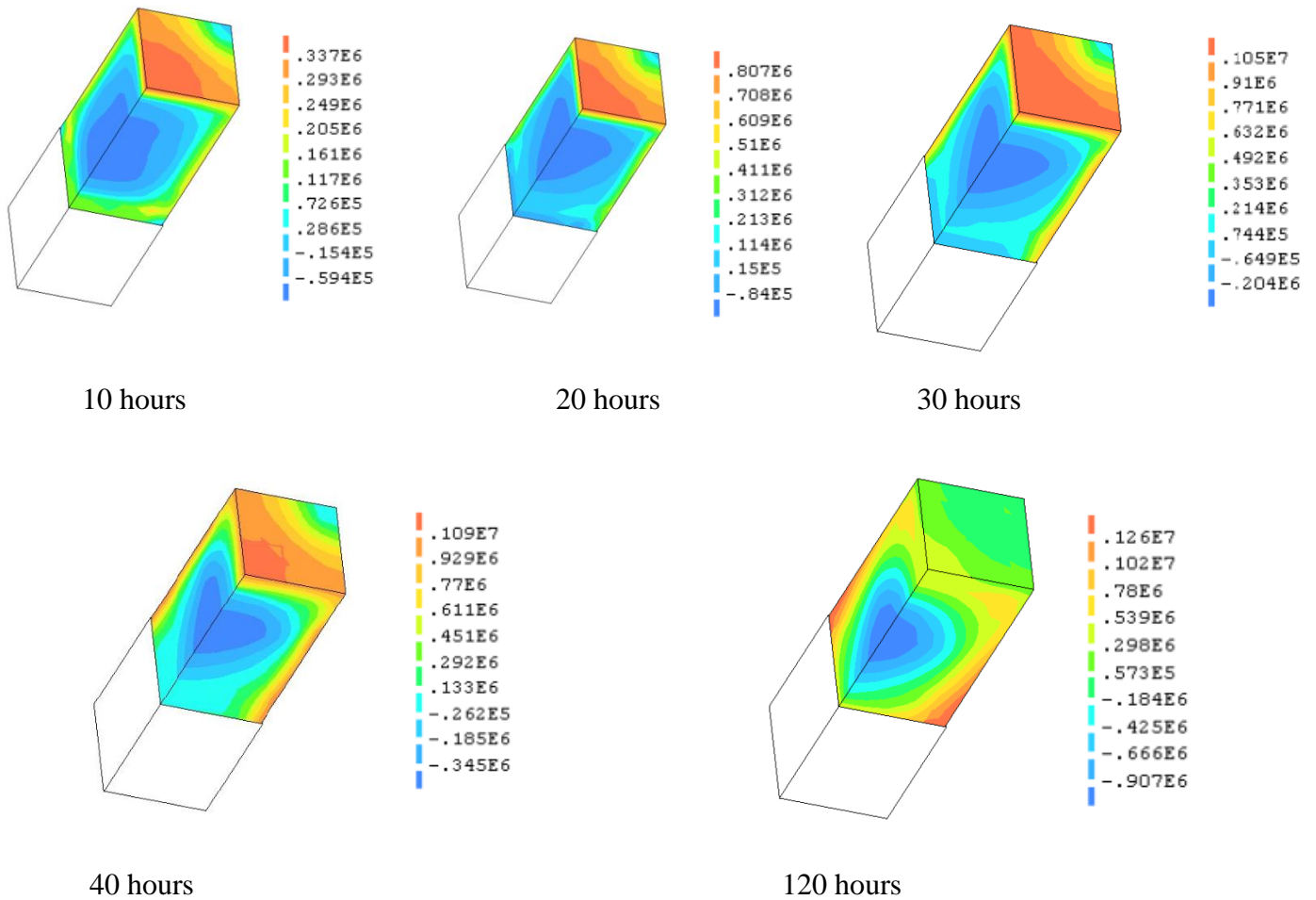


**Figure 7-46: Contour plots of Principal Stresses (S1) at Different Ages**

### 7.3.4 Stresses Results of Piles-Cap

The Piles-cap with dimensions of 9.1m×9.1m×1.7m was studied in this thesis. Due to symmetry, only quarter of piles cap is modeled. The stress analysis for piles-cap was carried out depending on the results of heat transfer. The change of tensile strength with maturity was taken into consideration. The effect of tension softening with maturity was also studied. The change of elasticity modulus with time was input to the FEM. The CEB – FIB model of shrinkage was used in the FEM, in which the input of relative humidity,

ambient temperature, cement type, curing type, and compressive strength of concrete at 28 days are required. The normal, shear, and principal stresses were obtained. The input file of pile-cap in finite element model is presented in Appendix B.

The focus is given to the results of stress in x direction ( $S_{xx}$ ). Figure 7-47 shows the predicted stress in x direction for the elements located at the top, center and bottom of the center line of pile-cap. It can be observed from Figure 7-47 that the elements located at the top and bottom are subjected to tensile stresses whereas the element located at the center is under compressive stresses. Due to the higher temperature gradient between the core and surface, the tensile stresses in the top surface element are higher than in the bottom element. After 30 hours from casting, the cracking index and stresses in x direction ( $S_{xx}$ ) across the central line AB of the piles-cap are shown in Figure 7-48. It can be noticed from Figure 7-48, the cracking index in the top center of piles-cap surface reached 0.6 after about 30 hours from casting. The elements located at height 0.4 m from the top to about 1.2m from bottom are subjected to compressive stresses

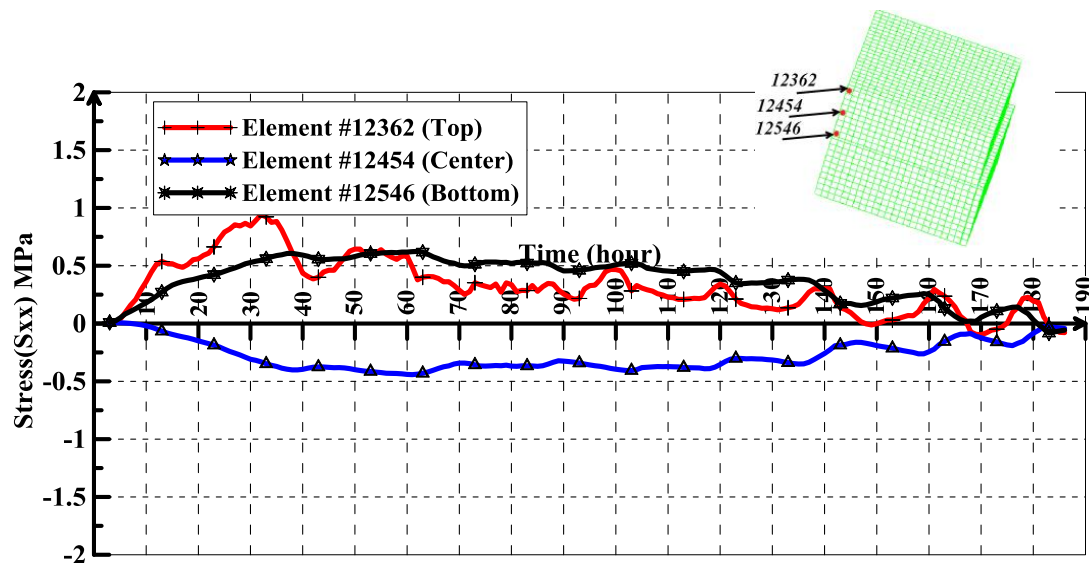


**Figure 7-47: Stresses in X Direction ( $S_{xx}$ ) for the Elements Located at Top, Center, and Bottom of Center Line of Piles-Cap**

. The zero cracking index indicated that the element is subjected to compressive stress. At 30 hours from casting, the tensile stresses in x direction reached about 0.8MPa which is less than the tensile strength of concrete at this age.

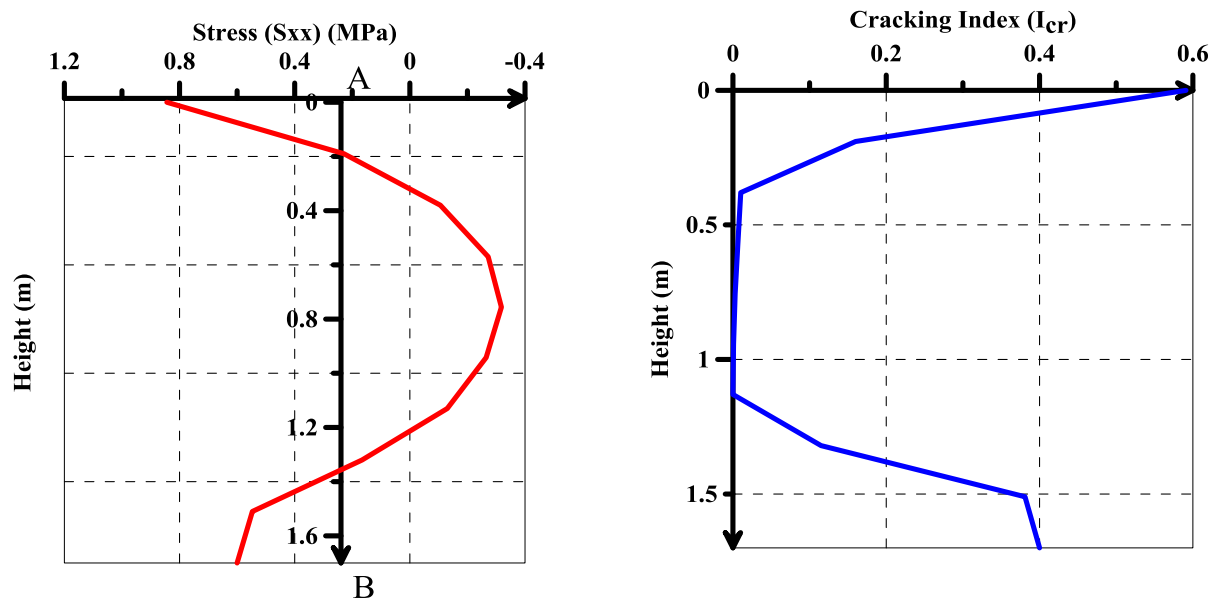


**Figure 7-48: Cracking Index, and Stresses ( $S_{xx}$ ) Across the Concrete Depth AB Piles-Cap (After 30 Hours from Casting)**

The temperature profile across the central depth of piles cap at different ages is shown in Figure 7-49. The evolution of temperature increases significantly during the first thirty hours. From 30 hours to 50 hours, there is a slight increase in temperature evolution. The temperature remains high for the next 160 hours, and the rate of the decrease in the temperature evolution was slow.

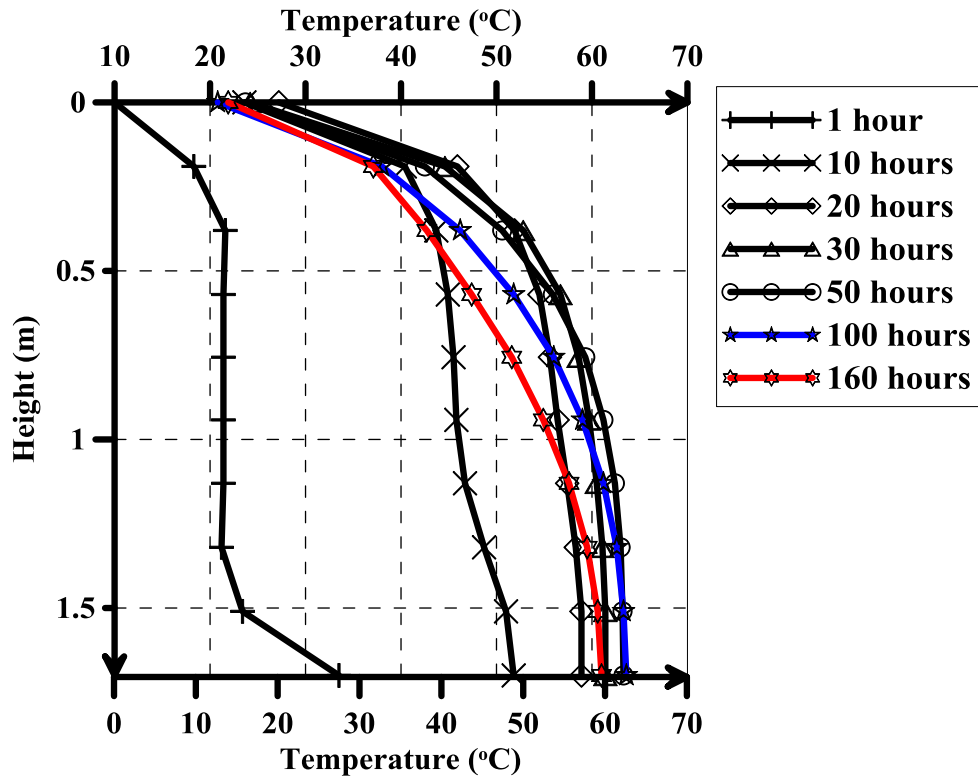


**Figure 7-49: Temperature Evolution across the Central Depth of Piles-Cap at Different Ages**

The change of cracking index with time for the elements located at top, center, and bottom across the central depth of piles-cap is shown in Figure 7-50.

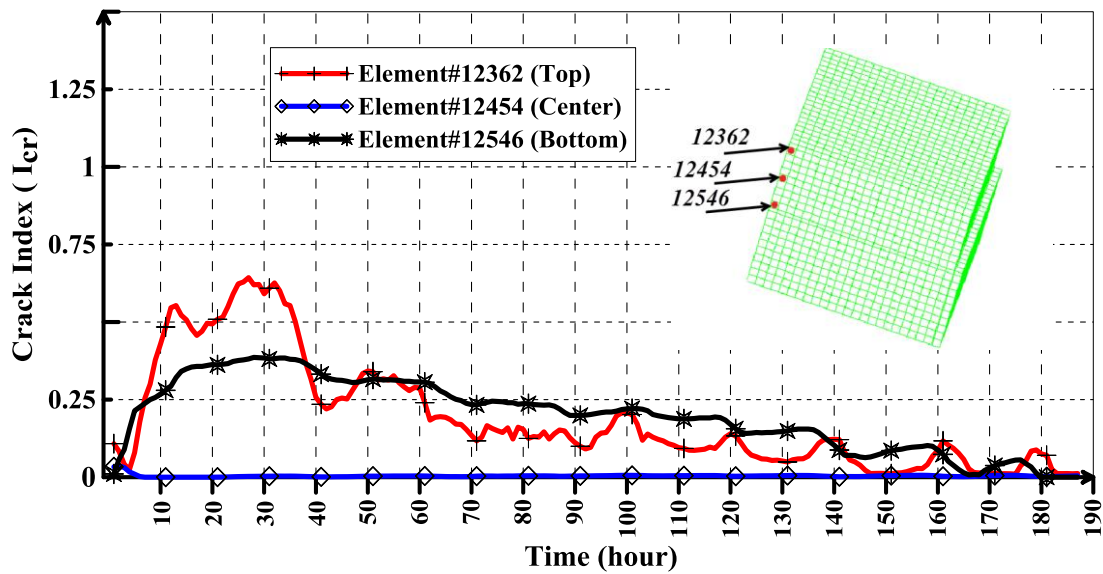


**Figure 7-50: Cracking Index of Elements 12362, 12454, and 12546.**

Figure 7-50 shows that the cracking index of the element #12362 (located at the top) increases from about 10 to 30 hours. Then, it decreases until it reaches a zero value. The cracking index for the element # 12454 (located at center) equals zero all times, which indicated that the core of JMUS is subjected to compressive stresses. The element#12546 undergoes tensile stresses in a less amount compared to the tensile stresses at the surface of piles cap.

The evolution of contours plot for the cracking index ( $I_{cr}$ ) in the pile-cap is shown in Figure 7-51. The tensile stresses were developed at the top surfaces and sides whereas the compressive stresses developed in the core of Piles cap. After 30 hours from casting, the cracking index of top surface becomes less than the cracking index of sides.

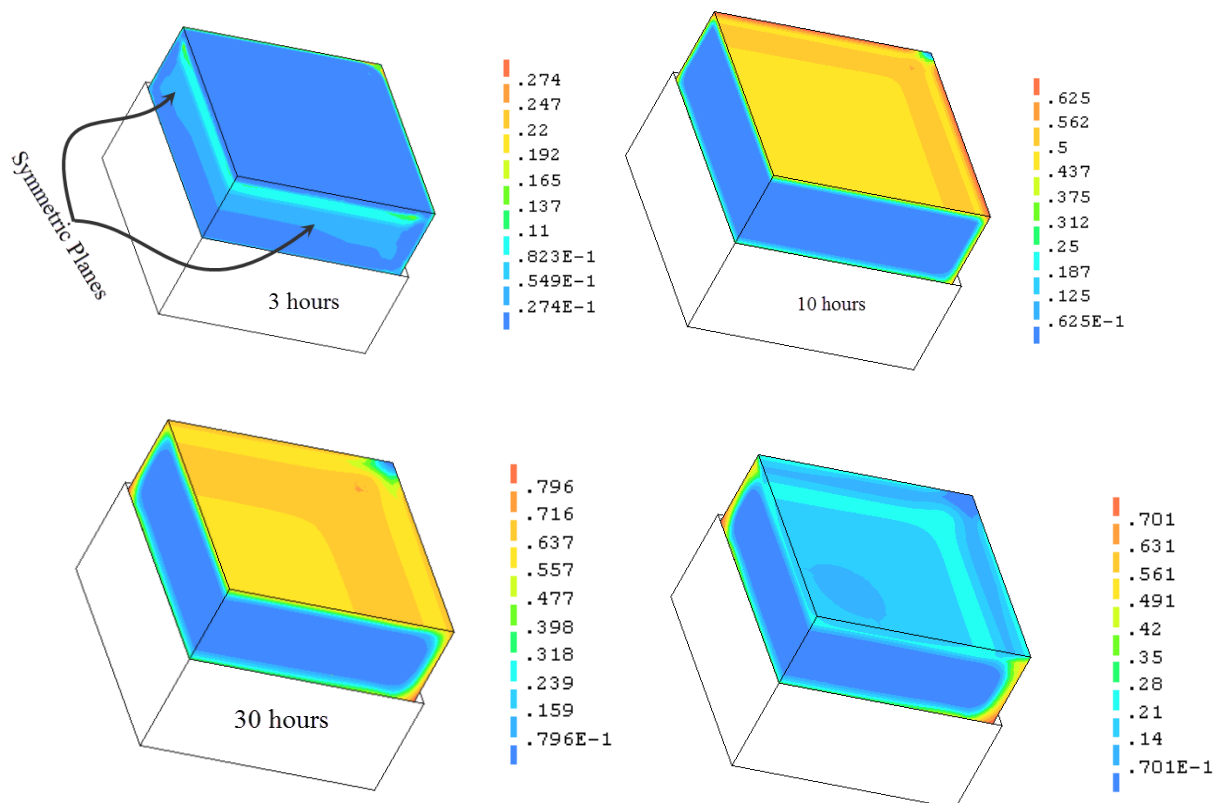


**Figure 7-51: evolution of Contours Plot for the Cracking Index ( $I_{cr}$ ) in the Pile-cap**



## **CHAPTER 8**

### **PARAMETRIC STUDY**

#### **8.1 Introduction**

A parametric study was conducted with the aid of the DIANA finite element program. The parameters investigated are size of the structure, placement temperature, solar radiation, type of mineral admixtures, type of formwork, amount of steel reinforcement, and interface element. The effect of these parameters on temperature rise and cracking index is presented in this chapter.

#### **8.2 Size of Mockup Specimens**

Finite element analysis was also carried out for three mock-up specimens with dimensions of 1m×1m×1m, 2m×2m×2m, 3m×3m×3m and 4m×4m×4m to study the effect of mock-up specimen size on temperature distribution due to heat of hydration. The adiabatic temperature rise curve of control mix (cement only) was used as a heat source in four mock-up specimens (1m<sup>3</sup>, 8m<sup>3</sup>, 27 m<sup>3</sup>, and 64m<sup>3</sup>). The mix contains 480 kg cement and 0.28 w/cm ratio. The temperature evolution with time at the core of the three mock-up specimens is shown in Figure 8-1. It is noticed from Figure 8-1, the larger size of mockup specimen, the higher temperature generated at the core. The increase in the size of mockup specimen or the dimension of mass concrete structures leads to an increase the distance between the core and the surfaces or sides. This increase in distance will resemble fully adiabatic conditions, since little heat losses to the environment occur.

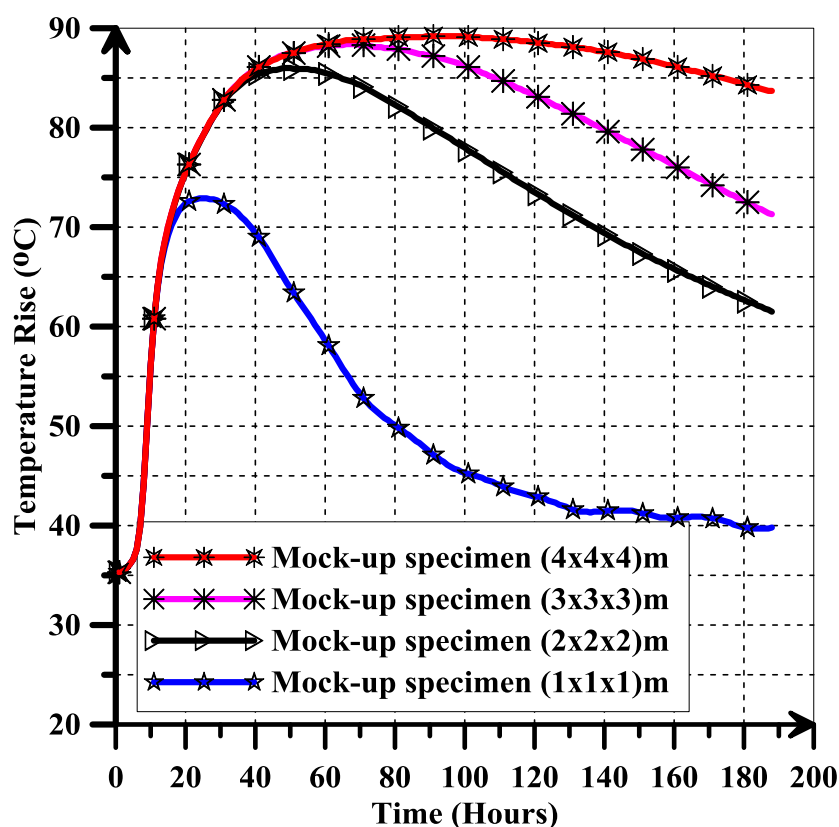


**Figure 8-1: Effect of Mass Concrete Sizes on the Temperature Rise.**

### 8.3 Effect of Placement Temperature

The effect of placement temperature on the temperature rise was studied. The adiabatic temperature rise curve of control mix (cement only) was used as a heat source in three mock-up specimens with dimensions of 2m×2m×2m. The mix contains 480 kg cement and 0.28 w/cm ratio. The temperature evolution with time at the core of the mock-up specimen for three different placement temperatures is shown in Figure 8-2. Figure 8-2 shows that the higher the placement temperature, the greater the potential temperature rise in the concrete. Lowering the placement temperature is one of the best methods to control temperature rise in a mass concrete structures. The use of ice water is one of the easiest ways to reduce the placement temperature of concrete. Many methods were reported in the literature to reduce the placement temperature of concrete such as

cooling of the mixed concrete with liquid nitrogen injection, cool coarse aggregates with refrigerated water or with cold air blasts, and insulate mixer drums or cool them with water sprays or wet burlap coverings ( ACI 305, 2000) [61].

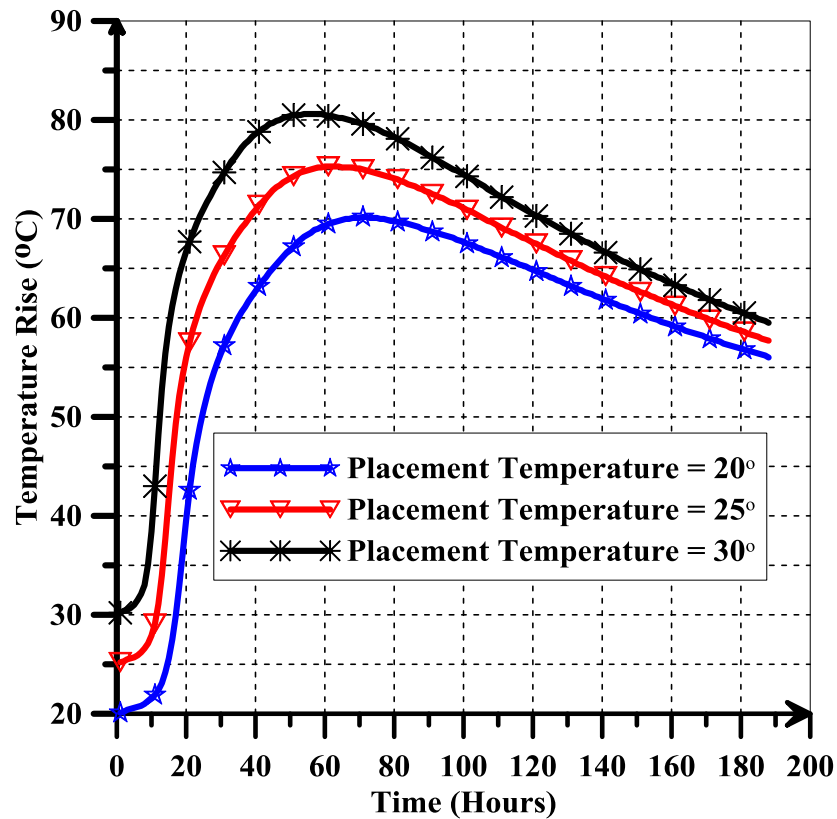


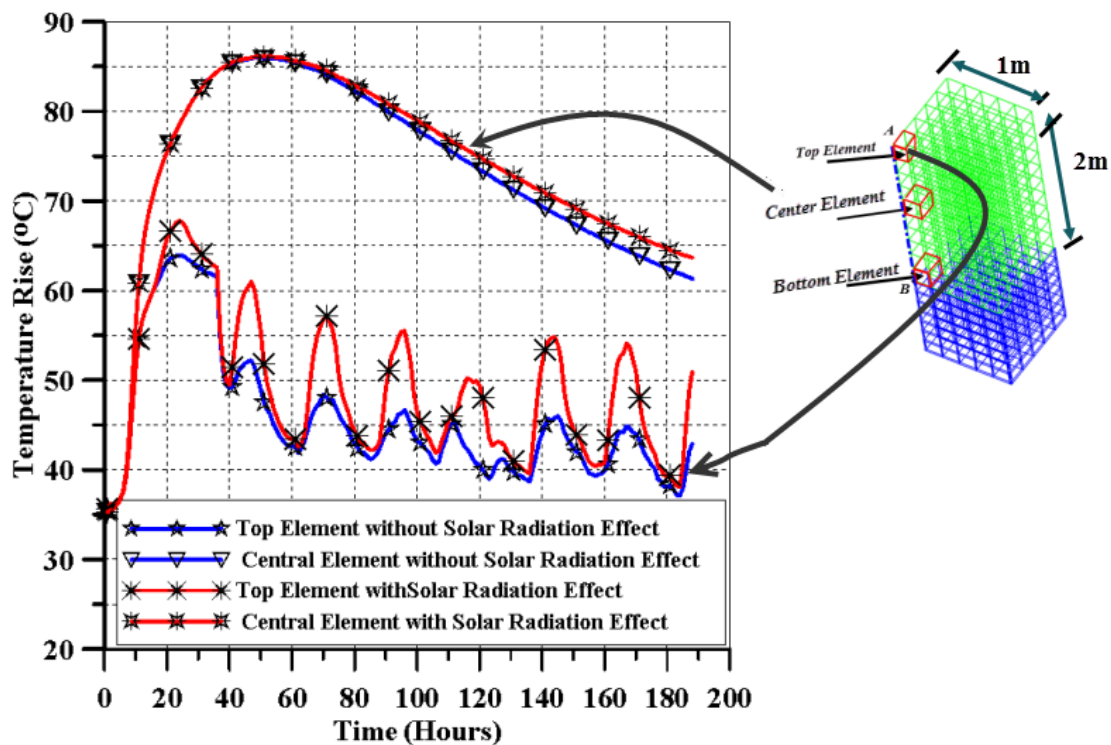
**Figure 8-2: Effect of Placement Temperature on the Temperature Rise**

#### **8.4 Effect of Solar Radiation**

An incident solar radiation is a radiant energy from the Sun which strikes an object or surface. The incident solar radiation consists of two parts: the direct component from the Sun itself (sunshine) and the diffuse component from the visible sky (skylight). It can also contain a reflected component from other surfaces in the model and the ground.

The radiation can impact the surface temperature of the concrete and can be considered heat sources. Irradiation (radiation emitted by the formwork) and reflected radiation act as heat sinks.

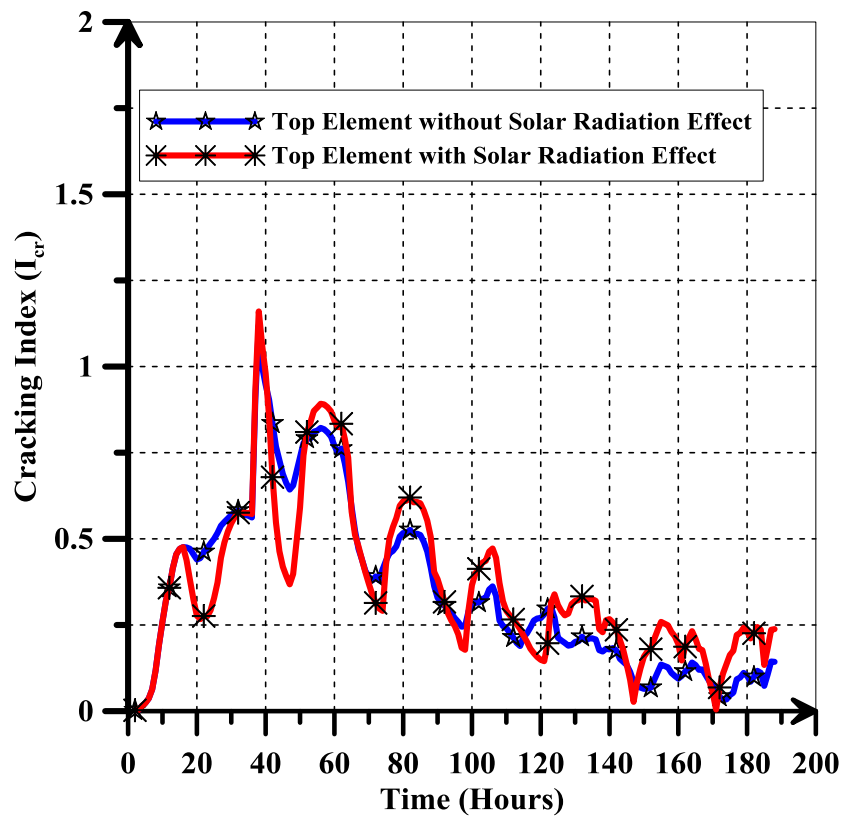
The effect of solar radiation on the temperature rise was studied. The adiabatic temperature rise curve of control mix (cement only) was used as a heat source in two mock-up specimens with dimensions of 2m×2m×2m. The mix contains 480 kg cement and 0.28 w/cm ratio. The temperature evolution with time at top surface and at the core of the mock-up specimen for two cases is shown in Figure 8-3. In the first case, the effect of solar radiation is not included whereas the second case includes the effect of solar radiation.



**Figure 8-3: Effect of Solar Radiation in the Temperature Rise on Mass Concrete**

Figure 8-3 shows that there is slight effect in the temperature rise of the element located at the core of mockup specimen whereas the temperature rise in the element located at the top surface changes significantly. The solar radiation increases the surface temperature of mockup specimen which leads to a reduction in the temperature difference between the core and the surface.

The effect of solar radiation on the cracking index for the elements located at the top and bottom of mockup specimen is also studied. Figure 8-4 shows the cracking index for the top in the both cases of inclusion the effect of solar radiation or not.



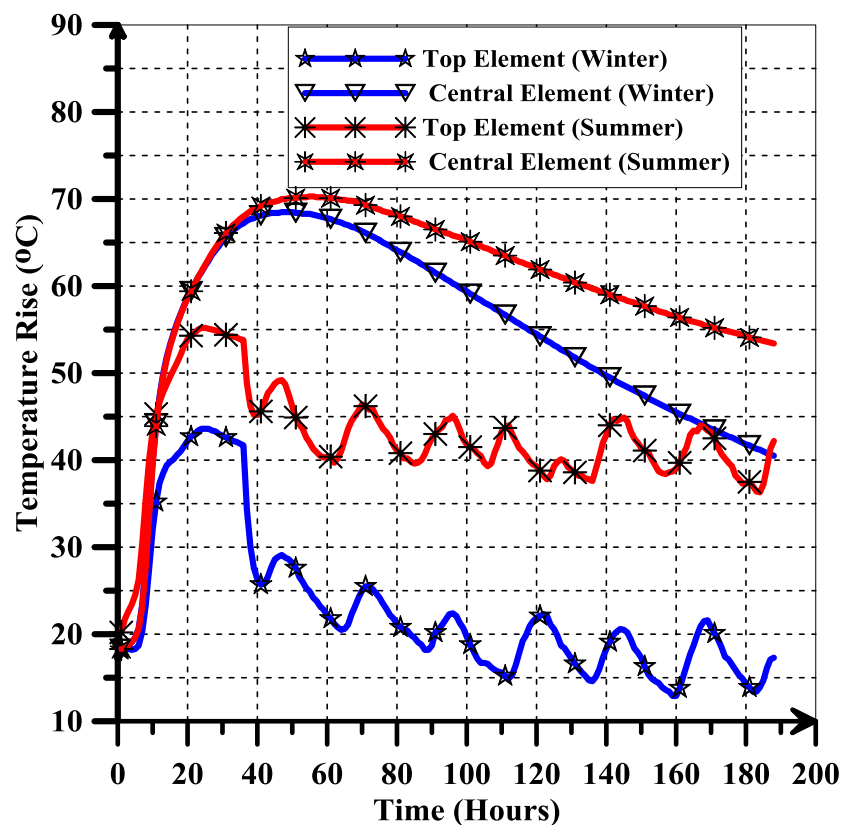
**Figure 8-4: Effect of Solar Radiation on Cracking Index**

Figure 8-4 shows that the solar radiation decreases the cracking index due to the reduction on the temperature difference between the core of mass concrete and its surface.

## 8.5 Effect of Ambient Temperature

The effect of casting time is studied on the temperature rise and cracking index is studied. The ambient temperatures vary significantly from summer to winter in KSA.

The data of ambient temperatures was taken from the weather data file in Echotect software. The same mockup specimen was assumed to cast in summer and winter and the change in temperature difference and the potential of cracking was analyzed. The placement temperature keeps the same for the two mockups specimens.



**Figure 8-5: Effect of Ambient Temperature in the Temperature Rise on Mass Concrete**

The adiabatic temperature rise curve of control mix (cement only) was used as a heat source in two mock-up specimens with dimensions of 2m×2m×2m. The mix contains 480 kg cement and 0.28 w/cm ratio. The finite element model shows that the

temperature difference between the core of mockup specimen and its surface in winter is significantly higher than in summer as shown in Figure 8-5. This leads to an increase in the potential of cracking as shown in Figure 8-6.

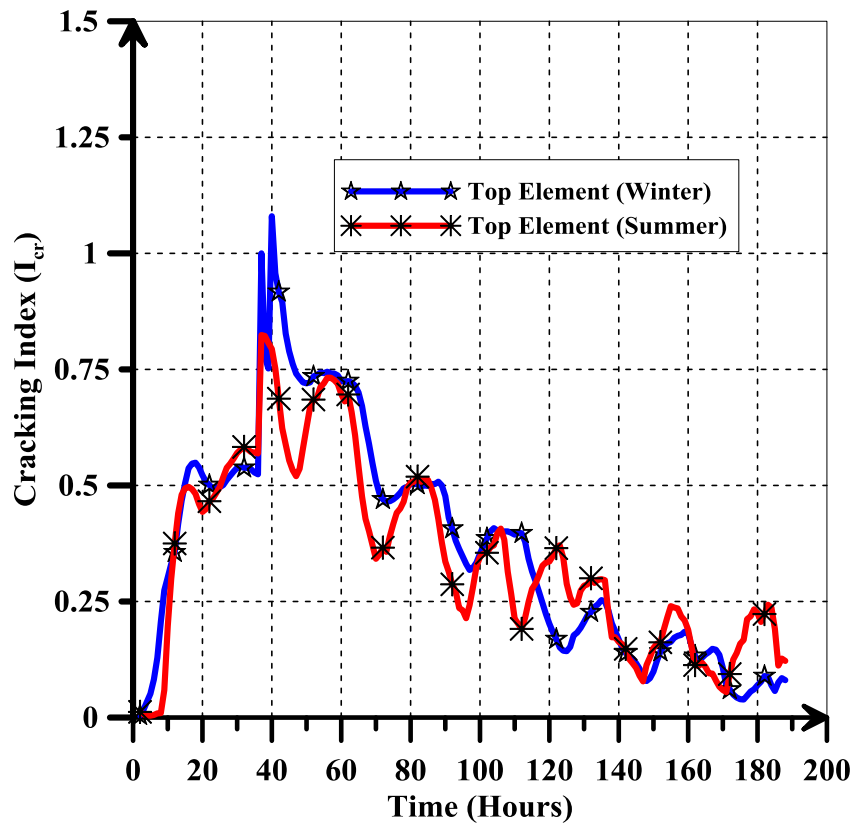


**Figure 8-6: Effect of Ambient Temperature in the Cracking Index of Mass Concrete**

## 8.6 Type of Formwork

The type of formwork plays an important role in the temperature rise of mass concrete structures. The plywood and steel formwork are the most widely used in the construction projects in KSA. The thermal conductivity of steel form work is estimated to be 50-150 times greater than thermal conductivity of plywood formwork. The effect of the plywood and steel formwork in the temperature rise and cracking index was studied. The adiabatic temperature rise curve of control mix (cement only) was used as a heat source in two mock-up specimens with dimensions of 2m×2m×2m. The mix contains 480 kg cement and 0.28 w/cm ratio.

The change of temperature rise with time for the two elements located at the top and core of the mockup specimen is shown in Figure 8-7.

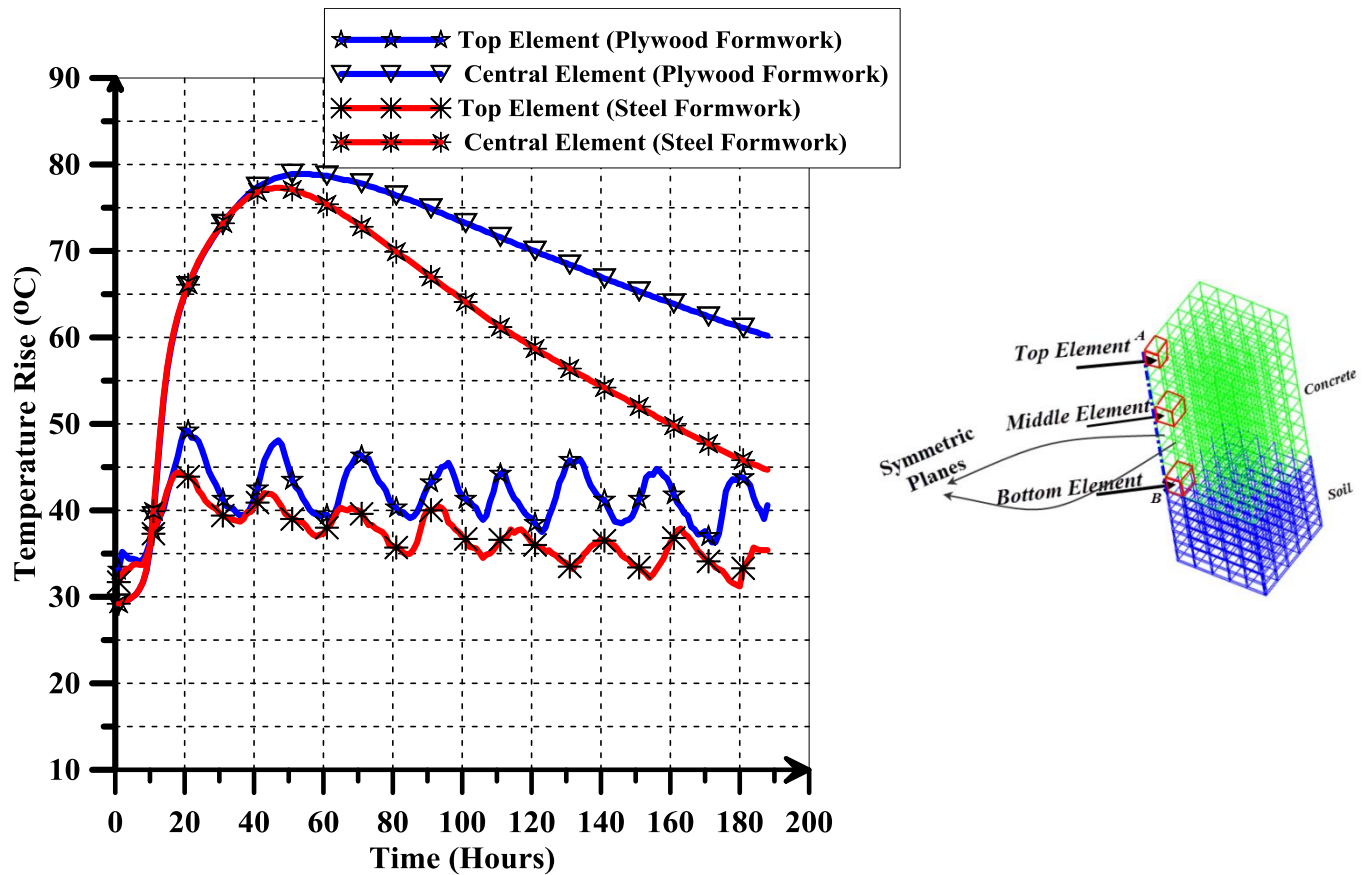


**Figure 8-7: Effect of Formwork Type in the Temperature Rise on Mass Concrete**

Figure 8-7 shows that the temperature rise at the top and core of mockup specimen with plywood formwork is higher than the mockup specimen with steel formwork. The difference between the temperature at the top and the core of the mockup specimen with plywood or steel formwork is almost the same during the period from 0 to 40 hours from casting. Then, the temperature difference became higher for the mockup specimen with plywood formwork as compared with the temperature difference in the mockup specimen with steel formwork. The temperature rise for the element located at the top and middle along the line located near to the side (formwork) is shown in Figure 8-8.



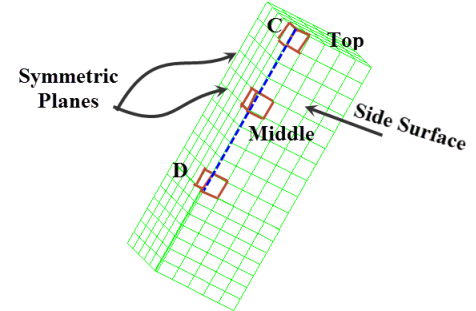
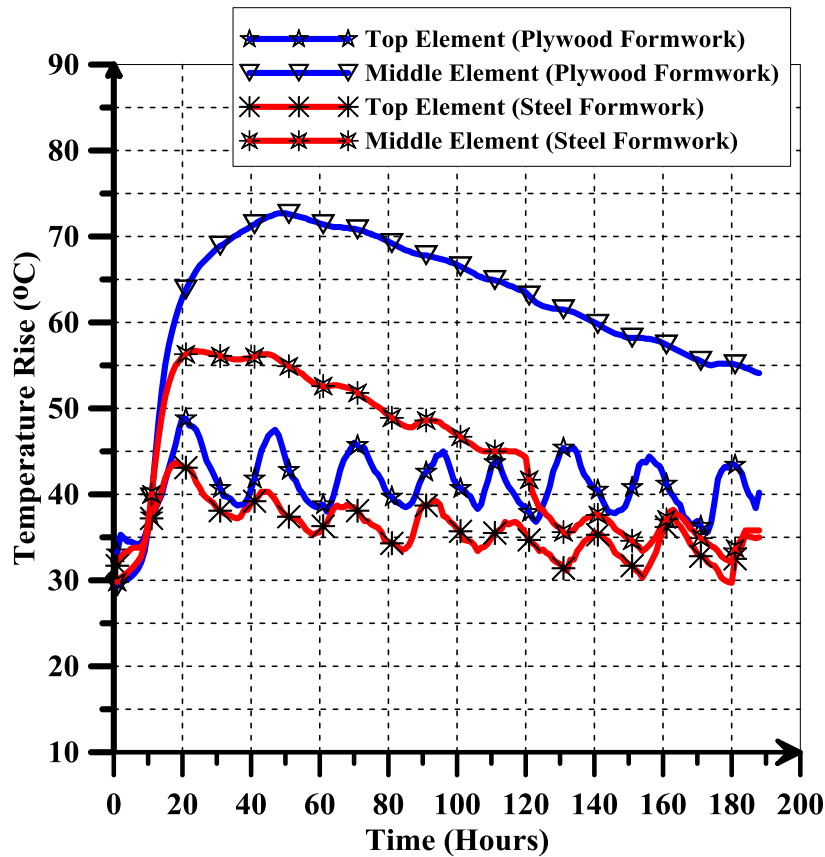


**Figure 8-8: Temperature Rise of the top and central elements neat to side.**

By comparing the temperature rise of the two elements located at the top and middle of center line AB (Figure 8-7) with temperature rise of the two elements located across the side line CD (Figure 8-8), it is noticed the temperature decreases significantly for the element located in the mid side of mockup specimen with steel formwork. The heat loss from steel formwork is high due to its high thermal conductivity.

The change of cracking index with time for the two elements located at the top and bottom of the mockup specimen is shown in Figure 8-9.

Figure 8-9 shows the cracking index of the elements located along the center line of mockup specimen with plywood or steel formwork is almost the same during the period from 0 to 20 hours from casting. Then, the cracking index became higher for the mockup

specimen with plywood formwork as compared with the cracking index of the mockup specimen with steel formwork.

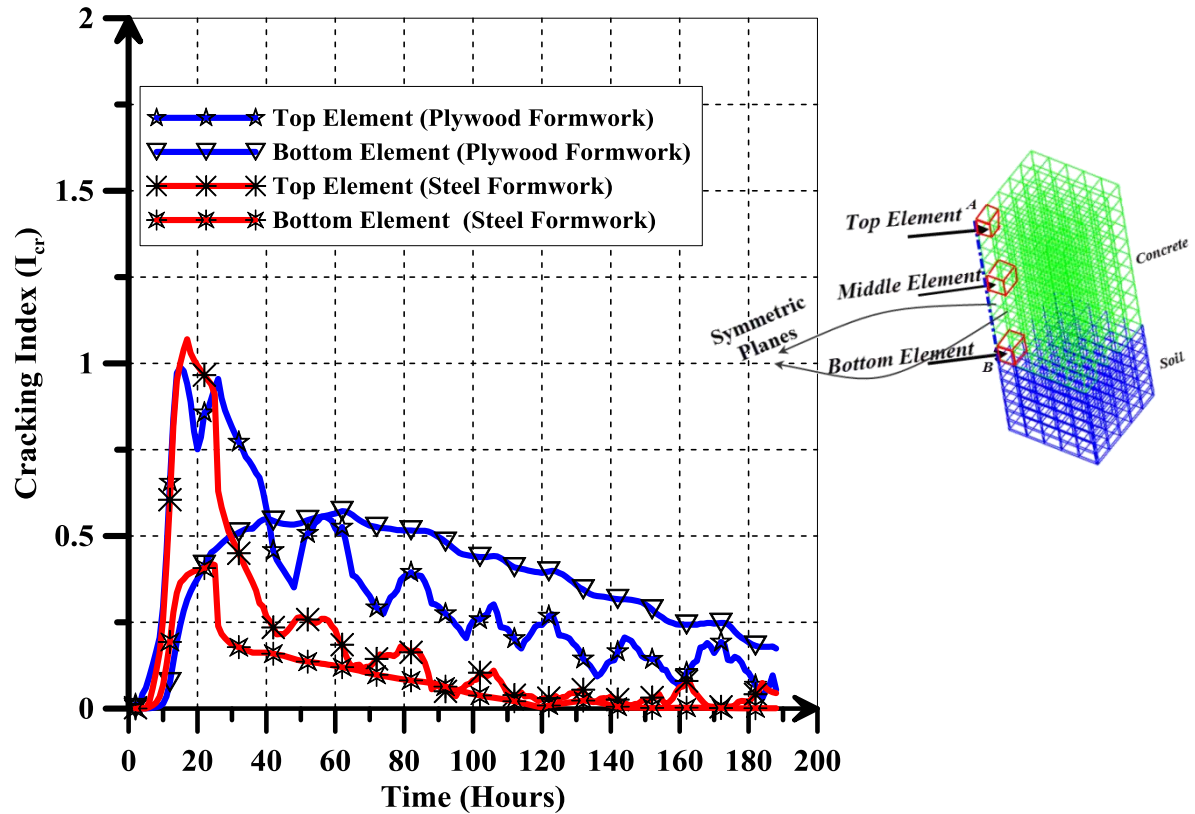


**Figure 8-9: Effect of Formwork Type in the Cracking Index of Mockup Specimen  
Along Center Line AB**

The cracking index for the elements located at the top and middle of a line CD located near to the side (formwork) is shown in Figure 8-10.

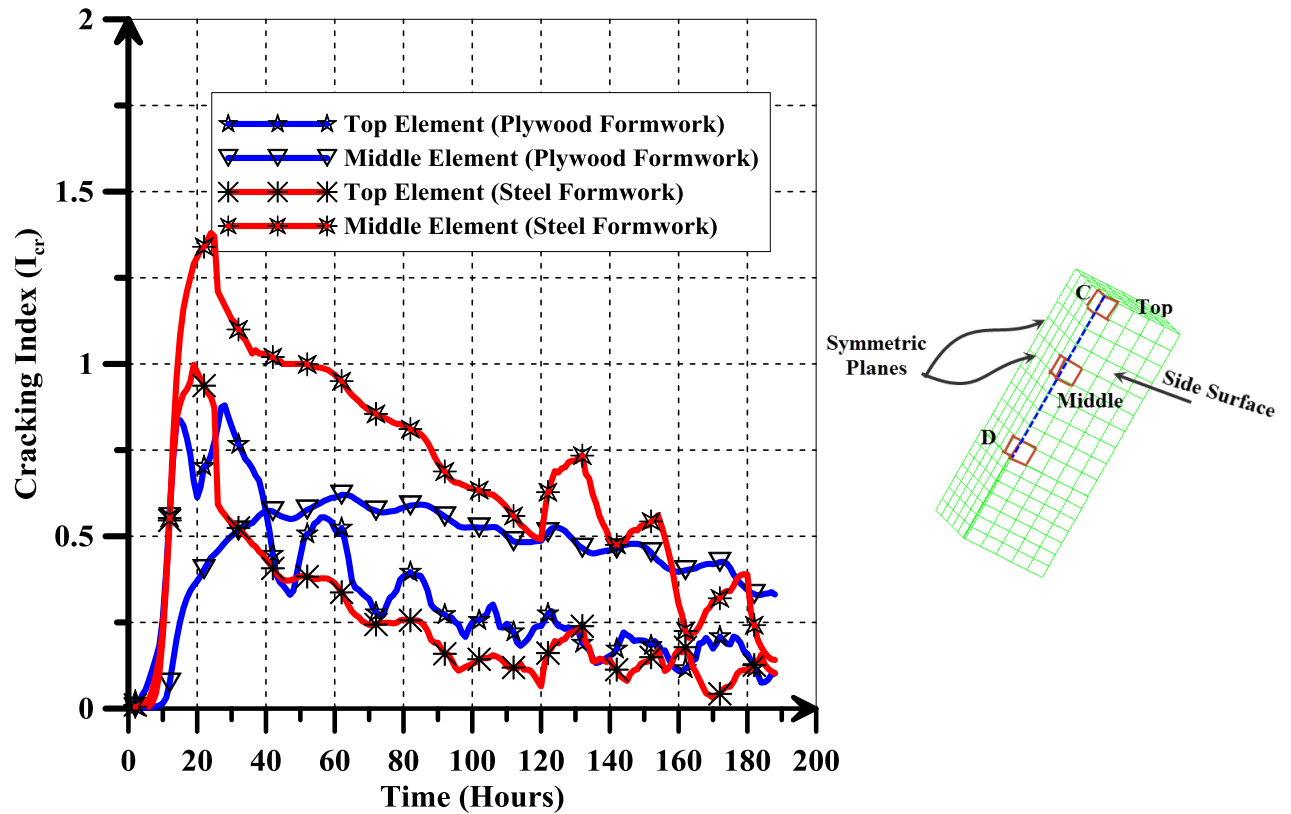
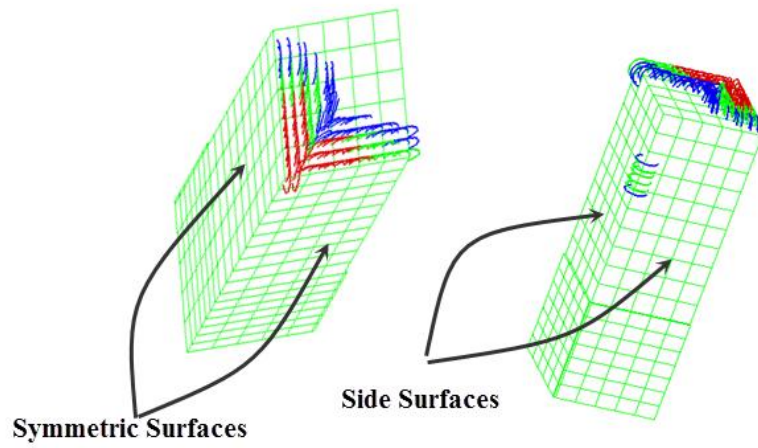
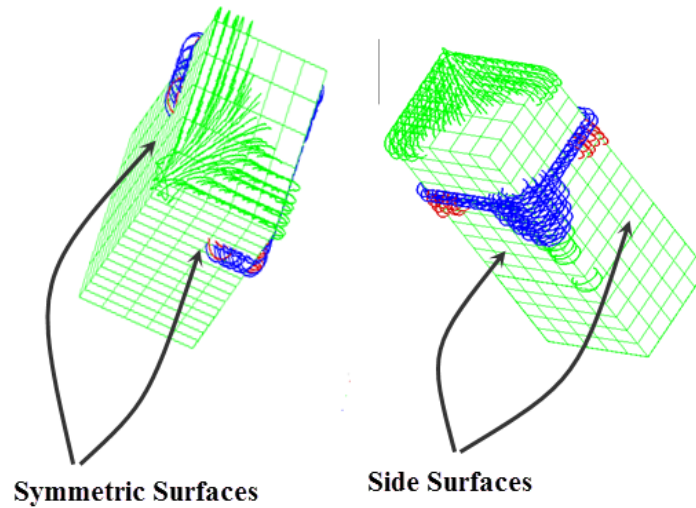


**Figure 8-10: Effect of Formwork Type in the Cracking Index of Mockup Specimen along Side Line CD**

It is noticed that the cracking index for the element located at the top is almost the same in case of using steel or plywood formwork. The cracking index of the element located at the middle of Line CD (near to side) is significantly higher for the mockup specimen with steel formwork. This increase in cracking index results from the big temperature difference between the core of mockup specimen and the side. The heat loss from steel formwork makes the temperature difference between the core and side higher than between the core and top surface. The crack patterns for the cases of using plywood and steel formwork are shown in Figure 8-11.



a)



b)

**Figure 8-11: Crack Patterns of Mockup Specimen with a) Plywood Formwork, b) Steel Formwork**

Figure 8-11 shows that the mockup specimen with steel formwork has been cracked in the top surface and sides whereas the mockup specimen with plywood formwork cracked only at the top surface. The high temperature difference between the core and sides in the mockup specimen with steel formwork is the cause of cracks developed in the sides of mockup specimen.

## 8.7 Effect of Mineral Admixtures

The effect of mineral admixtures (Fly Ash, GGBFS, and Silica Fume) on heat of hydration has been reported in Chapter 5. The parametric study was carried out to study the effect of these mineral admixtures on the temperature rise on mass concrete structures and on the potential of cracking. The fly ash has a significant effect on reducing the heat of hydration, however it reduces the compressive and tensile strength of concrete at early age. Reduction of heat of hydration does not necessarily lead to a decrease in the probability of cracking. The results of mechanical properties and the measurements of heat of hydration which have been shown in Chapter 5 were used as an input in the finite element simulation. The effect of the 46 mixes on the temperature rise and cracking index has been investigated. The mixes in the group#1 in which the control mix contained 480 kg cement and the other mixes in the group were designed by replacing the cement with different replacement ratio of Fly Ash (20%, 30%, 40%, 50%, and 60%).

The temperature rise at the core of a mockup specimen with dimensions of  $2 \times 2 \times 2$  m for the mixes of group#1 is shown in Figure 8-12. The control mix has the highest temperature at the core and the temperature decreases with an increase of replacement ratio of Fly Ash.

The development of cracking index with time in the element located at top center of mockup specimen is shown in Figure 8-13 for the mixes of group#1. This element is chosen, since it has the higher probability of cracking.

The finite element model indicates that the control mix which contains only cement has the highest probability of cracking as shown in Figure 8-13. During the first 36 hours from casting, as the content of fly ash increases, the crack index decreases.

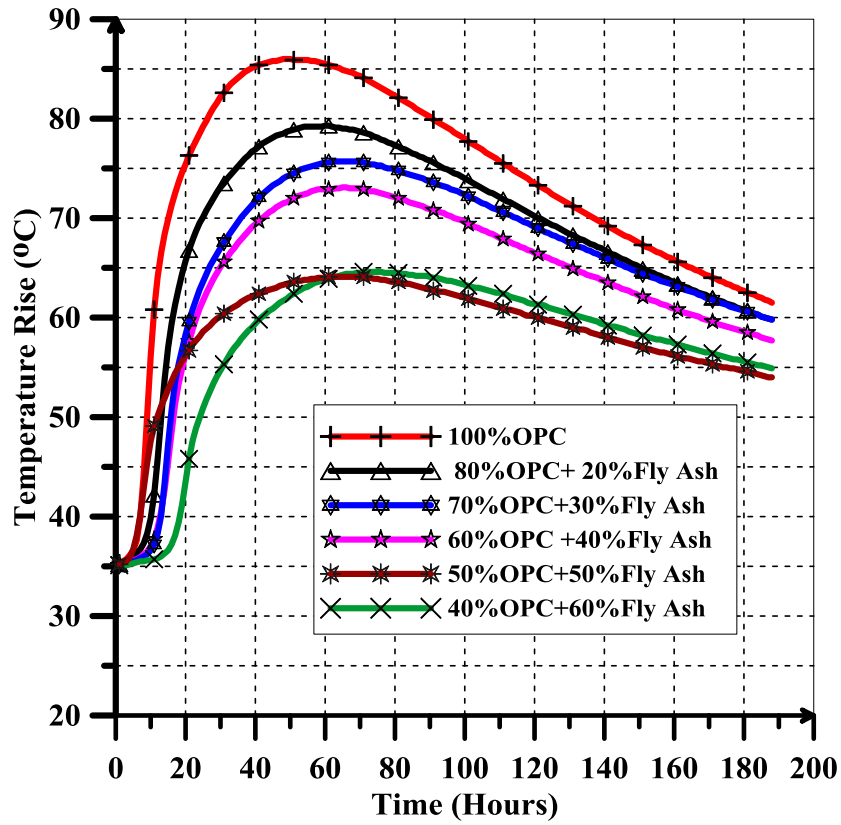


Figure 8-12: Temperature Rise at the Core of Mockup Specimen for the Mixes of Group#1

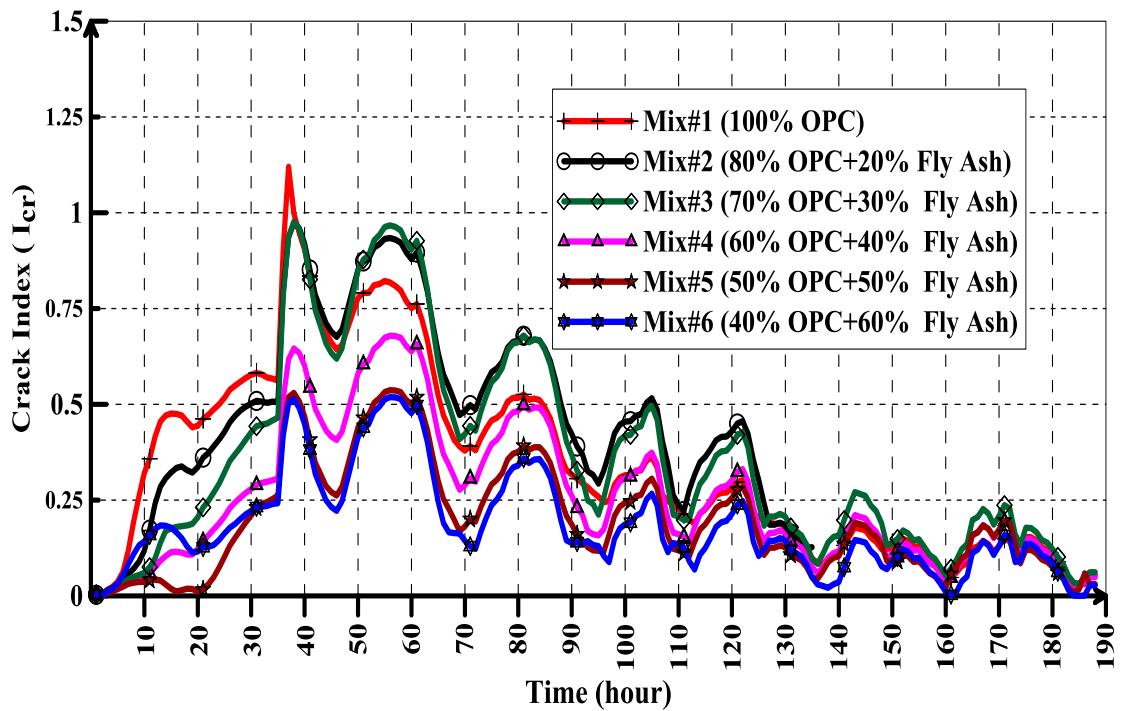
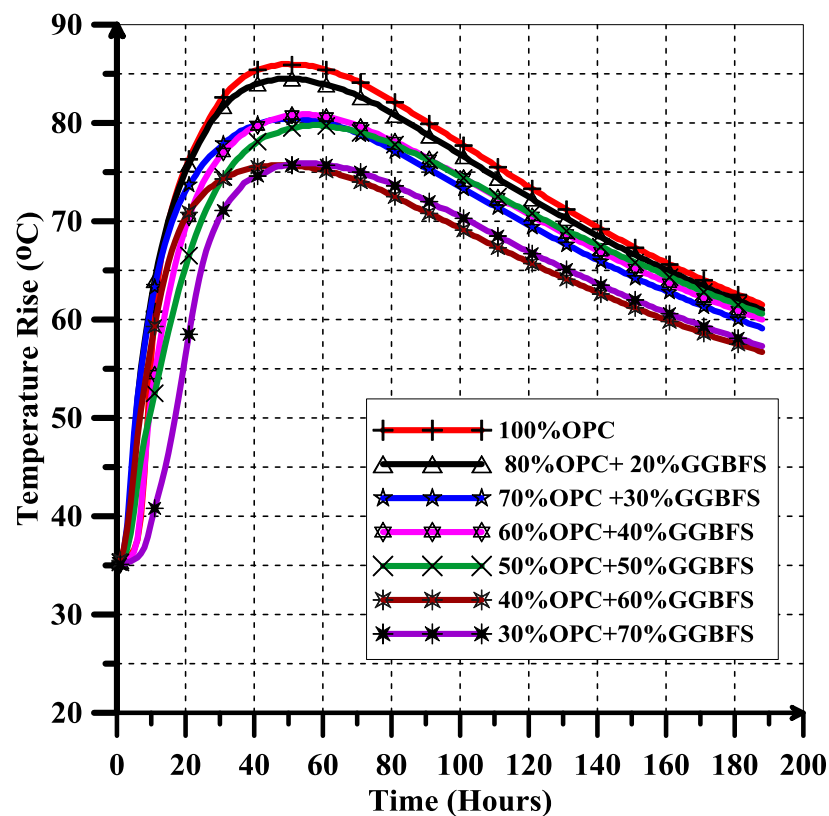


Figure 8-13: Cracking Index of the Element Located at Top Center of MUS For the Mixes of Group#1

After 36 hours from casting, the cracking index mixes with 20%, and 30% replacement percentage of Fly Ash is higher than that of control mix as shown in Figure 8-13.

In the group#2, Cement was replaced with GGBFS by different replacement percentage (20%, 30%, 40%, 50%, 60%, and 70%). The effect of replacing cement with GGBFS on the temperature rise on the core of mockup specimen with dimensions of 2×2×2m is shown in Figure 8-14.



**Figure 8-14: Temperature Rise at the Core of Mockup Specimen for the Mixes of Group#2**

Figure 8-14 shows that the GGBFS has a slight effect on the temperature rise in the core of the mockup specimen compared to the effect of Fly Ash. The replacement percentage of GGBFS should be more than 60% to reduce the temperature rise. The effect of GGBFS

in the cracking index at the top center of mockup specimen with dimensions of 2×2×2m is shown in Figure 8-15.

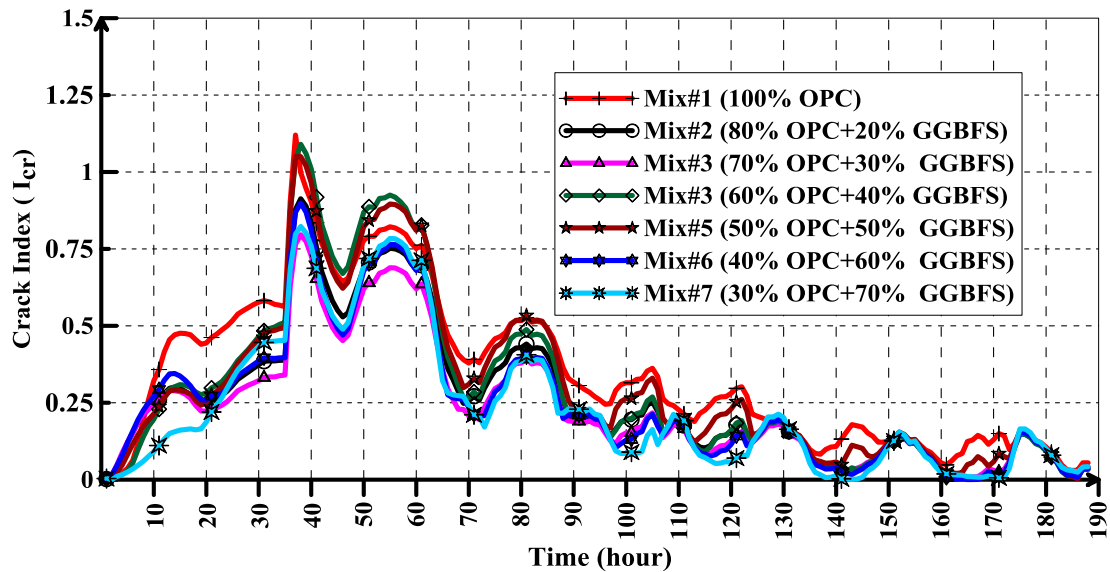


**Figure 8-15: Cracking Index of the Element Located at Top Center of MUS For the Mixes of Group#2**

It can be observed from Figure 8-15, the cracking index doesn't change significantly with an increase of the replacement percentage of GGBFS. The cracking index for the mix with 70 % GGBFS is higher than that of the mix with 30% GGBFS. The effect of GGBFS on the cracking index is fluctuation from replacement percentage to other.

In the group#3, GGBFS and Fly Ash were used with the same replacement percentage. The effect of using the mixes of group #3 on the temperature rise at the core of the mockup specimen with dimensions of 2×2×2m is shown in Figure 8-16.

The mix with (30% Fly Ash+30% GGBFS) seems to cause an excessive decrease in the temperature rise at the core compared to the other mixes of group#3 as shown in Figure 8-16. No big difference was noticed between the temperature rise curves of the mixes with (10% Fly Ash +10% GGBFS), (15% Fly Ash +15% GGBFS), and (20% Fly Ash +20% GGBFS).



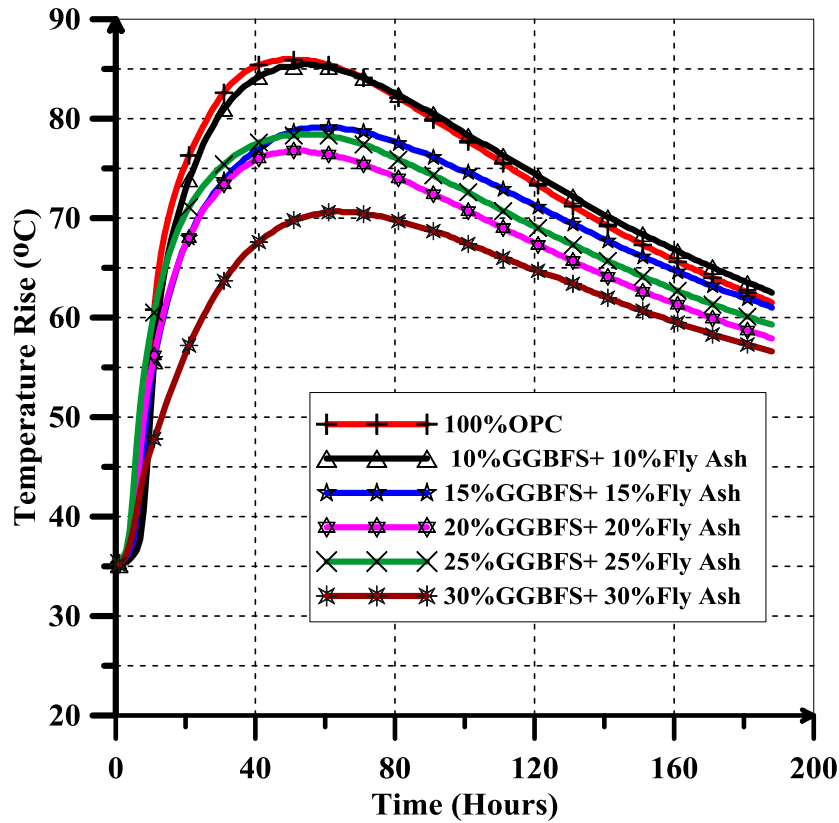


**Figure 8-16: Temperature Rise at the Core of Mockup Specimen for the Mixes of Group#3**

Also, it can be noticed from Figure 8-17, the cracking index of the mix with (30% Fly Ash+30% GGBFS) is the lowest in the mixes of group#3. Therefore, the optimum replacement percentage of Fly Ash + GGBFS is 60% (30%Fly Ash+30% GGBFS) to reduce both the temperature rise and the cracking index.

In the group #4, the cement replaced with different replacement ratio of fly ash (20%, 30%, 40%, and 50%). The control mix of this group contains 350kg cement. The temperature rise at the core of the mockup specimen with dimensions of 2×2×2m for the mixes of group#4 is shown in Figure 8-18. Figure 8-18 shows that the control mix has the highest temperature at the core and the peak temperatures decreases with an increase of replacement ratio of Fly Ash.

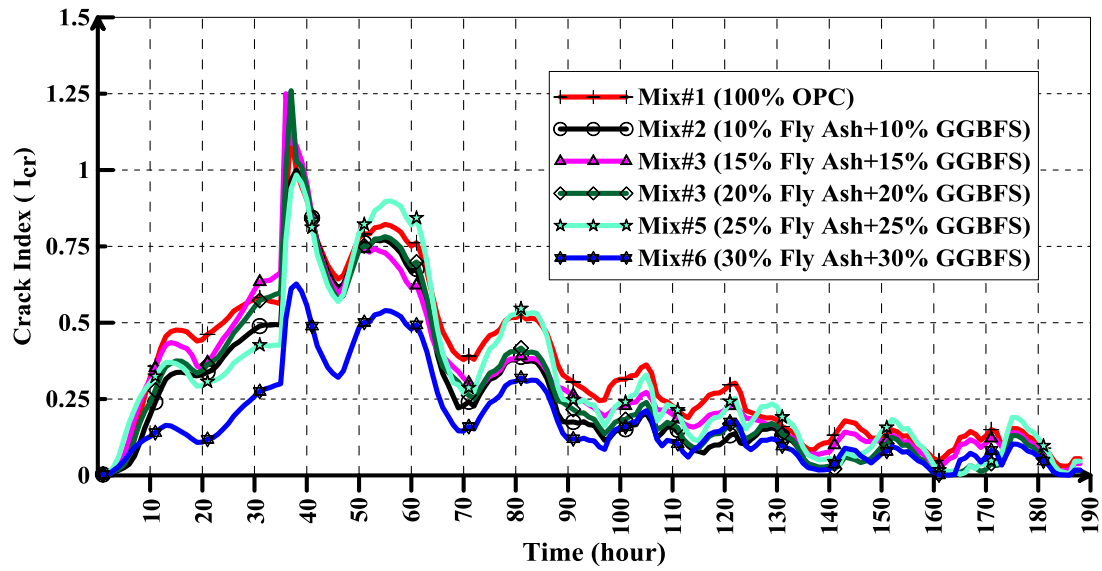


Figure 8-17: Cracking Index of the Element Located at Top Center of MUS For the Mixes of Group#3

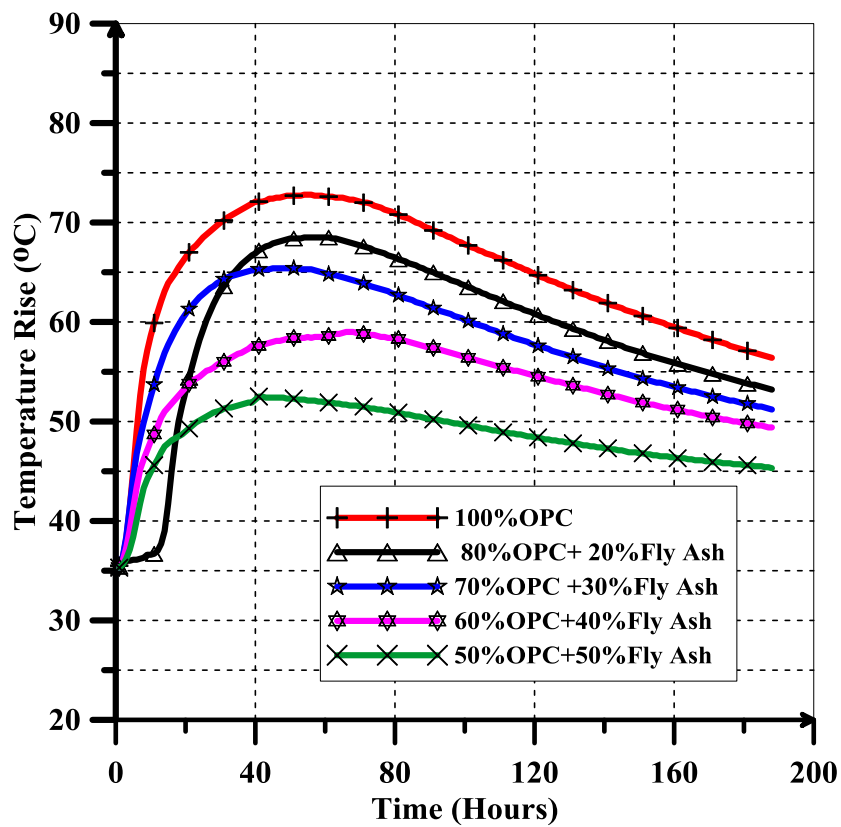
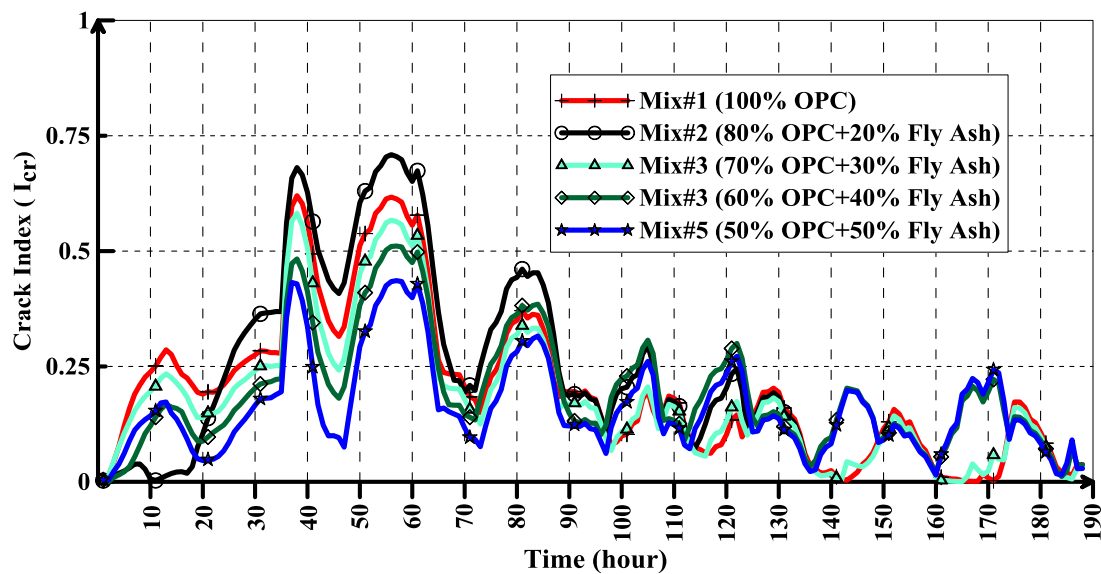


Figure 8-18: Temperature Rise at the Core of Mockup Specimen for the Mixes of Group#4

The development of cracking index with time in the element located at top center of mockup specimen is shown in Figure 8-19 for the mixes of group#4. The cracking indexes for the mixes of group #4 are less than 1 which indicates that no cracks will be formed in case of using one of the mixes in group#4. The cracking index for the mix with 20% Fly Ash is higher than that of control mix, since the modulus of elasticity of the mix with 20% Fly Ash is higher than that of control mix.

In the group #5, the cement replaced with different replacement ratio of GGBFS (20%, 30%, 40%, and 50%). The control mix of this group contains 350kg cement.



**Figure 8-19: Cracking Index of the Element Located at Top Center of MUS For the Mixes of Group#4**

The effects of different replacement percentages of GGBFS on the temperature rise at the core of the mockup specimen with dimensions of 2×2×2m are shown in Figure 8-20.

Increasing the replacement of GGBFS from 20% to 50% causes a slight reduction in the peak temperatures at the core of mockup specimen as shown in Figure 8-20. The replacement percentage of GGBFS should be more than 50% to reduce the temperature rise in mass concrete structures.

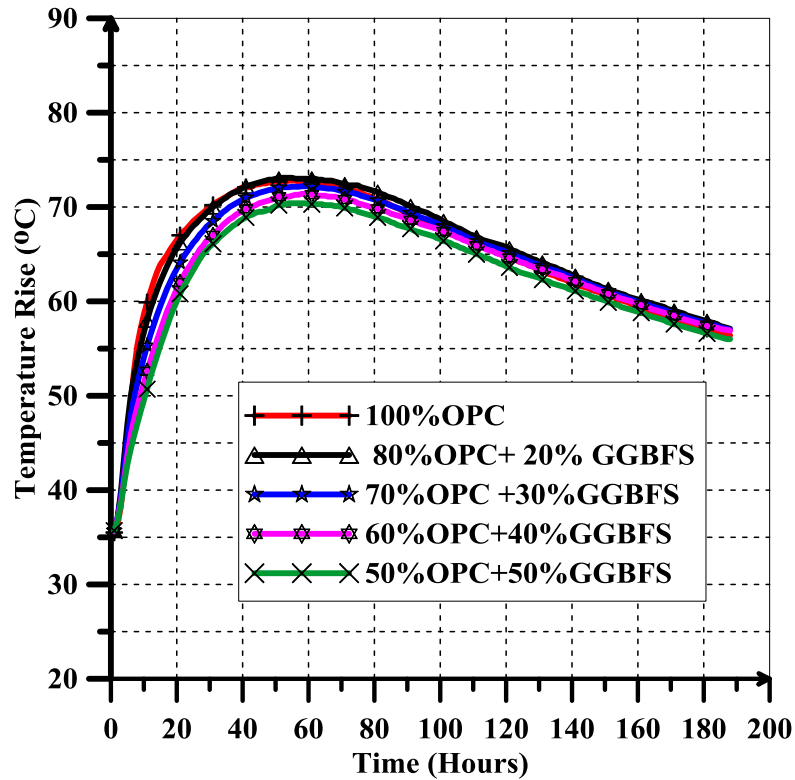


**Figure 8-20: Temperature Rise at the Core of Mockup Specimen for the Mixes of Group#5**

Figure 8-21 compares the cracking index of mixtures with different replacement percentages of GGBFS.

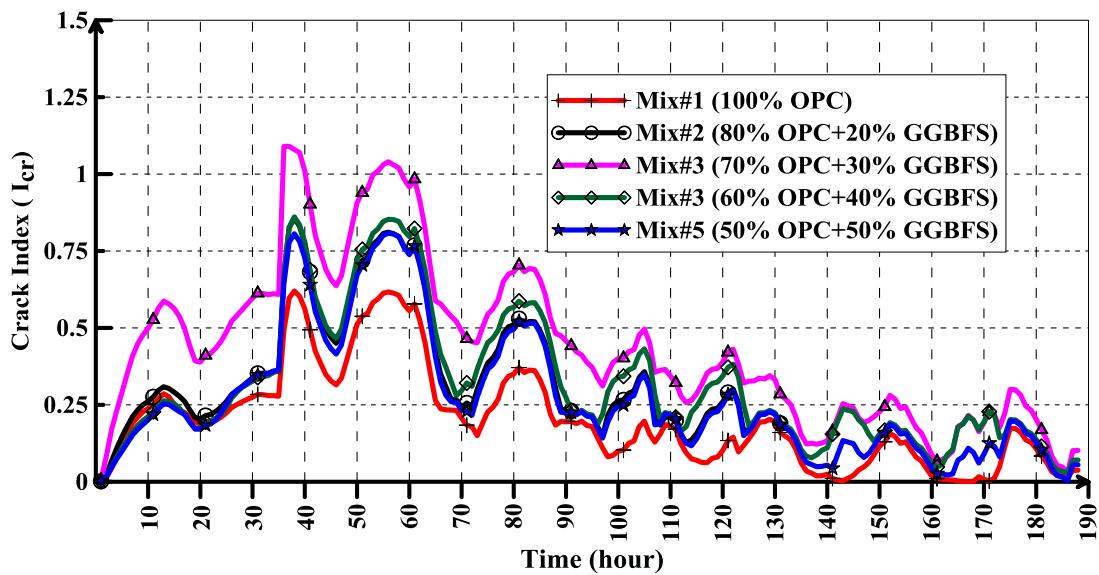


**Figure 8-21: Cracking Index of the Element Located at Top Center of MUS For the Mixes of Group#5**

Interestingly, the change of cracking index with time for the mixes with GGBFS is higher than that of control mix. This is because of higher values of elasticity modulus of the mixes with GGBFS compared to control mix.

The effects of different replacement percentages of Micro-Silica on the temperature rise at the core of the mockup specimen with dimensions of 2×2×2m are shown in Figure 8-22.

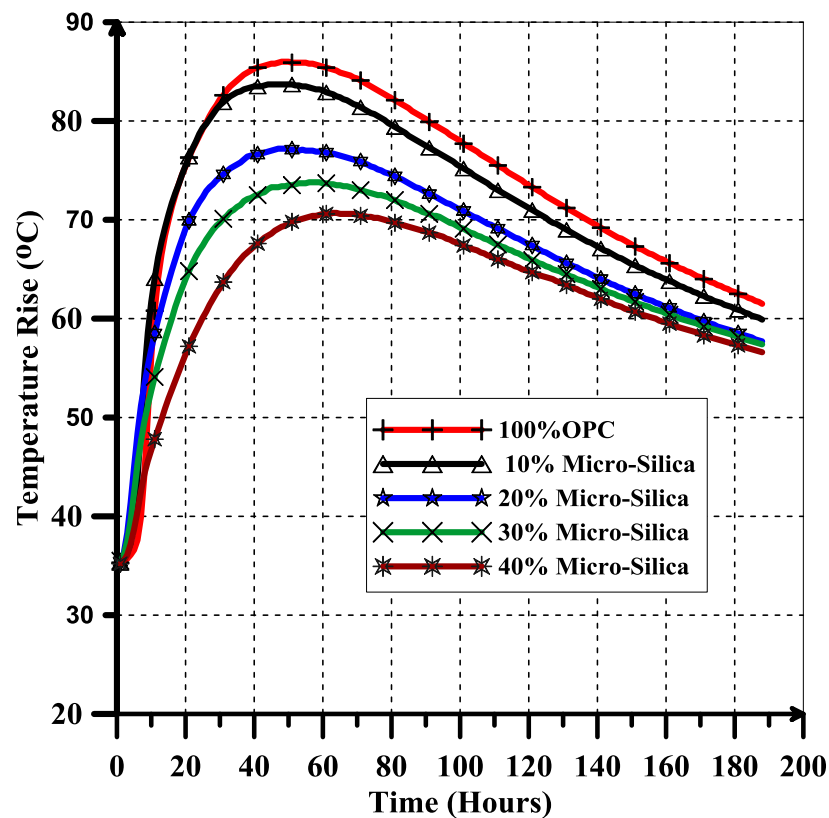


**Figure 8-22: Temperature Rise at the Core of Mockup Specimen for the Mixes of Group#6**

As the replacement percentage of Micro-Silica increases, the peak temperature decreases. This is likely due to the high percentage of silicon oxide on silica fume. The silicon oxide reacts with the calcium hydroxide which is resulting from the reaction of cement ( $C_3S$  or  $C_2S$ ) with water. Once replacement levels of micro silica are increased,

the CH levels resulting from the hydration of cement are rapidly depleted and not available for formation of further secondary CSH.

The development of cracking index for different replacements of Micro-Silica is shown in Figure 8-23.

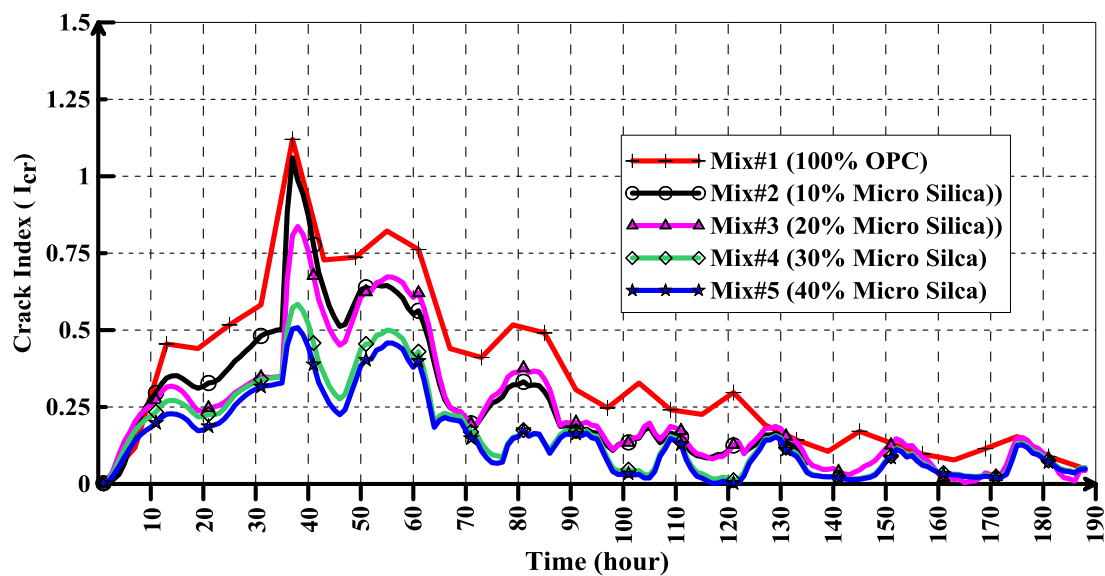


**Figure 8-23: Cracking Index of the Element Located at Top Center of MUS For the Mixes of Group#6**

Increasing the replacement percentage of Micro-Silica causes a reduction in the cracking index as shown in Figure 8-23. From start of casting to 40 hours, the cracking index increases until it reaches its peak, then it is decreasing until it becomes close to zero.

The water cementitious materials ratio plays a significant role in the development of mechanical properties of concrete. The effect of water cementitious materials ratio in the evolution of heat of hydration and in the temperature rise at the core of mockup specimen with dimensions of 2m×2m×2 m was investigated. The temperature rise with time for three mixes containing three different w/cm ratios is shown in Figure 8-24.

Figure 8-24 shows the effects of varying the w/cm (0.28, 0.33, and 0.38) on the temperature rise at the core of mockup specimen.

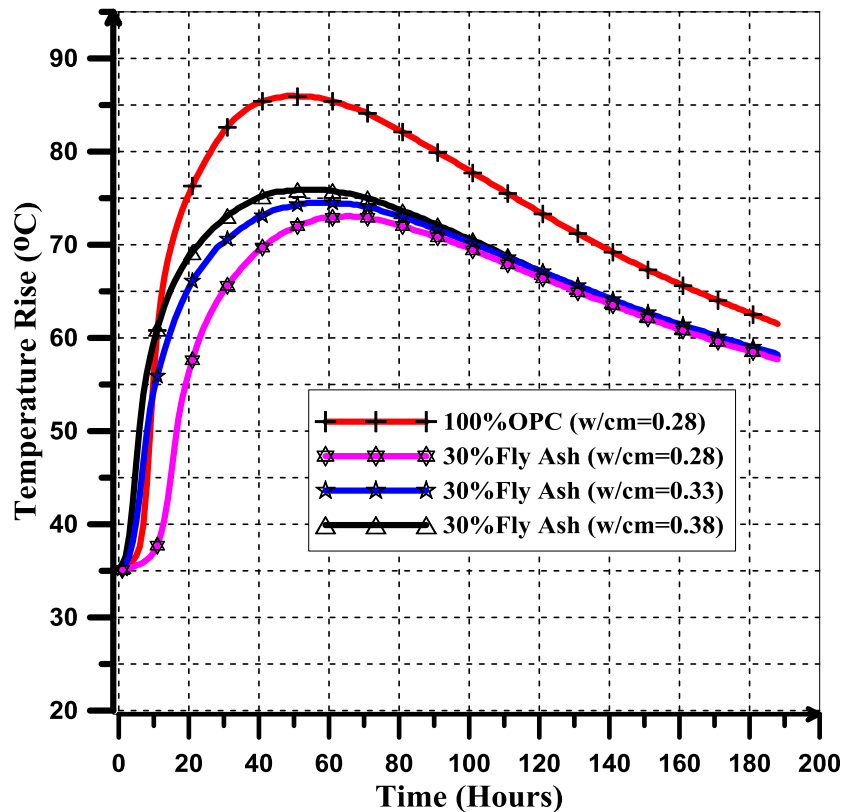
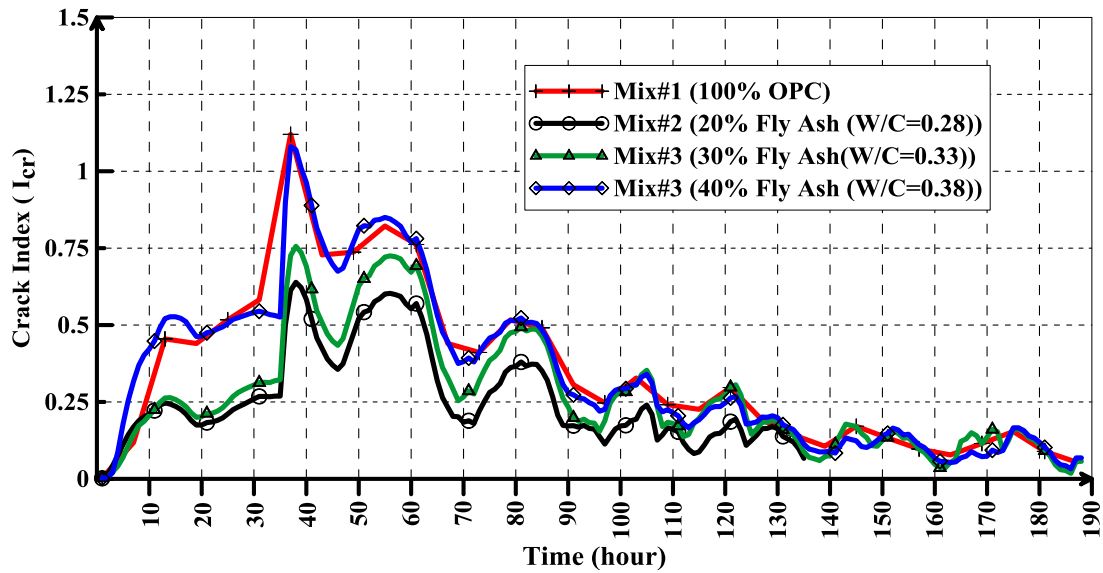


**Figure 8-24: Effect of w/cm Ratio in the Temperature Rise at the Core of Mock-up Specimen**

The higher w/cm ratio, the higher peak temperature at the core of mockup specimen. As the w/cm ratio increases, the temperature and its rate rise.

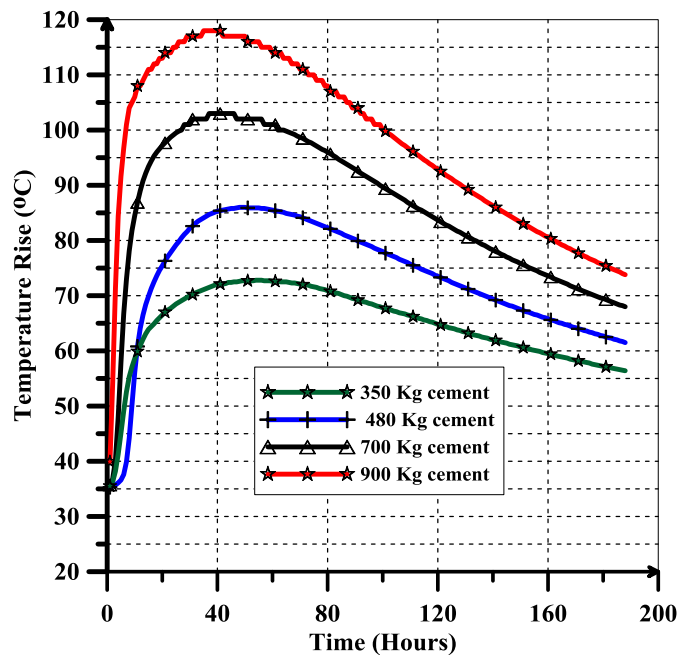
The effect of varying the w/cm ratio on the cracking index of element located at the top surface of mockup specimen with dimensions of 2m×2m×2 m is shown in Figure 8-25

Figure 8-25 shows that the cracking index of the top center element increases with an increase of w/cm ratio. The cracking index for the mix with 0.38w/cm has almost the same peak cracking index of control mix.



**Figure 8-25: Effect of Varying W/CM on the Cracking Index of Element Located at Top Center of MUS**

The effect of high content of cement on the temperature rise in a mockup specimen with dimensions of 2m×2m×2m was investigated. Figure 8-26 shows the differences between the temperature rise curve of three different content of cement Type I(480,700,and 900 kg).



**Figure 8-26: The Effect of Cement Content on the Temperature Rise at the Core of MUS**



As the cement content increases, the temperature rise at the core of a mockup specimen (with dimensions of 2m×2m×2m) increases. The peak temperature reaches to 120 °C for the mix with 900 kg cement which is considered a very high value. One of the easiest ways to reduce the temperature rise at the core of mockup specimen is using a mix with low content of cement on condition that no violation occurred for mechanical properties of concrete.

The cracking index in the top center of mockup specimen surface was predicted in case of using the mixes containing different contents of cement Type 1 as shown in Figure 8-27.

The mix with 900 kg cement has the higher cracking index compared to the mixes with 480 kg and 700 kg cement. The cracking index of the mix with 700kg is higher than that of mix with 480 kg. This is results from the higher temperature difference between the core and surface.

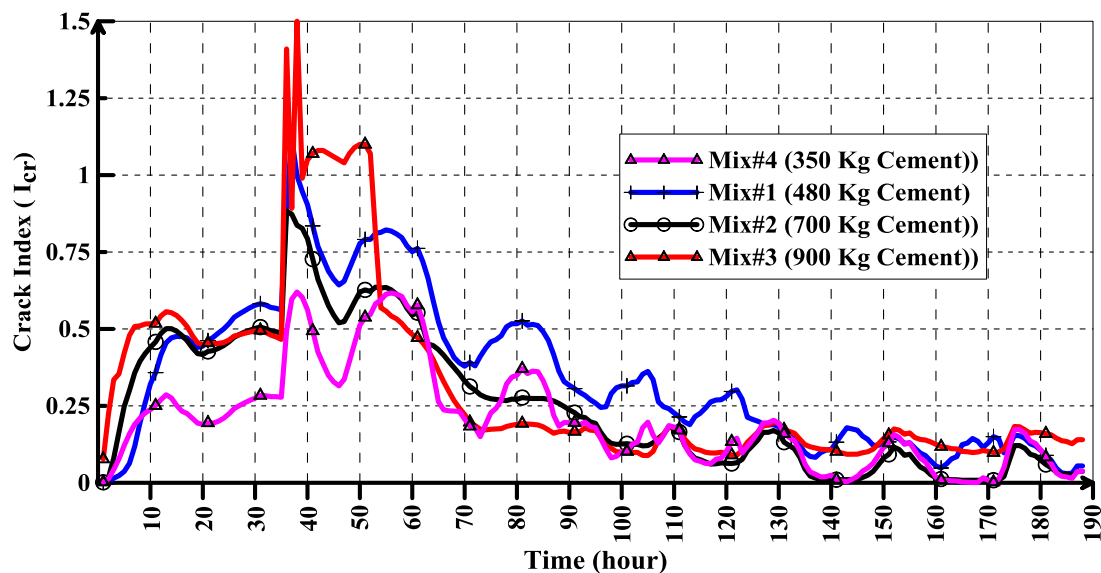


**Figure 8-27: The Effect of Cement Content on the Cracking Index of MUS**

The effect of polypropylene and steel fibers on the temperature rise at the core of mockup specimens with dimensions of 2m×2m×2m was investigated.

Two mixes contains steel fibers with 0.3% and 0.5% volume fractions respectively whereas the other two mixes contains polypropylene fibers with 0.3% and 0.5% volume fractions respectively.

Figure 8-28 shows that polypropylene fibers have a significant effect on decreasing the temperature rise compared to the effect of steel fibers. As the percentage of polypropylene or steel fibers increases, the evolution of temperature decreases.

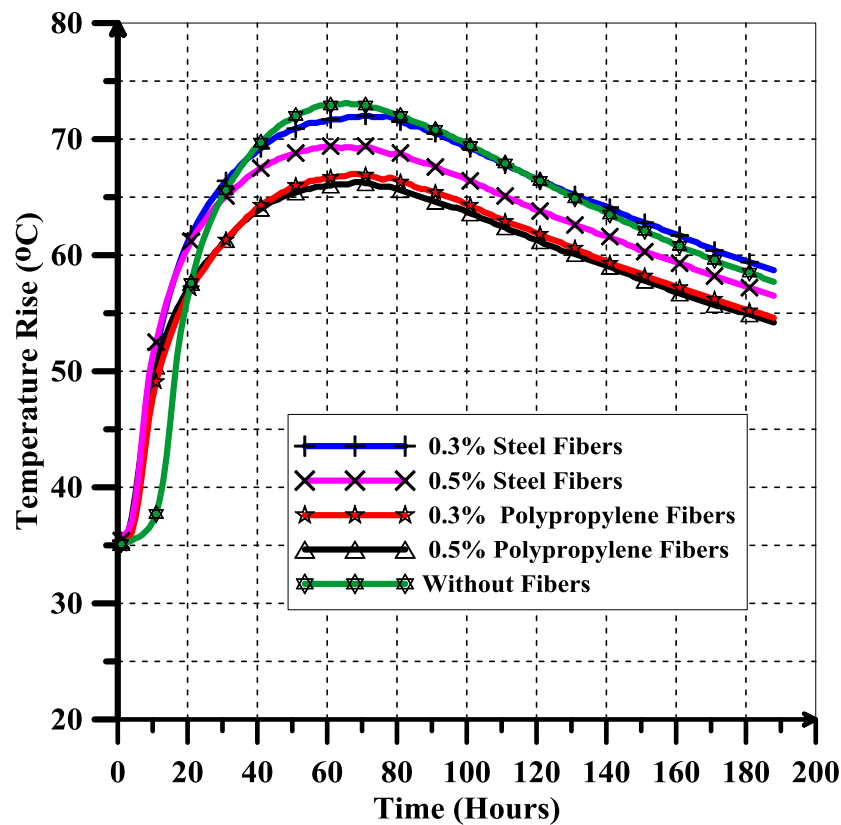


**Figure 8-28: Effect of Steel and Polypropylene fibers on Temperature Rise**

Figure 8-29 shows the effects of steel and polypropylene fibers on the cracking index of element located at the top center of mockup specimen surface. The cracking indexes for the mixes with polypropylene fibers are less than that of mixes with steel fibers. The reduction of temperature rise that caused by polypropylene fibers results in a decrease in the cracking indexes. The mix with 0.3% steel fibers has low tensile strength at early age

(two days from casting) and high temperature rise. Therefore, this mix has the highest cracking index.

It is interesting to note that the steel fibers have a slight effect on reducing either the temperature rise or the cracking index in the mockup specimen at early age.

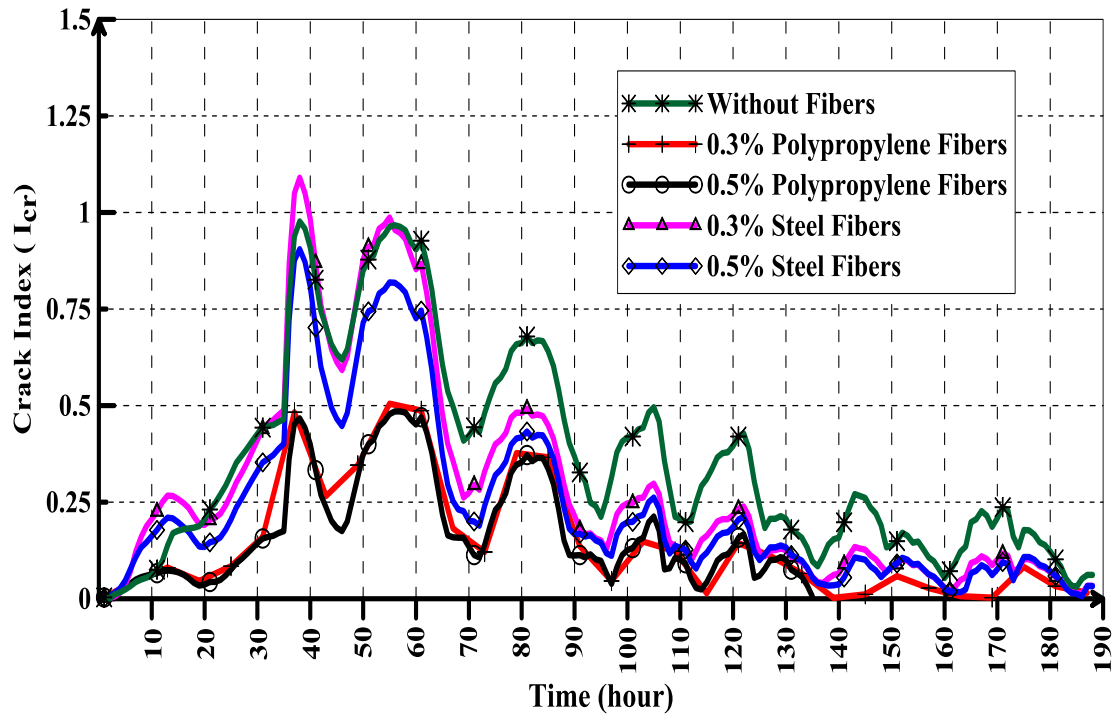


**Figure 8-29: Effect of Steel and Polypropylene fibers on the Cracking Index**

## 8.8 Effect of Interface Elements

Modeling the interaction between concrete and soil was carried out by using a special element which can simulate the interface behavior correctly. In this study, the eight noded element (Q24IF), having zero-thickness, was used to model the interface behavior. The interface elements relate the forces acting on the interface to the relative displacement of concrete and soil as mentioned in chapter 4. Three different cases were studied. In the first case, the interface element was used and the parameters of Mohr Coulomb friction model were estimated. The cohesion of the soil was assumed to be 0.001 MPa. The friction angle was input as 30 °C. The dilatancy angle is assumed to

equal zero (no volumetric change during shear stress). In the second case, the perfect bond between the soil and concrete was assumed. Neither slip nor detachment is allowed in that case. In the third case, the soil was neglected, and the pinned support was assigned for the nodes of the bases of mockup specimen.

The cracking index for the element located at the top center of mockup specimen surface was predicted for the three cases as shown in Figure 8-30. The period from time of casting to about 40 hours, the cracking index for the case of pinned support is higher than that of other cases. In case of using interface elements, the cracking index has become less than other cases. The number of cracked elements for three cases is shown in Figure 8-35 for ages 40, 60, and 80 hours. It is clear that the number of cracked elements is lowest for the case in which the interface elements were used. The case of using pinned support has the highest number of cracked elements as shown Figure 8-31.

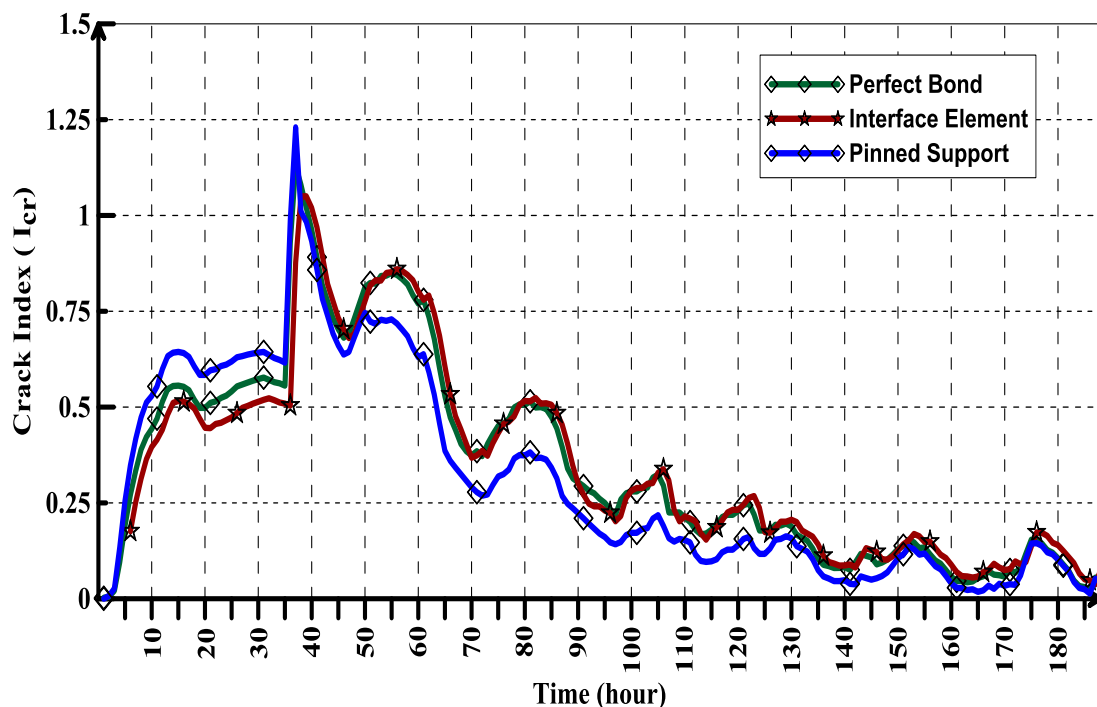


**Figure 8-30: Effect of Interaction between Concrete and Soil on the Cracking Index**

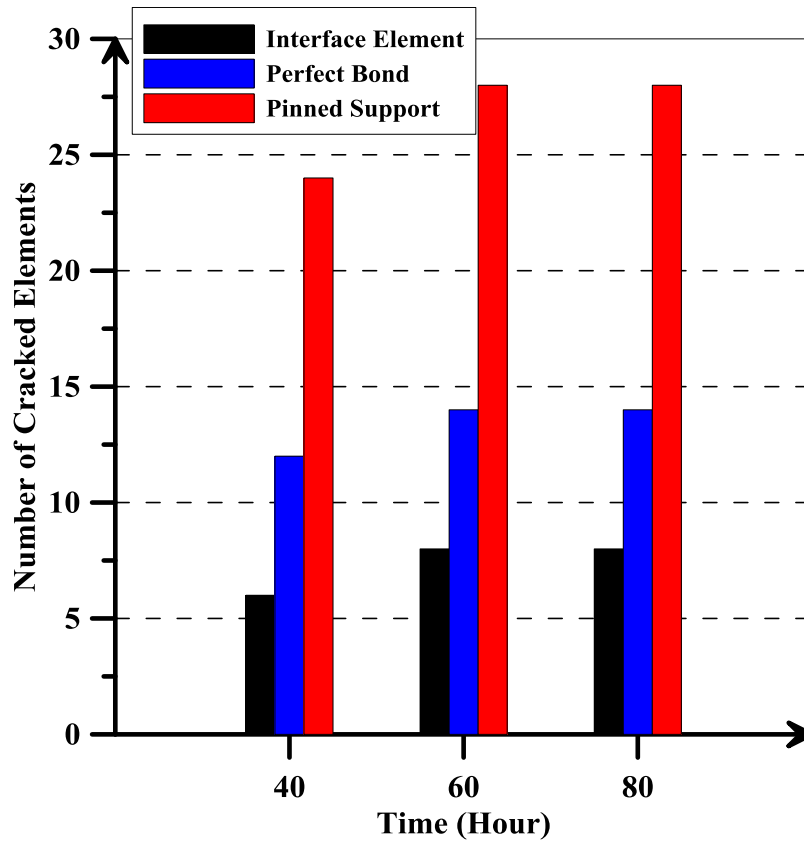


**Figure 8-31: Effect of Interaction between Concrete and Soil on the Number of Cracked Elements**

The cracked patterns for the three cases in study are shown in Figure 8-32. The locations of cracked elements are at the top surface or at sides of mockup specimen. The case of using pinned support has more numbers of cracked elements at sides of mockup specimen as compared to other two cases. This is occurred due to the increase of degree of restraint against volume changes. As the degree of restraint decreases, the cracking index and the number of cracked elements decreases. The interface surface can be modeled as smooth or rough depending on its cohesion and friction angle.

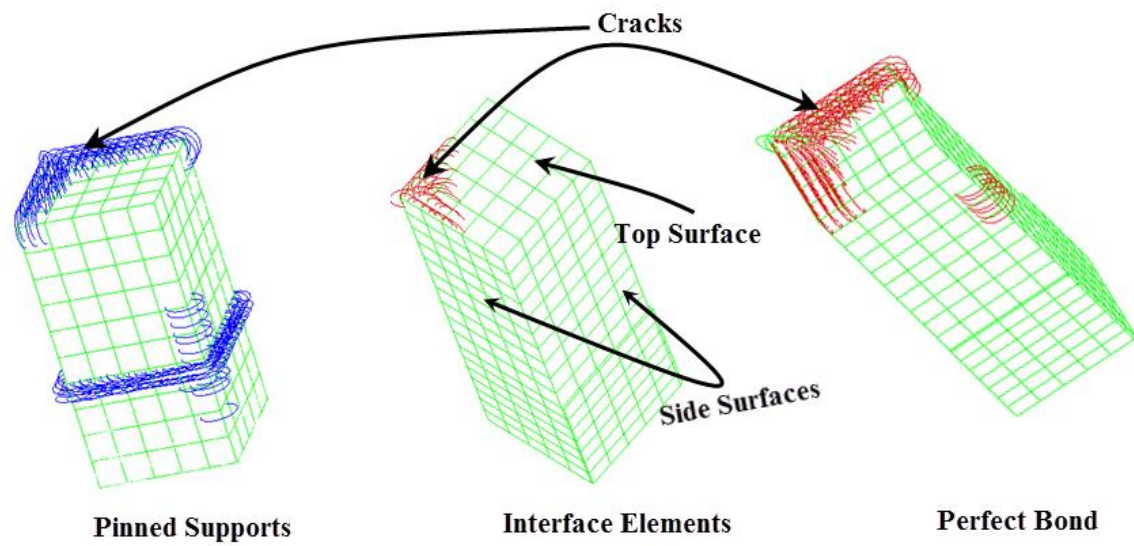


**Figure 8-32: Effect of Interaction between Concrete and Soil on the Crack Patterns**

## **CHAPTER 9**

### **SUMMARY, CONCLUSIONS AND RECOMMENDATIONS**

This chapter presents a summary of the work undertaken over this study. Conclusions regarding the significant findings are offered, and recommendations are provided.

#### **9.1 Summary**

To better understand the behavior of massive concrete structures in its early age, measurements of the heat of hydration using iQdrum calorimeter and heat box for various 46 concrete mixes were carried out. The mechanical properties of these concrete mixes such as tensile strength, compressive strength, and modulus of elasticity were also conducted. The effect of mineral admixtures such as Fly Ash, ground granulated blast furnace (GGBFS) slag, and silica fume on heat of hydration was investigated. The effect of steel and polypropylene fibers on the heat of hydration and on the cracking index of mass concrete at early age was studied.

The hydration parameters ( $\tau$ ,  $\beta$ , and  $H_u$ ) have been determined using the regression analysis. These parameters were used to differentiate between the various concrete mixes in terms of their behavior during hydration.

The temperature rise and strains on different seven mockup specimens and pile-cap was monitored. The finite element simulation for temperature distribution and stresses was carried out. Development of mechanical properties with time, influence of framework, solar radiation, and change of ambient temperature with time, and measurements of heat of hydration of cement are properly incorporated in the finite element model. The feature of staggered flow-stress analysis in TNO DIANA software

was utilized, in which the temperature distribution was calculated by heat flow analysis, followed by structural analysis.

The cracking behavior is simulated using a smeared cracking concept, in which the cracked material is treated as continuous, and the discontinuity of the displacement field caused by the crack is spread across the element by changing the constitutive equation. A constant shear retention factor  $\beta$  for the cracked concrete is assumed equal to 0.2 in the finite element simulation. The tension softening criterion is applied depending on the maturity.

The interface between the concrete and soil was modeled by 8-noded element (Q24IF), having zero-thickness. The interface elements have ability to relate the forces acting on the interface to the relative displacement of concrete and soil.

The nonlinear interface behavior was modeled with the Coulomb friction model. The interface surface can be modeled as smooth or rough depending on its cohesion and friction angle. The smooth surface is applied for a very low degree of restraint between the concrete and soil; however, the rough surface presents a high degree of restraint. The maximum restraint condition is assumed in case of the perfect bond between the two surfaces; neither slip nor detachment is allowed in that case.

A parametric study was conducted with the aid of the DIANA finite element program. The parameters investigated are size of the structure, placement temperature, solar radiation, type of mineral admixtures, type of formwork, amount of steel reinforcement, and interface element.



## 9.2 CONCLUSIONS

This study addressed many aspects of laboratory testing, field work and the development of finite element simulation. Based on the work documented in this dissertation, the following conclusions are made:

- The experimental and finite element simulation results shows that replacing cement with fly ash Type F results in a significant reduction in the heat of hydration in mass concrete, whereas, the influence of GGBFS on reducing heat of hydration is less than that of fly ash. This is due to the fact that GGBFS has a higher percentage of lime as compared to Fly Ash.
- An increase in the percentage of FA also leads to decrease in values of concrete compressive strength, and consequently its tensile strength and modulus of elasticity. Therefore, reduction in heat of hydration does not necessarily lead to a reduction in cracking index of mass concrete structures. One cannot view heat of hydration behavior in isolation but must be considered in tandem with early strength evolution with time.
- Increasing the replacement percentage of GGBFS to 70% does not lead to a significant decrease on heat of hydration in mass concrete structures. Therefore, to achieve a higher reduction in heat of hydration, the replacement percentage of GGBFS (Grade 120) may reach 70% or more. Due to presence of high amount of lime, this does not lead to a compromise in early strength evolution.
- Replacing cement with 10% Micro-Silica leads to an increase in the heat of hydration, however, the heat evolution decreases as the replacement levels of Micro-Silica exceeds 10%. This increase in heat of hydration due to addition of micro silica <10% is possibly due to formation of secondary CSH. However, once replacement levels of micro silica are increased beyond 10%, the CH levels resulting from the

hydration of cement are rapidly depleted and not available for formation of further secondary CSH.

- The heat of hydration increases with an increase of the cement content in concrete mixtures. Increasing the cement content to a quantity of  $900\text{kg/m}^3$  leads to an increase in the temperature at the core of mockup specimen with dimensions of  $2\text{m}\times 2\text{m}\times 2\text{m}$  to about  $122^\circ\text{C}$ . Additionally, the cracking index of the mixes with high content of cement increased significantly.
- As the water to cementitious materials ratio increases, the heat of hydration is noticed to increase. Coupled with decreased tensile strength, this leads to increased cracking index.
- The polypropylene fibers are noted to have a considerable effect on reducing the heat of hydration and the cracking indices of concrete mixtures. However, the presence of polypropylene fibers reduces the flow and hence the workability of the mixes, as water is absorbed by fibers. This reduces the heat of hydration evolution at early age.
- The steel fibers have a slight effect on reducing the heat of hydration evolution. It is interesting to conclude that the steel fibers have no effect on the tensile strength at early age (two to three days from casting). Therefore, cracking index of mixes with steel fibers remains approximately unchanged compared to the cracking index of the mix without steel fibers. It is worth mentioning, the steel fibers increases tremendously the tensile strength of concrete mixes at 7 and 28 days.
- The thermal conductivity of steel formwork is very high compared to the thermal conductivity of plywood formwork. Therefore, the heat loss from steel formwork makes the temperature difference between the core and side higher than between

the core and top surface, which is shown from the FEM model to result in increased potential of cracking at side surfaces of mass concrete structures.

- It is important to insulate the top surfaces and sides with polystyrene foam to reduce the probability of cracking due to thermal gradient. However precautions should be taken to avoid the occurrence of delayed ettringite formation (DEF) due to high concrete core temperatures ( $>70^{\circ}\text{C}$ ).
- The temperature at the surface of the mass concrete is lower than the temperature in its core due to the dissipation of heat to the surrounding environment. Due to this thermal gradient, the thermal cracks are initiated when the thermal stress in concrete exceeds its tensile strength at early age. Therefore, the highest tensile stresses were observed at the center of top surface and at side surfaces, since these surfaces were exposed to ambient conditions.
- The solar radiation increases the temperature of external surfaces which results in reduction of the temperature difference between the core of mass concrete and its surface. Consequently, the cracking index is noted to decrease.
- At present, it is widely considered that the temperature difference between the core of mass concrete and its surface should be limited to being between 20 and  $25^{\circ}\text{C}$ ; however, the concrete temperature difference in a mockup specimen with dimensions of  $2\text{m}\times 2\text{m}\times 2\text{m}$  (KMUS) and in pile-cap reached  $32^{\circ}\text{C}$  and  $31^{\circ}\text{C}$  respectively without cracking. It can be concluded that the criterion of limiting the temperature difference in mass concrete structures to  $25^{\circ}\text{C}$  is conservative and may be relaxed to  $30^{\circ}\text{C}$ .
- The interface elements with zero thickness give an accurate representation for the interaction between concrete and soil. The perfect bond case shows greater

cracking indexes and results in an increase of number of cracked elements due to higher degree of external restraint.

- Reduction in the heat of hydration does not necessarily lead to the decrease of cracking index. Therefore, the reduction of heat must be accompanied by the decrease in cracking risk to design a suitable mix for mass concrete structures.
- It is recommended in order to have mass concrete in KSA and other similar environments, GGBFS admixed concretes with cement replaced up to 70% by GGBFS have been found to be the most suitable in view of decreased heat of hydration, with no accompanying loss of tensile strength. This results in lowered values of cracking index.
- The developed finite element model using DIANA code can simulate the problem of thermal and shrinkage stresses in any type of structures -not only the mass concrete structures, such as retaining walls, water tanks, etc. and would indicate if the cracks will develop or not with the concrete mix specified. These way adjustments can be made prior to the start of the construction of the planned project.

### **9.3 Recommendations for Future Research**

To understand well the behavior of mineral and chemical admixture during hydration at early age, the 46 mixes can be investigated further using nanotechnology.

## REFERENCES

- [1] Concrete Information, "Concrete for Massive Structure," *Portland Cement Association*, 2006.
- [2] Emborg I., and Bernander S., "Temperature Stresses in Early Age Concrete Due to Hydration," *Structure.Comput.Struct*, 1995, pp. 287-296.
- [3] ACI Committee 207 "Mass Concrete," *ACI 207.IR-87 Manual of Concrete Practice*, Part I.
- [4] ACI Committee 207, "Cooling and Insulating System for Mass Concrete," *ACI 207.4R-80 Manual of Concrete Practice*.
- [5] John, G. and, Martha, V., "Controlling Temperature in Mass Concrete," *Concrete International Journal*, 2002, pp. 59-62.
- [6] Lawrence, C. D., "Delayed Ettringite Formation: An Issue? In: J. Skalny, S. Mindess (Eds.), *Materials Science of Concrete IV*." American Ceramic Society, Westerville, OH, 1995, pp. 113– 154.
- [7] Collepardi, M., "A State-Of-The-Art Review On Delayed Ettringite Attack on Concrete," *Cement and Concrete Composites J.*, 2003, pp. 401-407.
- [8] Y. Fu, "Delayed Ettringite Formation in Portland Cement Products," PhD thesis, CNRC, Ottawa, Canada, 1996.
- [9] Heinz D, Ludwig U. "Mechanism of Secondary Ettringite Formation in Mortars and Concretes Subjected to heat treatment Concrete Durability,"—Katharine and Bryant Mather International Symposium SP-100, ACI, Farmington Hills, Mich., 1987. pp.2059–71.
- [10] Schindler, A. K., "Concrete Hydration, Temperature Development, and Setting at Early-Ages," PHD Dissertation, University of Texas, Austin, 2002.

- [11] Neville, A.M.,” Properties of Concrete,” 4<sup>th</sup> Ed.1995, Essex: Pearson Education, Limited.
- [12] Mindless, S., Young, J.F. and Darwin, D., “Concrete, 2nd Edition.” *Pearson Education, Inc.*, Upper Saddle River, NJ, USA,(2002).
- [13] Zhi Ge and Kejin.W., Paul J., Sandberg and M. Ruiz. “Characterization and Performance Prediction of Cement-Based Materials Using a Simple Isothermal Calorimeter,” *Journal of Advanced Concrete Technology.*” 7(3), pp.1-12,(2009).
- [14] ACI 116R, Cement and Concrete Terminology
- [15] Silica Fume User's Manual - Silica Fume Association, APRIL 2005
- [16] De Schutter G, Taerwe L., “General Hydration Model for Portland Cement and Blast Furnace Slag Cement,” *Cement and Con Research Journal*, Vol.25, 1995, pp.593–604.
- [17] De Schutter G, Taerwe L., “Degree of hydration-based description of mechanical properties of early age concrete,” *Material and Structure Journal*, Vol.29, 1996, pp.335–344.
- [18] Alexandre G, Eduardo, M.R., Eto, F., Marcos, M. and Romildo D. “Modeling Adiabatic Temperature Rise During Concrete Hydration: A data Mining Approach,”*Computer and Structures*, Vol.84, 2006, pp.2351–2362.
- [19] D.P. Bentz, “CEMHYD3D: A Three-Dimensional Cement Hydration and Microstructure Development Modeling Package,” Version 2.0’, NISTIR 6485, U.S. Department of Commerce, April 2000.
- [20] K. Meakawa, R. Chaube, T. Kishi, Modeling of Concrete Performance:hydration, microstructure formation and mass transport,” E and FN SPON,London, 1999.

- [21] K. van Breugel, "Numerical Simulation of Hydration and Microstructural Development in Hardening Cement-Based Materials," *Cem. Concr. Res.* 25(2) (1995) 319–331.
- [22] Machida, N. and Uehara, K., "Nonlinear Thermal Stress Analysis of a Massive Concrete Structure," *Structure.Comput.Struct*, 1995, pp. 287-296.
- [23] Chiristophier, C. F., "Determination of Test Methods for The Prediction of The Behavior of Mass Concrete," PHD Dissertation, University of Florida, Austin 2009.
- [24] Radovanovic, S, "Thermal and Structural Finite Element Analysis of Early Age Mass Concrete Structures," *Nordic Concrete Research*, 1984, pp. 28-48.
- [25] Haung , C.X., "The Three Dimensional Modelling of Thermal Cracks in Concrete Structure," *Material and Structure*, Vol. 32, November 1999, pp. 673-678.
- [26] Ayotto, E., Massicotte, B., Houda, J., and Gocevski, V., "Modeling of Thermal Stresses at Early Ages in a Concrete Monolith," *ACI Material Journal*, Vol. 94, 1997, pp. 577-587.
- [27] De Schutter G., "Finite Element Simulation of Thermal Cracking in Massive Hardening Concrete Elements Using Degree of Hydration Base Material Laws," *Computer and Structures*, Vol.80, 2000, pp.2035–2042.
- [28] Upadhyaya, S., "Early Age Strength Prediction For High Volume Fly Ash Concrete Using Maturity Modeling," PHD Dissertation, University of Maryland, College Park, 2008.
- [29] Yan Zhou, N., "Numerical Modeling of Thermomechanical Properties of Early Age Concrete," PHD Dissertation, University of Akron, 1997.

- [30] Arshad, K., "Concrete Properties and Thermal Stress Analysis of Members at Early Ages," PHD Dissertation, University of McGill, Canada 1995.
- [31] Kyle, A., "Early Age Concrete Thermal Stress Measurement and Modeling," PHD Dissertation, University of Texas, Austin 2007.
- [32] Farro,F., "Concrete Temperature , Maturity, and Heat Signature," Concrete Technology Forum, NRMCA, Cincinnati, May 2009.
- [34] Nurse, R.W., "Steam Curing of Concrete," Magazine of Concrete Research, Vol.(5),No.2, June, 1949.
- [35] Carino, N. J. and Tank, R.C., "Maturity Functions for Concretes Made with various Cements and Mixtures," ACI Materials Journal, Vol. 89, No. 2, American Concrete Institute, March-April, 1992.
- [36] ASTM C 1074-93, "Practice for Estimating Concrete Strength by the Maturity Method," American Society of Testing and Materials, Vol. 4.02, 1993, pp. 534-540.
- [37] Hansen, P., and Pedersen,E, "Maturity Computer for Controlling Curing and Hardening of Concrete," Nordisk Betong. 19(1) (1977) pp.21-25.
- [38] TCE1, "Adiabatic and Semi-Adiabatic Calorimetry to Determine the Temperature Increase in Concrete Due to Hydration Heat of the Cement," Mater. Struct. 30 (1997) pp.451–464.
- [39] Gerstig, M., Wisdom, L., "A Method Based on Isothermal Calorimetry to Quantify the Influence of Moisture on the Hydration Rate of Young Cement Pastes," *Cem.Concr. Res.* 40 (2010) pp. 867–874.
- [40] Gruyaert, E., Robeyst, N., De Belie, N., "Study of the Hydration of Portland Cement Blended with Blast-Furnace Slag by Calorimetry and Thermogravimetry," *J. Therm. Anal. Calorim.* 102 (2010) 941–951.



- [41] A.K. Schindler, K.J., "Folliard, "Heat of hydration models for cementitious materials," *ACI Materials Journal* 102 (2005) 24–33.
- [42] ASTM C 150, "Standard Specification for Portland cement," Annual Book of ASTM Standards(2002), 1, 4.02.
- [43] Van Breugel, K., "Prediction of Temperature Development in Hardening Concrete," Prevention of Thermal Cracking in Concrete at Early Ages." RILEM Report 15, E & FN Spon, London 1998.
- [44] Emanuel JH, Hulsey JL. "Prediction of Thermal Coefficient of Expansion of concrete," *J ACI*. 1977;74(4):149–55.
- [45] Sellevold EJ, Bjntegaard Ø, "Coefficient of Thermal Expansion of Cement Paste and Concrete: Mechanisms of Moisture Interaction," *Mater. Struct*, 2006, 39, PP 809–815.
- [46] Incropera, F.P.; and Dewitt, D.P., (2002). "Fundamentals of Heat and Mass Transfer," John Wiley & Sons, Inc., New York, p. 931.
- [47] Shengxin W., Donghui H., Feng-Bao L., Haitao Z., Panxiu W. "Estimation of Cracking Risk of Concrete at Early Age Based on Thermal Stress Analysis." *Therm. Anal. Calorim.*, Vol. 17, No.1, April 2011, pp. 171-186.
- [48] Autodesk Ecotect Analysis Sustainable Design Analysis Software Manual.
- [49] Threlkeld, J.L., "Thermal environmental engineering," New Jersey: Prentice-Hall Inc.; 1970.
- [50] Kaska O, Yumrutas R, Arpa O., "Theoretical and Experimental Investigation of Total Equivalent Temperature Difference (TETD) Values for Building Walls and Flat Roofs in Turkey," *Appl. Energy*.2009;86(5):737–47.
- [51] Rashid, Y. R., "Analysis of Prestressed Concrete Pressure Vessels," *Nuclear Engineering and Design*, 1968, 7(4), pp. 334-344.

- [52] Suidan, M., and Schnobrich, W. C. (1973). "Finite Element Analysis of Reinforced Concrete," *Journal of the Structural Division, ASCE*, 99(10), pp. 2109-2122.
- [53] Cook, R. D., Malkus, D. S., Plesha, M. E., and Witt, R. J. (2001). "*Concepts and Applications of Finite Element Analysis*," John Wiley & Sons, Inc., New York.
- [54] Litton, R. W. A "Contribution to the Analysis of Concrete Structures under Cyclic Loading," PhD thesis, University of California, Berkeley, 1974.
- [55] DIANA Finite Element Analysis User's Manual Analysis Examples Release 9.4
- [56] CEB-FIP Model Code 1990. Comit e Euro-International du B ton, 1993.
- [57] Holt, E., and Leivo, M., "Cracking Risks Associated with Early Age Shrinkage," *Cem. Concr. Compos.*, 26(5) (2004) 521-530.
- [58] Lura, P., Winnefeld, F., and Klemm S, "Simultaneous Measurements of Heat of Hydration and Chemical Shrinkage on Hardening Cement Pastes," *J Therm. Anal. Calorim.* 101(3) (2004) 925-935
- [59] Boulon, M. And Nova, R., "Modeling Of Soil Structure Interface Behavior, A Comparison Between Elastoplastic and Rate Type Laws," *Computers and Geotechnics*, 9, 21-46 (1990).
- [60] Boulon, M., "Basic Features of Soil Structure Interface Behavior," *Computers and Geotechnics*, 7, 115-131 (1989).
- [61] ACI 305R, "Hot Weather Concreting – Reported by ACI Committee 305," *American Concrete Institute*, Farmington Hills, Michigan, 2000.

## APPENDIX A

### Parameters of Finite Element Model

**Table A1-1: Change of Tensile Strength with Equivalent Age**

	Mix Type		t <sub>e</sub> (Hour)	F <sub>t</sub> (N/m <sup>2</sup> )	t <sub>e</sub> (Hour)	F <sub>t</sub> (N/m <sup>2</sup> )	t <sub>e</sub> (Hour)	F <sub>t</sub> (N/m <sup>2</sup> )	t <sub>e</sub> (Hour)	F <sub>t</sub> (N/m <sup>2</sup> )
<b>Group#1</b>	Control Mix (100% OPC)	MATCRK	0.00	0.00	28.89	1.96E+06	124.09	2.54E+06	258.26	3.64E+06
	20 % Fly Ash	MATCRK	0.00	0.00	25.44	1.71E+06	87.05	2.22E+06	186.37	3.31E+06
	30% Fly Ash	MATCRK	0.00	0.00	24.34	1.66E+06	62.83	2.16E+06	134.86	3.25E+06
	40% Fly Ash	MATCRK	0.00	0.00	24.56	1.20E+06	69.79	1.56E+06	149.54	2.26E+06
	50 % Fly Ash	MATCRK	0.00	0.00	23.84	9.29E+05	49.38	1.21E+06	94.25	1.60E+06
	60 % Fly Ash	MATCRK	0.00	0.00	25.88	8.46E+05	74.23	1.10E+06	136.26	1.59E+06
<b>Group#2</b>	20 % GGBFS	MATCRK	0.00	0.00	31.56	1.69E+06	118.88	2.20E+06	244.69	2.90E+06
	30% GGBFS	MATCRK	0.00	0.00	32.87	1.74E+06	117.57	2.27E+06	231.25	3.20E+06
	40%GGBFS	MATCRK	0.00	0.00	26.43	1.25E+06	96.42	1.62E+06	205.48	1.98E+06
	50 % GGBFS	MATCRK	0.00	0.00	27.42	1.29E+06	86.45	1.67E+06	182.38	2.24E+06
	60 % GGBFS	MATCRK	0.00	0.00	34.81	1.35E+06	116.08	1.75E+06	219.81	2.46E+06
	70 % GGBFS	MATCRK	0.00	0.00	34.81	1.35E+06	116.08	1.75E+06	219.81	2.46E+06
<b>Group#3</b>	20 %FA+ GGBFS	MATCRK	0.00	0.00	26.98	1.42E+06	111.38	1.84E+06	238.08	2.40E+06
	30% FA+ GGBFS	MATCRK	0.00	0.00	28.71	1.03E+06	99.32	1.33E+06	199.04	1.70E+06
	40%FA+ GGBFS	MATCRK	0.00	0.00	81.10	1.30E+06	212.40	1.70E+06	351.40	2.46E+06
	50 %FA+ GGBFS	MATCRK	0.00	0.00	35.94	1.04E+06	119.80	1.35E+06	227.36	1.97E+06
	60 % FA+ GGBFS	MATCRK	0.00	0.00	28.32	1.01E+06	77.87	1.32E+06	147.43	1.70E+06
<b>Group#4</b>	(Control)350kg Cement	MATCRK	0.00	0.00	35.48	1.03E+06	109.30	1.34E+06	198.23	1.99E+06
	20 % Fly Ash	MATCRK	0.00	0.00	35.48	9.97E+05	109.30	1.30E+06	198.23	1.93E+06
	30% Fly Ash	MATCRK	0.00	0.00	31.22	1.02E+06	90.56	1.33E+06	161.71	2.01E+06
	40% Fly Ash	MATCRK	0.00	0.00	26.97	7.96E+05	71.89	1.04E+06	125.10	1.56E+06
	50 % Fly Ash	MATCRK	0.00	0.00	20.97	7.49E+05	51.89	9.74E+05	85.10	1.41E+06
<b>Group#5</b>	20 % GGBFS	MATCRK	0.00	0.00	37.38	9.96E+05	109.51	1.29E+06	199.04	1.90E+06
	30% GGBFS	MATCRK	0.00	0.00	35.42	1.08E+06	102.03	1.41E+06	185.00	2.14E+06
	40%GGBFS	MATCRK	0.00	0.00	33.46	1.06E+06	94.54	1.38E+06	175.08	2.08E+06
	50 % GGBFS	MATCRK	0.00	0.00	32.02	9.99E+05	89.53	1.30E+06	167.08	1.89E+06
<b>Group#6</b>	10 % Micro Silica	MATCRK	0.00	0.00	34.78	1.66E+06	132.77	2.16E+06	265.02	2.50E+06
	20 % Micro Silica	MATCRK	0.00	0.00	38.73	1.81E+06	139.48	2.35E+06	268.04	3.10E+06
	30% Micro Silica	MATCRK	0.00	0.00	34.78	1.66E+06	132.77	2.16E+06	265.02	2.50E+06
	40% Micro Silica	MATCRK	0.00	0.00	38.73	1.81E+06	139.48	2.35E+06	268.04	3.10E+06

**Table A1-1: Change of Tensile Strength with Equivalent Age (Cont..)**

	Mix Type		t <sub>e</sub> (Hour)	F <sub>t</sub> (N/m <sup>2</sup> )	t <sub>e</sub> (Hour)	F <sub>t</sub> (N/m <sup>2</sup> )	t <sub>e</sub> (Hour)	F <sub>t</sub> (N/m <sup>2</sup> )	t <sub>e</sub> (Hour)	F <sub>t</sub> (N/m <sup>2</sup> )
<b>Group#1</b>	Control Mix (100% OPC)	MATCRK	412.40	3.91E+06	574.94	4.10E+06	741.79	4.23E+06	910.79	4.34E+06
	20 % Fly Ash	MATCRK	304.02	3.42E+06	432.51	3.50E+06	567.37	3.56E+06	705.62	3.60E+06
	30% Fly Ash	MATCRK	224.09	3.32E+06	324.34	3.37E+06	431.61	3.41E+06	543.07	3.44E+06
	40% Fly Ash	MATCRK	247.83	2.41E+06	358.36	2.52E+06	477.14	2.61E+06	601.29	2.69E+06
	50 % Fly Ash	MATCRK	154.58	1.86E+06	223.67	2.03E+06	299.20	2.16E+06	379.23	2.26E+06
	60 % Fly Ash	MATCRK	205.66	1.69E+06	280.24	1.77E+06	358.85	1.84E+06	440.69	1.89E+06
<b>Group#2</b>	20 % GGBFS	MATCRK	391.00	3.38E+06	546.58	3.50E+06	706.94	3.60E+06	870.26	3.68E+06
	30% GGBFS	MATCRK	359.66	3.49E+06	496.17	3.68E+06	637.07	3.82E+06	780.05	3.93E+06
	40%GGBFS	MATCRK	332.55	2.50E+06	469.15	2.87E+06	610.99	3.16E+06	756.63	3.37E+06
	50 % GGBFS	MATCRK	301.51	2.58E+06	432.42	2.83E+06	570.16	3.03E+06	712.59	3.19E+06
	60 % GGBFS	MATCRK	331.60	2.70E+06	447.49	2.89E+06	565.99	3.05E+06	686.06	3.19E+06
	70 % GGBFS	MATCRK	331.60	2.70E+06	447.49	2.89E+06	565.99	3.05E+06	686.06	3.19E+06
<b>Group#3</b>	20 %FA+ GGBFS	MATCRK	386.48	2.83E+06	545.88	3.39E+06	711.25	3.77E+06	880.65	4.04E+06
	30% FA+ GGBFS	MATCRK	316.27	2.05E+06	445.51	2.86E+06	582.60	3.27E+06	725.21	3.48E+06
	40%FA+ GGBFS	MATCRK	446.11	2.61E+06	563.95	2.71E+06	700.34	2.79E+06	838.45	2.85E+06
	50 %FA+ GGBFS	MATCRK	347.76	2.08E+06	475.86	2.16E+06	609.19	2.23E+06	745.73	2.29E+06
	60 % FA+ GGBFS	MATCRK	232.24	2.03E+06	326.76	2.46E+06	427.27	2.74E+06	531.45	2.94E+06
<b>Group#4</b>	(Control)350kg Cement	MATCRK	296.67	2.06E+06	401.09	2.11E+06	509.79	2.15E+06	620.89	2.18E+06
	20 % Fly Ash	MATCRK	0.00	0.00	35.48	9.97E+05	109.30	1.30E+06	198.23	1.93E+06
	30% Fly Ash	MATCRK	296.67	1.99E+06	401.09	2.04E+06	509.79	2.08E+06	620.89	2.12E+06
	40% Fly Ash	MATCRK	240.03	2.05E+06	322.97	2.07E+06	409.48	2.09E+06	498.19	2.11E+06
	50 % Fly Ash	MATCRK	183.38	1.59E+06	244.85	1.62E+06	309.16	1.63E+06	375.49	1.65E+06
<b>Group#5</b>	20 % GGBFS	MATCRK	299.34	1.99E+06	406.26	2.05E+06	518.14	2.09E+06	650.00	2.12E+06
	30% GGBFS	MATCRK	283.30	2.16E+06	386.50	2.18E+06	494.00	2.20E+06	610.00	2.21E+06
	40%GGBFS	MATCRK	267.36	2.12E+06	367.03	2.16E+06	471.12	2.18E+06	570.00	2.20E+06
	50 % GGBFS	MATCRK	256.21	2.00E+06	352.12	2.07E+06	452.02	2.12E+06	545.00	2.15E+06
<b>Group#6</b>	10 % Micro Silica	MATCRK	406.33	3.62E+06	549.68	3.72E+06	695.97	3.80E+06	843.91	3.86E+06
	20 % Micro Silica	MATCRK	296.67	1.99E+06	401.09	2.04E+06	509.79	2.08E+06	620.89	2.12E+06
	30 % Micro Silica	MATCRK	331.20	1.79E+06	453.62	2.07E+06	579.80	2.29E+06	708.07	2.46E+06
	40 % Micro Silica	MATCRK	285.15	1.71E+06	393.26	2.04E+06	505.94	2.31E+06	621.66	2.52E+06

**Table A1-1: Change of Tensile Strength with Equivalent Age (Cont..)**

	Mix Type		t <sub>e</sub> (Hour)	F <sub>t</sub> (N/m <sup>2</sup> )	t <sub>e</sub> (Hour)	F <sub>t</sub> (N/m <sup>2</sup> )	t <sub>e</sub> (Hour)	F <sub>t</sub> (N/m <sup>2</sup> )	t <sub>e</sub> (Hour)	F <sub>t</sub> (N/m <sup>2</sup> )
<b>Group#1</b>	Control Mix (100% OPC)	MATCRK*	1081.59	4.42E+06	1253.16	4.48E+06	1425.50	4.54E+06	1773.07	1081.59
	20 % Fly Ash	MATCRK	846.42	3.64E+06	988.88	3.67E+06	1132.72	3.70E+06	1423.23	846.42
	30% Fly Ash	MATCRK	657.52	3.47E+06	773.80	3.49E+06	891.55	3.50E+06	1131.18	657.52
	40% Fly Ash	MATCRK	729.65	2.76E+06	861.02	2.82E+06	994.82	2.88E+06	1268.65	729.65
	50 % Fly Ash	MATCRK	462.74	2.33E+06	548.74	2.39E+06	636.78	2.44E+06	817.60	462.74
	60 % Fly Ash	MATCRK	525.07	1.93E+06	611.48	1.97E+06	699.80	2.01E+06	880.90	525.07
<b>Group#2</b>	20 % GGBFS	MATCRK	1035.24	3.75E+06	1201.37	3.82E+06	1368.51	3.87E+06	1705.52	1035.24
	30% GGBFS	MATCRK	924.75	4.02E+06	1070.46	4.09E+06	1217.13	4.14E+06	1512.74	924.75
	40%GGBFS	MATCRK	904.64	3.55E+06	1054.27	3.69E+06	1205.07	3.81E+06	1510.20	904.64
	50 % GGBFS	MATCRK	858.39	3.33E+06	1006.55	3.45E+06	1157.34	3.55E+06	1465.28	858.39
	60 % GGBFS	MATCRK	807.46	3.31E+06	929.94	3.42E+06	1053.52	3.52E+06	1302.48	807.46
	70 % GGBFS	MATCRK	807.46	3.31E+06	929.94	3.42E+06	1053.52	3.52E+06	1302.48	807.46
<b>Group#3</b>	20 %FA+ GGBFS	MATCRK	1053.64	4.25E+06	1229.88	4.40E+06	1407.83	4.52E+06	1768.05	1053.64
	30% FA+ GGBFS	MATCRK	872.51	3.60E+06	1023.69	3.67E+06	1176.91	3.72E+06	1489.31	872.51
	40%FA+ GGBFS	MATCRK	918.54	2.90E+06	1049.68	2.93E+06	1188.63	2.97E+06	1400.04	918.54
	50 %FA+ GGBFS	MATCRK	885.01	2.34E+06	1025.97	2.39E+06	1168.86	2.43E+06	1458.66	885.01
	60 % FA+ GGBFS	MATCRK	638.58	3.08E+06	747.43	3.19E+06	858.08	3.27E+06	1082.19	638.58
<b>Group#4</b>	(Control)350kg Cement	MATCRK	733.65	2.21E+06	847.76	2.23E+06	963.26	2.25E+06	1197.48	2.28E+06
	20 % Fly Ash	MATCRK	630.65	2.14E+06	730.76	2.17E+06	840.26	2.19E+06	1130.48	733.65
	30% Fly Ash	MATCRK	588.61	2.13E+06	679.22	2.14E+06	773.01	2.15E+06	961.23	588.61
	40% Fly Ash	MATCRK	443.56	1.66E+06	512.69	1.67E+06	582.76	1.68E+06	724.98	443.56
	50 % Fly Ash	MATCRK	340.00	1.67E+06	420.00	1.69E+06	410.00	1.71E+06	520.00	340.00
<b>Group#5</b>	20 % GGBFS	MATCRK	751.37	2.14E+06	871.19	2.15E+06	992.00	2.17E+06	1237.71	2.19E+06
	30% GGBFS	MATCRK	719.00	2.22E+06	834.00	2.23E+06	952.00	2.24E+06	1190.00	2.25E+06
	40%GGBFS	MATCRK	687.32	2.22E+06	798.78	2.23E+06	912.91	2.25E+06	1144.97	2.27E+06
	50 % GGBFS	MATCRK	659.17	2.18E+06	765.60	2.21E+06	874.34	2.23E+06	1094.99	2.25E+06
<b>Group#6</b>	10 % Micro Silica	MATCRK	1027.47	4.48E+06	1184.32	4.51E+06	1342.36	4.53E+06	1659.88	4.55E+06
	20 % Micro Silica	MATCRK	993.05	3.92E+06	1143.41	3.97E+06	1294.51	4.02E+06	1598.08	4.10E+06
	30 % Micro Silica	MATCRK	838.35	2.61E+06	969.12	2.72E+06	1099.89	2.82E+06	1361.42	2.98E+06
	40 % Micro Silica	MATCRK	740.09	2.70E+06	860.11	2.85E+06	981.87	2.97E+06	1228.74	3.18E+06

**\*MATCRK (Maturity Cracking) means change of tensile strength with maturity**

**Table A1-1: Change of Tensile Strength with Equivalent Age (Cont...)**

	Mix Type		$t_e$ (Hour)	$F_t(N/m^2)$	$t_e$ (Hour)	$F_t(N/m^2)$
<b>Group#1</b>	Control Mix (100% OPC)	MATCRK	2122.67	4.74E+06	2415.55	4.80E+06
	20 % Fly Ash	MATCRK	1717.50	3.78E+06	1831.86	3.80E+06
	30% Fly Ash	MATCRK	1374.97	3.55E+06	1580.85	3.57E+06
	40% Fly Ash	MATCRK	1548.18	3.06E+06	1785.42	3.13E+06
	50 % Fly Ash	MATCRK	1003.56	2.57E+06	1161.98	2.61E+06
	60 % Fly Ash	MATCRK	1067.20	2.11E+06	1225.91	2.14E+06
<b>Group#2</b>	20 % GGBFS	MATCRK	2045.71	4.06E+06	2331.08	4.12E+06
	30% GGBFS	MATCRK	1810.64	4.31E+06	2015.78	4.35E+06
	40%GGBFS	MATCRK	1818.71	4.13E+06	2078.09	4.22E+06
	50 % GGBFS	MATCRK	1777.48	3.86E+06	2039.36	3.96E+06
	60 % GGBFS	MATCRK	1550.08	3.84E+06	1589.15	3.95E+06
	70 % GGBFS	MATCRK	1550.08	3.84E+06	1589.15	3.95E+06
<b>Group#3</b>	20 %FA+ GGBFS	MATCRK	2132.10	4.80E+06	2439.38	4.87E+06
	30% FA+ GGBFS	MATCRK	1809.63	3.79E+06	2080.43	3.80E+06
	40%FA+ GGBFS	MATCRK	1674.43	3.06E+06	1911.77	3.09E+06
	50 %FA+ GGBFS	MATCRK	1753.13	2.57E+06	1813.05	2.61E+06
	60 % FA+ GGBFS	MATCRK	1310.27	3.45E+06	1502.74	3.49E+06
<b>Group#4</b>	(Control)350kg Cement	MATCRK	1435.37	2.31E+06	1634.60	2.33E+06
	20 % Fly Ash	MATCRK	1435.37	2.25E+06	1484.45	2.27E+06
	30% Fly Ash	MATCRK	1152.79	2.19E+06	1239.14	2.20E+06
	40% Fly Ash	MATCRK	870.22	1.72E+06	993.84	1.73E+06
	50 % Fly Ash	MATCRK	610.00	1.76E+06	715.00	1.77E+06
<b>Group#5</b>	20 % GGBFS	MATCRK	1487.69	2.20E+06	1699.09	2.21E+06
	30% GGBFS	MATCRK	1434.00	2.27E+06	1640.00	2.27E+06
	40%GGBFS	MATCRK	1381.39	2.28E+06	1581.08	2.30E+06
	50 % GGBFS	MATCRK	1319.15	2.28E+06	1507.63	2.29E+06
<b>Group#6</b>	10 % Micro Silica	MATCRK	1027.47	4.48E+06	1184.32	4.51E+06
	20 % Micro Silica	MATCRK	993.05	3.92E+06	1143.41	3.97E+06
	30 % Micro Silica	MATCRK	838.35	2.61E+06	969.12	2.72E+06
	40 % Micro Silica	MATCRK	740.09	2.70E+06	860.11	2.85E+06

**Table A1-2: Change of Tensile Strength with Equivalent Age**

	Mix Type		t <sub>e</sub> (Hour)	F <sub>t</sub> (N/m <sup>2</sup> )	t <sub>e</sub> (Hour)	F <sub>t</sub> (N/m <sup>2</sup> )	t <sub>e</sub> (Hour)	F <sub>t</sub> (N/m <sup>2</sup> )	t <sub>e</sub> (Hour)	F <sub>t</sub> (N/m <sup>2</sup> )
<b>Group#7</b>	30% Fly Ash(0.28W/C)	MATCRK	0.00	0.00	35.78	1.20E+06	114.96	1.56E+06	214.32	2.32E+06
	30% Fly Ash(0.33W/C)	MATCRK	0.00	0.00	31.22	1.10E+06	99.79	1.43E+06	190.18	2.14E+06
	30% Fly Ash(0.38W/C)	MATCRK	0.00	0.00	36.2	7.57E+05	115.1	9.85E+05	216.5	1.48E+06
<b>Group#8</b>	20 % Fly Ash(NC)	MATCRK	0.00	0.00	38.1	1.55E+06	125.2	2.02E+06	235.1	2.85E+06
	30% Fly Ash(NC)	MATCRK	0.00	0.00	39.01	1.26E+06	122.98	1.64E+06	229.37	2.41E+06
	40% Fly Ash(NC)	MATCRK	0.00	0.00	28.02	1.19E+06	81.84	1.55E+06	150.72	2.27E+06
	20 % Fly Ash(SCC)	MATCRK	0.00	0.00	31.61	1.55E+06	111.23	2.01E+06	216.93	3.02E+06
	30% Fly Ash(SCC)	MATCRK	0.00	0.00	29.83	1.29E+06	103.71	1.67E+06	202.38	2.48E+06
	40% Fly Ash(SCC)	MATCRK	0.00	0.00	29.87	1.32E+06	91.13	1.72E+06	169.22	2.58E+06
<b>Group#9</b>	480 kg (Cement)	MATCRK	0.00	0.00	28.89	1.96E+06	124.09	2.54E+06	258.26	3.64E+06
	700 kg (Cement)	MATCRK	0.00	0.00	64.36	1.40E+06	265.43	1.81E+06	509.93	2.48E+06
	900 kg (Cement)	MATCRK	0.00	0.00	145.90	1.53E+06	473.91	2.00E+06	852.47	2.91E+06
<b>Group#10</b>	0.3%Poly-Fibers	MATCRK	0.00	0.00	25.95	0.80 E+06	74.81	1.04E+06	138.63	1.50E+06
	0.5%Poly-Fibers	MATCRK	0.00	0.00	27.11	0.92 E+06	77.80	1.20E+06	141.97	1.75E+06
	0.3% steel Fibers	MATCRK	0.00	0.00	28.66	1.23 E+06	87.81	1.60E+06	165.77	1.68E+06
	0.5 %steel Fibers	MATCRK	0.00	0.00	30.12	1.67 E+06	89.78	2.18E+06	164.06	2.32E+06

**Table A1-2: Change of Tensile Strength with Equivalent Age (Cont..)**

	Mix Type		t <sub>e</sub> (Hour)	F <sub>t</sub> (N/m <sup>2</sup> )	t <sub>e</sub> (Hour)	F <sub>t</sub> (N/m <sup>2</sup> )	t <sub>e</sub> (Hour)	F <sub>t</sub> (N/m <sup>2</sup> )	t <sub>e</sub> (Hour)	F <sub>t</sub> (N/m <sup>2</sup> )
<b>Group#7</b>	30% Fly Ash(0.28W/C)	MATCRK	325.98	2.40E+06	444.80	2.45E+06	568.39	2.50E+06	694.98	2.54E+06
	30% Fly Ash(0.33W/C)	MATCRK	293.22	2.21E+06	404.36	2.26E+06	521.20	2.29E+06	641.99	2.33E+06
	30% Fly Ash(0.38W/C)	MATCRK	295.30	1.51E+06	410.31	1.54E+06	525.10	1.57E+06	650.23	1.59E+06
<b>Group#8</b>	20 % Fly Ash(NC)	MATCRK	350.2	3.10E+06	485.10	3.17E+06	620.45	3.21E+06	751.99	3.25E+06
	30% Fly Ash(NC)	MATCRK	349.88	2.52E+06	479.05	2.60E+06	613.69	2.66E+06	751.89	2.72E+06
	40% Fly Ash(NC)	MATCRK	229.63	2.39E+06	315.35	2.48E+06	405.78	2.54E+06	499.66	2.60E+06
	20 % Fly Ash(SCC)	MATCRK	337.08	3.09E+06	465.80	3.15E+06	600.20	3.19E+06	738.78	3.23E+06
	30% Fly Ash(SCC)	MATCRK	316.22	2.57E+06	440.25	2.65E+06	571.47	2.70E+06	708.22	2.75E+06
	40% Fly Ash(SCC)	MATCRK	257.18	2.64E+06	351.96	2.69E+06	451.90	2.73E+06	555.72	2.76E+06
<b>Group#9</b>	480 kg (Cement)	MATCRK	412.40	3.91E+06	574.94	4.10E+06	741.79	4.23E+06	910.79	4.34E+06
	700 kg (Cement)	MATCRK	774.75	2.79E+06	1048.21	2.98E+06	1326.58	3.10E+06	1607.17	3.19E+06
	900 kg (Cement)	MATCRK	1258.61	3.07E+06	1675.72	3.17E+06	2097.54	3.24E+06	2521.02	3.30E+06
<b>Group#10</b>	0.3%Poly-Fibers	MATCRK	212.88	1.60E+06	294.71	1.70E+06	382.34	1.79E+06	473.72	1.83E+06
	0.5%Poly-Fibers	MATCRK	215.51	1.87E+06	296.13	1.67E+06	381.83	1.94E+06	471.14	2.20E+06
	0.3% steel Fibers	MATCRK	255.92	1.79E+06	354.95	2.09E+06	461.63	2.60E+06	574.97	3.06E+06
	0.5 %steel Fibers	MATCRK	248.70	2.47E+06	340.50	2.89E+06	438.02	3.41E+06	540.04	3.85E+06

**Table A1-2: Change of Tensile Strength with Equivalent Age (Cont..)**

	Mix Type		t <sub>e</sub> (Hour)	F <sub>t</sub> (N/m <sup>2</sup> )	t <sub>e</sub> (Hour)	F <sub>t</sub> (N/m <sup>2</sup> )	t <sub>e</sub> (Hour)	F <sub>t</sub> (N/m <sup>2</sup> )	t <sub>e</sub> (Hour)	F <sub>t</sub> (N/m <sup>2</sup> )
<b>Group#7</b>	30% Fly Ash(0.28W/C)	MATCRK	824.01	2.57E+06	954.69	2.60E+06	1087.19	2.63E+06	1355.95	2.68E+06
	30% Fly Ash(0.33W/C)	MATCRK	765.80	2.35E+06	891.62	2.38E+06	1019.48	2.40E+06	1279.38	2.44E+06
	30% Fly Ash(0.38W/C)	MATCRK	770.12	1.60E+06	895.22	1.62E+06	1026.11	1.63E+06	1285.13	1.66E+06
<b>Group#8</b>	20 % Fly Ash(NC)	MATCRK	891.20	3.28E+06	1040.3	3.30E+06	1192.32	3.32E+06	1480.21	3.35E+06
	30% Fly Ash(NC)	MATCRK	893.02	2.76E+06	1035.84	2.80E+06	1180.39	2.83E+06	1473.44	2.89E+06
	40% Fly Ash(NC)	MATCRK	596.19	2.64E+06	694.74	2.68E+06	795.32	2.71E+06	1001.58	2.76E+06
	20 % Fly Ash(SCC)	MATCRK	880.34	3.26E+06	1024.60	3.29E+06	1171.30	3.31E+06	1470.41	3.35E+06
	30% Fly Ash(SCC)	MATCRK	848.15	2.78E+06	991.08	2.82E+06	1135.63	2.84E+06	1429.42	2.89E+06
	40% Fly Ash(SCC)	MATCRK	662.88	2.79E+06	772.47	2.81E+06	884.35	2.83E+06	1113.62	2.87E+06
<b>Group#9</b>	480 kg (Cement)	MATCRK	412.40	3.91E+06	574.94	4.10E+06	741.79	4.23E+06	910.79	4.34E+06
	700 kg (Cement)	MATCRK	1888.42	3.25E+06	2169.44	3.30E+06	2452.18	3.34E+06	3020.62	3.39E+06
	900 kg (Cement)	MATCRK	2943.83	3.34E+06	3366.16	3.37E+06	3789.31	3.39E+06	4635.13	3.43E+06
<b>Group#10</b>	0.3%Poly-Fibers	MATCRK	567.54	2.05E+06	662.72	2.27E+06	759.29	2.47E+06	955.20	2.85E+06
	0.5%Poly-Fibers	MATCRK	562.56	2.43E+06	655.38	2.65E+06	749.14	2.86E+06	939.73	3.24E+06
	0.3% steel Fibers	MATCRK	692.01	3.47E+06	811.42	3.82E+06	934.12	4.14E+06	1188.05	4.69E+06
	0.5 %steel Fibers	MATCRK	644.75	4.23E+06	751.37	4.56E+06	860.41	4.86E+06	1084.13	5.35E+06

**Table A1-2: Change of Tensile Strength with Equivalent Age (Cont..)**

	Mix#		t <sub>e</sub> (Hour)	F <sub>t</sub> (N/m <sup>2</sup> )	t <sub>e</sub> (Hour)	F <sub>t</sub> (N/m <sup>2</sup> )
<b>Group#7</b>	30% Fly Ash(0.28W/C)	MATCRK	1629.40	2.72E+06	1860.21	2.75E+06
	30% Fly Ash(0.33W/C)	MATCRK	1544.00	2.47E+06	1767.78	2.49E+06
	30% Fly Ash(0.38W/C)	MATCRK	1561.2	1.68E+06	1780.31	1.69E+06
<b>Group#8</b>	20 % Fly Ash(NC)	MATCRK	1745.32	3.37E+06	1780.45	3.39E+06
	30% Fly Ash(NC)	MATCRK	1737.13	2.94E+06	1776.20	2.97E+06
	40% Fly Ash(NC)	MATCRK	1211.98	2.81E+06	1390.46	2.83E+06
	20 % Fly Ash(SCC)	MATCRK	1774.81	3.39E+06	1989.13	3.42E+06
	30% Fly Ash(SCC)	MATCRK	1727.83	2.93E+06	1772.13	2.96E+06
	40% Fly Ash(SCC)	MATCRK	1349.68	2.90E+06	1552.07	2.93E+06
<b>Group#9</b>	480 kg (Cement)	MATCRK	2122.67	4.74E+06	2415.55	4.80E+06
	700 kg (Cement)	MATCRK	3574.71	3.43E+06	3613.78	3.45E+06
	900 kg (Cement)	MATCRK	5481.51	3.46E+06	5537.40	3.48E+06
<b>Group#10</b>	0.3%Poly-Fibers	MATCRK	1153.67	3.19E+06	1320.52	3.45E+06
	0.5%Poly-Fibers	MATCRK	1132.65	3.58E+06	1294.76	3.83E+06
	0.3% steel Fibers	MATCRK	1449.35	5.14E+06	16811.89	5.45E+06
	0.5 %steel Fibers	MATCRK	1312.85	5.75E+06	1506.51	6.03E+06



**Table A1-3: Change of Tensile Strength with Time**

	Mix Type	FTTIME (Hour)	0	12	24	36	48	60	72	84
<b>Group#1</b>	Control Mix (100% OPC)	FTVALU (N/m <sup>2</sup> )	0.00E+00	1.96E+06	2.54E+06	3.64E+06	3.91E+06	4.10E+06	4.23E+06	4.34E+06
	20 % Fly Ash	FTVALU	0.00E+00	1.71E+06	2.22E+06	3.31E+06	3.42E+06	3.50E+06	3.56E+06	3.60E+06
	30% Fly Ash	FTVALU	0.00E+00	1.66E+06	2.16E+06	3.25E+06	3.32E+06	3.37E+06	3.41E+06	3.44E+06
	40% Fly Ash	FTVALU	0.00E+00	1.20E+06	1.56E+06	2.26E+06	2.41E+06	2.52E+06	2.61E+06	2.69E+06
	50 % Fly Ash	FTVALU	0.00E+00	9.29E+05	1.21E+06	1.60E+06	1.86E+06	2.03E+06	2.16E+06	2.26E+06
	60 % Fly Ash	FTVALU	0.00E+00	8.46E+05	1.10E+06	1.59E+06	1.69E+06	1.77E+06	1.84E+06	1.89E+06
<b>Group#2</b>	20 % GGBFS	FTVALU	0.00E+00	1.69E+06	2.20E+06	2.90E+06	3.38E+06	3.50E+06	3.60E+06	3.68E+06
	30% GGBFS	FTVALU	0.00E+00	1.74E+06	2.27E+06	3.20E+06	3.49E+06	3.68E+06	3.82E+06	3.93E+06
	40% GGBFS	FTVALU	0.00E+00	1.25E+06	1.62E+06	2.98E+06	3.20E+06	2.87E+06	3.16E+06	3.37E+06
	50 % GGBFS	FTVALU	0.00E+00	1.29E+06	1.67E+06	2.24E+06	2.58E+06	2.83E+06	3.03E+06	3.19E+06
	60 % GGBFS	FTVALU	0.00E+00	1.35E+06	1.75E+06	2.46E+06	2.70E+06	2.89E+06	3.05E+06	3.19E+06
	70 % GGBFS	FTVALU	0.00E+00	1.42E+06	1.84E+06	2.40E+06	2.83E+06	3.39E+06	3.77E+06	4.04E+06
<b>Group#3</b>	20 %FA+ GGBFS	FTVALU	0.00E+00	1.03E+06	1.33E+06	1.70E+06	2.05E+06	2.86E+06	3.27E+06	3.48E+06
	30% FA+ GGBFS	FTVALU	0.00E+00	1.30E+06	1.70E+06	2.46E+06	2.61E+06	2.71E+06	2.79E+06	2.85E+06
	40%FA+ GGBFS	FTVALU	0.00E+00	1.04E+06	1.35E+06	1.97E+06	2.08E+06	2.16E+06	2.23E+06	2.29E+06
	50 %FA+ GGBFS	FTVALU	0.00E+00	1.01E+06	1.32E+06	1.70E+06	2.03E+06	2.46E+06	2.74E+06	2.94E+06
	60 % FA+ GGBFS	FTVALU	0.00E+00	1.96E+06	2.54E+06	3.64E+06	3.91E+06	4.10E+06	4.23E+06	4.34E+06
<b>Group#4</b>	(Control)350kg Cement	FTVALU	0.00E+00	1.03E+06	1.34E+06	1.99E+06	2.06E+06	2.11E+06	2.15E+06	2.18E+06
	20 % Fly Ash	FTVALU	0.00E+00	9.97E+05	1.30E+06	1.93E+06	1.99E+06	2.04E+06	2.08E+06	2.12E+06
	30% Fly Ash	FTVALU	0.00E+00	1.02E+06	1.33E+06	2.01E+06	2.05E+06	2.07E+06	2.09E+06	2.11E+06
	40% Fly Ash	FTVALU	0.00E+00	7.96E+05	1.04E+06	1.56E+06	1.59E+06	1.62E+06	1.63E+06	1.65E+06
	50 % Fly Ash	FTVALU	0.00E+00	7.49E+05	9.74E+05	1.41E+06	1.50E+06	1.56E+06	1.61E+06	1.64E+06
<b>Group#5</b>	20 % GGBFS	FTVALU	0.00E+00	9.96E+05	1.29E+06	1.90E+06	1.99E+06	2.05E+06	2.09E+06	2.12E+06
	30% GGBFS	FTVALU	0.00E+00	1.08E+06	1.41E+06	2.14E+06	2.16E+06	2.18E+06	2.20E+06	2.21E+06
	40% GGBFS	FTVALU	0.00E+00	1.06E+06	1.38E+06	2.08E+06	2.12E+06	2.16E+06	2.18E+06	2.20E+06
	50 % GGBFS	FTVALU	0.00E+00	9.99E+05	1.30E+06	1.89E+06	2.00E+06	2.07E+06	2.12E+06	2.15E+06
<b>Group#6</b>	10 % Micro Silica	FTVALU	0.00E+00	1.66E+06	2.16E+06	2.50E+06	3.33E+06	4.03E+06	4.31E+06	4.43E+06
	20 % Micro Silica	FTVALU	0.00E+00	1.81E+06	2.35E+06	3.10E+06	3.62E+06	3.72E+06	3.80E+06	3.86E+06
	30% Micro Silica	FTVALU	0.00E+00	8.96E+05	1.17E+06	1.42E+06	1.79E+06	2.07E+06	2.29E+06	2.46E+06
	40% Micro Silica	FTVALU	0.00E+00	8.56E+05	1.11E+06	1.29E+06	1.71E+06	2.04E+06	2.31E+06	2.52E+06

**Table A1-3: Change of Tensile Strength with Time (Cont..)**

	Mix Type	FTTIME (Hour)	96	108	120	144	168	188
<b>Group#1</b>	Control Mix (100% OPC)	FTVALU (N/m <sup>2</sup> )	4.42E+06	4.48E+06	4.54E+06	4.69E+06	4.74E+06	4.80E+06
	20 % Fly Ash	FTVALU	3.64E+06	3.67E+06	3.70E+06	3.72E+06	3.78E+06	3.80E+06
	30% Fly Ash	FTVALU	3.47E+06	3.49E+06	3.50E+06	3.52E+06	3.55E+06	3.57E+06
	40% Fly Ash	FTVALU	2.76E+06	2.82E+06	2.88E+06	2.95E+06	3.06E+06	3.13E+06
	50 % Fly Ash	FTVALU	2.33E+06	2.39E+06	2.44E+06	2.49E+06	2.57E+06	2.61E+06
	60 % Fly Ash	FTVALU	1.93E+06	1.97E+06	2.01E+06	2.04E+06	2.11E+06	2.14E+06
<b>Group#2</b>	20 % GGBFS	FTVALU	3.75E+06	3.82E+06	3.87E+06	3.94E+06	4.06E+06	4.12E+06
	30% GGBFS	FTVALU	4.02E+06	4.09E+06	4.14E+06	4.20E+06	4.31E+06	4.35E+06
	40%GGBFS	FTVALU	3.55E+06	3.69E+06	3.81E+06	3.93E+06	4.13E+06	4.22E+06
	50 % GGBFS	FTVALU	3.33E+06	3.45E+06	3.55E+06	3.66E+06	3.86E+06	3.96E+06
	60 % GGBFS	FTVALU	3.31E+06	3.42E+06	3.52E+06	3.63E+06	3.84E+06	3.95E+06
	70 % GGBFS	FTVALU	4.25E+06	4.40E+06	4.52E+06	4.68E+06	4.80E+06	4.87E+06
<b>Group#3</b>	20 %FA+ GGBFS	FTVALU	3.60E+06	3.67E+06	3.72E+06	3.76E+06	3.79E+06	3.80E+06
	30% FA+ GGBFS	FTVALU	2.90E+06	2.93E+06	2.97E+06	3.02E+06	3.06E+06	3.09E+06
	40%FA+ GGBFS	FTVALU	2.34E+06	2.39E+06	2.43E+06	2.51E+06	2.57E+06	2.61E+06
	50 %FA+ GGBFS	FTVALU	3.08E+06	3.19E+06	3.27E+06	3.38E+06	3.45E+06	3.49E+06
	60 % FA+ GGBFS	FTVALU	4.42E+06	4.48E+06	4.54E+06	4.69E+06	4.74E+06	4.80E+06
<b>Group#4</b>	(Control)350kg Cement	FTVALU	2.21E+06	2.23E+06	2.25E+06	2.28E+06	2.31E+06	2.33E+06
	20 % Fly Ash	FTVALU	2.14E+06	2.17E+06	2.19E+06	2.22E+06	2.25E+06	2.27E+06
	30% Fly Ash	FTVALU	2.13E+06	2.14E+06	2.15E+06	2.17E+06	2.19E+06	2.20E+06
	40% Fly Ash	FTVALU	1.66E+06	1.67E+06	1.68E+06	1.70E+06	1.72E+06	1.73E+06
	50 % Fly Ash	FTVALU	1.67E+06	1.69E+06	1.71E+06	1.74E+06	1.76E+06	1.77E+06
<b>Group#5</b>	20 % GGBFS	FTVALU	2.14E+06	2.15E+06	2.17E+06	2.19E+06	2.20E+06	2.21E+06
	30% GGBFS	FTVALU	2.22E+06	2.23E+06	2.24E+06	2.25E+06	2.27E+06	2.27E+06
	40%GGBFS	FTVALU	2.22E+06	2.23E+06	2.25E+06	2.27E+06	2.28E+06	2.30E+06
	50 % GGBFS	FTVALU	2.18E+06	2.21E+06	2.23E+06	2.25E+06	2.28E+06	2.29E+06
<b>Group#6</b>	10 % Micro Silica	FTVALU	4.48E+06	4.51E+06	4.53E+06	4.55E+06	4.55E+06	4.56E+06
	20 % Micro Silica	FTVALU	3.92E+06	3.97E+06	4.02E+06	4.10E+06	4.17E+06	4.22E+06
	30% Micro Silica	FTVALU	4.48E+06	4.51E+06	4.53E+06	4.55E+06	4.55E+06	4.56E+06
	40% Micro Silica	FTVALU	3.92E+06	3.97E+06	4.02E+06	4.10E+06	4.17E+06	4.22E+06

**Table A1-4: Change of Tensile Strength with Time**

	Mix Type	FTTIME (Hour)	0	12	24	36	48	60	72	84
<b>Group#7</b>	30% Fly Ash(0.28W/C)	FTVALU (N/m <sup>2</sup> )	0.00E+00	1.20E+06	1.56E+06	2.32E+06	2.40E+06	2.45E+06	2.50E+06	2.54E+06
	30% Fly Ash(0.33W/C)	FTVALU	0.00E+00	1.10E+06	1.43E+06	2.14E+06	2.21E+06	2.26E+06	2.29E+06	2.33E+06
	30% Fly Ash(0.38W/C)	FTVALU	0.00E+00	7.57E+05	9.85E+05	1.48E+06	1.51E+06	1.54E+06	1.57E+06	1.59E+06
<b>Group#8</b>	20 % Fly Ash(NC)	FTVALU	0.00E+00	1.55E+06	2.02E+06	2.85E+06	3.10E+06	3.17E+06	3.21E+06	3.25E+06
	30% Fly Ash(NC)	FTVALU	0.00E+00	1.26E+06	1.64E+06	2.41E+06	2.52E+06	2.60E+06	2.66E+06	2.72E+06
	40% Fly Ash(NC)	FTVALU	0.00E+00	1.19E+06	1.55E+06	2.27E+06	2.39E+06	2.48E+06	2.54E+06	2.60E+06
	20 % Fly Ash(SCC)	FTVALU	0.00E+00	1.55E+06	2.01E+06	3.02E+06	3.09E+06	3.15E+06	3.19E+06	3.23E+06
	30% Fly Ash(SCC)	FTVALU	0.00E+00	1.29E+06	1.67E+06	2.48E+06	2.57E+06	2.65E+06	2.70E+06	2.75E+06
	40% Fly Ash(SCC)	FTVALU	0.00E+00	1.32E+06	1.72E+06	2.58E+06	2.64E+06	2.69E+06	2.73E+06	2.76E+06
<b>Group#9</b>	480 kg (Cement)	FTVALU	0.00E+00	1.96E+06	2.54E+06	3.64E+06	3.91E+06	4.10E+06	4.23E+06	4.34E+06
	700 kg (Cement)	FTVALU	0.00E+00	1.40E+06	1.81E+06	2.48E+06	2.79E+06	2.98E+06	3.10E+06	3.19E+06
	900 kg (Cement)	FTVALU	0.00E+00	1.53E+06	2.00E+06	2.91E+06	3.07E+06	3.17E+06	3.24E+06	3.30E+06
<b>Group#10</b>	0.3%Poly-Fibers	FTVALU	0.00E+00	4.00E+05	4.47E+05	7.54E+05	1.05E+06	1.32E+06	1.58E+06	1.83E+06
	0.5%Poly-Fibers	FTVALU	0.00E+00	4.50E+05	6.67E+05	1.03E+06	1.36E+06	1.67E+06	1.94E+06	2.20E+06
	0.3% steel Fibers	FTVALU	0.00E+00	4.50E+05	7.53E+05	1.20E+06	1.52E+06	2.09E+06	2.60E+06	3.06E+06
	0.5 %steel Fibers	FTVALU	0.00E+00	5.00E+05	8.18E+05	1.59E+06	2.29E+06	2.89E+06	3.41E+06	3.85E+06

**Table A1-4: Change of Tensile Strength with Time (Cont..)**

	Mix Type	FTTIME (Hour)	96	108	120	144	168	188
<b>Group#7</b>	30% Fly Ash(0.28W/C)	FTVALU (N/m <sup>2</sup> )	2.57E+06	2.60E+06	2.63E+06	2.68E+06	2.72E+06	2.75E+06
	30% Fly Ash(0.33W/C)	FTVALU	2.35E+06	2.38E+06	2.40E+06	2.44E+06	2.47E+06	2.49E+06
	30% Fly Ash(0.38W/C)	FTVALU	1.60E+06	1.62E+06	1.63E+06	1.66E+06	1.68E+06	1.69E+06
<b>Group#8</b>	20 % Fly Ash(NC)	FTVALU	3.28E+06	3.30E+06	3.32E+06	3.35E+06	3.37E+06	3.39E+06
	30% Fly Ash(NC)	FTVALU	2.76E+06	2.80E+06	2.83E+06	2.89E+06	2.94E+06	2.97E+06
	40% Fly Ash(NC)	FTVALU	2.64E+06	2.68E+06	2.71E+06	2.76E+06	2.81E+06	2.83E+06
	20 % Fly Ash(SCC)	FTVALU	3.26E+06	3.29E+06	3.31E+06	3.35E+06	3.39E+06	3.42E+06
	30% Fly Ash(SCC)	FTVALU	2.78E+06	2.82E+06	2.84E+06	2.89E+06	2.93E+06	2.96E+06
	40% Fly Ash(SCC)	FTVALU	2.79E+06	2.81E+06	2.83E+06	2.87E+06	2.90E+06	2.93E+06
<b>Group#9</b>	480 kg (Cement)	FTVALU	4.42E+06	4.48E+06	4.54E+06	4.69E+06	4.74E+06	4.80E+06
	700 kg (Cement)	FTVALU	3.25E+06	3.30E+06	3.34E+06	3.39E+06	3.43E+06	3.45E+06
	900 kg (Cement)	FTVALU	3.34E+06	3.37E+06	3.39E+06	3.43E+06	3.46E+06	3.48E+06
<b>Group#10</b>	0.3%Poly-Fibers	FTVALU	2.05E+06	2.27E+06	2.47E+06	2.85E+06	3.19E+06	3.45E+06
	0.5%Poly-Fibers	FTVALU	2.43E+06	2.65E+06	2.86E+06	3.24E+06	3.58E+06	3.83E+06
	0.3% steel Fibers	FTVALU	3.47E+06	3.82E+06	4.14E+06	4.69E+06	5.14E+06	5.45E+06
	0.5 %steel Fibers	FTVALU	4.23E+06	4.56E+06	4.86E+06	5.35E+06	5.75E+06	6.03E+06

**Table A1-5: Change of Young Modulus with Time**

	Mix Type	FTTIME (Hour)	0	12	24	36	48	60	72	84
<b>Group#1</b>	Control Mix (100% OPC)	YOUNG (N/m <sup>2</sup> )	1.00E+09	2.04E+10	2.65E+10	2.72E+10	2.91E+10	3.05E+10	3.17E+10	3.27E+10
	20 % Fly Ash	YOUNG	1.00E+09	1.79E+10	2.17E+10	2.37E+10	2.50E+10	2.60E+10	2.68E+10	2.74E+10
	30% Fly Ash	YOUNG	1.00E+09	1.10E+10	1.43E+10	1.98E+10	2.20E+10	2.35E+10	2.47E+10	2.56E+10
	40% Fly Ash	YOUNG	1.00E+09	1.10E+10	1.43E+10	1.98E+10	2.20E+10	2.35E+10	2.47E+10	2.56E+10
	50 % Fly Ash	YOUNG	1.00E+09	6.12E+09	7.96E+09	1.06E+10	1.22E+10	1.35E+10	1.45E+10	1.54E+10
	60 % Fly Ash	YOUNG	1.00E+09	4.19E+09	5.44E+09	7.02E+09	8.37E+09	9.45E+09	1.03E+10	1.11E+10
<b>Group#2</b>	20 % GGBFS	YOUNG	1.00E+09	1.24E+10	1.61E+10	2.24E+10	2.48E+10	2.66E+10	2.79E+10	2.89E+10
	30% GGBFS	YOUNG	1.00E+09	1.32E+10	1.72E+10	2.31E+10	2.64E+10	2.88E+10	3.06E+10	3.21E+10
	40%GGBFS	YOUNG	1.00E+09	1.22E+10	1.58E+10	2.01E+10	2.44E+10	2.75E+10	3.00E+10	3.19E+10
	50 % GGBFS	YOUNG	1.00E+09	1.22E+10	1.59E+10	2.13E+10	2.44E+10	2.68E+10	2.86E+10	3.01E+10
	60 % GGBFS	YOUNG	1.00E+09	1.27E+10	1.66E+10	2.15E+10	2.55E+10	2.84E+10	3.06E+10	3.24E+10
	70 % GGBFS	YOUNG	1.00E+09	1.10E+10	1.43E+10	1.76E+10	2.20E+10	2.54E+10	2.80E+10	3.00E+10
<b>Group#3</b>	20 %FA+ GGBFS	YOUNG	1.00E+09	1.25E+10	1.62E+10	2.32E+10	2.50E+10	2.63E+10	2.73E+10	2.81E+10
	30% FA+ GGBFS	YOUNG	1.00E+09	1.16E+10	1.50E+10	2.13E+10	2.31E+10	2.45E+10	2.55E+10	2.63E+10
	40%FA+ GGBFS	YOUNG	1.00E+09	1.01E+10	1.31E+10	1.77E+10	2.02E+10	2.21E+10	2.37E+10	2.50E+10
	50 %FA+ GGBFS	YOUNG	1.00E+09	7.04E+09	9.15E+09	1.18E+10	1.41E+10	1.59E+10	1.74E+10	1.86E+10
	60 % FA+ GGBFS	YOUNG	1.00E+09	2.04E+10	2.65E+10	2.72E+10	2.91E+10	3.05E+10	3.17E+10	3.27E+10
<b>Group#4</b>	(Control)350kg Cement	YOUNG	1.00E+09	8.26E+09	1.07E+10	1.26E+10	1.65E+10	1.93E+10	2.15E+10	2.31E+10
	20 % Fly Ash	YOUNG	1.00E+09	7.72E+09	1.00E+10	1.18E+10	1.54E+10	1.81E+10	2.02E+10	2.17E+10
	30% Fly Ash	YOUNG	1.00E+09	8.54E+09	1.11E+10	1.48E+10	1.71E+10	1.87E+10	2.00E+10	2.10E+10
	40% Fly Ash	YOUNG	1.00E+09	6.10E+09	7.94E+09	1.15E+10	1.22E+10	1.27E+10	1.31E+10	1.35E+10
	50 % Fly Ash	YOUNG	1.00E+09	6.79E+09	8.83E+09	1.31E+10	1.36E+10	1.40E+10	1.43E+10	1.46E+10
<b>Group#5</b>	20 % GGBFS	YOUNG	1.00E+09	9.72E+09	1.26E+10	1.77E+10	1.94E+10	2.06E+10	2.15E+10	2.21E+10
	30% GGBFS	YOUNG	1.00E+09	9.49E+09	1.23E+10	1.65E+10	1.90E+10	2.07E+10	2.20E+10	2.30E+10
	40%GGBFS	YOUNG	1.00E+09	1.04E+10	1.35E+10	1.99E+10	2.08E+10	2.15E+10	2.21E+10	2.25E+10
	50 % GGBFS	YOUNG	1.00E+09	1.00E+10	1.30E+10	1.63E+10	2.00E+10	2.21E+10	2.34E+10	2.43E+10
<b>Group#6</b>	10 % Micro Silica	YOUNG	1.00E+09	1.32E+10	1.71E+10	2.28E+10	2.64E+10	2.89E+10	3.07E+10	3.21E+10
	20 % Micro Silica	YOUNG	1.00E+09	1.32E+10	1.71E+10	2.36E+10	2.63E+10	2.84E+10	3.01E+10	3.16E+10
	30% Micro Silica	YOUNG	1.00E+09	6.73E+09	8.75E+09	5.94E+09	1.35E+10	1.96E+10	2.40E+10	2.71E+10
	40% Micro Silica	YOUNG	1.00E+09	6.27E+09	8.15E+09	4.69E+09	1.25E+10	1.96E+10	2.49E+10	2.87E+10

**Table A1-5: Change of Young Modulus with Time (Cont..)**

	Mix Type	FTTIME (Hour)	96	108	120	144	168	188
<b>Group#1</b>	Control Mix (100% OPC)	YOUNG (N/m <sup>2</sup> )	3.36E+10	3.44E+10	3.51E+10	3.58E+10	3.73E+10	3.80E+10
	20 % Fly Ash	YOUNG	2.79E+10	2.83E+10	2.87E+10	2.91E+10	2.99E+10	3.02E+10
	30% Fly Ash	YOUNG	2.63E+10	2.70E+10	2.75E+10	2.81E+10	2.90E+10	2.95E+10
	40% Fly Ash	YOUNG	2.63E+10	2.70E+10	2.75E+10	2.81E+10	2.90E+10	2.95E+10
	50 % Fly Ash	YOUNG	1.61E+10	1.68E+10	1.74E+10	1.80E+10	1.92E+10	1.97E+10
	60 % Fly Ash	YOUNG	1.18E+10	1.23E+10	1.28E+10	1.34E+10	1.44E+10	1.49E+10
<b>Group#2</b>	20 % GGBFS	YOUNG	2.98E+10	3.05E+10	3.11E+10	3.17E+10	3.28E+10	3.33E+10
	30% GGBFS	YOUNG	3.33E+10	3.44E+10	3.52E+10	3.62E+10	3.82E+10	3.89E+10
	40%GGBFS	YOUNG	3.35E+10	3.48E+10	3.59E+10	3.71E+10	3.90E+10	3.99E+10
	50 % GGBFS	YOUNG	3.14E+10	3.25E+10	3.34E+10	3.44E+10	3.62E+10	3.71E+10
	60 % GGBFS	YOUNG	3.38E+10	3.50E+10	3.60E+10	3.71E+10	3.90E+10	3.98E+10
	70 % GGBFS	YOUNG	3.17E+10	3.31E+10	3.42E+10	3.61E+10	3.75E+10	3.85E+10
<b>Group#3</b>	20 %FA+ GGBFS	YOUNG	2.88E+10	2.94E+10	2.98E+10	3.06E+10	3.12E+10	3.17E+10
	30% FA+ GGBFS	YOUNG	2.70E+10	2.76E+10	2.81E+10	2.89E+10	2.96E+10	3.00E+10
	40%FA+ GGBFS	YOUNG	2.61E+10	2.71E+10	2.79E+10	2.94E+10	3.06E+10	3.14E+10
	50 %FA+ GGBFS	YOUNG	1.97E+10	2.06E+10	2.15E+10	2.29E+10	2.40E+10	2.48E+10
	60 % FA+ GGBFS	YOUNG	3.36E+10	3.44E+10	3.51E+10	3.58E+10	3.73E+10	3.80E+10
<b>Group#4</b>	(Control)350kg Cement	YOUNG	2.43E+10	2.54E+10	2.62E+10	2.75E+10	2.85E+10	2.91E+10
	20 % Fly Ash	YOUNG	2.30E+10	2.40E+10	2.48E+10	2.61E+10	2.71E+10	2.77E+10
	30% Fly Ash	YOUNG	2.18E+10	2.25E+10	2.31E+10	2.40E+10	2.47E+10	2.52E+10
	40% Fly Ash	YOUNG	1.38E+10	1.40E+10	1.43E+10	1.47E+10	1.50E+10	1.53E+10
	50 % Fly Ash	YOUNG	1.48E+10	1.51E+10	1.53E+10	1.56E+10	1.59E+10	1.61E+10
<b>Group#5</b>	20 % GGBFS	YOUNG	2.26E+10	2.31E+10	2.34E+10	2.40E+10	2.44E+10	2.47E+10
	30% GGBFS	YOUNG	2.38E+10	2.44E+10	2.50E+10	2.59E+10	2.65E+10	2.69E+10
	40%GGBFS	YOUNG	2.29E+10	2.32E+10	2.35E+10	2.40E+10	2.44E+10	2.47E+10
	50 % GGBFS	YOUNG	2.49E+10	2.53E+10	2.56E+10	2.60E+10	2.63E+10	2.65E+10
<b>Group#6</b>	10 % Micro Silica	YOUNG	3.32E+10	3.41E+10	3.48E+10	3.60E+10	3.68E+10	3.74E+10
	20 % Micro Silica	YOUNG	3.28E+10	3.39E+10	3.48E+10	3.64E+10	3.78E+10	3.87E+10
	30% Micro Silica	YOUNG	2.93E+10	3.09E+10	3.21E+10	3.38E+10	3.48E+10	3.54E+10
	40% Micro Silica	YOUNG	3.15E+10	3.35E+10	3.50E+10	3.70E+10	3.83E+10	3.90E+10

**Table A1-6: Change of Young Modulus with Time**

	Mix Type	FTTIME (Hour)	0	12	24	36	48	60	72	84
<b>Group#7</b>	30% Fly Ash(0.28W/C)	YOUNG (N/m <sup>2</sup> )	1.00E+09	8.46E+09	1.10E+10	1.52E+10	1.69E+10	1.82E+10	1.93E+10	2.01E+10
	30% Fly Ash(0.33W/C)	YOUNG	1.00E+09	8.23E+09	1.07E+10	1.49E+10	1.65E+10	1.77E+10	1.88E+10	1.97E+10
	30% Fly Ash(0.38W/C)	YOUNG	1.00E+09	8.64E+09	1.12E+10	1.64E+10	1.73E+10	1.80E+10	1.85E+10	1.90E+10
<b>Group#8</b>	20 % Fly Ash(NC)	YOUNG	1.00E+09	9.95E+09	1.29E+10	1.16E+10	1.99E+10	2.58E+10	2.98E+10	3.27E+10
	30% Fly Ash(NC)	YOUNG	1.00E+09	1.10E+10	1.43E+10	1.97E+10	2.20E+10	2.37E+10	2.49E+10	2.59E+10
	40% Fly Ash(NC)	YOUNG	1.00E+09	7.57E+09	9.84E+09	1.28E+10	1.51E+10	1.70E+10	1.86E+10	2.00E+10
	20 % Fly Ash(SCC)	YOUNG	1.00E+09	7.24E+09	9.41E+09	1.33E+10	1.45E+10	1.54E+10	1.62E+10	1.69E+10
	30% Fly Ash(SCC)	YOUNG	1.00E+09	1.13E+10	1.47E+10	2.08E+10	2.27E+10	2.41E+10	2.52E+10	2.61E+10
	40% Fly Ash(SCC)	YOUNG	1.00E+09	8.21E+09	1.07E+10	1.39E+10	1.64E+10	1.82E+10	1.97E+10	2.08E+10
<b>Group#9</b>	480 kg (Cement)	YOUNG	1.00E+09	2.04E+10	2.65E+10	2.72E+10	2.91E+10	3.05E+10	3.17E+10	3.27E+10
	700 kg (Cement)	YOUNG	1.00E+09	1.11E+10	1.45E+10	1.69E+10	2.23E+10	2.59E+10	2.84E+10	3.03E+10
	900 kg (Cement)	YOUNG	1.00E+09	1.36E+10	1.77E+10	2.48E+10	2.72E+10	2.88E+10	3.00E+10	3.10E+10
<b>Group#10</b>	0.3%Poly-Fibers	YOUNG	1.00E+09	2.20E+09	5.50E+09	1.09E+10	1.55E+10	1.87E+10	2.10E+10	2.27E+10
	0.5%Poly-Fibers	YOUNG	1.00E+09	5.50E+09	1.19E+10	1.84E+10	2.24E+10	2.50E+10	2.68E+10	2.82E+10
	0.3% steel Fibers	YOUNG	1.00E+09	1.41E+10	2.00E+10	2.39E+10	2.68E+10	2.91E+10	3.10E+10	3.27E+10
	0.5 %steel Fibers	YOUNG	1.00E+09	1.22E+10	1.95E+10	2.44E+10	2.80E+10	3.10E+10	3.34E+10	3.54E+10

**Table A1-6: Change of Young Modulus with Time (Cont..)**

	Mix Type	FTTIME (Hour)	96	108	120	144	168	188
<b>Group#7</b>	30% Fly Ash(0.28W/C)	YOUNG	2.05E+10	2.12E+10	2.19E+10	2.30E+10	2.39E+10	2.47E+10
	30% Fly Ash(0.33W/C)	YOUNG	1.94E+10	1.98E+10	2.01E+10	2.07E+10	2.11E+10	2.14E+10
	30% Fly Ash(0.38W/C)	YOUNG	1.28E+10	1.33E+10	1.38E+10	1.44E+10	1.50E+10	1.53E+10
<b>Group#8</b>	20 % Fly Ash(NC)	YOUNG	2.67E+10	2.73E+10	2.79E+10	2.88E+10	2.94E+10	2.99E+10
	30% Fly Ash(NC)	YOUNG	2.12E+10	2.22E+10	2.32E+10	2.48E+10	2.62E+10	2.72E+10
	40% Fly Ash(NC)	YOUNG	1.75E+10	1.80E+10	1.85E+10	1.93E+10	2.01E+10	2.06E+10
	20 % Fly Ash(SCC)	YOUNG	2.69E+10	2.76E+10	2.82E+10	2.92E+10	3.00E+10	3.05E+10
	30% Fly Ash(SCC)	YOUNG	2.17E+10	2.25E+10	2.32E+10	2.43E+10	2.51E+10	2.57E+10
	40% Fly Ash(SCC)	YOUNG	2.09E+10	2.15E+10	2.21E+10	2.31E+10	2.39E+10	2.44E+10
<b>Group#9</b>	480 kg (Cement)	YOUNG	3.36E+10	3.44E+10	3.51E+10	3.58E+10	3.73E+10	3.80E+10
	700 kg (Cement)	YOUNG	3.16E+10	3.27E+10	3.35E+10	3.47E+10	3.56E+10	3.61E+10
	900 kg (Cement)	YOUNG	3.18E+10	3.25E+10	3.30E+10	3.39E+10	3.46E+10	3.51E+10
<b>Group#10</b>	0.3%Poly-Fibers	YOUNG	2.41E+10	2.52E+10	2.61E+10	2.74E+10	2.85E+10	2.91E+10
	0.5%Poly-Fibers	YOUNG	2.93E+10	3.02E+10	3.09E+10	3.20E+10	3.28E+10	3.33E+10
	0.3% steel Fibers	YOUNG	3.42E+10	3.55E+10	3.66E+10	3.86E+10	4.04E+10	4.16E+10
	0.5 %steel Fibers	YOUNG	3.72E+10	3.88E+10	4.02E+10	4.26E+10	4.46E+10	4.61E+10

**Table A1-7: Change of Ultimate Strain with Equivalent Age**

	Mix Type		t <sub>e</sub> (Hour)	ε <sub>tu</sub> (m/m)	t <sub>e</sub> (Hour)	ε <sub>tu</sub> (m/m)	t <sub>e</sub> (Hour)	ε <sub>tu</sub> (m/m)	t <sub>e</sub> (Hour)	ε <sub>tu</sub> (m/m)
<b>Group#1</b>	Control Mix (100% OPC)	MATTEN*	0.00	0.00	28.89	0.000362	124.09	0.000322	258.26	0.000261
	20 % Fly Ash	MATTEN	0.00	0.00	25.44	0.000392	87.05	0.000344	186.37	0.000267
	30% Fly Ash	MATTEN	0.00	0.00	24.34	0.000365	62.83	0.000313	134.86	0.000224
	40% Fly Ash	MATTEN	0.00	0.00	24.56	0.000517	69.79	0.000446	149.54	0.000338
	50 % Fly Ash	MATTEN	0.00	0.00	23.84	0.0006	49.38	0.000503	94.25	0.000414
	60 % Fly Ash	MATTEN	0.00	0.00	25.88	0.000606	74.23	0.000495	136.26	0.000358
<b>Group#2</b>	20 % GGBFS	MATTEN	0.00	0.00	31.56	0.000374	118.88	0.000324	244.69	0.000266
	30% GGBFS	MATTEN	0.00	0.00	32.87	0.000395	117.57	0.000349	231.25	0.000278
	40%GGBFS	MATTEN	0.00	0.00	26.43	0.000532	96.42	0.000466	205.48	0.000412
	50 % GGBFS	MATTEN	0.00	0.00	27.42	0.000447	86.45	0.000378	182.38	0.000284
	60 % GGBFS	MATTEN	0.00	0.00	34.81	0.000426	116.08	0.000361	219.81	0.000246
	70 % GGBFS	MATTEN	0.00	0.00	26.98	0.000453	111.38	0.000394	238.08	0.000319
<b>Group#3</b>	20 %FA+ GGBFS	MATTEN	0.00	0.00	28.71	0.000653	99.32	0.000574	199.04	0.000513
	30% FA+ GGBFS	MATTEN	0.00	0.00	81.10	0.0005	212.40	0.000437	351.40	0.000341
	40%FA+ GGBFS	MATTEN	0.00	0.00	35.94	0.000601	119.80	0.000519	227.36	0.00039
	50 %FA+ GGBFS	MATTEN	0.00	0.00	28.32	0.00056	77.87	0.000472	147.43	0.000391
	60 % FA+ GGBFS	MATTEN	0.00	0.00	28.89	0.000362	124.09	0.000322	258.26	0.000261
<b>Group#4</b>	(Control)350kg Cement	MATTEN	0.00	0.00	35.48	0.000572	109.30	0.000487	198.23	0.000337
	20 % Fly Ash	MATTEN	0.00	0.00	35.48	0.000581	109.30	0.000492	198.23	0.000341
	30% Fly Ash	MATTEN	0.00	0.00	31.22	0.000581	90.60	0.000496	161.66	0.000355
	40% Fly Ash	MATTEN	0.00	0.00	26.97	0.000688	71.89	0.000574	125.10	0.000417
	50 % Fly Ash	MATTEN	0.00	0.00	20.97	0.000749	51.89	0.000629	85.10	0.000484
<b>Group#5</b>	20 % GGBFS	MATTEN	0.00	0.00	37.38	0.000619	109.51	0.000533	199.04	0.000405
	30% GGBFS	MATTEN	0.00	0.00	35.42	0.000566	102.03	0.000487	185.00	0.000349
	40%GGBFS	MATTEN	0.00	0.00	33.46	0.000568	94.54	0.000487	175.08	0.000354
	50 % GGBFS	MATTEN	0.00	0.00	32.02	0.000604	89.53	0.000517	167.08	0.000386
<b>Group#6</b>	10 % Micro Silica	MATTEN	0.00	0.00	35.48	0.000572	109.30	0.000487	198.23	0.000337
	20 % Micro Silica	MATTEN	0.00	0.00	35.48	0.000581	109.30	0.000492	198.23	0.000341
	30% Micro Silica	MATTEN	0.00	0.00	34.47	0.000636	111.18	0.000536	214.93	0.000484
	40% Micro Silica	MATTEN	0.00	0.00	31.52	0.000756	95.89	0.000659	184.23	0.000643

**\*MATTEN (Maturity Tension Softening) means change of ultimate Strain with maturity**

**Table A1-7: Change of Ultimate Strain with Equivalent Age (Cont..)**

	Mix Type		$t_e$ (Hour)	$\varepsilon_{tu}$ (m/m)	$t_e$ (Hour)	$\varepsilon_{tu}$ (m/m)	$t_e$ (Hour)	$\varepsilon_{tu}$ (m/m)	$t_e$ (Hour)	$\varepsilon_{tu}$ (m/m)
<b>Group#1</b>	Control Mix (100% OPC)	MATTEN	412.40	0.000252	574.94	0.000247	741.79	0.000245	910.79	0.000243
	20 % Fly Ash	MATTEN	304.02	0.000266	432.51	0.000265	567.37	0.000265	705.62	0.000265
	30% Fly Ash	MATTEN	224.09	0.000235	324.34	0.000242	431.61	0.000248	543.07	0.000253
	40% Fly Ash	MATTEN	247.83	0.000337	358.36	0.000335	477.14	0.000333	601.29	0.000331
	50 % Fly Ash	MATTEN	154.58	0.000367	223.67	0.000344	299.20	0.00033	379.23	0.000321
	60 % Fly Ash	MATTEN	205.66	0.00035	280.24	0.000346	358.85	0.000343	440.69	0.000341
<b>Group#2</b>	20 % GGBFS	MATTEN	391.00	0.000246	546.58	0.00025	706.94	0.000253	870.26	0.000255
	30% GGBFS	MATTEN	359.66	0.000271	496.17	0.000268	637.07	0.000267	780.05	0.000266
	40%GGBFS	MATTEN	332.55	0.000359	469.15	0.000333	610.99	0.000318	756.63	0.000308
	50 % GGBFS	MATTEN	301.51	0.000279	432.42	0.000278	570.16	0.000277	712.59	0.000277
	60 % GGBFS	MATTEN	331.60	0.000266	447.49	0.000279	565.99	0.000286	686.06	0.000289
	70 % GGBFS	MATTEN	268.18	0.000335	382.42	0.000326	500.02	0.00032	619.31	0.000315
<b>Group#3</b>	20 %FA+ GGBFS	MATTEN	386.48	0.0003	545.88	0.00027	711.25	0.000255	880.65	0.000248
	30% FA+ GGBFS	MATTEN	316.27	0.000442	445.51	0.000326	582.60	0.000291	725.21	0.000278
	40%FA+ GGBFS	MATTEN	446.11	0.000335	563.95	0.000331	700.34	0.000329	838.45	0.000328
	50 %FA+ GGBFS	MATTEN	347.76	0.000393	475.86	0.000394	609.19	0.000395	745.73	0.000396
	60 % FA+ GGBFS	MATTEN	232.24	0.000347	326.76	0.000298	427.27	0.000276	531.45	0.000265
<b>Group#4</b>	(Control)350kg Cement	MATTEN	296.67	0.000362	401.09	0.000379	509.79	0.000391	620.89	0.000399
	20 % Fly Ash	MATTEN	296.67	0.000364	401.09	0.00038	509.79	0.000391	620.89	0.000399
	30% Fly Ash	MATTEN	240.03	0.00037	322.97	0.00038	409.48	0.000388	498.19	0.000394
	40% Fly Ash	MATTEN	183.38	0.000417	244.85	0.000417	309.16	0.000417	375.49	0.000417
	50 % Fly Ash	MATTEN	127.38	0.000461	166.73	0.000447	209.00	0.000439	275.00	0.000433
<b>Group#5</b>	20 % GGBFS	MATTEN	299.34	0.000402	406.26	0.000402	518.14	0.000402		0.000403
	30% GGBFS	MATTEN	283.30	0.000367	386.00	0.000379	494.00	0.000387	610.00	0.000393
	40%GGBFS	MATTEN	267.36	0.000365	367.03	0.000371	471.12	0.000374	570.00	0.000376
	50 % GGBFS	MATTEN	256.21	0.000387	352.12	0.000389	452.02	0.00039	545.00	0.000391
<b>Group#6</b>	10 % Micro Silica	MATTEN	410.80	0.00028	562.21	0.000243	715.95	0.000236	871.22	0.000235
	20 % Micro Silica	MATTEN	406.33	0.000258	549.68	0.000262	695.97	0.000265	843.91	0.000267
	30 % Micro Silica	MATTEN	331.20	0.000395	453.62	0.00035	579.80	0.000323	708.07	0.000305
	40 % Micro Silica	MATTEN	285.15	0.000504	393.26	0.000435	505.94	0.000395	621.66	0.000368



**Table A1-7: Change of Ultimate Strain with Equivalent Age (Cont..)**

	Mix Type		$t_e$ (Hour)	$\epsilon_{tu}(m/m)$	$t_e$ (Hour)	$\epsilon_{tu}(m/m)$	$t_e$ (Hour)	$\epsilon_{tu}(m/m)$	$t_e$ (Hour)	$\epsilon_{tu}(m/m)$
<b>Group#1</b>	Control Mix (100% OPC)	MATTEN*	1081.59	0.000243	1253.16	0.000242	1425.50	0.000242	1773.07	0.000239
	20 % Fly Ash	MATTEN	846.42	0.000265	988.88	0.000265	1132.72	0.000265	1423.23	0.000266
	30% Fly Ash	MATTEN	657.52	0.000257	773.80	0.000261	891.55	0.000264	1131.18	0.000269
	40% Fly Ash	MATTEN	729.65	0.000328	861.02	0.000326	994.82	0.000324	1268.65	0.000324
	50 % Fly Ash	MATTEN	462.74	0.000316	548.74	0.000312	636.78	0.000309	817.60	0.000309
	60 % Fly Ash	MATTEN	525.07	0.000339	611.48	0.000338	699.80	0.000337	880.90	0.000339
<b>Group#2</b>	20 % GGBFS	MATTEN	1035.24	0.000256	1201.37	0.000257	1368.51	0.000257	1705.52	0.000259
	30% GGBFS	MATTEN	924.75	0.000266	1070.46	0.000266	1217.13	0.000267	1512.74	0.000269
	40%GGBFS	MATTEN	904.64	0.000301	1054.27	0.000297	1205.07	0.000293	1510.20	0.000293
	50 % GGBFS	MATTEN	858.39	0.000277	1006.55	0.000276	1157.34	0.000276	1465.28	0.000279
	60 % GGBFS	MATTEN	807.46	0.00029	929.94	0.00029	1053.52	0.000288	1302.48	0.000289
	70 % GGBFS	MATTEN	740.18	0.00031	861.42	0.000307	983.74	0.000303	1229.09	0.000298
<b>Group#3</b>	20 %FA+ GGBFS	MATTEN	1053.64	0.000244	1229.88	0.000241	1407.83	0.00024	1768.05	0.000239
	30% FA+ GGBFS	MATTEN	872.51	0.000272	1023.69	0.00027	1176.91	0.000269	1489.31	0.000269
	40%FA+ GGBFS	MATTEN	918.54	0.000327	1049.68	0.000326	1188.63	0.000326	1400.04	0.000325
	50 %FA+ GGBFS	MATTEN	885.01	0.000396	1025.97	0.000396	1168.86	0.000396	1458.66	0.000395
	60 % FA+ GGBFS	MATTEN	638.58	0.000259	747.43	0.000255	858.08	0.000254	1082.19	0.000253
<b>Group#4</b>	(Control)350kg Cement	MATTEN	733.65	0.000406	847.76	0.00041	963.26	0.000414	1197.48	0.000419
	20 % Fly Ash	MATTEN	733.65	0.000405	847.76	0.00041	963.26	0.000413	1197.48	0.000418
	30% Fly Ash	MATTEN	588.60	0.000398	680.23	0.000402	773.01	0.000405	961.23	0.000409
	40% Fly Ash	MATTEN	443.56	0.000417	512.69	0.000417	582.76	0.000418	724.98	0.000418
	50 % Fly Ash	MATTEN	340.00	0.000428	420.00	0.000425	470.00	0.000423	520.00	0.000419
<b>Group#5</b>	20 % GGBFS	MATTEN	751.37	0.000403	871.19	0.000404	992.00	0.000405	1237.71	0.000406
	30% GGBFS	MATTEN	719.00	0.000398	834.00	0.000402	952.00	0.000405	1190.00	0.00041
	40%GGBFS	MATTEN	687.32	0.000377	798.78	0.000378	912.91	0.000378	1144.97	0.000379
	50 % GGBFS	MATTEN	659.17	0.000391	765.60	0.000392	874.34	0.000392	1094.99	0.000393
<b>Group#6</b>	10 % Micro Silica	MATTEN	1027.47	0.000237	1184.32	0.000239	1342.36	0.000241	1659.88	0.000245
	20 % Micro Silica	MATTEN	993.05	0.000269	1143.41	0.000271	1294.51	0.000272	1598.08	0.000274
	30 % Micro Silica	MATTEN	838.35	0.000293	969.12	0.000284	1099.89	0.000278	1361.42	0.000269
	40 % Micro Silica	MATTEN	740.09	0.00035	860.11	0.000336	981.87	0.000325	1228.74	0.00031

**\*MATTEN (Maturity Tension Softening) means change of ultimate Strain with maturity**

**Table A1-7: Change of Ultimate Strain with Equivalent Age (Cont..)**

	Mix Type		$t_e$ (Hour)	$\epsilon_{tu}(m/m)$	$t_e$ (Hour)	$\epsilon_{tu}(m/m)$
<b>Group#1</b>	Control Mix (100% OPC)	MATTEN	2122.67	0.000241	2415.55	0.000241
	20 % Fly Ash	MATTEN	1717.50	0.000265	1831.86	0.000265
	30% Fly Ash	MATTEN	1374.97	0.000272	1580.85	0.000274
	40% Fly Ash	MATTEN	1548.18	0.000317	1785.42	0.000314
	50 % Fly Ash	MATTEN	1003.56	0.000305	1161.98	0.000305
	60 % Fly Ash	MATTEN	1067.20	0.000335	1225.91	0.000334
<b>Group#2</b>	20 % GGBFS	MATTEN	2045.71	0.000257	2331.08	0.000256
	30% GGBFS	MATTEN	1810.64	0.000268	2015.78	0.000268
	40%GGBFS	MATTEN	1818.71	0.000284	2078.09	0.000282
	50 % GGBFS	MATTEN	1777.48	0.000273	2039.36	0.000272
	60 % GGBFS	MATTEN	1550.08	0.00028	1589.15	0.000276
	70% GGBFS	MATTEN	1475.98	0.000293	1682.54	0.00029
<b>Group#3</b>	20 %FA+ GGBFS	MATTEN	2132.10	0.000239	2439.38	0.000239
	30% FA+ GGBFS	MATTEN	1809.63	0.000271	2080.43	0.000272
	40%FA+ GGBFS	MATTEN	1674.43	0.000325	1911.77	0.000325
	50 %FA+ GGBFS	MATTEN	1753.13	0.000395	1813.05	0.000394
	60 % FA+ GGBFS	MATTEN	1310.27	0.000254	1502.74	0.000255
<b>Group#4</b>	(Control)350kg Cement	MATTEN	1435.37	0.000422	1634.60	0.000423
	20 % Fly Ash	MATTEN	1435.37	0.000422	1634.60	0.000422
	30% Fly Ash	MATTEN	1435.37	0.000421	1484.45	0.000414
	40% Fly Ash	MATTEN	1152.79	0.000412	1239.14	0.000418
	50 % Fly Ash	MATTEN	870.22	0.000418	993.84	0.000416
<b>Group#5</b>	20 % GGBFS	MATTEN	610.00	0.000417	715.00	0.000408
	30% GGBFS	MATTEN	1487.69	0.000407	1699.09	0.000415
	40%GGBFS	MATTEN	1434.00	0.000413	1640.00	0.000378
	50 % GGBFS	MATTEN	1381.39	0.000379	1581.08	0.000394
<b>Group#6</b>	10 % Micro Silica	MATTEN	1978.08	0.000249	2244.32	0.000251
	20 % Micro Silica	MATTEN	1903.52	0.000276	2159.59	0.000277
	30 % Micro Silica	MATTEN	1622.96	0.000263	1840.91	0.000259
	40 % Micro Silica	MATTEN	1480.08	0.0003	1692.46	0.000294

**Table A1-8: Change of Ultimate Strain with Equivalent Age**

	Mix Type		$t_e$ (Hour)	$\epsilon_{tu}$ (m/m)	$t_e$ (Hour)	$\epsilon_{tu}$ (m/m)	$t_e$ (Hour)	$\epsilon_{tu}$ (m/m)	$t_e$ (Hour)	$\epsilon_{tu}$ (m/m)
<b>Group#7</b>	30% Fly Ash(0.28W/C)	MATTEN	0.00	0.00	35.78	0.000467	114.96	0.000392	214.32	0.000235
	30% Fly Ash(0.33W/C)	MATTEN	0.00	0.00	31.22	0.0005	99.79	0.000418	190.18	0.000243
	30% Fly Ash(0.38W/C)	MATTEN	0.00	0.00	36.2	0.00082	115.1	0.000708	216.5	0.000442
<b>Group#8</b>	20 % Fly Ash(NC)	MATTEN	0.00	0.00	38.1	0.000382	125.1	0.000326	235.1	0.000253
	30% Fly Ash(NC)	MATTEN	0.00	0.00	39.01	0.000481	122.98	0.000413	229.37	0.000303
	40% Fly Ash(NC)	MATTEN	0.00	0.00	28.02	0.00048	81.84	0.000406	150.72	0.000302
	20 % Fly Ash(SCC)	MATTEN	0.00	0.00	31.61	0.000336	111.23	0.000275	216.93	0.000189
	30% Fly Ash(SCC)	MATTEN	0.00	0.00	29.83	0.0005	103.71	0.000435	202.38	0.000304
	40% Fly Ash(SCC)	MATTEN	0.00	0.00	29.87	0.000523	91.13	0.000462	169.22	0.00035
<b>Group#9</b>	480 kg (Cement)	MATTEN	0.00	0.00	28.89	0.000362	124.09	0.000322	258.26	0.000261
	700 kg (Cement)	MATTEN	0.00	0.00	64.36	0.00046	265.43	0.0004	509.93	0.000326
	900 kg (Cement)	MATTEN	0.00	0.00	145.90	0.000375	473.91	0.000318	852.47	0.000232
<b>Group#10</b>	0.3%Poly-Fibers	MATTEN	0.00	0.00	25.95	0.001264	74.811	0.001262	138.625	0.000803
	0.5%Poly-Fibers	MATTEN	0.00	0.00	27.11	0.001313	77.8	0.001863	141.97	0.000584
	0.3% steel Fibers	MATTEN	0.00	0.00	28.66	0.001969	87.81	0.001863	165.77	0.000765
	0.5 %steel Fibers	MATTEN	0.00	0.00	30.12	0.000926	89.78	0.001535	164.06	0.000673

**Table A1-8: Change of Ultimate Strain with Equivalent Age (Cont..)**

	Mix Type		$t_e$ (Hour)	$\epsilon_{tu}$ (m/m)	$t_e$ (Hour)	$\epsilon_{tu}$ (m/m)	$t_e$ (Hour)	$\epsilon_{tu}$ (m/m)	$t_e$ (Hour)	$\epsilon_{tu}$ (m/m)
<b>Group#7</b>	30% Fly Ash(0.28W/C)	MATTEN	325.98	0.000287	444.80	0.000328	568.39	0.000355	694.98	0.000373
	30% Fly Ash(0.33W/C)	MATTEN	293.22	0.000304	404.36	0.000357	521.20	0.000395	641.99	0.00042
	30% Fly Ash(0.38W/C)	MATTEN	295.3	0.000535	410.31	0.000597	525.1	0.000638	650.25	0.000664
<b>Group#8</b>	20 % Fly Ash(NC)	MATTEN	350.2	0.000243	485.1	0.000246	620.45	0.000248	741.99	0.000251
	30% Fly Ash(NC)	MATTEN	349.88	0.00031	479.05	0.000315	613.69	0.000318	751.89	0.000321
	40% Fly Ash(NC)	MATTEN	229.63	0.000299	315.35	0.000298	405.78	0.000297	499.66	0.000297
	20 % Fly Ash(SCC)	MATTEN	337.08	0.000196	465.80	0.0002	600.20	0.000203	738.78	0.000206
	30% Fly Ash(SCC)	MATTEN	316.22	0.000332	440.25	0.00035	571.47	0.00036	708.22	0.000367
	40% Fly Ash(SCC)	MATTEN	257.18	0.000359	351.96	0.000364	451.90	0.000368	555.72	0.00037
<b>Group#9</b>	480 kg (Cement)	MATTEN	412.40	0.000252	574.94	0.000247	741.79	0.000245	910.79	0.000243
	700 kg (Cement)	MATTEN	774.75	0.000305	1048.21	0.000296	1326.58	0.000292	1607.17	0.00029
	900 kg (Cement)	MATTEN	1258.61	0.000235	1675.72	0.000238	2097.54	0.000243	2521.02	0.000247
<b>Group#10</b>	0.3%Poly-Fibers	MATTEN	212.88	0.000609	294.71	0.000501	382.34	0.000433	473.72	0.000386
	0.5%Poly-Fibers	MATTEN	215.51	0.00049	296.13	0.000418	381.83	0.000371	471.14	0.000337
	0.3% steel Fibers	MATTEN	255.916	0.000482	354.95	0.000363	461.63	0.0003	574.97	0.000262
	0.5 %steel Fibers	MATTEN	248.7	0.000447	340.5	0.000351	438.0167	0.0003	540.042	0.000268

**Table A1-8: Change of Ultimate Strain with Equivalent Age (Cont..)**

	Mix Type		$t_e$ (Hour)	$\epsilon_{tu}$ (m/m)	$t_e$ (Hour)	$\epsilon_{tu}$ (m/m)	$t_e$ (Hour)	$\epsilon_{tu}$ (m/m)	$t_e$ (Hour)	$\epsilon_{tu}$ (m/m)
<b>Group#7</b>	30% Fly Ash(0.28W/C)	MATTEN	824.01	0.000384	954.69	0.000392	1087.19	0.000396	1355.95	0.000401
	30% Fly Ash(0.33W/C)	MATTEN	765.80	0.000437	891.62	0.000449	1019.48	0.000457	1279.38	0.000466
	30% Fly Ash(0.38W/C)	MATTEN	770.12	0.000681	895.22	0.000692	1026.11	0.000699	1285.13	0.000708
<b>Group#8</b>	20 % Fly Ash(NC)	MATTEN	891.2	0.000253	1040.3	0.000255	1192.32	0.000257	1480.21	0.00026
	30% Fly Ash(NC)	MATTEN	893.02	0.000323	1035.84	0.000324	1180.39	0.000326	1473.44	0.000327
	40% Fly Ash(NC)	MATTEN	596.19	0.000296	694.74	0.000296	795.32	0.000296	1001.58	0.000296
	20 % Fly Ash(SCC)	MATTEN	880.34	0.000207	1024.60	0.000209	1171.30	0.000209	1470.41	0.000211
	30% Fly Ash(SCC)	MATTEN	848.15	0.000371	991.08	0.000374	1135.63	0.000376	1429.42	0.000378
	40% Fly Ash(SCC)	MATTEN	662.88	0.000372	772.47	0.000373	884.35	0.000374	1113.62	0.000375
<b>Group#9</b>	480 kg (Cement)	MATTEN	1081.59	0.000243	1253.16	0.000242	1425.50	0.000242	1773.07	0.000239
	700 kg (Cement)	MATTEN	1888.42	0.000289	2169.44	0.000288	2452.18	0.000288	3020.62	0.000288
	900 kg (Cement)	MATTEN	2943.83	0.00025	3366.16	0.000254	3789.31	0.000257	4635.13	0.000263
<b>Group#10</b>	0.3%Poly-Fibers	MATTEN	567.54	0.000351	662.72	0.000325	759.29	0.000303	955.2	0.000272
	0.5%Poly-Fibers	MATTEN	562.56	0.000311	655.38	0.000291	749.14	0.000275	939.73	0.00025
	0.3% steel Fibers	MATTEN	692.005	0.000236	811.416	0.000218	934.12	0.000204	1188.05	0.000185
	0.5 %steel Fibers	MATTEN	644.75	0.000247	751.37	0.000232	860.407	0.00022	1084.13	0.000205

**Table A1-8: Change of Ultimate Strain with Equivalent Age (Cont..)**

	Mix#		$t_e$ (Hour)	$\epsilon_{tu}$ (m/m)	$t_e$ (Hour)	$\epsilon_{tu}$ (m/m)
<b>Group#7</b>	30% Fly Ash(0.28W/C)	MATTEN	1629.40	0.000402	1860.21	0.000402
	30% Fly Ash(0.33W/C)	MATTEN	1544.00	0.000471	1767.78	0.000472
	30% Fly Ash(0.38W/C)	MATTEN	1561.2	0.000711	1780.31	0.000711
<b>Group#8</b>	20 % Fly Ash(NC)	MATTEN	1745.32	0.000263	1780.45	0.000265
	30% Fly Ash(NC)	MATTEN	1737.13	0.000329	1776.20	0.000329
	40% Fly Ash(NC)	MATTEN	1211.98	0.000295	1390.46	0.000295
	20 % Fly Ash(SCC)	MATTEN	1774.81	0.000211	1989.13	0.000212
	30% Fly Ash(SCC)	MATTEN	1727.83	0.000378	1772.13	0.000378
	40% Fly Ash(SCC)	MATTEN	1349.68	0.000376	1552.07	0.000376
<b>Group#9</b>	480 kg (Cement)	MATTEN	2122.67	0.000241	2415.55	0.000241
	700 kg (Cement)	MATTEN	3574.71	0.000289	3613.78	0.00029
	900 kg (Cement)	MATTEN	5481.51	0.000268	5537.40	0.000272
<b>Group#10</b>	0.3%Poly-Fibers	MATTEN	1153.67	0.000249	1320.52	0.000234
	0.5%Poly-Fibers	MATTEN	1132.65	0.000231	1294.76	0.000219
	0.3% steel Fibers	MATTEN	1449.35	0.000173	16811.89	0.000166
	0.5 %steel Fibers	MATTEN	1312.85	0.000194	1506.51	0.000188

## Appendix B

Input File of Pile-Cap

FEMGEN MODEL : Pile-Cap

ANALYSIS TYPE : Heatflow-Stress Staggered 3D

'UNITS'

LENGTH M

TIME HOUR

TEMPER CELSIU

FORCE N

'COORDINATES'

1 0.40 0.20 -1.90

2 0.20 0.20 -1.90

3 0.00 0.20 -1.90

4 0.40 0.20 -2.10

5 0.20 0.20 -2.10

6 0.00 0.20 -2.10

7 0.40 0.40 -1.90

8 0.20 0.40 -1.90

9 0.00 0.40 -1.90

10 0.40 0.40 -2.10

11 0.20 0.40 -2.10

12 0.00 0.40 -2.10

13 0.40 0.18 -1.90

14 0.40 0.00 -1.90

15 0.40 0.18 -2.10

16 0.40 0.00 -2.10

17 0.20 0.18 -1.90

18 0.20 0.00 -1.90

19 0.20 0.18 -2.10

20 0.20 0.00 -2.10

21 0.00 0.18 -1.90

22 0.00 0.00 -1.90

.

.

.

.

.

30459 4.35 4.75 1.42

30460 4.57 4.75 1.51

30461 4.57 4.35 1.51

30462 4.57 4.55 1.51

30463 4.57 4.75 1.70

30464 4.57 4.35 1.70

30465 4.57 4.55 1.70

30466 4.55 4.35 1.72  
 30467 4.35 4.35 1.72  
 30468 4.55 4.55 1.72  
 30469 4.35 4.55 1.72  
 30470 4.55 4.75 1.72  
 30471 4.35 4.75 1.72

# 'ELEMENTS'

## CONNECTIVITY

1 HX24L 27569 27570 27546 27545 27567 27568 27544 27543  
 2 HX24L 27570 25031 25015 27546 27568 25029 25013 27544  
 3 HX24L 25031 25032 25016 25015 25029 25030 25014 25013  
 4 HX24L 25032 22297 22281 25016 25030 22295 22279 25014  
 5 HX24L 22297 22298 22282 22281 22295 22296 22280 22279  
 6 HX24L 22298 19803 19787 22282 22296 19801 19785 22280  
 7 HX24L 19803 19804 19788 19787 19801 19802 19786 19785  
 8 HX24L 19804 17309 17293 19788 19802 17307 17291 19786  
 9 HX24L 17309 17310 17294 17293 17307 17308 17292 17291  
 10 HX24L 17310 13853 13829 17294 17308 13850 13826 17292  
 11 HX24L 13853 13854 13830 13829 13850 13851 13827 13826  
 12 HX24L 13854 13855 13831 13830 13851 13852 13828 13827  
 13 HX24L 13855 11314 11298 13831 13852 11312 11296 13828  
 14 HX24L 11314 11315 11299 11298 11312 11313 11297 11296  
 15 HX24L 11315 8820 8804 11299 11313 8818 8802 11297  
 16 HX24L 8820 8821 8805 8804 8818 8819 8803 8802  
 17 HX24L 8821 6086 6070 8805 8819 6084 6068 8803  
 .  
 .  
 .  
 .  
 7239 HX24L 29954 29953 29949 29947 29943 29944 29941 29939  
 7240 HX24L 29683 29954 29947 29679 29674 29943 29939 29671  
 7241 HX24L 29684 29683 29679 29677 29673 29674 29671 29669  
 7242 HX24L 29434 29433 29429 29427 29423 29424 29421 29419  
 7243 HX24L 29183 29434 29427 29179 29174 29423 29419 29171  
 7244 HX24L 29184 29183 29179 29177 29173 29174 29171 29169  
 7245 HX24L 28871 29184 29177 28866 28858 29173 29169 28854  
 7246 HX24L 28872 28871 28866 28864 28857 28858 28854 28852  
 7247 HX24L 28873 28872 28864 28862 28856 28857 28852 28850  
 7248 HX24L 28578 28873 28862 28574 28569 28856 28850 28566  
 7249 HX24L 28579 28578 28574 28572 28568 28569 28566 28564  
 7250 HX24L 28328 28579 28572 28324 28319 28568 28564 28316  
 7251 HX24L 28329 28328 28324 28322 28318 28319 28316 28314  
 7252 HX24L 28058 28329 28322 28054 28049 28318 28314 28046  
 7253 HX24L 28059 28058 28054 28052 28048 28049 28046 28044  
 7254 HX24L 27808 28059 28052 27804 27799 28048 28044 27796  
 7255 HX24L 27809 27808 27804 27802 27798 27799 27796 27794  
 7256 HX24L 27565 27809 27802 27557 27548 27798 27794 27545  
 7257 HX8HT 27720 27721 27693 27692 27718 27719 27689 27688  
 7258 HX8HT 27721 25189 25159 27693 27719 25187 25155 27689  
 7259 HX8HT 25189 25190 25160 25159 25187 25188 25156 25155

7260 HX8HT 25190 22475 22441 25160 25188 22473 22437 25156  
 7261 HX8HT 22475 22476 22442 22441 22473 22474 22438 22437  
 7262 HX8HT 22476 19961 19931 22442 22474 19959 19927 22438  
 7263 HX8HT 19961 19962 19932 19931 19959 19960 19928 19927  
 7264 HX8HT 19962 17467 17437 19932 19960 17465 17433 19928  
 7265 HX8HT 17467 17468 17438 17437 17465 17466 17434 17433  
 7266 HX8HT 17468 14070 14029 17438 17466 14067 14023 17434  
 7267 HX8HT 14070 14071 14030 14029 14067 14068 14024 14023  
 7268 HX8HT 14071 14072 14031 14030 14068 14069 14025 14024  
 7269 HX8HT 14072 11472 11442 14031 14069 11470 11438 14025  
 .  
 .  
 .  
 .  
 7774 HX8HT 17217 17218 17164 17163 17214 17215 17158 17157  
 7775 HX8HT 17218 13716 13676 17164 17215 13714 13672 17158  
 7776 HX8HT 13716 13717 13677 13676 13714 13715 13673 13672  
 7777 HX8HT 13717 11222 11182 13677 13715 11220 11178 13673  
 7778 HX8HT 11222 11223 11183 11182 11220 11221 11179 11178  
 7779 HX8HT 11223 8728 8682 11183 11221 8726 8678 11179  
 7780 HX8HT 8728 8729 8683 8682 8726 8727 8679 8678  
 7781 HX8HT 8729 5994 5954 8683 8727 5992 5950 8679  
 7782 HX8HT 5994 5995 5955 5954 5992 5993 5951 5950  
 7783 HX8HT 5995 3499 3445 5955 5993 3496 3439 5951  
 7784 HX8HT 3499 3500 3446 3445 3496 3497 3440 3439  
 7785 HX8HT 3500 3501 3447 3446 3497 3498 3441 3440  
 7786 CHX60 27695 27706 27691 27702 27690 27707 27694 27697 27698 27701 27703  
 27696 27693 27704 27689 27700 27688 27705 27692 27699  
 7787 CHX60 25161 25170 25157 25168 27691 27706 27695 25163 25164 25167 27701  
 27698 25159 25169 25155 25166 27689 27704 27693 25165  
 7788 CHX60 25162 25178 25158 25176 25157 25170 25161 25171 25172 25175 25167  
 25164 25160 25177 25156 25174 25155 25169 25159 25173  
 7789 CHX60 22443 22452 22439 22450 25158 25178 25162 22445 22446 22449 25175  
 25172 22441 22451 22437 22448 25156 25177 25160 22447  
 7790 CHX60 22444 22460 22440 22458 22439 22452 22443 22453 22454 22457 22449  
 22446 22442 22459 22438 22456 22437 22451 22441 22455  
 7791 CHX60 19933 19938 19929 22464 22440 22460 22444 22461 19935 19936 22457  
 22454 19931 19937 19927 22463 22438 22459 22442 22462  
 7792 CHX60 19934 19946 19930 19944 19929 19938 19933 19939 19940 19943 19936  
 19935 19932 19945 19928 19942 19927 19937 19931 19941  
 7793 CHX60 17439 17444 17435 19950 19930 19946 19934 19947 17441 17442 19943  
 19940 17437 17443 17433 19949 19928 19945 19932 19948  
 .  
 .  
 .  
 .  
 12537 CHX60 13503 13541 13501 13527 13500 13538 13502 13539 13540 13528 13525  
 13537 13509 13535 13507 13521 13506 13532 13508 13533  
 12538 CHX60 11008 11044 11006 11030 13501 13541 13503 11042 11043 11031 13528  
 13540 11014 11038 11012 11024 13507 13535 13509 11036

12539 CHX60 11009 11047 11007 11033 11006 11044 11008 11045 11046 11034 11031  
 11043 11015 11041 11013 11027 11012 11038 11014 11039  
 12540 CHX60 8484 8525 8482 8509 11007 11047 11009 8523 8524 8510 11034  
 11046 8490 8518 8488 8502 11013 11041 11015 8516  
 12541 CHX60 8485 8528 8483 8512 8482 8525 8484 8526 8527 8513 8510 8524  
 8491 8521 8489 8505 8488 8518 8490 8519  
 12542 CHX60 5780 5815 5778 8515 8483 8528 8485 8529 5814 5802 8513 8527  
 5786 5809 5784 8508 8489 8521 8491 8522  
 12543 CHX60 5781 5818 5779 5804 5778 5815 5780 5816 5817 5805 5802 5814  
 5787 5812 5785 5798 5784 5809 5786 5810  
 12544 CHX60 3208 3255 3205 5807 5779 5818 5781 5819 3254 3238 5805 5817  
 3217 3247 3214 5801 5785 5812 5787 5813  
 12545 CHX60 3209 3258 3206 3240 3205 3255 3208 3256 3257 3241 3238 3254  
 3218 3250 3215 3232 3214 3247 3217 3248  
 12546 CHX60 3210 3261 3207 3243 3206 3258 3209 3259 3260 3244 3241 3257  
 3219 3253 3216 3235 3215 3250 3218 3251  
 12547 BQ4HT 27692 27693 27689 27688  
 12548 BQ4HT 27693 25159 25155 27689  
 12549 BQ4HT 25159 25160 25156 25155  
 12550 BQ4HT 25160 22441 22437 25156  
 12551 BQ4HT 22441 22442 22438 22437  
 12552 BQ4HT 22442 19931 19927 22438  
 12553 BQ4HT 19931 19932 19928 19927  
 12554 BQ4HT 19932 17437 17433 19928  
 12555 BQ4HT 17437 17438 17434 17433  
 12556 BQ4HT 17438 14029 14023 17434  
 12557 BQ4HT 14029 14030 14024 14023

.  
 .  
 .  
 .  
 .  
 .  
 .

14011 BQ4HT 11222 11223 11221 11220  
 14012 BQ4HT 11223 8728 8726 11221  
 14013 BQ4HT 8728 8729 8727 8726  
 14014 BQ4HT 8729 5994 5992 8727  
 14015 BQ4HT 5994 5995 5993 5992  
 14016 BQ4HT 5995 3499 3496 5993  
 14017 BQ4HT 3499 3500 3497 3496  
 14018 BQ4HT 3500 3501 3498 3497

#### MATERIALS

/ 623-1036 / 1  
 / 12547-14018 / 2  
 / 7786-12546 / 3  
 / 1-622/ 4  
 / 1037-7256/ 5  
 / 7257-7785/ 6

'REINFO'

LOCATION



14019 BAR  
     LINE 36599 36600  
 14020 BAR  
     LINE 36600 36601  
 14021 BAR  
     LINE 36601 36341  
 14022 BAR  
     LINE 36341 36342  
 14023 BAR  
     LINE 36342 36056  
 14024 BAR  
     LINE 36056 36057  
 14025 BAR  
     LINE 36057 36058  
 14026 BAR  
     LINE 36058 35814  
 14027 BAR  
     LINE 35814 35815  
 14028 BAR  
     LINE 35815 35533  
 14029 BAR  
     LINE 35533 35534  
 14030 BAR  
     LINE 35534 35535  
 14031 BAR  
     LINE 35535 35275  
 .  
 .  
 .  
 .  
 .  
 .  
 38440 BAR  
     LINE 479 476  
 38441 BAR  
     LINE 193 195  
 38442 BAR  
     LINE 472 193  
 38443 BAR  
     LINE 473 472  
 38444 BAR  
     LINE 476 473  
 38445 BAR  
     LINE 194 193  
 38446 BAR  
     LINE 473 194  
 GEOMETRY  
 /14019-15999 23501-38446/ 1  
 /16000-23500/2  
 MATERIALS

'MATERIALS'

1 CONDUCT 4.800000E+02  
CAPACI 7.943999E+05  
2 CONVEC 9.126000E+04  
Emissi 0.2  
CONDUCT 7.92000E+003  
CAPACI 2.67560E+006  
ARRHEN 4.11775E+003  
EQUAGE ARRTYP  
TEMREF 2.00000E+001  
POISON 2.00000E-001  
YOUNG 2.52350E+010  
DENSIT 2.24800E+003  
THERMX 9.16000E-006  
TAUCRI 1  
BETA 2.00000E-001  
CRACK 1  
MATCRK 0.00000E+000 0.00000E+000 2.38400E+001 9.29000E+005  
4.93800E+001 1.21000E+006 9.42500E+001 1.60000E+006  
1.54580E+002 1.86000E+006 2.23670E+002 2.03000E+006  
2.99200E+002 2.16000E+006 3.79230E+002 2.26000E+006  
4.62740E+002 2.33000E+006 5.48740E+002 2.39000E+006  
6.36780E+002 2.44000E+006 8.17600E+002 2.49000E+006  
1.00356E+003 2.57000E+006 1.16198E+003 2.61000E+006  
TENSIO 1  
MATTEN 0.00000E+000 0.00000E+000 2.38400E+001 5.99742E-004  
4.93800E+001 5.02764E-004 9.42500E+001 4.14103E-004  
1.54580E+002 3.67185E-004 2.23670E+002 3.43554E-004  
2.99200E+002 3.29901E-004 3.79230E+002 3.21358E-004  
4.62740E+002 3.15747E-004 5.48740E+002 3.11951E-004  
6.36780E+002 3.09346E-004 8.17600E+002 3.09475E-004  
1.00356E+003 3.05073E-004 1.16198E+003 3.04759E-004  
ADIAB 1.00000E+000 2.04700E+001 2.00000E+000 2.05900E+001  
3.00000E+000 2.07700E+001 4.00000E+000 2.17000E+001  
5.00000E+000 2.33500E+001 6.00000E+000 2.57800E+001  
7.00000E+000 2.86900E+001 8.00000E+000 3.23100E+001  
9.00000E+000 3.57800E+001 1.00000E+001 3.83500E+001  
1.10000E+001 4.06600E+001 1.20000E+001 4.28700E+001  
1.30000E+001 4.49000E+001 1.40000E+001 4.68000E+001  
1.50000E+001 4.85900E+001 1.60000E+001 5.02200E+001  
1.70000E+001 5.16700E+001 1.80000E+001 5.29400E+001  
1.90000E+001 5.40100E+001 2.00000E+001 5.49000E+001  
2.10000E+001 5.57000E+001 2.20000E+001 5.63500E+001  
2.30000E+001 5.69500E+001 2.40000E+001 5.74300E+001  
2.50000E+001 5.78700E+001 2.60000E+001 5.82800E+001  
2.70000E+001 5.86700E+001 2.80000E+001 5.90200E+001  
2.90000E+001 5.92600E+001 3.00000E+001 5.95500E+001

3.10000E+001	5.99000E+001	3.20000E+001	6.01300E+001
3.30000E+001	6.03100E+001	3.40000E+001	6.05100E+001
3.50000E+001	6.07400E+001	3.60000E+001	6.09000E+001
3.70000E+001	6.10900E+001	3.80000E+001	6.12700E+001
3.90000E+001	6.14000E+001	4.00000E+001	6.15500E+001
4.10000E+001	6.16400E+001	4.20000E+001	6.17600E+001
4.30000E+001	6.19200E+001	4.40000E+001	6.19700E+001
4.50000E+001	6.21200E+001	4.60000E+001	6.22300E+001
4.70000E+001	6.23000E+001	4.80000E+001	6.23800E+001
4.90000E+001	6.24800E+001	5.00000E+001	6.25600E+001
5.10000E+001	6.26500E+001	5.20000E+001	6.27400E+001
5.30000E+001	6.28200E+001	5.40000E+001	6.28800E+001
5.50000E+001	6.29400E+001	5.60000E+001	6.29900E+001
5.70000E+001	6.30600E+001	5.80000E+001	6.31300E+001
5.90000E+001	6.31500E+001	6.00000E+001	6.32000E+001
6.10000E+001	6.33200E+001	6.20000E+001	6.33900E+001
6.30000E+001	6.34200E+001	6.40000E+001	6.34500E+001
6.50000E+001	6.35400E+001	6.60000E+001	6.35500E+001
6.70000E+001	6.35600E+001	6.80000E+001	6.35900E+001
6.90000E+001	6.36900E+001	7.00000E+001	6.37400E+001
7.10000E+001	6.37400E+001	7.20000E+001	6.37700E+001
7.30000E+001	6.37700E+001	7.40000E+001	6.38000E+001
7.50000E+001	6.38500E+001	7.60000E+001	6.38600E+001
7.70000E+001	6.38600E+001	7.80000E+001	6.39500E+001
7.90000E+001	6.39900E+001	8.00000E+001	6.40000E+001
8.10000E+001	6.40700E+001	8.20000E+001	6.41000E+001
8.30000E+001	6.41100E+001	8.40000E+001	6.41600E+001
8.50000E+001	6.41800E+001	8.60000E+001	6.42200E+001
8.70000E+001	6.42400E+001	8.80000E+001	6.42500E+001
8.90000E+001	6.42500E+001	9.00000E+001	6.42800E+001
9.10000E+001	6.43000E+001	9.20000E+001	6.43200E+001
9.30000E+001	6.43600E+001	9.40000E+001	6.43600E+001
9.50000E+001	6.44000E+001	9.60000E+001	6.44200E+001
9.70000E+001	6.44400E+001	9.80000E+001	6.44500E+001
9.90000E+001	6.44800E+001	1.00000E+002	6.45000E+001
1.01000E+002	6.45500E+001	1.02000E+002	6.45600E+001
1.03000E+002	6.45700E+001	1.04000E+002	6.46100E+001
1.05000E+002	6.46100E+001	1.06000E+002	6.46200E+001
1.07000E+002	6.46400E+001	1.08000E+002	6.47000E+001
1.09000E+002	6.47300E+001	1.10000E+002	6.47400E+001
1.11000E+002	6.48000E+001	1.12000E+002	6.48200E+001
1.13000E+002	6.48400E+001	1.14000E+002	6.48500E+001
1.15000E+002	6.48600E+001	1.16000E+002	6.48700E+001
1.17000E+002	6.48700E+001	1.18000E+002	6.48900E+001
1.19000E+002	6.49100E+001	1.20000E+002	6.49100E+001
1.21000E+002	6.49100E+001	1.22000E+002	6.49300E+001
1.23000E+002	6.49300E+001	1.24000E+002	6.49300E+001
1.25000E+002	6.49400E+001	1.26000E+002	6.49500E+001
1.27000E+002	6.49800E+001	1.28000E+002	6.49900E+001
1.29000E+002	6.50100E+001	1.30000E+002	6.50200E+001

1.31000E+002	6.50200E+001	1.32000E+002	6.50300E+001
1.33000E+002	6.50500E+001	1.34000E+002	6.51000E+001
1.35000E+002	6.51200E+001	1.36000E+002	6.51300E+001
1.37000E+002	6.51500E+001	1.38000E+002	6.51500E+001
1.39000E+002	6.51700E+001	1.40000E+002	6.51800E+001
1.41000E+002	6.51900E+001	1.42000E+002	6.52100E+001
1.43000E+002	6.52300E+001	1.44000E+002	6.52500E+001
1.45000E+002	6.52800E+001	1.46000E+002	6.53100E+001
1.47000E+002	6.53200E+001	1.48000E+002	6.53200E+001
1.49000E+002	6.53400E+001	1.50000E+002	6.53400E+001
1.51000E+002	6.53500E+001	1.52000E+002	6.53500E+001
1.53000E+002	6.53800E+001	1.54000E+002	6.53800E+001
1.55000E+002	6.53800E+001	1.56000E+002	6.54000E+001
1.57000E+002	6.54000E+001	1.58000E+002	6.54300E+001
1.59000E+002	6.54500E+001	1.60000E+002	6.54700E+001
1.61000E+002	6.55000E+001	1.62000E+002	6.55100E+001
1.63000E+002	6.55100E+001	1.64000E+002	6.55100E+001
1.65000E+002	6.55500E+001	1.66000E+002	6.55600E+001
1.67000E+002	6.55700E+001	1.68000E+002	6.55700E+001
1.69000E+002	6.55800E+001	1.70000E+002	6.55900E+001
1.71000E+002	6.56000E+001	1.72000E+002	6.56100E+001
1.73000E+002	6.56200E+001	1.74000E+002	6.56300E+001
1.75000E+002	6.56400E+001	1.76000E+002	6.56500E+001
1.77000E+002	6.56600E+001	1.78000E+002	6.56700E+001
1.79000E+002	6.56800E+001	1.80000E+002	6.56900E+001
1.81000E+002	6.57000E+001	1.82000E+002	6.57100E+001
1.83000E+002	6.57200E+001	1.84000E+002	6.57300E+001
1.85000E+002	6.57400E+001	1.86000E+002	6.57500E+001
1.87000E+002	6.57600E+001	1.88000E+002	6.57700E+001
FTVALU	0.00000E+000	9.29000E+005	1.21000E+006
	1.60000E+006	2.03000E+006	2.16000E+006
	2.26000E+006	2.33000E+006	2.39000E+006
	2.44000E+006	2.49000E+006	2.57000E+006
	2.61000E+006		
FTTIME	0.00000E+000	1.20000E+001	2.40000E+001
	3.60000E+001	4.80000E+001	6.00000E+001
	7.20000E+001	8.40000E+001	9.60000E+001
	1.08000E+002	1.20000E+002	1.44000E+002
	1.68000E+002	1.88000E+002	
FTMATU	0.00000E+000	2.38400E+001	4.93800E+001
	9.42500E+001	1.54580E+002	2.23670E+002
	2.99200E+002	3.79230E+002	4.62740E+002
	5.48740E+002	6.36780E+002	8.17600E+002
	1.00356E+003	1.16198E+003	
MAXWEL	1		
,1 TIME	0.00000E+000	1.20000E+001	2.40000E+001
	3.60000E+001	4.80000E+001	6.00000E+001
	7.20000E+001	8.40000E+001	9.60000E+001
	1.08000E+002	1.20000E+002	1.44000E+002
	1.68000E+002	1.88000E+002	
YOUNG	1.00000E+009	6.12000E+009	7.96000E+009
	1.06000E+010	1.22000E+010	1.35000E+010
	1.45000E+010	1.54000E+010	1.61000E+010
	1.68000E+010	1.74000E+010	1.80000E+010
	1.92000E+010	1.97000E+010	

```

4 CONDUCT 1.91000E+002
  CAPACI 3.20000E+003
  YOUNG 6.30000E+006
  POISON 3.00000E-001
  DENSIT 1.72000E+003
  THERMX 7.00000E-006
4 CONDUCT 2.530000E+03
  CAPACI 1.20000E+06
  YOUNG 2.000000E+10
  POISON 2.000000E-01
  DENSIT 1.6000000E+03
  THERMX 9.600000E-06

5 CONDUCT 1.910000E+02
  CAPACI 3.200000E+03
  YOUNG 6.300000E+07
  POISON 3.000000E-01
  DENSIT 1.720000E+03
  THERMX 7.000000E-06
6 CONDUCT 2.08E+03
  CAPACI 7.053999E+05
7 YOUNG 20E+10
  CONDUCT 154.8E+03
  THERMX 13.0000E-06
  CAPACI 3.800000E+06
  DENSIT 7.80000E+03
  POISON 0.3
  YIELD VMISES
  HARDIA 250.0E+06 0. 260.0E+06 .0001 270.0E+06 .0002 290.0E+06 0.02
  HARDEN WORK
'GEOMETRY'
1 CROSSE 0.00049
2 CROSSE 0.00201
'SUPPORTS'
/ 2, 4, 14, 20,....., 38977, 38984, 38985, 38988, 38989 / TR 1
/ 6, 8, 10, 12, 16,....., 39101, 39107, 39108, 39109/ TR 2
/ 3, 4, 198, 199,..., 38741, 38743, 38927, 38929 / TR 3
'GROUPS'
ELEMENTS
1 concrete / 7786-12546 /
2 boundary / 12547-14018 /
3 wood /623-1036/
4 blindconcrete /1-622/
5 soil /1037-7256/
6 WATER /7257-7785/
NODES
7 group1 / 1-1000/
8 group2 / 1001-30471/
'BOUNDARY'
CASE 1

```

```

ELEMEN
12547 EXTEMP 1.00000E+000
12548 EXTEMP 1.00000E+000
12549 EXTEMP 1.00000E+000
12550 EXTEMP 1.00000E+000
12551 EXTEMP 1.00000E+000
12552 EXTEMP 1.00000E+000
12553 EXTEMP 1.00000E+000
12554 EXTEMP 1.00000E+000
12555 EXTEMP 1.00000E+000
12556 EXTEMP 1.00000E+000
.
.
.
. 14008 EXTEMP 1.00000E+000
14009 EXTEMP 1.00000E+000
14010 EXTEMP 1.00000E+000
14011 EXTEMP 1.00000E+000
14012 EXTEMP 1.00000E+000
14013 EXTEMP 1.00000E+000
14014 EXTEMP 1.00000E+000
14015 EXTEMP 1.00000E+000
14016 EXTEMP 1.00000E+000
14017 EXTEMP 1.00000E+000
'TIMEBO'
BOUND A 1
TIMES 0.00000E+000 1.00000E+000 2.00000E+000 3.00000E+000 4.00000E+000
5.00000E+000 6.00000E+000 7.00000E+000 8.00000E+000 9.00000E+000
1.00000E+001 1.10000E+001 1.20000E+001 1.30000E+001 1.40000E+001
1.50000E+001 1.60000E+001 1.70000E+001 1.80000E+001 1.90000E+001
2.00000E+001 2.10000E+001 2.20000E+001 2.30000E+001 2.40000E+001
2.50000E+001 2.60000E+001 2.70000E+001 2.80000E+001 2.90000E+001
3.00000E+001 3.10000E+001 3.20000E+001 3.30000E+001 3.40000E+001
3.50000E+001 3.60000E+001 3.70000E+001 3.80000E+001 3.90000E+001
4.00000E+001 4.10000E+001 4.20000E+001 4.30000E+001 4.40000E+001
4.50000E+001 4.60000E+001 4.70000E+001 4.80000E+001 4.90000E+001
5.00000E+001 5.10000E+001 5.20000E+001 5.30000E+001 5.40000E+001
5.50000E+001 5.60000E+001 5.70000E+001 5.80000E+001 5.90000E+001
6.00000E+001 6.10000E+001 6.20000E+001 6.30000E+001 6.40000E+001
6.50000E+001 6.60000E+001 6.70000E+001 6.80000E+001 6.90000E+001
7.00000E+001 7.10000E+001 7.20000E+001 7.30000E+001 7.40000E+001
7.50000E+001 7.60000E+001 7.70000E+001 7.80000E+001 7.90000E+001
8.00000E+001 8.10000E+001 8.20000E+001 8.30000E+001 8.40000E+001
8.50000E+001 8.60000E+001 8.70000E+001 8.80000E+001 8.90000E+001
9.00000E+001 9.10000E+001 9.20000E+001 9.30000E+001 9.40000E+001
9.50000E+001 9.60000E+001 9.70000E+001 9.80000E+001 9.90000E+001
1.00000E+002 1.01000E+002 1.02000E+002 1.03000E+002 1.04000E+002
1.05000E+002 1.06000E+002 1.07000E+002 1.08000E+002 1.09000E+002
1.10000E+002 1.11000E+002 1.12000E+002 1.13000E+002 1.14000E+002
1.15000E+002 1.16000E+002 1.17000E+002 1.18000E+002 1.19000E+002

```

1.20000E+002	1.21000E+002	1.22000E+002	1.23000E+002	1.24000E+002
1.25000E+002	1.26000E+002	1.27000E+002	1.28000E+002	1.29000E+002
1.30000E+002	1.31000E+002	1.32000E+002	1.33000E+002	1.34000E+002
1.35000E+002	1.36000E+002	1.37000E+002	1.38000E+002	1.39000E+002
1.40000E+002	1.41000E+002	1.42000E+002	1.43000E+002	1.44000E+002
1.45000E+002	1.46000E+002	1.47000E+002	1.48000E+002	1.49000E+002
1.50000E+002	1.51000E+002	1.52000E+002	1.53000E+002	1.54000E+002
1.55000E+002	1.56000E+002	1.57000E+002	1.58000E+002	1.59000E+002
1.60000E+002	1.61000E+002	1.62000E+002	1.63000E+002	1.64000E+002
1.65000E+002	1.66000E+002	1.67000E+002	1.68000E+002	1.69000E+002
1.70000E+002	1.71000E+002	1.72000E+002	1.73000E+002	1.74000E+002
1.75000E+002	1.76000E+002	1.77000E+002	1.78000E+002	1.79000E+002
1.80000E+002	1.81000E+002	1.82000E+002	1.83000E+002	1.84000E+002
1.85000E+002	1.86000E+002	1.87000E+002	1.88000E+002 /	
FACTOR	3.40000E+001	3.40000E+001	3.30000E+001	3.20000E+001 3.10000E+001
3.20000E+001	3.40000E+001	3.20000E+001	3.20000E+001	3.30000E+001
3.10000E+001	3.10000E+001	3.00000E+001	3.00000E+001	3.20000E+001
3.50000E+001	3.60000E+001	3.80000E+001	3.90000E+001	3.80000E+001
3.70000E+001	3.80000E+001	3.70000E+001	3.70000E+001	3.50000E+001
3.30000E+001	3.20000E+001	3.20000E+001	3.10000E+001	3.20000E+001
3.10000E+001	3.20000E+001	3.00000E+001	2.90000E+001	3.00000E+001
3.10000E+001	3.00000E+001	3.20000E+001	3.40000E+001	3.60000E+001
3.70000E+001	3.90000E+001	4.00000E+001	3.90000E+001	3.70000E+001
3.60000E+001	3.60000E+001	3.60000E+001	3.40000E+001	3.30000E+001
3.20000E+001	3.20000E+001	3.20000E+001	3.30000E+001	3.20000E+001
3.20000E+001	3.10000E+001	3.20000E+001	3.20000E+001	3.20000E+001
3.10000E+001	3.10000E+001	3.30000E+001	3.50000E+001	3.70000E+001
3.80000E+001	3.90000E+001	3.90000E+001	3.80000E+001	4.00000E+001
3.80000E+001	3.60000E+001	3.40000E+001	3.30000E+001	3.20000E+001
3.30000E+001	3.30000E+001	3.30000E+001	3.20000E+001	3.40000E+001
3.10000E+001	3.20000E+001	3.30000E+001	3.20000E+001	3.20000E+001
3.10000E+001	3.30000E+001	3.60000E+001	3.80000E+001	3.80000E+001
3.50000E+001	3.40000E+001	3.30000E+001	3.20000E+001	3.10000E+001
3.00000E+001	3.00000E+001	3.00000E+001	2.90000E+001	2.80000E+001
2.80000E+001	2.80000E+001	2.80000E+001	2.90000E+001	3.10000E+001
3.40000E+001	3.20000E+001	3.20000E+001	3.20000E+001	3.10000E+001
3.10000E+001	3.00000E+001	3.00000E+001	2.90000E+001	2.90000E+001
2.90000E+001	2.90000E+001	2.80000E+001	2.90000E+001	3.20000E+001
3.50000E+001	3.70000E+001	3.70000E+001	3.50000E+001	3.30000E+001
3.20000E+001	3.20000E+001	3.10000E+001	3.10000E+001	3.00000E+001
3.00000E+001	2.90000E+001	2.80000E+001	2.80000E+001	2.80000E+001
2.80000E+001	2.90000E+001	3.20000E+001	3.50000E+001	3.70000E+001
3.80000E+001	4.00000E+001	4.20000E+001	3.70000E+001	3.60000E+001
3.70000E+001	3.60000E+001	3.40000E+001	3.20000E+001	3.10000E+001
3.00000E+001	3.00000E+001	3.00000E+001	3.00000E+001	2.90000E+001
2.90000E+001	2.90000E+001	2.90000E+001	2.80000E+001	3.00000E+001
3.40000E+001	3.60000E+001	4.10000E+001	4.00000E+001	4.10000E+001
4.10000E+001	4.00000E+001	3.70000E+001	3.70000E+001	3.10000E+001
3.10000E+001	3.00000E+001	3.00000E+001	3.00000E+001	2.90000E+001
2.90000E+001	3.00000E+001	3.50000E+001	3.60000E+001	4.10000E+001

```

4.20000E+001 4.20000E+001 4.40000E+001 3.80000E+001 3.70000E+001
3.60000E+001 3.50000E+001 3.50000E+001 3.30000E+001 /
'LOADS'
CASE 2
WEIGHT
3 -9.81000
'TIMELO'
LOAD 2
TIMES 0.00000E+000 1.88000E+002 /
FACTOR 1.00000E+000 1.00000E+000 /
'INIVAR'
TEMPER 1
/ 145 146 147 152 156 157 161.....27710 27711 27718 27719/ 34
/ 350 351 352 353 354 355 636 ....30468 30469 30470 30471/10
/ 1 2 3 4 5 6 7 8 9 10 11 12.... 14 28 42 56 70 84 98 / 30
/ 148 149 150 151 153 154 155.....30282 30289 30291 30292 / 34
'DIRECTIONS'
1 1.000000E+00 0.000000E+00 0.000000E+00
2 0.000000E+00 1.000000E+00 0.000000E+00
3 0.000000E+00 0.000000E+00 1.000000E+00
'END'

```



## **VITA**

**NAME** : Muneer Qaid Saeed Abdo  
**Nationality** : Yemeni  
**Date of Birth** : 6/5/1977  
**E-MAIL** : Mounir \_Almekhlafi@ hotmail.com  
**ADDRESS** : Almekhlaf- Sharaab Alsalam  
Taiz City  
Yemen

### **Academic Background:**

**M.S (Civil Engineering – Structures)**

**February 2005-April 2009**

**King Fahd University of Petroleum and Minerals,**

**Dhahran, Saudi Arabia**

**GPA- 3.906/4.00**

**B.E. (Civil Engineering)**

**September 1996-April 2001**

**Tishreen University – Syria**

**Concrete Technology:** including Self compacting concrete , High performance concrete

**Simulation and Modeling** Using Finite Element method

### **Academic Experience**

King Fahd University of Petroleum and Minerals (KFUPM), Dhahran, Saudi Arabia  
Lecturer assistant

1- Statics

2- Mechanics of materials 3- Structural Analysis 4- Steel design and analysis 5- Concrete design using STAADPPR

Sana'a University, Sana'a, Yemen

Lecturer assistant

- Mechanics of materials.
- Computer programs for engineering
- Structural Analysis

### Carrier Experience

- Albukhaiti office for construction – Sana'a –Yemen  
As a design engineer from 12/6/2001-30/1/2002
- International De Development Et De Construction Company – Sana'a –Yemen  
As a section engineer (Supervisor) from 7/2/2002-15/9/2002
- Social Fund for Development – Tamar –Yemen  
As a designer and supervisor for many projects specially schools from 7/2/2002-15/9/2004
- Worked with a team in KFUPM to investigate and analyze the causes of Collapse of bridge in Makah City.
- Worked with a team in KFUPM to investigate and analyze the causes of Collapse building in Dammam City.

### Publications

1. **M.K. Said** ,M.K. Rahman, and M.H. Baluch, "Analysis and Design of Prestressed Precast Hollow Core Slabs Using Strut and Tie Method" *AJSE Journal*, March 2012, Volume 37, [Issue 2](#), pp 457-468
2. M.K. Rahman, M.H. Baluch, **M.K. Said** and M.A.Shazali, "Flexural and Shear Strength of Prestressed Precast Hollow-Core Slabs" *AJSE Journal* ,March 2012, Volume 37, [Issue 2](#), pp 443-455
3. **M.K. Said** ,M.H. Baluch, and M.K. Rahman, "Modeling Shear and Flexural Response of Hollow Core Slabs Using Truss Analogy." *The 9h International Conference on Concrete August 2008, University of Coimbra, Portugal*
4. M.K. Rahman, **M.K. Said** and M.H. Baluch, "Proposed Revision in ACI Code Equation for Flexure-Shear Capacity of Prestressed Hollow Core Slabs." *The 9h International Conference on Concrete August 2008, University of Coimbra, Portugal*
5. **M.K. Said** ,M.H. Baluch, and M.K. Rahman," Finite Element Simulation of Thermal Cracking in Mass Concrete at Early Age." *9th Intl Concrete Conference and Exhibition, Bahrain, February 2013.*

6. M.K. Rahman, **M.K. Said**, M.H. Baluch, and Khaldoon S, "Finite Element Simulation of Evolution of Temperature and Thermal Stresses in Mass Self Compacting Concrete Elements at an Early Age." *Fifth North American Conference on the Design and Use of Self-Consolidating Concrete (SCC2013)*, Chicago, IL, USA, May 2013.
7. **M.K. Said**, M.H. Baluch, M.K. Rahman, and Khaldoon S, "Investigations of Early Age Thermal Cracking of Mass Concrete With GGBFS and Fly Ash." *The Seventh International Conference on Concrete Under Severe Conditions-Environment and Loading Chicago, Nanjing, China, Sep 2013*.
8. M.K. Rahman, **M.K. Said**, M.H. Baluch, and Khaldoon S, "Finite Element Modeling And Field Measurement Of Temperature And Stress Evolution In A Bridge Piles Cap." *The Seventh International Conference on Concrete Under Severe Conditions-Environment and Loading Chicago, Nanjing, China, Sep 2013*.
9. **M.K. Said**, M.K. Rahman, M.H. Baluch, "Investigation Of Temperature Rise And Cracking Index In Mass Concrete At Early Age " Ready for submission.
10. M.K. Rahman, **M.K. Said**, M.H. Baluch, "Experimental and Numerical Investigations of Cracking Risk n Mass Concrete Using GGBFS And Fly Ash in Hot Weather Conditions in Saudi Arabia." Ready for submission.

### Major Achievements and Awards

1. Received a teaching position from Ministry of Education in Yemen as an award for achieving advance level in high school certificate.(out of 10 in the Republic)
2. Received full scholarships from Ministry of Higher Education in Yemen to complete BS. degree in Tishreen University in 1995.
3. Award from Tishreen University for achieving the 3<sup>rd</sup> rank over the University.
4. Received full scholarships from Ministry of Higher Education in Yemen to complete Master and PhD. degree in KFUPM University, 2005.